University of Illinois at Urbana-Champaign

ACRC

Air Conditioning and Refrigeration Center A National Science Foundation/University Cooperative Research Center

Single Phase, Two-Phase Modeling; X-Ray Visualization for a Microchannel Manifold Distribution System

D. M. Tompkins, T. A. Newell, and P. S. Hrnjak

ACRC TR-206 December 2002

For additional information:

Air Conditioning and Refrigeration Center
University of Illinois
Mechanical & Industrial Engineering Dept.
1206 West Green Street
Urbana, IL 61801

(217) 333-3115

Prepared as part of ACRC Project #138
Flow Distribution and Pressure Drop in Microchannel Manifolds
T. A. Newell, and P. S. Hrnjak, Principal Investigators

The Air Conditioning and Refrigeration Center was founded in 1988 with a grant from the estate of Richard W. Kritzer, the founder of Peerless of America Inc. A State of Illinois Technology Challenge Grant helped build the laboratory facilities. The ACRC receives continuing support from the Richard W. Kritzer Endowment and the National Science Foundation. The following organizations have also become sponsors of the Center.

Alcan Aluminum Corporation
Amana Refrigeration, Inc.
Arçelik A. S.
Brazeway, Inc.
Carrier Corporation
Copeland Corporation
Dacor
Daikin Industries, Ltd.
Delphi Harrison Thermal Systems
Embraco S. A.
General Motors Corporation
Hill PHOENIX
Honeywell, Inc.
Hydro Aluminum Adrian, Inc.
Ingersoll-Rand Company
Kelon Electrical Holdings Co., Ltd.
Lennox International, Inc.
LG Electronics, Inc.
Modine Manufacturing Co.
Parker Hannifin Corporation
Peerless of America, Inc.
Samsung Electronics Co., Ltd.
Tecumseh Products Company
The Trane Company
Valeo, Inc.
Visteon Automotive Systems
Wolverine Tube, Inc.

For additional information:

Air Conditioning & Refrigeration Center
Mechanical & Industrial Engineering Dept.
University of Illinois
1206 West Green Street
Urbana, IL 61801

217 333 3115

Abstract

In Chapter 1, an experimental investigation of single phase fluid distribution through an array of microchannel discharge tubes was conducted. Span-wise pressure profiles were also obtained. The working fluids were air and water. The distribution manifold was oriented horizontally and the microchannels vertically downward. All tests were adiabatic. The discharge tubes are 6-port aluminum microchannel tubes having a hydraulic diameter of 1.54mm and a cross-sectional area of 1.669x10-5 m2.

Three spacer plates (12.7mm, 6.35mm, and 3.175mm) were employed to change the cross sectional area of the manifold distribution channel. This changes the area ratio, defined as the ratio of total available discharge area to total inlet manifold channel area. Several models are developed to predict single phase discharge distribution along the length of the manifold. Special case and approximation-type models are found to grossly under-predict distribution; satisfactory agreement was obtained for generalized non-dimensional and physical, integral models which do not make limiting assumptions.

In Chapter 2, the same system was used for two-phase flows of air and water. The inlet mass flux ranged from 50 $kg/m^2 \cdot s$ to 400 $kg/m^2 \cdot s$ and the quality ranged from 0 to 0.5. The concept of modeling for two-phase flows is first explored in detail, and various approaches are explained. An original model is developed from first principles and applied to the current system. Predictions for quantities such as the total discharge mass flow rate, run quality, and exit qualities are obtained. The model has an advantage over previous models in that only inlet quantities and manifold geometry are specified.

In Chapter 3, flow visualization and two-phase pressure drop data were taken for 60.9cm test sections of the microchannels. The working two-phase fluids are air-water and R134a vapor-liquid. Mass fluxes of 50 $kg/m^2 \cdot s$ to 300 $kg/m^2 \cdot s$ and vapor flux qualities ranging from 0 to 1 were employed. In total, six different microchannel orientations are analyzed. Flow maps describing the two-phase flow regimes are constructed using probabilistic time functions instead of conventional maps found in literature. Visualization is performed using an X-ray diagnostic device capable of peering through aluminum, in contrast to standard idealized transparent test section visualization methods.

Table of Contents

List of Figures

Page

List of Tables

Page

Nomenclature

D_h	hydraulic diameter [mm]
G	total mass flux, based on microchannel area [$\mathrm{kg/m^2 \cdot s}$]
x	vapor flux quality [-]
C_t	turning loss coefficient [-]
A_r	area ratio [-]
C_d	contraction coefficient [-]
f_c	friction factor of the channel [-]
D_c	hydraulic diameter of the manifold channel [mm]
A_c	cross sectional area of the channel [m^2]
V_{mc}	exit velocity of fluid through the lateral microchannel [m/s]
N	number of microchannels
D_{mc}	diameter of the microchannels [mm]
P_{mc}	fluid pressure in the microchannel [kPa]
L_{mc}	length of the microchannel [m]
f_{mc}	microchannel friction factor [-]
H	flow resistance which combines velocity, pressure, and friction
$\hat{x}$	dimensionless distance [-]
$\hat{V}_c$	dimensionless channel velocity [-]
Pa	Pascals, units of pressure
mV	millivolts
mdot	mass flow rate [kg/s] ([g/s] when noted)
DimX	dimensionless distance [x/length]

Subscripts

mc	microchannel
c	channel (i.e. manifold channel)
V	vapor phase
L	liquid phase

Greek Symbols

?	density [kg/m^3]
μ	dynamic viscosity [$\mathrm{kg/m \cdot s}$]
s	surface tension [N/m]
?	static pressure regain factor [-]
ß	momentum parameter [-]
a	friction parameter [-]
$?_d$	pressure regain coefficient [-]
?	kinematic viscosity [m^2/s]

Chapter 1. Single Phase Modeling of a Microchannel Distribution Manifold

1.1 Introduction

Recent trends in heat exchanger technology have prompted the use of microchannel tubes. These special tubes have gained interest, showing promise for higher performance under ever-tightening design constraints. However, though the body of knowledge concerning microchannels continues to grow, some gaps remain. Specifically, little research has been performed as to the nature of the distribution of an inlet fluid into a microchannel distribution array.

Single phase flow is but a limiting special case of the more general occurrence of two-phase flow in a heat exchanger. Furthermore, refrigerants are typically employed in such applications and much research has focused upon the behavior of refrigerant flow through microchannel tubes. However, the research of microchannel manifold distribution is quite sparse. The aim of this chapter is to establish a fundamental understanding of distributive behavior of a microchannel manifold, through experimentation and modeling, when single phase water and single phase air are independent working fluids.

First, a comprehensive literature review is performed which encompasses research in distribution systems, akin to the system under study. The facility is quite versatile, allowing for a large test matrix of experimental variation even for single phase flow. Three models are developed and presented in thorough detail, then adapted for the microchannel manifold distribution system under study. These models are then applied to predict microchannel manifold discharge mass distribution, followed by model and experimental data comparison. It is hoped that this general information will be useful for the future design and operation of microchannel manifold distribution systems.

1.2 Literature Review

1.2.1 Broad Overview

Pioneering manifold research was studied in great detail by Keller [1949]. While a large body of data had been obtained for a single pipe, up to that point little data were obtained on manifold discharge behavior. There are two effects to consider in manifold flow: inertia and friction. Regarding inertia, according to the Bernoulli principle the pressure increase corresponds to a deceleration of fluid along the length of the manifold because part of the initial flow discharges through the laterals. Regarding friction, friction creates a loss in the pressure along the length of the manifold. Either of these effects can be dominant. Conversely, these effects can be equalized for a manifold capable of variable geometry, resulting in uniform pressure distribution and thus uniform discharge.

For a manifold with uniformly spaced holes and constant manifold geometry, there are two parameters which define the manifold: (1) the ratio of the manifold length to manifold diameter, and (2) the area ratio, defined by the sum of discharge areas to the manifold cross sectional area. Pressure regain, a phenomenon in which static pressure rises in the direction of flow, becomes dominant over friction as the manifold length is reduced in proportion to its diameter. Keller [1949] demonstrates that the assumption of no friction is sometimes a good approximation.

It was previously believed that having an area ratio of 1 would produce uniform distribution, but this equality does not take into account the effect of the length/diameter ratio (L/D). For large L/D ratios, an area ratio near 1 may produce uniform flow. However, for small L/D ratios, an area ratio of 1 does not lead to uniform flow.

For L/D above 70, the distribution of the inlet is higher than toward the exit. Thus, Keller [1949] was one of the first to explain the existence of end effects. These effects are present in the current experiment, as will be seen later.

McKnown & Asce [1952] further expanded the early body of knowledge of manifold behavior. A general treatment of manifolds with laterals is provided from a physical, integral approach examining changes in piezometric head. Equations for the head losses for the manifold and laterals are provided for the dividing flow case can be found in Appendix A. The manifold cited in experiments is a 50.8mm diameter brass pipe with 12.7mm diameter laterals. Pressure drop was measured along the manifold and along the discharge branch itself.

1.2.2 Interesting Applications

Qu & Mudawar [2002] studied the heat transfer and pressure drop properties of fine microchannel heat sinks on the order of micrometers in dimension. Previous studies have found that microchannel heat sinks possess a great deal of promise to dissipate heat. Thus, understanding and modeling them are quite important topics. The Navier-Stokes equations were solved and were found to be adequate to predict the pressure drop. Numerical predictions were obtained, as well as experimental data for the temperature distribution along the channel walls.

Another interesting application of single phase microchannel flow modeling is provided by Subaygo et al. [1998]. Single phase fluid flows in a packed bed, such as those found in the metallurgical sciences, was examined. A standard mechanics equation relating velocity, friction, and change in pressure head was employed. A model was developed for the flow downstream of the bed. This research is addressed because it demonstrates how flow in small channels can be related to standard energy mechanics equations.

1.2.3 Single Phase Manifold Examples

Kim et al. [1995] performed manifold distribution studies with water as the working fluid. The primary experimental variable was the manifold itself. Trapezoidal, triangular, and rectangular manifolds were used; the triangular manifold was found to provide the best distribution. The area ratio, defined as the ratio of total channel cross-sectional area to dividing manifold cross-sectional area, was examined. In addition the width ratio was also studied. The width ratio is defined as the ratio of the combining manifold cross-sectional area to the dividing manifold cross-sectional area.

The key finding of Kim et al. [1995] was that small area ratio and large width ratio are required to obtain uniform distribution. The problem for rectangular manifolds is the flow rate concentration in the last channel, which is often much different than the discharge of the first channel. Findings similar to those obtained in the present experiment were obtained.

Wang & Yu [1989] studied dividing and combining flow manifolds for solar collectors. As an example of the pitfalls of maldistribution, it was noted that for the manifold system under study, nonuniformity reduces efficiency and may even lead to equipment damage due to overheating. It is postulated that there are two fundamental manifold types: “pressure regain” and “pressure decrease”. For dividing flow, which pertains to this system under study, pressure regain types occur when the effects of friction and loss are smaller, whereas pressure decrease types occur if friction and loss are larger. A model based upon physical energy equations was developed and applied to the data. However, this model suffers from a dependence upon empirical tuning coefficients.

It was concluded that if large diameter branch pipes and small diameter manifolds are avoided, there is a greater likelihood of uniformity. The branch interval was found to have had a pronounced effect on both the pressure and velocity distributions. For pressure regain type manifolds, uniformity is enhanced by having smaller branch spacing.

1.2.4 Mathematical Approaches

Jones & Galliera [1998] used a Computational Fluid Dynamics (CFD) approach to predict 3-D steady flow and pressure fields in a T-junction coupled manifold with three risers, which consists of dividing and combining flow. There are two main divisions of manifolds: combining and dividing. These can be combined to form two more combinations, reverse and parallel. This is demonstrated in Figure 1.1.

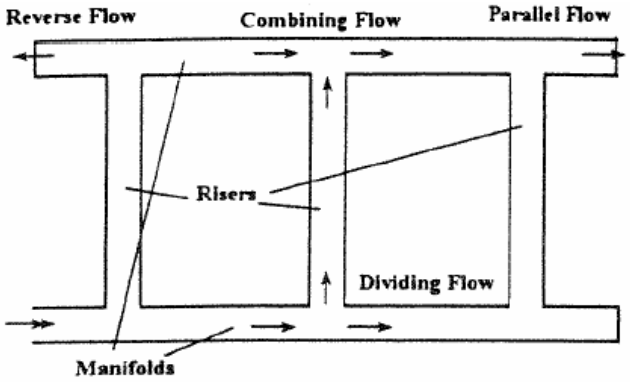

Figure 1.1: Types of Distribution Manifolds (Jones & Galliera [1998])

Using the program Fluent ® the entire system was modeled as a mesh and the governing equations were solved for pressure, velocity, and distribution. Miner [1996] used CFD to determine the distribution for a water filtration system with eight laterals. A mesh of several thousand 2-D finite elements was employed to solve the Reynolds Averaged Navier-Stokes Equations for velocity and pressure fields.

For comparison to CFD results, Jones & Galliera [1998] developed an integral, physical model considering changes in velocity and pressure. It was based upon fundamental principles such as continuity, energy, and Bernoulli considerations. Good agreement was obtained among experimental data, the Fluent® model, and the integral model. Thus, physical models have exhibited nearly the same accuracy in obtaining physical values as does a CFD model. An integral physical model has been developed for this present system and shall be developed later.

1.3 Overview of Previous Models

1.3.1 Bajura [1976]—Non-Dimensional

Bajura [1976] proposes a “continuous” approach, in which flow variables are solved along the manifold. This continuous model is governed by continuity and momentum. A variety of parameters such as the lateral area, manifold channel area, and frictional properties were examined. These have a great effect on distribution. To prevent dependence on an abundance of empirical parameters, and owing to the large number of differences that exist among manifolds, the optimum approach is to develop a generalized, non-dimensional model. This present experiment is a study of purely dividing flow; hence, no treatments of the other manifold flow possibilities will be given.

The mechanism by which the fluid in the dividing manifold is decelerated is the loss of fluid through a lateral discharge. Frictional effects are an important consideration. If frictional effects are small or negligible, a pressure regain phenomena occurs along the length of the manifold; for large frictional effects the pressure will decrease due to frictional losses (Bajura [1976]).

Bajura [1976] applied continuity, momentum, and energy conservation in a pair of fully descriptive governing differential equations. The first set is comprised of two first order differential equations for pressure drop and manifold velocity; when solved simultaneously, they describe the velocity and pressure manifold behavior. The second of the descriptive pair is a second order, nonlinear differential equation which yields the manifold velocity and outlet flow distribution. What is so elegant about his model is its generality; a table of parameters specific to each type of manifold (dividing, combining, reverse, and parallel) is provided. Furthermore, each quantity represented in the equations is non-dimensional. The application of this model to the present system is presented in Section 1.5.2.

1.3.2 Bajura [1971]—Porous Approximation

Bajura [1971] treats the special case in which the manifold is modeled as a uniformly porous media, which is for a large number of lateral discharge branches relative to the length of the manifold. This is written in an overall governing non-dimensional form. The uniformly porous special case is then expanded to consider the case of frictionless or negligible friction. A trigonometric function is obtained which depends upon manifold geometric properties.

A combination of dimensionless parameters is used. The static pressure regain factor ? accounts for the transfer of axial momentum into the discharge lateral. The momentum parameter ß expresses the effects of momentum, discharge flow resistance, and the ratio of discharge to manifold areas. It was found that decreasing the area ratio produces more uniform discharge (for dividing) or uniform intake (for combining). This treatment shall be applied to the present system in Section 1.5.1.

1.3.3 Shen [1992]

Shen [1992] builds upon Bajura [1971]. Two configurations are studied: purely dividing and purely combining flow. In order to provide for a simplified model, a constant friction factor is assumed along the length of the manifold, which of course is not true to the actual situation. The friction parameter a and the momentum loss parameter ß are examined. ß is described as a measure of the turning loss to the total head loss. a is defined as the ratio of fL/D to the total head loss. Sinusoidal, exponential equations are obtained as solutions to the original Bajura governing equation. The friction was found to have a greater effect on manifolds with “moderate” area ratios; furthermore, that friction has a greater effect on dividing flow manifolds.

1.3.4 Chou & Cheng [2001]

Groundbreaking work was performed by Chou & Cheng [2001]. Due to its pertinence to this specific system, this work shall be given detailed treatment. The authors cite two fundamental approaches to manifold modeling, the energy and momentum approaches. From an energy standpoint, one may employ the end condition and satisfy the energy point by point to solve for distribution along the manifold length. This type of algorithm is ultimately iterative or trial-and-error, since some dead end pressure head must be assumed. However, it must be

stressed that this approach maintains a level of robustness since one can vary manifold parameters (e. g. geometry) quite readily. This is the approach that such authors as Keller [1949] employ. Researchers such as Bajura [1971, 1976] have opted for the momentum approach, which solves for the momentum equation directly and assumes constant geometric properties. It is noted that previous research has focused upon such parameters as the discharge geometry and friction coefficient, such as the observation that reducing friction or increasing the lateral discharge coefficient (total lateral area to manifold area) leads to more even distribution. However, such parameters are not completely independent and a satisfactory distribution model must study the parametric effects simultaneously.

The distribution system used by Chou & Cheng [2001] consisted of a 2 m. long, 2 cm. diameter manifold with 20 lateral orifices of 5mm diameter, spaced 10cm apart. The experimental methods were quite similar to the methods of the present experiment; a pressure transducer was affixed at two ports to gage the pressure drop, which led to the determination of flow velocity having known the friction factor. The manifold was configured for 6, 12, and 20 ports. The experimental parameters are in Table 1.1.

Table 1.1: Parameters used in Chou & Cheng [2001]

No. of Ports	**Ar**	**Cd**	a	b
6	0.236	0.629	0.203	0.334
12	0.469	0.625	0.524	0.663
20	0.75	0.6	1.01	1.06

Where A_r is the area ratio, C_d is the contraction coefficient (ratio of lateral discharge to lateral area and manifold energy), a is the wall friction parameter, and ß is the momentum parameter. It is noted that for an increase in port number, all the parameters presented in the above table increase and the uniformity parameter deviates further from 1 in the process.

The work of Chou & Cheng [2001] is intricately tied to the works of Bajura [1971, 1976]. Therefore, two models shall be developed later in Section 1.5, termed the Bajura-Chou-Cheng (BCC) Frictionless Approximation Model, and the Bajura-Chou-Cheng (BCC) Non-Dimensional Model.

1.4 Presentation of Experiment

1.4.1 Equipment

A manifold test section was designed and constructed. Initial tests used air and water; however, the test section has been designed to withstand refrigerant (R134a) level pressures. The manifold consists of a 28cm by 56cm poly-vinyl carbonate (PVC) top plate. Five pressure tap ports are machined into the top plate to provide for static pressure measurements directly within the flow. The bottom plate is either AL 2024 or PVC. A PVC spacer plate is located between the top and bottom plates and is available in sizes of 3.75mm, 6.35mm, and 12.7mm. Changing the spacer plate allows for a change in the manifold cross-sectional area. Altering this area, in turn, allows for variations in the mass flux.

A typical microchannel tube can be seen in Figure 1.2. The 6-port microchannel used in this experiment has a hydraulic diameter of 1.54mm and a cross-sectional area of 1.669×10^{-5} m^2. The ports are housed in a rectangle as seen below. The length of the tube is approximately 31.75cm with an aluminum connector piece with a length of approximately 8.25cm.

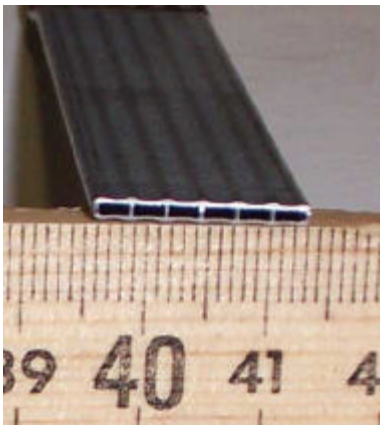

Figure 1.2: Typical Microchannel View

The setup used for air and water experimentation is presented in schematic form in Figure 1.3.

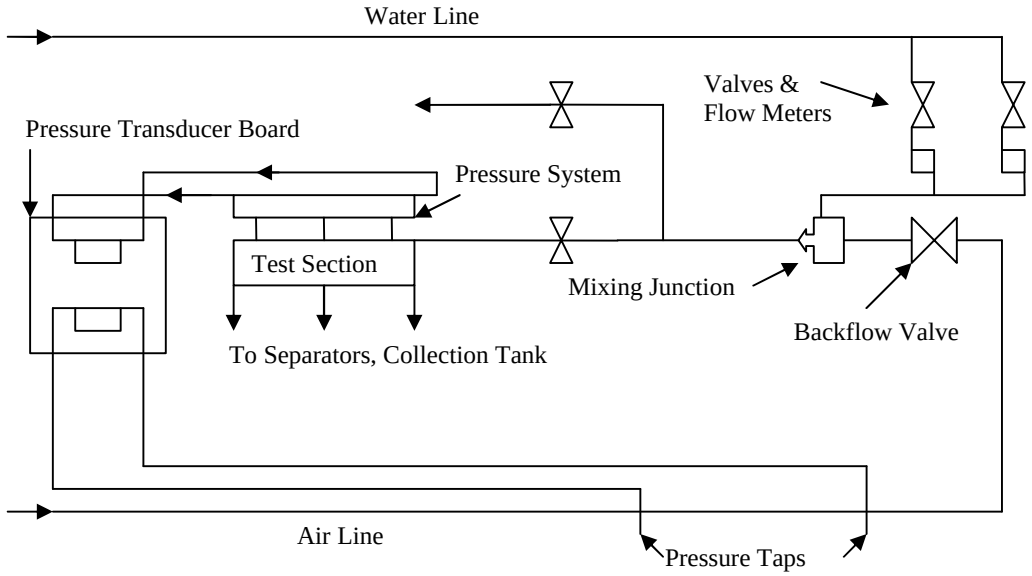

Figure 1.3: Schematic of Air-Water Loop

Pressurized air is supplied through 25.4mm diameter SCH 40 PVC piping from the building supply. Two taps are interjected in the supply line which feed to a pressure transducer (64.5 Pa/mV, ±3% linearity). A regulating valve at the supply entrance, used in conjunction with a digital multimeter (DMM) (±0.01mV) readout of the pressure transducer, controls the amount flow rate of air. The flow rate of air was known based on a simple pressure drop relation between the two static pressure taps. A blow-off valve exists in the event that water is introduced into the air line. Water is supplied from the building supply source through 12.7mm diameter PVC line. It travels through a water filter to eliminate particulates. A 12.7mm gate valve regulates the flow of water through a parallel bank of flow meters (0-40GPH and 0-7GPH). The two supply lines meet at a mixing T-junction (for two-phase flow, See Section 2.3), behind which a 25.4mm ball valve is placed to eliminate liquid backflow.

The flow traverses through 25.4mm SCH 40 PVC section of suitable length to allow for flow development. This flow can either go through the manifold test section or through a bypass line (used to establish flow conditions)

by a series of 12.7mm ball valves. The flow travels to the test section via 9.525mm reinforced PVC tubing. The two-phase flow then distributes among the array of 15 aluminum discharge microchannels. Flow exits the microchannels via PVC tubing and into fifteen separation tanks.

Each tank is fitted with a vapor exit to allow for vapor mass flow determination via a bank of 47 LPM and 20LPM rotameters. The total liquid collection of each separator tank over a given time interval is weighed using a weight balance. Static pressure is measured at five locations inside of the manifold using a system of three way valves and a pressure transducer (677 Pa/mV, ±3% linearity) fed to the DMM. In addition, two submersible pumps of 60Hz and 124W can reject water or establish closed loop supply systems. See Figures 1.4, 1.5, and 1.6 for figures of the manifold, collection system, and overall system.

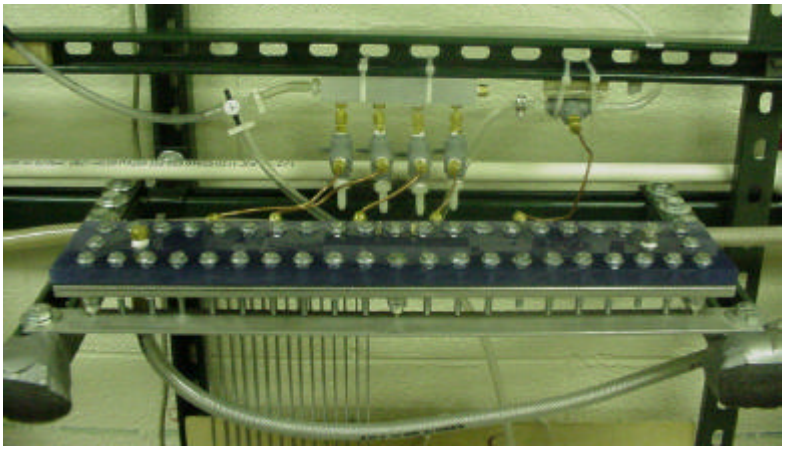

Figure 1.4: Manifold Used in Experimentation

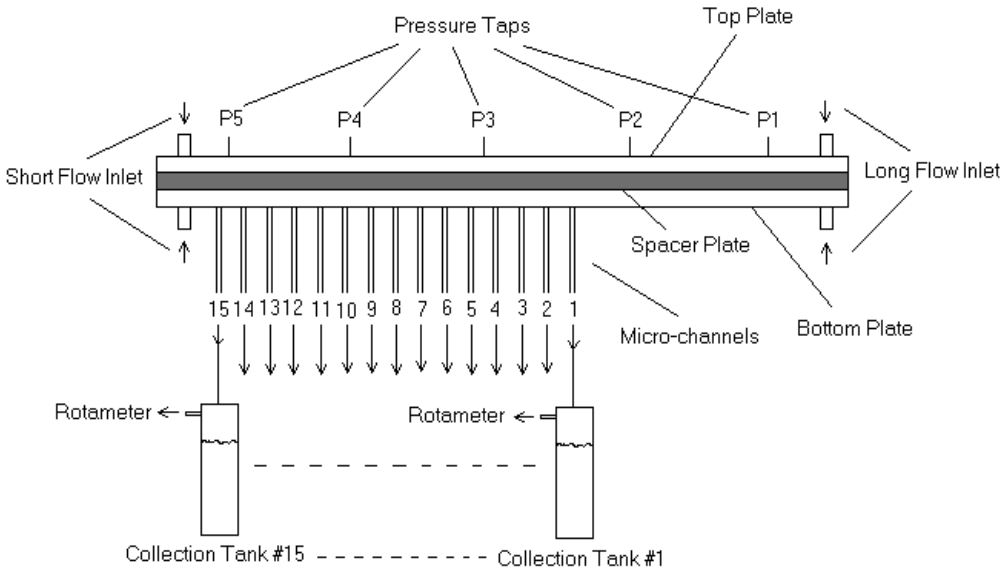

Figure 1.5: Manifold and Experimental Setup

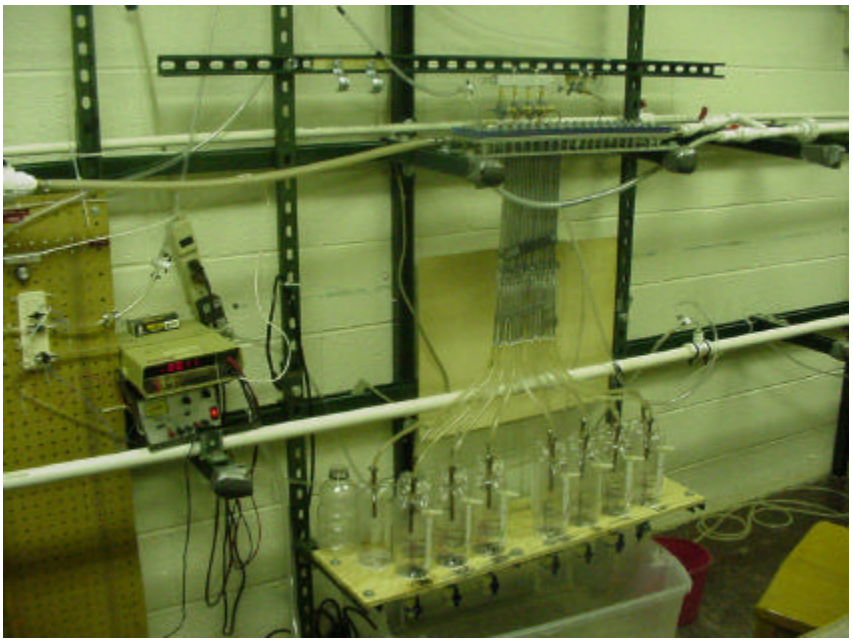

Figure 1.6: Overall System

1.4.2 Procedure

Single phase experiments are performed in the following manner. First, the proper inlet entrance conditions are identified (top, bottom, left, or right), and manifold channel area (determined by spacer plate). For each test case, the micro-channel air volumetric flow rate is determined by a gas rotameter (±0.5L/min). For single phase liquid (quality = 0), the volume of water is weighed on a balance (±0.1g) and the time interval is obtained via a quartz stopwatch (±0.25s reaction time). Through propagation of error, each data point is subject to 5.1% variance. This error bar is represented on the graphs when the data and models are presented in later sections. During single phase air (quality = 1.0) testing, atmospheric pressure is first read, and then each local pressure differential with respect to this reading is obtained, resulting in local static pressures P1, P2, P3, P4, and P5.

1.5 Detailed Presentation of Models

1.5.1 Bajura-Chou-Cheng (BCC) Frictionless Approximation Model

A control volume around a junction discharging from the manifold channel can be seen in Figure 1.7. Beginning with the assumption of the manifold as a continuously porous media (the criteria is that lateral interval is less than 10% of the manifold length), Chou & Cheng [2001] expand on Bajura [1971]. The overall governing equation is given by:

$$\frac{1}{r}\frac{dP_c}{dx} + \frac{f_c}{2D_c}V_c\frac{dV_c}{dx} + g_d V_c V_{mc}\frac{lpD_c}{A_c} = 0 \qquad (1.1)$$

where

V_c is the average velocity of fluid flow in the channel

P_c is the pressure of the fluid in the channel

$?$ is the fluid density

f_c is the friction factor of the channel

D_c is the hydraulic diameter of the manifold channel

A_c is the cross sectional area of the channel

V_{mc} is the exit velocity of fluid through the lateral microchannel

$?_d$ is the pressure regain coefficient

and ? is the porosity, defined by

$$l = \frac{ND_{mc}^{\ 2}}{4A_{cs}} \tag{1.2}$$

where

N is the number of microchannels

D_{mc} is the diameter of the microchannels

A_{cs} is the wetted surface area of the distribution channel

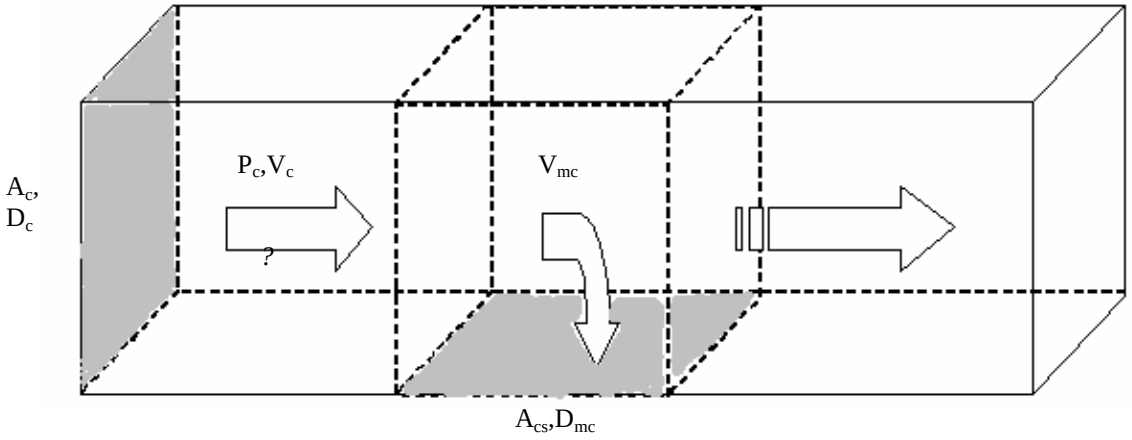

Figure 1.7: Control Volume for Channel

Applying the continuity equation yields

$$\frac{l\,pD_c}{A_c}V_{mc} + \frac{dV_c}{dx} = 0 \tag{1.3}$$

The energy equation at a specific location x which lay along the vertical axis of the microchannel is

$$P_c(x) - P_{mc} = r\left(1 + C_{td} + f_{mc}\frac{L_{mc}}{D_{mc}}\right)\frac{V_{mc}^{\ 2}}{2} = rH\frac{V_{mc}^{\ 2}}{2} \tag{1.4}$$

where

P_{mc} is the fluid pressure in the microchannel

L_{mc} is the length of the microchannel

f_{mc} is the microchannel friction factor

H is the flow resistance (combines velocity, pressure, and friction heads)

At this stage it is convenient to put the governing equations in non-dimensional form. First scale the local distance to the manifold channel length L_c to obtain the dimensionless distance $\hat{x} = \frac{x}{L_c}$. Shen [1992] and Chou & Cheng [2001] next non dimensionalize the channel flow velocity by scaling it to the inlet velocity and obtain

$$\hat{V}_c = \frac{V_c(x)}{V_c(0)} \tag{1.5}$$

Now define two critical parameters a and ß. The friction parameter a describes the microchannel friction effects. One may also define the momentum parameter ß, which describes the change in momentum across a control volume drawn at the microchannel-manifold channel junction. They are defined by Shen [1992], Chou & Cheng [2001] as

$$a = \sqrt{\frac{f_c L_c}{D_c H}} A_r \tag{1.6}$$

$$b = \sqrt{\frac{\left(2 - g_d\right)}{H}} A_r \tag{1.7}$$

The area ratio A_r is a critical parameter and is defined by

$$A_r = \frac{N D_{mc}{}^2}{D_c{}^2} \tag{1.8}$$

Note the departure from the standard energy approach. By employing this momentum algorithm, one may define parameters which combine several effects into one dimensionless parameter. The friction parameter combines overall head loss, distribution channel to microchannel area ratio, and microchannel friction. The momentum parameter includes the area ratio, overall head loss, and lateral discharge momentum.

Thus, one may arrive at a governing non-linear, second order differential equation given by

$$\frac{d}{d\hat{x}}\left[\left(\frac{d\hat{V}_c}{d\hat{x}}\right)^2 + \left(b\hat{V}_c\right)^2\right] + \left(a\hat{V}_c\right)^2 = 0 \tag{1.9}$$

with boundary conditions $\hat{V}_c = 1$ at $\hat{x} = 0$ and $\hat{V}_c = 0$ at $\hat{x} = 1$. Owing to the nature of this differential equation, analytical solutions are extremely difficult. A trigonometric-exponential solution was proposed by Shen [1992] but was later refuted by Chou & Cheng [2001].

Chou & Cheng [2001] consider three treatments of a and ß:

1) a=0 and ß dominates
2) a and ß are of same order
3) a dominates and ß=0

Only the first of these cases will be addressed in detail; the remaining two cases are interesting and are deferred to Appendix A.

The first class of solution is termed the frictionless solution. Here, the manifold is considered ideally short and frictionless. Thus a vanishes and one is left with

$$\frac{d}{d\hat{x}}\left[\left(\frac{d\hat{V}_c}{d\hat{x}}\right)^2+\left(b\hat{V}_c\right)^2\right]=0 \tag{1.10}$$

Bajura [1971] provides the following solution:

$$\hat{V}_c(\hat{x})=\frac{\sin\left[b\left(1-\hat{x}\right)\right]}{\sin b} \tag{1.11}$$

Employing continuity, the dimensionless microchannel lateral discharge scaled to the upstream microchannel lateral discharge is (Shen [1992])

$$\hat{V}_{mc}(\hat{x})=\frac{V_{mc}(\hat{x})}{V_{mc}(0)}=\frac{V'_c(\hat{x})}{V'_c(0)}=\frac{\cos\left[b\left(1-\hat{x}\right)\right]}{\cos b} \tag{1.12}$$

This equation predicts the characteristics of an idealized frictionless manifold distribution system. Consider the following graph for β=0.6 and β=0.8.

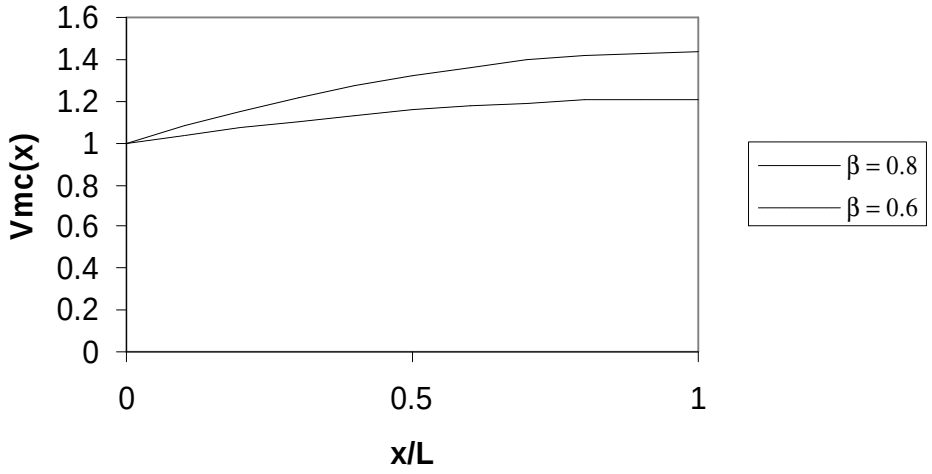

Figure 1.8: Discharge Velocity for Momentum Parameter ß

Thus, as ß increases, the flow distribution becomes more uneven because the denominator of Equation (1.12) increases. Furthermore, the manifold discharge increases downstream of the inlet.

1.5.2 Bajura-Chou-Cheng (BCC) Non-Dimensional Model

The BCC Non-Dimensional Model is based upon Bajura [1976]; credit for this model is also attributed to Chou-Cheng [2001] because of the authors' extended treatment. The following control volume is used for the present dividing flow manifold:

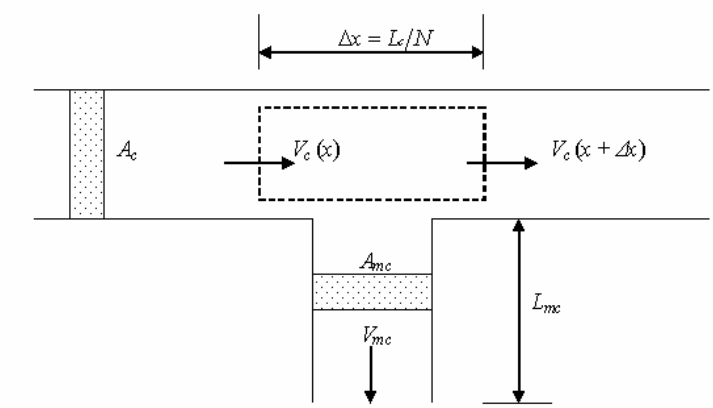

Figure 1.9: Control Volume for BCC Non-Dimensional Model

The control volume has a length *?x*, a small portion of the overall channel length L_c, and the manifold has *N* manifold laterals. The microchannels possess a length L_{mc} and area A_{mc}. All geometric properties are considered constant; furthermore, the fluid is considered to be incompressible. The gradient of channel velocity in the direction of flow is:

$$\frac{dVc}{dx} = -\frac{Amc}{Ac}\frac{N}{Lc}Vmc \tag{1.13}$$

Any solution from subsequent analysis must satisfy the following:

$$Vc(0) = 1; Vc(1) = 0 \tag{1.14}$$

Furthermore, the negative sign of Equation (1.13) indicates that the flow must decelerate in the direction of the manifold; a logical consequence is that the pressure gradient must be in the increasing direction (e.g. a positive pressure differential).

Bajura [1976] is credited with defining the following:

Axial Momentum Flow Correction Factor $$b = \frac{\int V_c^{\,2} A_c dA_c}{V_c^{\,2} A_c} \tag{1.15}$$

Lateral Flow Momentum Correction Factor $$g = \frac{\int V_x(A_{mc}) V_y(A_{mc}) dA_{mc}}{V_c V_{mc} A_{mc}} \tag{1.16}$$

Overall Momentum Correction Factor $$q = 2b - g \tag{1.17}$$

Wall Shear Stress $$\mathrm{T} = \frac{fcrVc^2}{8} \tag{1.18}$$

where f_c is the manifold channel friction factor. With *p* as the perimeter of the manifold channel and using a momentum control volume balance, the following overall momentum equation is defined:

$$\frac{1}{r}\frac{dP}{dx} + \left(\frac{f_c p}{8A_c} + \frac{db}{dx}\right)V_c^2 + qV_c\frac{dV_c}{dx} = 0 \tag{1.19}$$

Bajura then generalizes the equation by non-dimensionalizing it according to the following:

$$\tilde{x} = x / L_c \qquad \tilde{Q} = V_c A_c / Q_o \qquad \tilde{V} = V_c / V_o \qquad \Delta\tilde{P} = \Delta P_{cv} / \rho V_o^2 \tag{1.13}$$

where the subscripts *o* and *cv* represent the entrance quantities and pressure across the control volume, respectively.

Though non-dimensional models for a variety of manifolds are presented in Bajura [1976], the non-dimensional equations specific to the dividing flow manifold are the following:

Pressure Flow Equations

$$\frac{dV}{dx} = -A_r \sqrt{\frac{2}{H}} \left(\frac{P_c - P_\infty}{\rho V_o^2} \right)^{1/2} \tag{1.14}$$

and

$$\frac{d\left(\frac{P_c - P_\infty}{\rho V_o^2} \right)}{dx} = -A_{c,1}\tilde{V} + A_{c,2}\left(1 - \tilde{V}\right)^2 - q\,\tilde{V}\frac{d\tilde{V}}{dx} \tag{1.15}$$

One may eliminate the non-dimensional pressure from the above equations to eventually arrive at the following distribution equation:

Discharge Equation

$$2\tilde{Q}'\tilde{Q}'' + \frac{A_r^2}{H}\frac{f_c L_c}{2D_c}\tilde{Q}^2 + \frac{A_r^2}{H} q\,\tilde{Q}\tilde{Q}' = 0 \tag{1.16}$$

Bajura suggests a value of ~1.05 for *?*, further stating that this value is fixed and does not depend strongly on lateral and manifold parameters. The boundary conditions on the dimensionless flow distribution equation are:

$$\begin{aligned} \tilde{Q}(0) &= 1 \\ \tilde{Q}(1) &= 0 \end{aligned} \tag{1.17}$$

Note that the area ratio A_r is present in Equations (1.21) and (1.23). Examine the definition of the area ratio, Equation (1.8), which is defined as the ratio of the discharge area to the manifold area. Suppose that the discharge area of the first few channels of a multi-channel manifold became infinite. This would represent the worst possible form of maldistribution, since the first few channels would not only receive a fraction of the total inlet flow, but the entirety of the inlet flow. Thus, as the area ratio becomes large, one may suppose that the flow becomes more uneven. This fact applies quite readily to the system under study and will be addressed later.

One may also make similar arguments for the other parameters contained in the above equations. The lateral flow resistance is inversely proportional to the diameter of the discharge lateral. One may imagine that as the diameter of the lateral decreases, the flow is more able to distribute itself evenly because there is no preferential discharge point, as would be the case if the lateral discharge diameter grew infinitely large, as was mentioned in the previous paragraph. Thus, high values of the lateral discharge flow resistance are desirable; of course an obvious payoff in system requirements results. This was verified by the experiments of Bajura [1976].

The so-called “Pressure-Flow” equations, Equations (1.21) & (1.22), provide a readily discernible physical connection between changes in manifold pressure and changes in velocity. The overall governing flow distribution equation, Equation (1.23), along with the boundary conditions of Equation (1.24), provides a fully descriptive analysis with only one variable, the manifold distribution $\tilde{Q}$. Equation (1.24) is applicable for systems with constant

properties, such as the present system. However, it is not easily amenable to solution, given its second order, non-linear behavior. Its application and solution to the system under study shall be developed.

1.5.3 Physical Model

Thus far presented two models have been presented to describe the microchannel manifold under study. Though based solidly on mechanical energy principles, an overall integral model has not yet been presented. As mentioned earlier, physical models may possess the same descriptive and predictive capabilities as such methods as a complex CFD mesh solution provide (Jones & Galliera [1998]).

The solution method adopted in this physical model assumes fifteen nodes at the discharge locations, such as in Figure 1.10.

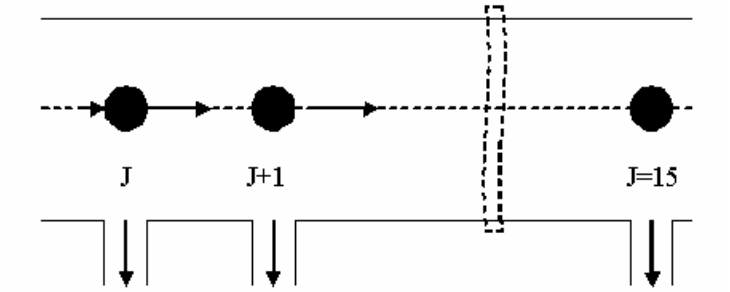

Figure 1.10: Nodes for the Physical Model

Momentum, mass, and energy (though this flow is considered adiabatic) must be satisfied at each node. Draw a control volume around a node *j* as in Figure 1.11.

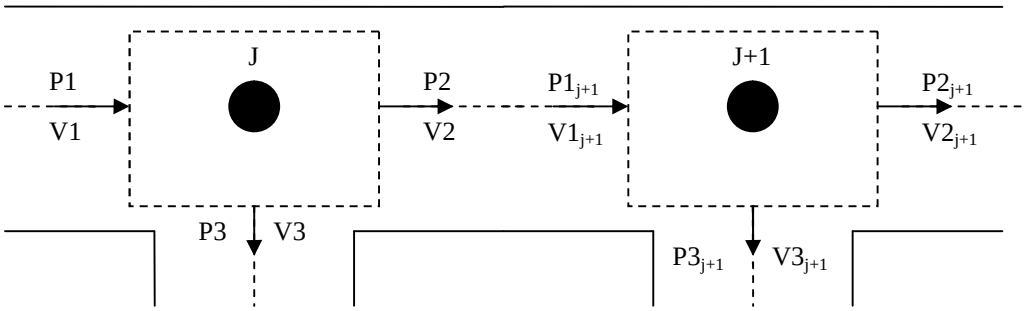

Figure 1.11: Control Volume for Physical Model

One may perform a momentum balance resulting in the following:

$$P2_j - P1_j = \rho \cdot \left[V1_j^2 - V2_j^2 - \gamma \cdot V1_j \cdot V3_j \cdot \frac{Amc}{Ac} \right] \quad \text{for } j = 1 \text{ to } N \tag{1.18}$$

where the velocities are defined according to the drawn control volume and the areas have been defined in previous sections. The factor ? is the static pressure regain coefficient. Its function is to account for the change in transport of axial momentum. A value of 1 means that the fluid loses no axial momentum as it passes over a discharge lateral; conversely a value of 0 means that all of the flow's axial momentum is discharged into the lateral and therefore the

axial flow velocity is 0. Bajura [1971] cites that for a discharge diameter/channel diameter ratio of 0.25 and less, and for spacing between infinity and four times the channel diameter, the value of ? is roughly 0.8.

The pressure difference between the average nodal pressure and the ambient pressure is related to a head loss due to friction and turning. The average nodal pressure for an infinitesimal control volume is

$$P_j = \frac{P1_j + P2_j}{2} \quad \text{for } j = 1 \text{ to } N \tag{1.19}$$

and the pressure head loss is given by:

$$P_j = \left[1 + Ctd + fmc_j \cdot \frac{Lmc}{Dmc}\right] \cdot \frac{V3_j^2}{2} \cdot \rho + Pinf \quad \text{for } j = 1 \text{ to } N \tag{1.20}$$

The ambient pressure P_8 is a constant 101.3kPa. Based on similar experiments of a sharp-edged right-angled manifold junction, Bajura [1971] determined a value for C_{td} of roughly 0.5.

Due to manifold friction, there is a pressure loss between nodes along the length of manifold. This pressure difference is given by:

$$P1_{j+1} - P2_j = fc_j \cdot \left[\frac{mdot1_j}{Ac}\right]^2 \cdot \frac{L2}{\rho \cdot Dc} - K \cdot \rho \cdot \frac{V1_j^2}{2} \quad \text{for } j = 1 \text{ to } N \tag{1.21}$$

where (*j+1*) refers to the subsequent node in the flow direction. The first term in Equation (1.28) is readily verified by conventional pressure drop-friction equations, and the second term needs justification.

Suppose the above equation was recast into the following form:

$$P1_{j+1} - P2_j + K \cdot \rho \cdot \frac{V1_j^2}{2} = fc_j \cdot \left[\frac{mdot1_j}{Ac}\right]^2 \cdot \frac{L2}{\rho \cdot Dc} \quad \text{for } j = 1 \text{ to } N \tag{1.22}$$

Total losses in pressure head are proportional to frictional losses and area changes. Recall that one of the primary experimental procedures is to change the available manifold diameter by decreasing the manifold spacer by a factor of 2 each time. Thus, for the largest manifold a value of *K* near 1 is chosen. A linear relationship was obtained for the change in manifold area and K. For the 12.7mm spacer, K=0.9; for 6.35mm, K=0.5; for 3.175mm, K=0.25.

To determine the friction factors of the manifold and microchannel laterals, the Colebrook equation (White [1994]) is used in the following manner:

$$\frac{1}{fmc_j^{0.5}} = -2 \cdot \log\left[\frac{0.0015}{Dmc \cdot 1000 \cdot 3.7} + \frac{2.51}{Remc_j \cdot fmc_j^{0.5}}\right] \quad \text{for } j = 1 \text{ to } N \tag{1.23}$$

and

$$\frac{1}{fc_j^{0.5}} = -2 \cdot \log\left[\frac{0.0015}{Dc \cdot 1000 \cdot 3.7} + \frac{2.51}{Rec_j \cdot fc_j^{0.5}}\right] \quad \text{for } j = 1 \text{ to } N \tag{1.31}$$

with the classical definition of the Reynolds number defined by:

$$Remc_j = V3_j \cdot \frac{Dmc}{\nu} \quad \text{for } j = 1 \text{ to } N \tag{1.32}$$

and

$$Rec_j = V1_j \cdot \frac{Dc}{\nu} \quad \text{for } j = 1 \text{ to } N \tag{1.33}$$

All the diameters in Equations (1.30-1.33) are given as hydraulic diameters.

Naturally, the following continuity equations are valid:

$$\begin{aligned} mdot1_j &= mdot2_j + mdot3_j \quad \text{for } j = 1 \text{ to } N \\ mdot1_j &= \rho \cdot Ac \cdot V1_j \quad \text{for } j = 1 \text{ to } N \\ mdot2_j &= \rho \cdot Ac \cdot V2_j \quad \text{for } j = 1 \text{ to } N \\ mdot3_j &= \rho \cdot Amc \cdot V3_j \quad \text{for } j = 1 \text{ to } N \end{aligned} \tag{1.34}$$

1.6 Presentation of Sample Data

Single phase distribution data were obtained according to the procedure outlined in Section 1.4.2. The full spectrum of data can be found in Appendix A. For purposes of explanation, some representative data shall be presented here. To arrive at a satisfactory sample set, some criteria must be set forth. Regarding entrance conditions, very little difference existed when the entrance was from the top or the bottom, where “top” and “bottom” refer to whether the inlet flow is vertically downward or vertically upward into the manifold. Regarding the entrance length, there are “short” entrance and “long” entrance, where “short” and “long” refer to the available length in the manifold before the inlet flow encounters the first microchannel. Data analysis reveals that the difference between top and bottom entrance for a given entrance length is less than 10%, as can be seen in Table 1.2.

Table 1.2: Overall Average % Difference between Top and Bottom Entrance

Top/Bottom Overall Average % Difference			
Entrance	Individual Mdot	Mass Flow Sum	Individual Pressure
Short	6.96	6.33	5.45
Long	7.47	3.31	8.38

This table does not compare the long and short entrances, but the differences in values when comparing the top and bottom entrances for a given entrance length. Overall, these deviations are not significant.

Table 1.3 compares the differences in quantities between the short and long entrance configurations.

Table 1.3: Overall Average % Difference between Long and Short Entrance

Long/Short Overall Average % Difference		
Individual Mdot	Mass Flow Sum	Individual Pressure
19.95	3.85	14.23

Table 1.3 indicates that the distribution quantities of mass flow in the flow direction are approximately 20% different, but with a small difference in overall sum, and a somewhat significant difference of 14% for quantities of pressure in the flow direction. However, overall qualitative trends remain the same. Therefore, to provide for an ample explanation of data, one entrance shall be chosen with the remainder of the data presented in Appendix A.

The entrance condition chosen for a sample set is the short entrance. As mentioned previously, three spacer plates are available to change the manifold channel mass flux: 12.7mm, 6.35mm, and 3.175mm, yielding manifold cross sectional areas of $2.35 \times 10^{-4}\ m^2$, $2.173 \times 10^{-6}\ m^2$, and $1.005 \times 10^{-8}\ m^2$, respectively.

Figures 1.12, 1.14, and 1.16 show typical air distribution data through the microchannels with their corresponding static pressure profiles in the direction of flow, Figures 1.13, 1.15, and 1.17, for the short entrance for all three spacer plates. The legend in Figures 1.12-1.17 for distribution data indicates the *sum* of all microchannel discharges, which is the total inlet mass flow.

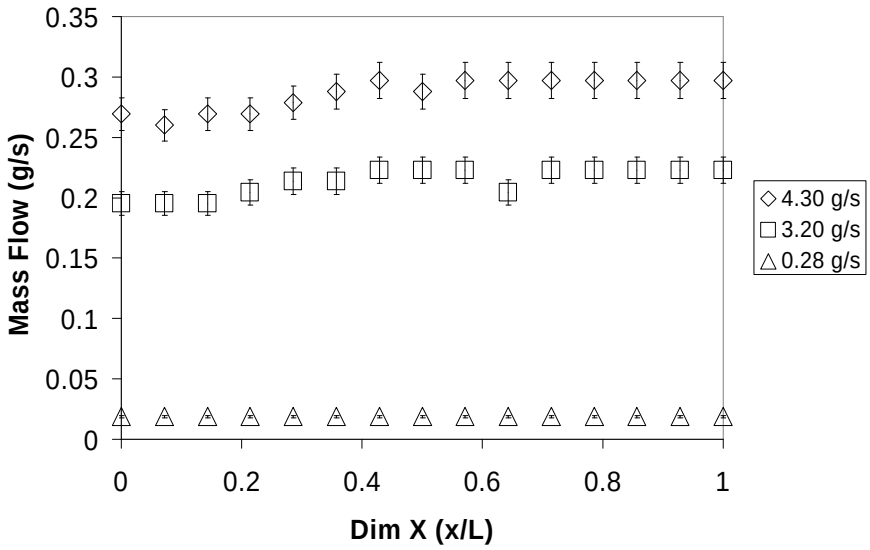

Figure 1.12: 12.7mm Spacer Plate Air Distribution, Short Entrance

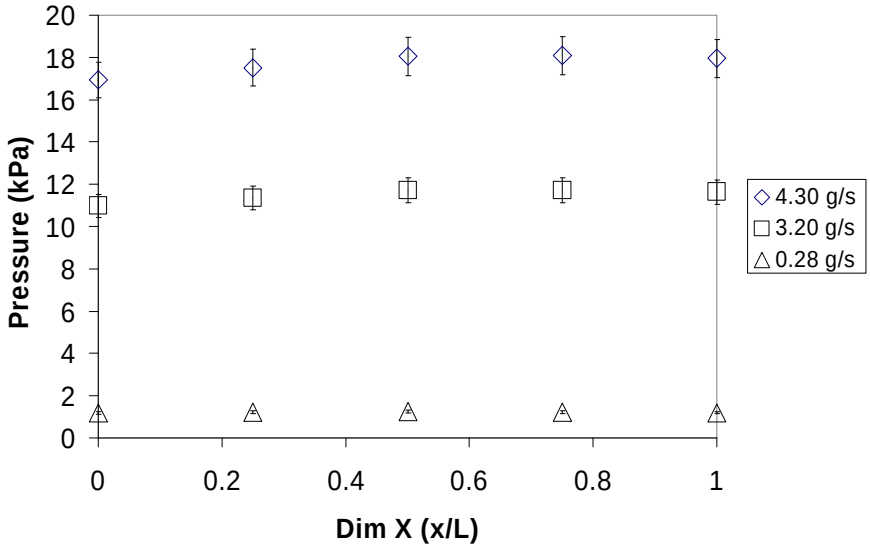

Figure 1.13: 12.7mm Spacer Plate Air Pressure, Short Entrance

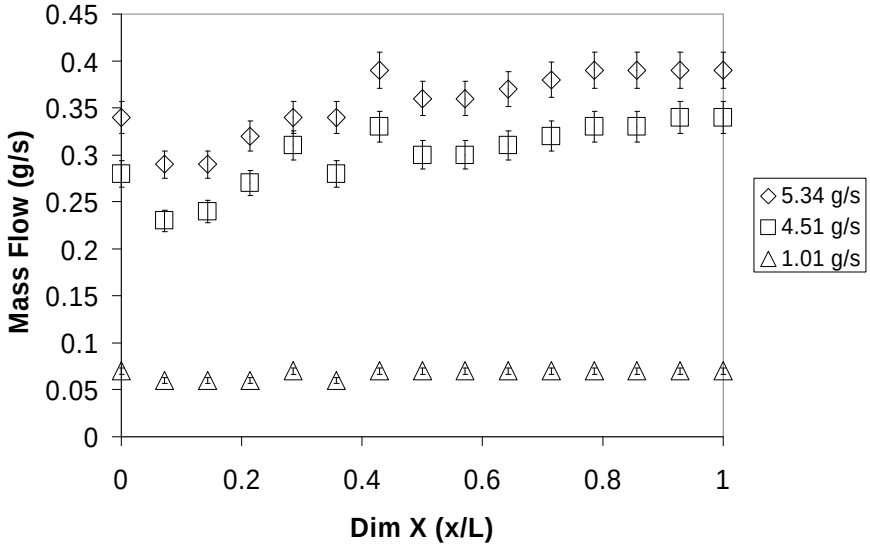

Figure 1.14: 6.35mm Spacer Plate Air Distribution, Short Entrance

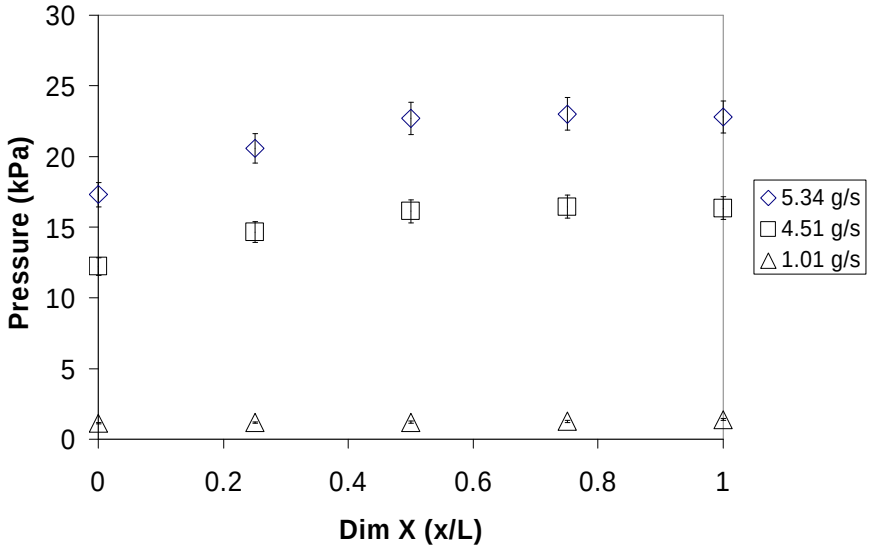

Figure 1.15: 6.35mm Spacer Plate Air Pressure, Short Entrance

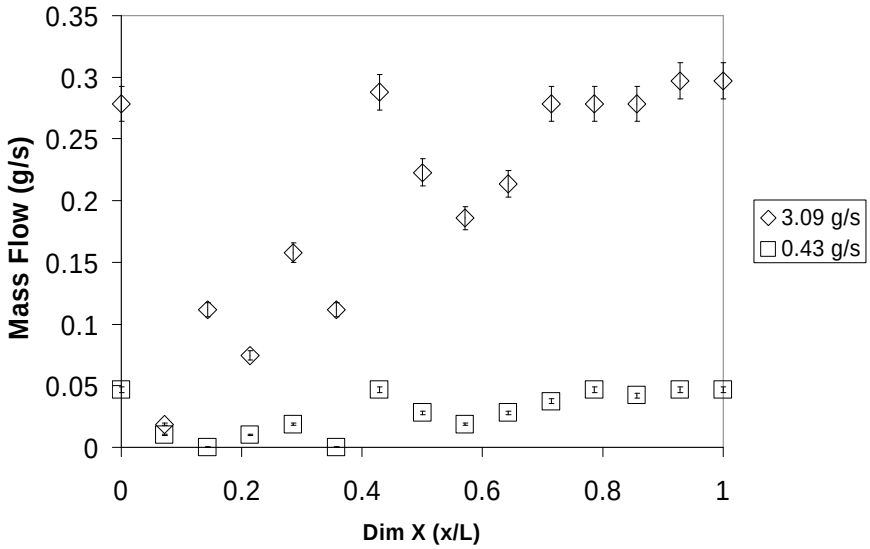

Figure 1.16: 3.175mm Spacer Plate Air Distribution, Short Entrance

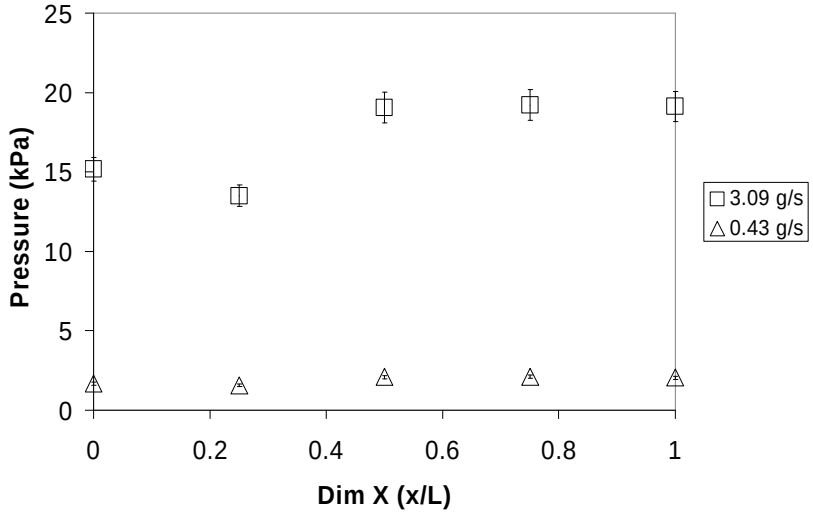

Figure 1.17: 3.175mm Spacer Plate Air Pressure, Short Entrance

Some common trends emerge:

1) With a decrease in flux area, the flow becomes more non-uniform
2) The pressure profile generally follows the same trend as the distribution
3) Pressure increases in the direction of flow, indicating pressure regain
4) A corresponding increase in discharge mass flow occurs in the flow direction
5) For low inlet flow rates, the distribution appears uniform regardless of manifold flux area
6) For higher inlet flow rates, the distribution profiles demonstrate relatively the same degree of regain in the flow direction

These patterns are present as well for the water distribution. No experimental pressure profiles for water were obtained, since water interfered with the ability of the differential transducer to generate a coherent signal. Note Figure 1.18, which depicts the water distribution for each of the three spacer plates simultaneously.

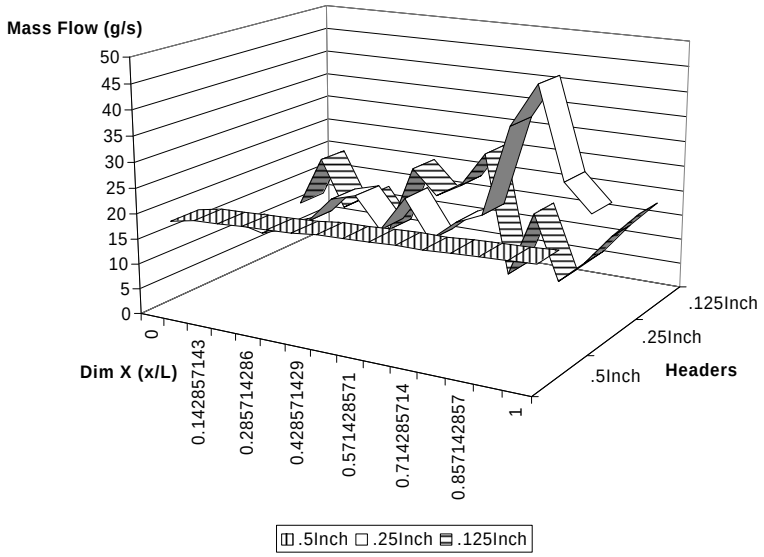

Figure 1.18: Short Entrance Water Data

It is apparent that decreasing the manifold flux area, or increasing the area ratio A_r has a more pronounced effect on increasing flow non-uniformity. The water distribution data for each spacer now follows in Figures 1.19-1.21. Again, the legend indicates the total inlet mass flow rate of water to the manifold.

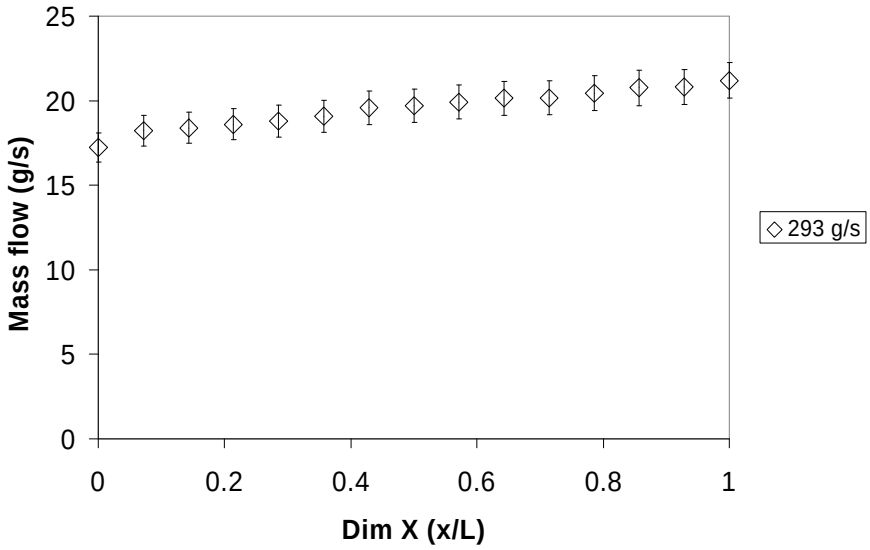

Figure 1.19: 12.7mm Spacer Plate Water Distribution, Short Entrance

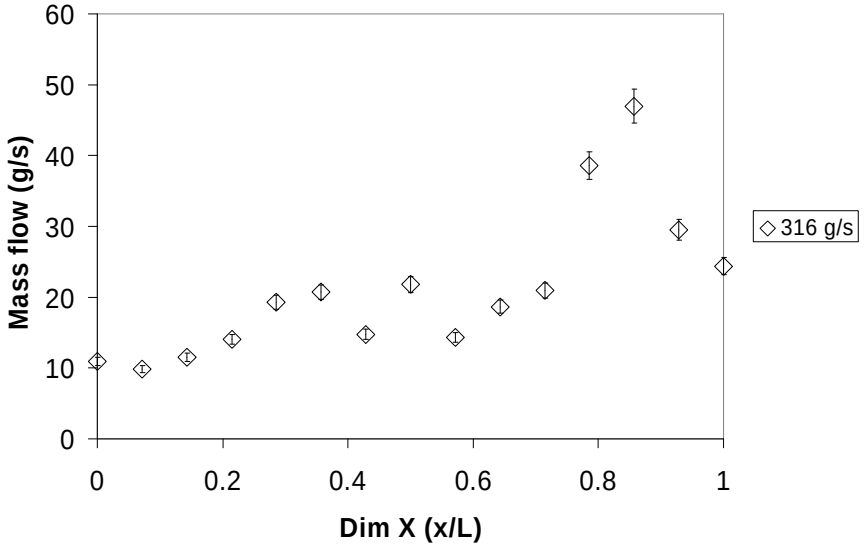

Figure 1.20: 6.35mm Spacer Plate Water Distribution, Short Entrance

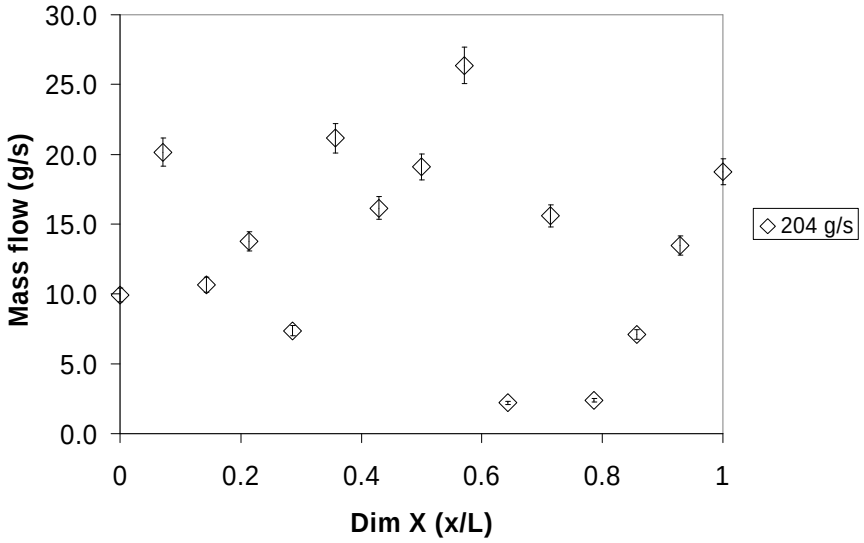

Figure 1.20: 3.175mm Spacer Plate Water Distribution, Short Entrance

1.7 Application of Models

1.7.1 Bajura-Chou-Cheng (BCC) Frictionless Approximation Model

The BCC Frictionless Porous Approximation Model results from Bajura [1971] and Chou-Cheng [2001]. Owing to the complex nature of the overall governing differential equation given by Equation (1.9), consideration was given for the case when the frictional parameter a is negligible. Bajura [1971] found the following sinusoidal solution:

$$\frac{Q'(x)}{Q'(0)} = \cos\left(b\,\frac{x}{L}\right) + Kd\,\sin\left(b\,\frac{x}{L}\right) \qquad (1.35)$$

where ß is the momentum parameter as defined in Equation (1.7), $Q'(x)$ is the lateral discharge along the length of the manifold, $Q'(0)$ is the upstream initial discharge, and

$$Kd = \tan(b) \qquad (1.36)$$

It is interesting to note that Equation (1.35) is precisely the same equation that Chou-Cheng [2001] obtained in Equation (1.12).

Using the definitions of a, ß, and A_r given in Equations (1.6-1.8), the following table of parameters, Table 1.4, was obtained for air as the working fluid in the system under study. A similar table, Table 1.5, may be obtained for single phase water. It must be noted at this point, however, that the frictional parameter a is far from negligible, as seen in Table 1.6.

Table 1.4: Parameters (Air) in BCC Frictionless Approximation Model

Parameters for the Bajura—Chou Cheng Frictionless, Porous Approximation						
Spacer	**d**	**D**	**H**	**Ar**	b	**Kd**
[m]	**[m]**	**[m]**	**[Pa]**	**[-]**	**[-]**	**[-]**
0.012700	0.00154	0.01506	37.86364	1.07	0.19	0.192002
0.006350	0.00154	0.00945	37.86364	2.13	0.38	0.398701
0.003175	0.00154	0.00542	37.86364	4.26	0.76	0.948118

Table 1.5: Parameters (Water) in BCC Frictionless Approximation Model

Parameters for the Bajura—Chou Cheng Frictionless, Porous Approximation						
Spacer	**d**	**D**	**H**	**Ar**	b	**Kd**
[m]	**[m]**	**[m]**	**[Pa]**	**[-]**	**[-]**	**[-]**
0.012700	0.00154	0.01506	19.68182	1.07	0.26	0.26935
0.006350	0.00154	0.00945	19.68182	2.13	0.53	0.580839
0.003175	0.00154	0.00542	19.68182	4.26	1.05	1.753142

Table 1.6: Frictional Parameters for Single Phase Air and Water

Frictional Parameters α		
Spacer	a**, Air**	a**, Water**
[m]	**[-]**	**[-]**
0.012700	0.205691	0.220988
0.006350	0.519213	0.557828
0.003175	1.371536	1.473538

Using these parameters and Equation (1.35) (or Equation (1.12)), plots of expected distribution were obtained for given initial discharges. Table 1.7 shows the overall discharge sum percent differences between the experimental data of the sample set and the frictionless, porous approximation.

Table 1.7: Sum Mass Flow % Differences—BCC Approximation Model

	Top or Bottom Entrance								
	3.175 mm (0.125 inch)			6.35 mm (0.25 inch)			12.7 mm (0.5 inch)		
Discharge Sum	0.43 g/s	3.09 g/s		1.01 g/s	4.51 g/s	5.34 g/s	0.282 g/s	3.204 g/s	4.298 g/s
Sum % Diff	104.04	88.63		6.43	19.68	14.47	1.20	7.59	4.92

Results and discussion shall be presented after the applications of all the models have been presented.

1.7.2 Bajura-Chou-Cheng (BCC) Non-Dimensional Model

The BCC Non-Dimensional Model is based upon Bajura [1976] and later expounded upon by Chou & Cheng [2001]. Equation (1.23), along with the boundary conditions of Equation (1.24), is the governing equation for this model. Owing to its complexity as a second order, non-linear differential equation with two prescribed boundary conditions, analytical solutions are extremely difficult to formulate.

A "shooting method" procedure was developed to solve Equation (1.23) for the system of study. First, the equations were rewritten as a series of first-order, coupled differential equations. One of the boundary conditions, that of $\tilde{Q}(0) = 1$, was prescribed. Recall that $\tilde{Q}$ is *not* the discharge through the lateral, but the mass flow rate

along the length of the manifold. It is the same quantity as “mdot2” given in the presentation of the physical model in Section 1.5.3. The remaining boundary condition was satisfied by assuming an initial derivative of manifold mass flow $\tilde{Q}'(0) = prescribed$ such that $\tilde{Q}(h = 1) = 1$, where *?* is a dimensionless variable similar to $\tilde{x} = x / L_c$. A FORTRAN program (see Appendix A) was written to solve the system of first-order coupled differential equations using a fourth-order Runge-Kutta method. The solutions consist of stepwise determinations of manifold mass flow and individual discharge mass flow along the length of the manifold from ?=0 to ?=1.

Thus, for a given spacer and working fluid, $\tilde{Q}(0) = 1$ is invoked and an initial discharge mass flow is supplied as an input. Satisfactory solutions are provided only when $\tilde{Q}(h = 1) = 1$. Generally good agreement with the data was obtained. Table 1.8 presets the overall discharge sum percent differences between the experimental data of the sample set and the non-dimensional model.

Table 1.8: Sum Mass Flow % Differences—BCC Non-Dimensional Model

	Top or Bottom Entrance								
	3.175 mm (0.125 inch)			6.35 mm (0.25 inch)			12.7 mm (0.5 inch)		
Discharge Sum	0.43 g/s	3.09 g/s		1.01 g/s	4.51 g/s	5.34 g/s	0.282 g/s	3.204 g/s	4.298 g/s
Sum % Diff	10.479	18.638		4.297	1.897	0.116	0.683	1.250	1.308

A more detailed explanation follows in the results and discussion section following the presentation of the Physical Model.

1.7.3 Physical Model

The presentation of the Physical Model was provided previously in Section 1.5.3.

The equations are solved stepwise along a dimensionless distance $\tilde{x}$, where $\tilde{x} = 0$ implies the header entrance and $\tilde{x} = 1$ implies the end of the header. For the “short entrance” condition, microchannel #15 is the initial discharge microchannel. Therefore the dimensionless distance is defined by:

$$DimX_i = \frac{N - i}{N - 1} \quad \text{for } i = 1 \text{ to } N \tag{1.37}$$

When input as an array into a simultaneous equation solver such as EES® (Engineering Equation Solver), a large array of equations is generated and solved simultaneously. The outputs are:

1) Individual microchannel discharge mass flow rate (g/s)
2) Mass flow rate along the manifold
3) Nodal pressures
4) Velocities along the manifold and exiting the microchannel
5) Manifold and microchannel Reynolds numbers
6) Manifold and microchannel friction factors

The solution procedure is as follows:

1) Decide the working fluid—either air or water
2) Decide the spacer—either 12.7mm, 6.35mm, or 3.175mm
3) Input the initial mass flow rate—determined by the sum of the fifteen individual discharges from experiment
4) Alternatively, one may input the initial pressure determined from experiment
5) Input the area-dependent K loss coefficient
6) Solve the equations
7) Compare output to experimental data

Generally, good agreement was provided with the experimental data, which shall be presented in the model comparison section. Table 1.9 presents the overall discharge sum percent differences between the data sample set and model.

Table 1.9: Sum Mass Flow % Differences—Physical Model.

	Top or Bottom Entrance								
	3.175 mm (0.125 inch)			6.35 mm (0.25 inch)			12.7 mm (0.5 inch)		
Discharge Sum	0.43 g/s	3.09 g/s		1.01 g/s	4.51 g/s	5.34 g/s	0.282 g/s	3.204 g/s	4.298 g/s
Sum % Diff	0.701	0.016		0.000	0.887	0.002	0.120	0.013	0.005

1.8 Model and Data Comparison

At this point, a representative sample set of data has been justified and presented, and three models have been developed to predict the discharge mass flow distribution of single phase air and single phase water through the microchannel manifold array. Graphical comparisons shall be performed for air and water, followed by a discussion.

1.8.1 Presentation of Results

Figures 1.22-1.24 display the graphical agreement between representative sample air data and the three models presented.

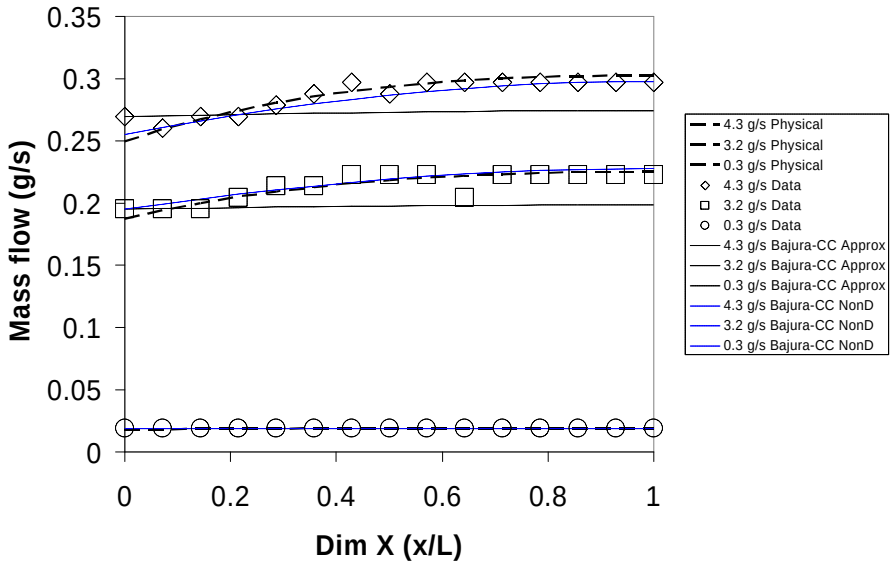

Figure 1.21: 12.7mm Spacer Plate Air Data and Models, Short Entrance

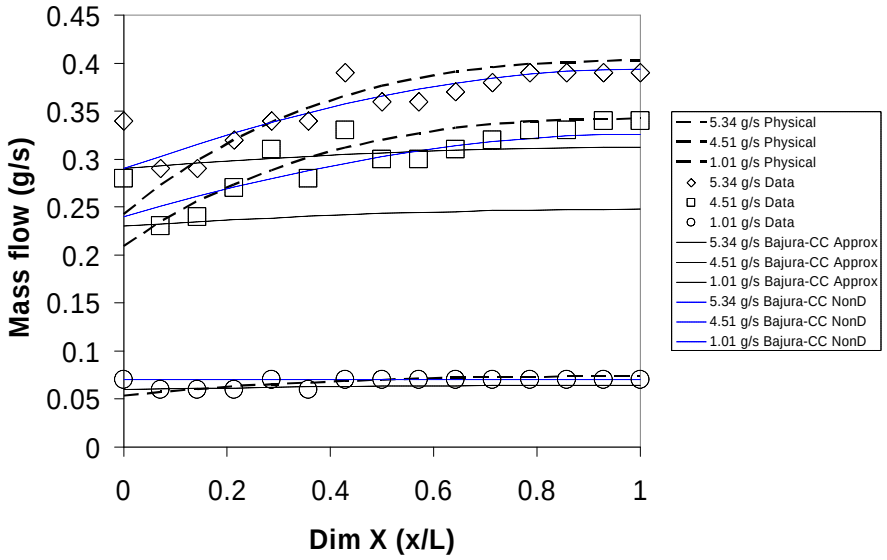

Figure 1.22: 6.35mm Spacer Plate Air Data and Models, Short

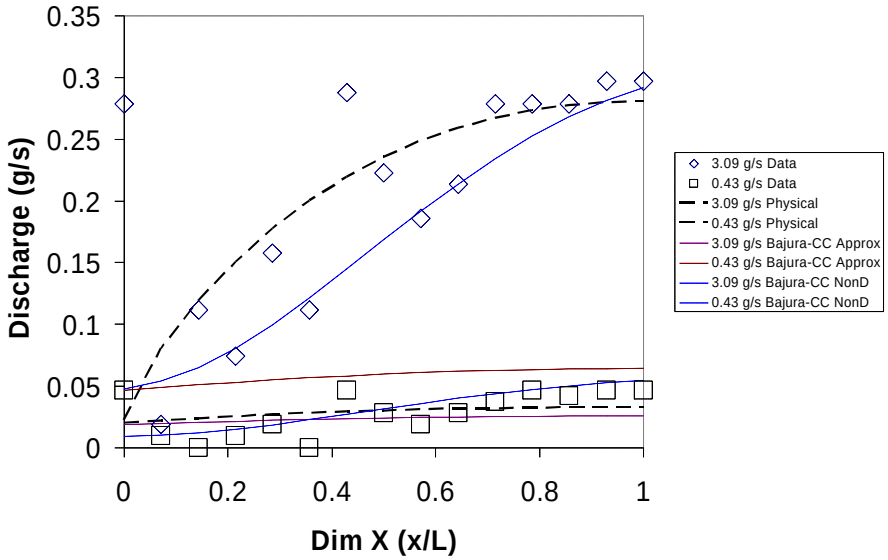

Figure 1.23: 3.175mm Spacer Plate Air Data and Models

Figures 1.25-1.27 display the graphical agreement between representative sample water data and the three models presented.

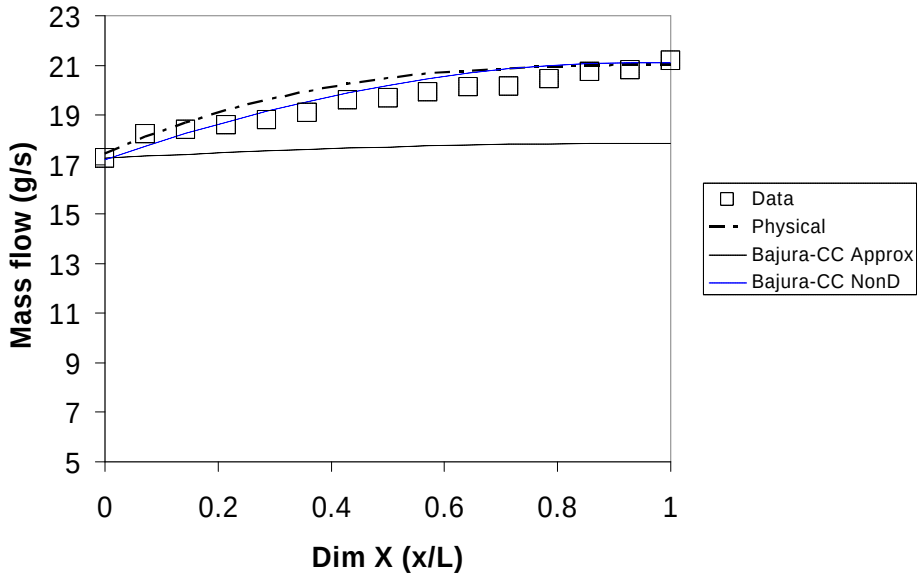

Figure 1.24: 12.7mm Spacer Plate Water Data and Models, Short Entrance

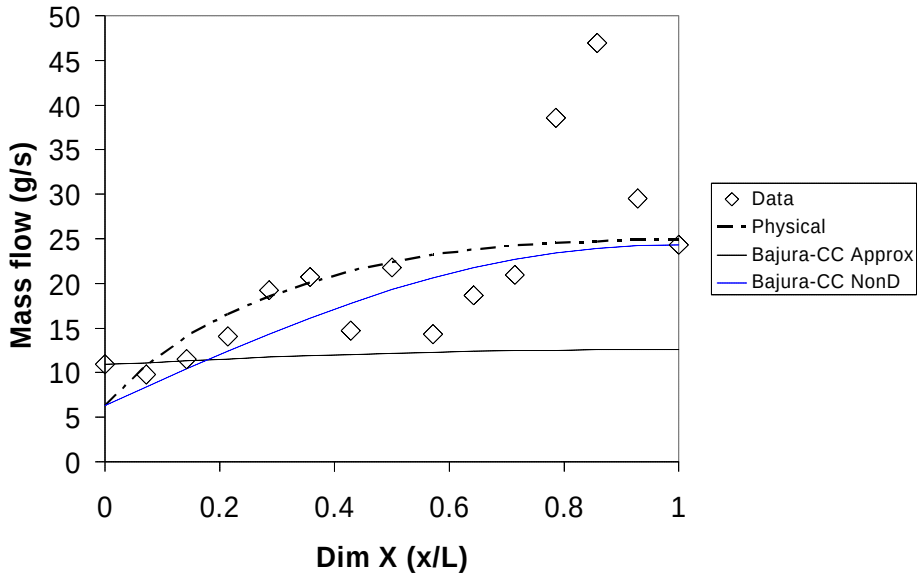

Figure 1.26: 6.35mm Spacer Plate Water Data and Models, Short Entrance

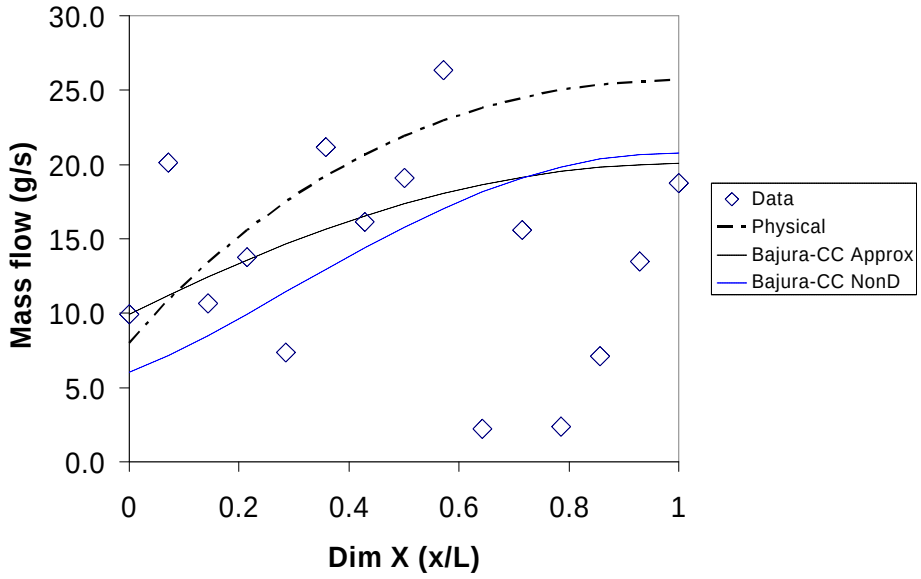

Figure 1.25: 3.175mm Spacer Plate Water Data and Models, Short Entrance

1.8.2 BCC Frictionless Approximation Model Discussion

Of all three models, the BCC Frictionless Porous Approximation Model provides the lowest degree of agreement. In all cases, this model grossly under-predicts the lateral discharge, as evidenced by the percent differences of Table 1.7. The degree of regain is far less, resulting in a severe under-prediction of the discharge flow rate at the end of the manifold.

Recall that this model is based on the assumption that a is negligible, an assumption which precludes its existence from the overall governing differential equation, leaving only ß to adequately describe the manifold discharge behavior. However, as evidenced by Tables 1.4-1.6, a and ß are roughly of the same magnitude. It is not correct to assume that the manifold system is non-dissipative. The purpose of the inclusion of this model is to gain an insight into where this type of manifold lays on the spectrum of frictional domination or momentum domination. Apparently, the system lays somewhere in between, necessitating a solution which considers both momentum and friction. Thus, a non-dimensional, general model needed to be developed, which led to the formation of the BCC Non-Dimensional Model.

1.8.3 BCC Non-Dimensional Model Discussion

The BCC Non-Dimensional Model provides a good deal of accuracy for single phase air and water, as evidenced by the percent differences presented in Table 1.8. Its accuracy may be attributed to the fact that it accounts for the combined effects of friction and momentum.

Regarding the air distribution for the 12.7mm spacer data, nearly each data point is predicted. For low and high mass flow rates, the same “flattening” and “widening” behavior is obtained. There is an increased departure from experimental data when the spacer is reduced by a factor of two, as evidenced by the 6.35mm data. When the spacer plate thickness decreases, the area ratio increases, and for reasons mentioned before the flow is more non-uniform than for larger manifold cross sectional areas. Still, this increased departure from uniformity is fairly predicted. When the spacer decreases by another factor of two, the model departs from an “arc”-like distribution to a

slight “S” curve. It is difficult to ascertain whether this is the true behavior of the data, or whether it fails in its predictive ability, since the data is so widely scattered itself and the flow is at its most non-uniform state of the three conditions.

Similar behavior is noted for the water distribution curves. This model has decreasing accuracy with an increase in area ratio; agreement is initially satisfactory for the 12.7mm, moderately successful for the 6.35mm case, and the agreement is indiscernible for the 3.175mm case. As mentioned for the air distribution predictions, an “S” curve is obtained for the highest area ratio rather than the typical arc curve seen previously.

1.8.4 Physical Model Discussion

As noted by Jones & Galliera [1998], physical models based on mechanical principles may often create nearly the same accuracy as more complex numerical methods. This is the case for the physical model, providing excellent accuracy as noted in the percent differences of Table 1.9.

For the 12.7mm air distribution data, the shape of the curve and its agreement with experimentally obtained values seems accurate. A further observation is that the curve seems to approach a slope of zero at the end of the manifold, which is commensurate with the boundary condition that manifold mass flow rate is zero at the end of the manifold. As the manifold spacer plate is decreased by a factor of two for the 6.35mm and 3.175mm cases, it was mentioned previously that there is a greater departure of distribution from uniformity. The Physical Model seems to predict the correct amount of non-uniformity, obtaining an arc distribution with an initial slope which is quite steep. This is the same as stating that the derivative of the manifold mass flow is changing to a greater degree when the flow encounters the microchannel array. This would be the logical expected behavior for an orifice which is decreasing in area.

Regarding the water distribution data, the agreement is once again satisfactory for the 12.7mm and 6.35mm spacers, but poor for the lowest value of spacer thickness.
This demonstrates an inability to predict accurate distributions for higher area ratios. Nonetheless, it possesses an ability to predict the changes in the derivative of the mass flow along the length of the manifold in the direction of flow.

1.9 Conclusions

Flow maldistribution increases with an increase in area ratio in single phase flow. To obtain more uniform distribution, designers should aim to construct a distribution system with fairly low area ratios. An increase in area ratio is caused by decreasing the manifold area while holding the total discharge area constant; alternatively, holding the channel area constant and decreasing the outflow discharge area. In this experiment, it was not possible to alter the area ratio by the second method mentioned.

Models which exclude or approximate as negligible either friction or momentum are not adequate, since the friction and momentum parameters are of the same magnitude. Overall, generalized physical or non-dimensional models are preferred. This is significant because this demonstrates that such microchannel array distributions adhere to expected physical trends which are exhibited by more conventional and larger diameter tubes.

Three models were presented. The Physical Model and BCC Non-Dimensional Model showed reasonable agreement with the experimental data. The second order derivatives of the two models for high flow and high area

ratios are different at the manifold inlet; however, it is difficult to know from the experimental data which is more correct. The BCC Frictionless Approximation Model shows poor agreement with the data except for a few cases with negligible dissipation/regain effects. Agreement with experimental data decreased with an increase in area ratio.

1.10 Bibliography

Bajura, R.A. *A Model for Flow Distribution in Manifolds.* Journal of Engineering for Power. pp. 7-12. January 1971.

Bajura, R.A and Jones Jr., E. H. *Flow Distribution Manifolds*. Transactions of the ASME. Gas Turbine and Fluids Engineering Conference. Paper No. 76-FE-7. March 1976.

Chou, H.T.; Cheng, R.Y. *Outflow Distribution Along Multiple-Port Diffusers*. Proceedings of the Natl. Sci. Council. ROC(A). Vol. 25, No 2. pp 94-101. 2001.

Jones, G.F.; Galliera, J.M. *Isothermal Flow Distribution in Coupled Manifolds: Comparison of Results from CFD and an Integral Model*. FED-Vol 247, Proceedings of the ASME Fluids Engineering Division, ASME. pp. 189-195. 1998.

Keller, J.D. *The Manifold Problem.* Journal of Applied Mechanics. Vol. 71. pp 77-85. March 1949.

Kim, S.; Choi, E.; Cho, Y.I. *The Effect of Manifold Shapes on the Flow Distribution in a Manifold for Electric Packaging Applications.* Int'l Communications in Heat and Mass Transfer, Vol. 22, No. 3. pp. 329-341. 1995.

McNown, J. S.; Asce, M. *Mechanics of Manifold Flow*. Transactions of the American Society of Civil Engineers, Paper #2714. pp. 1103-1142. 1952.

Miner, S. M. *CFD Analysis of the Flow Distribution in the Manifold of a Filtration System.* FED-Vol. 239, Fluids Engineering Division Conference. Vol 4. ASME 1996. pp. 509-513. 1996.

Shen, P.I. *The Effect of Friction on Flow Distribution in Dividing and Combining Flow Manifolds*. Journal of Fluids Engineering. Vol. 114. pp. 121-123. March 1992.

Subagyo; Standish, N.; Brooks, G.A. *A New Model of Velocity Distribution of a Single-Phase Fluid Flowing in Packed Beds*. Chemical Engineering Science. Vol. 53, No. 7. pp. 1375-1385. 1998.

Qu, W.; Mudawar, I. *Experimental and Numerical Study of Pressure Drop and Heat Transfer in a Single-phase Micro-Channel Heat Sink*. Intl. J. of Heat and Mass Transfer. Vol. 45. pp. 2549-2565. 2002.

Wang, X.A.; Yu, P. *Isothermal Flow Distribution in Manifold Systems*. Int. J. of Solar Energy. Vol. 7. pp. 159-169. 1989.

White, F. *Fluid Mechanics*. 3rd Ed. p. 317. 1994.

Chapter 2. Two-Phase Modeling of Microchannel Distribution Manifold

2.1 Introduction

Chapter 1 presented models for the prediction of single phase air and single phase water distribution through the current system. Ultimately this model can only serve as a baseline or starting point for more complex and realistic flows. The fluid mechanics involved in the creation of such a model are a necessity for the predominant mode of flow in heat exchangers and other systems which may employ these microchannels. Specifically, this predominant flow mode is two-phase flow.

Chapter 2 extends the fluid mechanics of single phase flow to the application of a model which may predict mass distribution for two-phase flows of varying mass flux and quality which enter the current manifold distribution system. A comprehensive literature review provides the necessary background for the model's development. From this foundation, a two-phase model is formulated and applied to the two-phase distribution data. Following this, the model is critiqued regarding its formulation and applicability.

2.2 Literature Review

2.2.1 Manifold Distribution

This section is meant to provide the reader with a framework to understand the vast class of real situations in which two-phase manifold distribution exists. Indeed, such a class of problems has a wide variety of applications and is pertinent to several fields. Examples of two-phase manifold distribution are presented in the areas of nuclear engineering, refrigerant heat exchangers, and air-water systems.

2.2.1.1 Nuclear Engineering

An area in which two-phase manifold distribution situations frequently arise is nuclear engineering. Hsia & Griffith [1980] studied two-phase flow phenomena in a nuclear reactor. Such phenomena include T-junction phase separation and two-phase pressure losses. The experimental distribution manifold did not distribute the phases uniformly. To analytically describe the data, the THERMIT code (Reed & Stewart [1978]) was implemented. There were several computational problems: the interface gave divergent solutions, inaccurate void fraction, artificial damping terms were required, and it was unclear how to model larger numbers of tubes.

There are inherent instabilities which occur in nuclear-reactor two-phase flows, as studied by Chan & Yadigaroglu [1979]. They examined instabilities due to flow-rate and pressure drop characteristics in heat exchangers. Further treatments of two-phase flow in nuclear engineering can be found in Costa [1981], Hsu [1981a], and Mayinger [1978].

2.2.1.2 Heat Exchangers

Çabuk & Modi [1989] state that the manifold must provide uniform flow in order to maximize heat transfer with an acceptable level of pressure loss within the constraints of system geometry. Chisholm & Wanniarachchi [1992] make a connection between flow maldistribution and temperature maldistribution.

Asoh et al. [1991] studied two-phase refrigerant flow (R113) in a simulated automobile air conditioner system using three downward branch pipes from a central line. Refrigerant maldistribution was found to be due to non-uniform distribution of thermal load, and two-phase fluid dynamics. Distribution in heat exchangers is an important area because uniformity of distribution is related to evaporator efficiency.

Bernoux et al. [2001] studied the two-phase distribution of a horizontal manifold for a compact heat exchanger with parallel vertical downflow branches. An understanding of the effect of inlet mass flow rate and quality on distribution was desired. Their test section included eight vertically downward rectangular channels [2 x 55mm], with R113 as the working fluid. The inlet conditions were: $0.1 < x < 0.8$ and G=35 $\mathrm{kg/m^2 \cdot s}$, 70 $\mathrm{kg/m^2 \cdot s}$, and 100 $\mathrm{kg/m^2 \cdot s}$.

For low inlet quality (x=0.1), Bernoux et al. [2001] noted that the vapor prefers the first few channels, while liquid is preferentially drawn in the final channels. For medium inlet quality (x=0.35) the liquid nonuniformity increases above the low quality condition, while the vapor distribution improves. Vapor uniformity increases for high inlet quality (x=0.8) and the liquid distribution becomes its most non-uniform. The inlet flow pattern was visually observed and a transition was noted from pseudo-slug to wavy-annular to fully annular with increasing quality. Furthermore, the authors visualized the entrances of these patterns into the distribution manifold and how this affected the behavior of the incoming stream.

For low quality flows, an incoming jet of liquid flow fills the channels upon which it impinges; for medium quality this liquid jet rebounds off the far wall of the inlet manifold and fills the first channels it encounters; for high quality the inlet flow is a mass of droplets which then congeal on the far wall, resulting in liquid flow predominantly in the last channel. These effects are pertinent to the present system.

Fei et al. [2002] examined the distribution of R134a in manifold of a plate evaporator. The following undesirable effects of refrigerant maldistribution were noted: reduced effectiveness, uneven air temperature profile, and uneven evaporator frosting. Heggs & Scheidat [1992] made an in-depth study of heat exchanger performance as related to plate flow distribution. Lalot et al. [1999] found that maldistribution causes a 7% loss in effectiveness for condensers and counterflow heat exchangers, and up to 25% for cross flow exchangers. It was found that backward flow may occur for certain manifolds.

Watanabe et al. [1995] studied experimental evaporator for an automobile air conditioner with a horizontal manifold and four vertically upward branch pipes, with R11 as the refrigerant. Several factors were noted which make it difficult to predict two-phase refrigerant manifold flow: cross sectional area ratio of branches and distributor, angular displacement, location, and branch orientation. Pressure drop along the manifold must be taken into account when predicting flow uniformity or lack thereof. It was found that single T-junction data are useful in predicting flow distribution in multi-pass tubes.

Vist & Pettersen [2002] studied a manifold distribution system for two-phase R134a flow with ten parallel downflow branches. They cite that maldistribution leads to reduced thermal performance of a compact heat exchanger because charge enters the tubes unevenly. For evaporators dry-out is to be avoided; for condensers, high liquid levels diminish heat transfer.

2.2.1.3 Air-Water Systems

Kubo & Ueda [1973] studied a combining flow manifold of ten distribution tubes for an air-water two-phase flow system. Using fundamental mechanics an equation is derived which solves for the ratio of branch discharge to total inlet flow, stepwise along the manifold. Critical to this formulation is the definition of a “nozzle factor” which is essentially a two-phase pressure drop factor dependent upon the branch-to-inlet diameter ratio and

flow rate ratio. This discharge ratio equation formulation is lacking, however, in its foundation. For instance, pressure drops are with respect to the inlet pressure, when in fact each junction pressure drop is related to its pressure difference with the previous junction. Also, the void fraction is not considered.

Rong et al. [1995] studied air-water distribution with multiple channels in vertical upward and downward orientations. The primary parameters are the inlet flow and quality, reflective of the inlet flow pattern. Other parameters which affect distribution are: channel orientation, inlet channel geometry. It was found that overall the vertical downward configuration produced relatively poor distributions. They cite that the manifold geometry is a crucial factor in two-phase distribution because this determines the inlet two-phase flow characteristics. Annular flow was found to be dominant especially for high flow quality of high air and low water flow rate, though there were occasions of annular-wavy flow. To explain how the first channel received the most water and less air, and the last channel received more air and less water, it is stated that the air in the annular flow core misses the first several channels and is propelled to the manifold end. This effect was found to be applicable for the vertically upward and vertically downward configurations.

Samson et al. [1988] developed three distribution manifold prototypes to study two-phase refrigerant flow in a real heat exchanger device. Similar to the present system, air-water was employed as a precursor to understanding refrigerant behavior. The function of a two-phase manifold is to distribute the flow uniformly to the boiling side of the heat exchanger, giving each branch equal heat capacity.

2.2.2 Approaches to Two-Phase Modeling

This section is meant to familiarize the reader with approaches to modeling two-phase manifold distribution systems. Currently there is no overall two-phase applicable to all systems, and there may never be, owing to the vast permutations of manifold assembly and flow conditions. The best one may achieve is a judicious employment of previous research, combined with current data and insight. A background is provided, followed by general sketches of current approaches.

2.2.2.1 General

Bouré [1978] gives a general treatment of the formulation of equations for two-phase flow. “First kind” equations are derived from conservation laws (energy, mass, momentum). “Second kind” equations describe the fluid properties and behavior and are the constitutive fluid laws. It is noted that generality is very difficult to achieve when applying fundamental laws to a specific system, since in the process extra relations are necessary which are specific to the system under study.

Delhaye [1981] discusses in detail the formulation of a two-phase descriptive model based on conservation of mass, momentum, and energy for the two-phases. To solve these overall equations, constitutive equations must also be solved. These constitutive equations are for the interface (mass, momentum, energy transfer) and wall (friction and heat transfer). This progression can be seen in Figure 2.1.

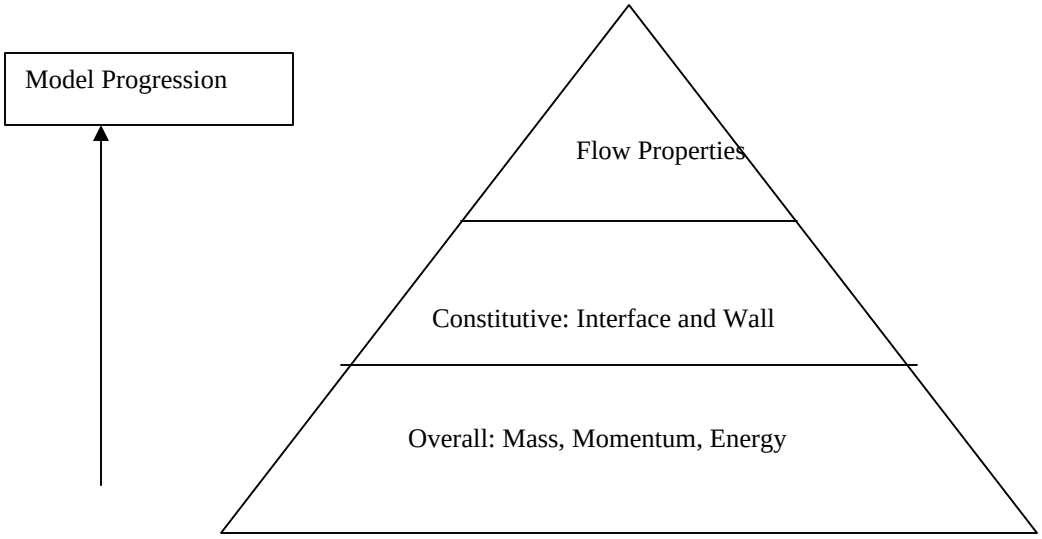

Figure 2.1: Progression of Two-Phase Model from First Principles

Complications arise from the formulation of simultaneous equations; the matrix of equation coefficients may not be mathematically simple and may be ill-conditioned/singular for certain values of flow properties. Bouré [1975] arranged the equations in such a manner as to make them more amenable to numerical solution.

Friedel [1976] discussed in comprehensive terms the relation between pressure drop, its constituent sub-components, and momentum in two-phase flow applications. Several factors are cited which make two-phase pressure drop formulation particularly formidable:

1) the phase surface boundaries are not separate but interact
2) interface effects are very significant
3) there are many more flow variables to solve for in comparison to single phase flow
4) there are parameters specific to two-phase flow (i.e. flow regime and void fraction) which affect the governing equations

Collier [1976a] also mentioned these factors.

Friedel [1976] categorizes model formulation approaches into three main types:

1) Homogeneous Flow Approach—Two-phases are mixed in such a manner that the resulting stream is comprised of weighted thermodynamic property averages and flows as a single phase fluid. This is the simplest baseline case.
2) Separated Flow Approach —Two-phases have different velocities and properties, thus necessitating sets of simultaneous equations to solve for the individual phasic properties. This is a more complicated case.
3) Flow Pattern Approach—Considers the flow pattern in which the two-phases are configured and adopts correlations specific to these regimes

Two-phase pressure drop is comprised of three main components: friction, acceleration, and gravitational, the latter two representing reversible pressure components. The acceleration component results from expansion of the gas with channel length, and the heating/cooling of two-phase flows; this component is often considered negligible for adiabatic flows. The frictional contribution is the most important. Larger energy losses result for two-

phase flow than single phase flow, due to the irreversible losses of vapor work on the liquid and the reduction in effective channel area due to two phases flowing simultaneously.

Delhaye [2001] studied the two-phase interface. For the two fluid approach, mass, momentum, energy equations are made for each phase and then coupling equations for the interface. These coupling terms or relations should specify the phase interactions and accommodate the information which is lost when averaging the governing balance equations. These terms must satisfy the interface conditions, some of which depend on an interfacial area.

2.2.2.2 VOF, Eulerian-Langrangian, Eulerian Approaches

Ranade [2002] provides an excellent treatment of two-phase modeling issues. Three main methods of modeling are posited: Volume of Fluid, Eulerian-Langrangian, Eulerian-Eulerian. These are seen in Figure 2.2.

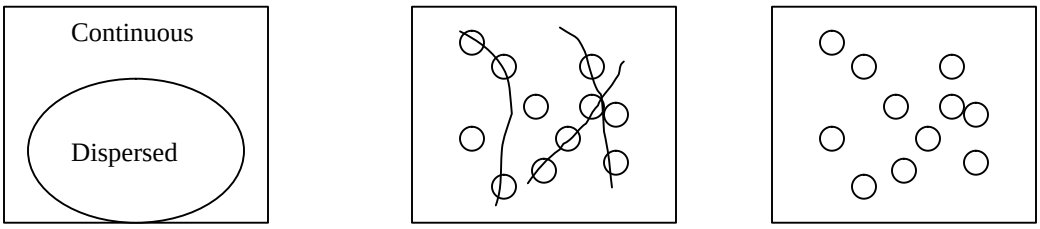

Figure 2.2: Three Methods of Modeling (Ranade [2002])

In the Volume of Fluid (VOF) method, all the phases are tracked separately by solving local and instantaneous conservation (mass, momentum, energy) equations. Boundary conditions are supplied at the phase interface; however, this surface is in a constant state of motion. In the Eulerian-Lagrangian method, the interface is not modeled but the motion of the dispersed fluid particles is described. The equations of motion, or trajectories, of each particle are simulated. When averaged over a large number of trajectories, the motions of individual particles are described. When modeled purely from a Eulerian perspective, all phases are treated as a continuum that is free to penetrate into neighboring particles' vicinity. Thus, particle-particle interactions can be examined.

Chen & Li [1998] took a VOF approach to model the difficult region of the interface between two fluids.

They gave an accurate mathematical description of two bubbles congealing and a bubble rising to the gas-liquid interface in a highly viscous fluid. Kuo et al. [1997] treats the fluid phase of two-phase flow as a continuum and solves the Eulerian conservation equation. Gas phase bubbles are tracked in Lagrangian sense by solving time-averaged multidimensional mass and momentum equations. Pokharna et al. [1997] attempted to bridge the gap between empirically based relatively simple models to multidimensional local instant models. A program was developed which involves a 1-D Eulerian description for the continuous phase and a Lagrangian description of the dispersed bubbly phases. This work is an attempt to describe bubble migration due to turbulence.

2.2.2.3 CFD/Numerical Approaches

Faille & Heintze [1999] were concerned with a numerical solution of the conservation laws of a two-phase flow of oil and gas in a pipeline. To aid in solution, a finite volume method was employed. Hazi et al. [2002] used the lattice-Boltzmann method, in which the molecules are tracked in a lattice formation. This is in contrast to conventional CFD codes which attempt to solve the Navier-Stokes Equations. The uses of the single phase

approach, multi-field approach, interface tracking approach, and volume of fluid approach in numerical modeling are demonstrated. Lahey & Drew [2001] use a multidimensional four-field, two-fluid CFD model to predict a wide variety of two-phase flow data.

Hsu [1981b] discussed issues relevant to computer codes. It is noted that writing codes for two-phase flows is an extremely difficult process. A simplified approach may be taken for the homogeneous treatment, but ultimately greater accuracy is achieved for the separated flow model in which the phases have their distinct velocities and closure constitutive equations are written for the interface. There are advanced three-dimensional codes incorporating flow regime-dependencies and varied-mode heat transfer relations as well.

2.2.2.4 Homogeneous Flow Approach

One may consider the two-phases as a mixture traveling with no relative velocity between the phases, and possessing average fluid properties based on the fluid quality. Such an approach is termed the homogeneous fluid approach. This will be explained in detail in Section 2.4.2.

2.2.2.5 Drift Flux Approach

Ishii [1976] explains the concept of a drift flux model in great detail. The essence of the drift flux model (Zuber & Findlay [1965]) is to ease the mathematical difficulty that arises when the simultaneous sets of equations for the phase momentum, mass, and energy try to account for interface phenomena. In the drift flux model the mixture is treated as a whole, rather than two distinct phases. The motion of the whole mixture is expressed by a mixture momentum equation and a kinematic constitutive equation is used to express the relative motion of the phases. The velocity field is expressed by a "mixture center-of-mass" velocity and $\tilde{u}_{Gj}$, the vapor velocity at the mixture's volume center. An advantage of this approach is that $\tilde{u}_{Gj}$ can be formulated for specific flow regimes, such as particle, churn-turbulent, bubbly flows. For annular flow conditions, the drift velocity (relative velocity between the phases) can even be formulated for turbulent or laminar conditions.

Inayatullah & Nicoll [1976] applied the drift flux model to a wide range of two- phase flow situations. A detailed derivation is provided for the four governing equations, which is closed by a mixture momentum equation. The specific inputs are the distribution functions, rate of vapor generation (due to wall heat transfer and pressure change), and the wall shear stress. To solve the differential equations an implicit finite difference method, coupled with a Runge-Kutta scheme, was employed.

An excellent work applying this approach is given by Lahey [1979], in which a one-dimensional drift flux method is employed to analyze transient effects in a nuclear reactor. A detailed description is provided, which shall not be repeated. The key conclusion is that the drift flux method is quite powerful and capable of handling a wide variety of physically significant flows with their transients, and it can yield exact analytical solutions for highly complex flows.

2.2.2.6 Separated Flow Approach

Uygur-Onbasioglu [1998] modeled the interfacial transport effects (advection and diffusion) of air water two-phase flow by numerical methods. The author adopts a separated phase flow model, which needs to account for interfacial interaction. To emphasize this separation, equations were even found for the individual phasic Reynolds numbers.

2.2.3 Model Foundations

Having established a general framework for approaches to two-phase modeling for distribution systems, this section provides the reader with the fundamental building blocks to arrive at a satisfactory model, and set the background for the current model. Research in the area of phase separation and two-phase pressure drop, which are central to the models developed in later sections, is presented.

2.2.3.1 Dividing Flow Phase Separation

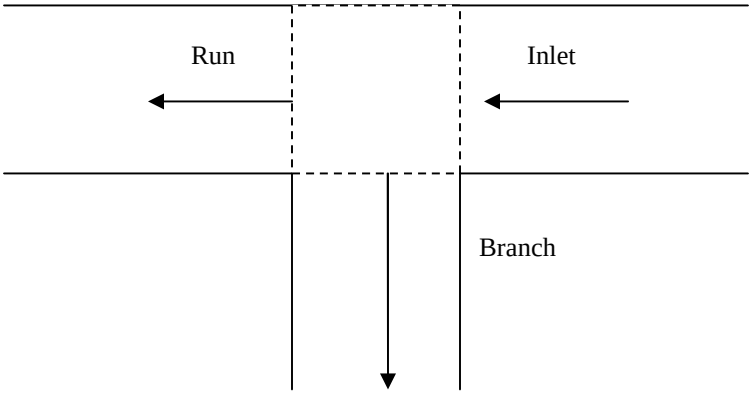

Figure 2.3: Inlet, Run, and Branch at a T-Junction

Saba & Lahey [1984] developed empirical model to predict phase distribution of two-phase flow downstream of a conduit. See Figure 2.3 (above) for references to “inlet”, “branch”, and “run”. Typically eight parameters are of interest when examining phase separation: inlet flux, inlet-branch pressure difference, inlet-run pressure difference, inlet flux, run flux, branch flux, run quality, and branch quality. Usually three of these can be specified, leaving five parameters, thus five equations. These five equations describe mixture continuity, vapor phase continuity, mixture linear momentum, mixture linear momentum equation for the run, and vapor-phase linear momentum equation for the branch. The first four are straightforward, whereas the fifth equation requires integration along a streamline entering the discharge branch from the inlet. The selection of such a streamline is based on the fact that phase distribution of two-phase flows is primarily affected by the ability of the vapor to turn the corner into the discharge branch. The authors note that when two-phase flow reaches branching junction, water continues on due to its greater inertia whereas the vapor goes into the branch because its inertia is not sufficient to overcome adverse pressure gradient. Thus, a higher quality flow goes into the branch than continued down the run.

Lahey [1986] summarized, explained, and identified key issues related to the study of two-phase separation. Ultimately, it was determined that no comprehensive phase separation model exists which can adequately describe separation behavior for an arbitrary branching conduit. Models must be based upon physical principles yet empirical formulations from the data need to be interjected where gaps in the formulation exist.

Lahey [1986] postulates that there is a “zone of influence” (ZOI) related to the discharge-to-inlet withdrawal ratio. For low withdrawal ratios, liquid is preferentially drawn into the conduit, even though the vapor has lower inertia and can turn a corner more readily. When the withdrawal ratio is high, the ZOI is larger and more vapor is extracted. The author further notes that when a flow turns a sharp corner (e.g. 90°), there is an immediate pressure undershoot and recovery; however, there is a pressure recovery in the run section after the fluid has

discharged into the conduit. This generation of an adverse pressure gradient encourages the lower inertia vapor to flow into the branch.

Lahey [1986] builds upon the mechanistic model of Saba & Lahey [1984], which was valid for relatively high withdrawal ratios, and incorporates the relatively low withdrawal ratio model of Azzopardi & Whalley [1980]. The model of Lahey [1986] incorporates the flow rate of liquid film traveling in the channel as an annular flow. An alternative “fifth equation” is found that can be used instead of the vapor-phase linear momentum equation for small mass withdrawal ratios and annular flows. Other researchers have posited alternative “fifth equations”.

Seeger et al. [1986] found that phase separation depends on orientation, flow regime, inlet mass flux to branch mass flux. Strong phase separation occurs for vertical upward flow, since inertia and gravity act in same direction. Inertia and gravity act in different directions for downward branch. Also phase distribution in inlet affects phase separation in the branch

Reimann & Seeger [1986] performed experiments to obtain pressure differences between pipe inlet and run, and inlet branch for air-water and steam-water flow in T-junction for horizontal, vertically upward or downward. The authors built upon the work of Saba & Lahey [1984] to arrive at more accurate model for two-phase flow in T-junction.

Roberts et al. [1995] studied phase separation in annular flow for industrial-scale pipes (12.5cm). To arrive at a phase separation model, the authors incorporated the phenomenon of “film stop”. Film stop occurs when, as annular flow encounters a T- junction, a pressure increase occurs and the film slows down, creating a sudden increase in extracted liquid. Similar data trends were observed for a smaller diameter pipes (3.8cm). Model predictions greatly improved when film-stop was incorporated. For additional information concerning entrainment fraction and film momentum, see Williams [1986] and Laurinat et al. [1984].

Buell et al. [1994] studied low-pressure air water phase distribution and differential junction pressure drops for equal diameter (inlet=run=branch=37.6mm) dividing T-junctions. It was desired to compare the inlet-run and inlet-branch pressure drops against five models: homogeneous flow of Saba & Lahey [1984], separated flow of Fouda & Rhodes [1974], Hwang & Lahey [1988], Ballyk et al. [1988], and Reimann & Seeger et al. [1986]. Each of these is an extension of a single-phase model “fitted” with a two-phase multiplier and semi-empirical loss coefficients. In general, it was found that when the liquid velocity increases for a fixed gas velocity, the gas is more apt to exit through the branch.

Buell et al. [1994] also discuss the principle of “relative momentum”. As a general rule, which is in agreement with Seeger et al. [1986], the phase with lower momentum enters the discharge branch. An increase in liquid velocity for a fixed gas velocity results in an increase in liquid momentum; hence, the liquid is less likely to enter the branch. In a similar light, if the gas momentum lowers, there is a higher probability of gas extraction. This principle is also explained in Walters et al. [1998].

Ballyk & Shoukri [1990] attempted to develop a model for annular flow in a T-junction. It was noted that the flow component that is most easily extracted is the liquid film turning the corner into the branching conduit. They found that when quality is increased for a given mass flux, it was noted that more of the liquid film exists at the bottom and is available for extraction.

Ballyk & Shoukri [1990] follow generally the same approach as that of Lahey [1986] and Saba & Lahey [1984]. The key forces are viscous, pressure, inertia, gravity, and interfacial drag. Interfacial drag forces are neglected because the vapor streamlines interact with the liquid film in a very small region, thus yielding a balance between the dominant pressure and inertia forces (viscous and gravity effects are considered small in comparison). A net pressure force is exerted on a fluid element which is directed downward and toward the inlet. The response of the fluid depends on the density. The less dense phase accelerates toward the branch more than the liquid phase. They arrive at a "fifth equation" by examining pressure gradients in the junction, and arrive at an expression for the discharge quality from the extracted areas of liquid and gas. *A priori* knowledge of the film thickness, development lengths, and pressure changes is needed, or empirical relations must be developed.

Ballyk et al. [1988] studied separation in dividing steam-water annular flow in horizontal T-junction. Pressure, void fraction, flow rate, total and branch qualities were measured. Hassan et al. [1996] measured two-phase discharge from the stratified region through two side branches of same diameter, separated by a vertical distance from center to center. Mudde et al. [1993] studied pressure drop and phase redistribution for an industrial-scale (branch diameter=10cm, inlet & run diameter=23cm) T-junction. A treatment is given as to how to apply two-phase multipliers to single phase models to treat two-phase flow.

Charron & Whalley [1995] studied annular flow in a vertical T-junction with horizontal branch (D_h=32mm, length=5m). Visualization of phase split could be seen using a clear T-junction test section. For low water flow rates, liquid is preferentially drawn into the side branch because there is very little liquid in the gas core, and a high pressure gradient at the junction, and "stops" the film ("film stop", as mentioned previously).

Hwang et al. [1988] studied air-water, horizontal test section phase separation in dividing T- and Y-junctions and developed a model using dividing streamlines. The emphasis is on low extraction rates (branch mass flow / inlet mass flow < 0.3). A similar treatment as that presented in Lahey [1986] is followed, yielding a detailed visual presentation of the dividing streamline and "zone of influence" concepts. Starting from the case of a dividing T-junction, the model is expanded to incorporate various angular displacements of the branching arm and its subsequent effect on phase distribution. The model of Smoglie et al. [1987] is recommended.

Peng et al. [1996] studied the effect of branch orientation on phase distribution using a horizontal inlet. For lower branch flow rates, the majority of discharge flow is liquid, yielding branch qualities lower than that of the inlet. For higher branch flow rates, more vapor is extracted because of its lower momentum, resulting in a higher branch flow quality. When flow divides at a T-junction, a deceleration results and causes a reversible pressure rise in both run and branch due to Bernoulli effects. Pressure data was modeled using mechanics-based correlations using two-phase multipliers independent of branch orientation.

Peng & Shoukri [1997], extending from Peng et al. [1996], develop a physical model for annular flow at a T-junction and examine branch orientation. Two key observations affect phase separation phenomena: inlet and geometrical conditions, and phase inertia interaction. "Phenomenological" models start with the assumption of "zones of influence" bounded by dividing streamlines and the phase interfaces. The dividing streamlines separate the inlet flow into branch and run flows. If the inlet phase distribution is known, it is then possible to find the areas

from which the phases are diverted into the branch. The resulting model predicted much better agreement than previous research, such as Ballyk [1990].

Penmatcha et al. [1996] investigate two-phase splitting under stratified wavy flow at a T-junction. The header arm was angularly displaced (downward and upward) to examine gravity effects on distribution. A model was developed to predict phase separation for downward or upward inclined run arm.

Shoham et al. [1987] studied flow splitting for an equal diameter (D_h=51mm) T-junction, the arms of which lay in a horizontal plane; annular and stratified were the predominant flow patterns. For low liquid flow rates (V=0.0029 to 0.0051m/s) it was found that the liquid phase preferentially flows through the discharge; for higher liquid flow rates, the run arm is the preferred route. The authors propose that this "preferential" behavior is due to centripetal forces acting along its curved streamline path. This centripetal force is incorporated into the phase separation model. Centripetal forces are dominant for annular flow and the liquid preferentially flows into the branch.

Smoglie & Reimann [1986] predicted quality and mass flux through breaks in a horizontal coolant pipe using two-phase air and water, and studied the effects of vortex generation in flow with downward branch. The model enabled predictions of branch quality and mass flux for steam-water flows. Entrainment influences flow through branches in stratified two-phase flow. When this occurs, there is a local pressure decrease produced by fluid acceleration toward the break. They considered the break as a point sink and formulated expected entrainment in upward, downward, and horizontal branches. Branch quality is predicted. For additional information about horizontal flow with breaks, see Reimann & Kahn [1984] and Smoglie et al. [1987].

Yong et al. [1996] performed two-phase air-water experiments and examined phase separation by looking at inlet mass quality, mass extraction rate, and fraction of extracted liquid on phase redistribution. Walters et al. [1998], building on the work of Buell et al. [1994], examined two-phase phenomena for a T-junction of reduced diameter (19mm and 7.85mm, run diameter of 38.1mm). The Azzopardi [1988] model gave the best predictions for annular flow phase distribution.

Walters et al. [1998] found that when the branch to inlet diameter ratio is 0.5 most of the stratified, stratified-wavy, wavy and semi-annular data show a preference for the gas phase to exit through the branch. For branch to inlet diameter ratios of 0.206 and the same flow regimes, the data showed the same behavior for low extraction rates. For larger extraction rates, slug-flow data displayed a strong preference for the gas phase to exit through the branch. The annular flow data showed large variations in the distribution of the phases depending on the inlet liquid velocity. As the inlet liquid velocity increases, less liquid will exit through the branch. More liquid enters the branch for an increase in the inlet gas velocity. More liquid is entrained in annular flow for an increase in liquid flow rate. This would decrease the fraction of liquid in the film. The major source of liquid in the branch is this film. The fraction of liquid entering the branch thus decreases. Regarding diameter, a smaller fraction of the liquid could be taken off into the branch as the branch diameter decreases. The liquid flowing along the bottom of the main tube would have to climb the wall before exiting through the branch.

2.2.3.2 Two-Phase Pressure Drop

Collier [1976b] examined multiple features inherent in two-phase flow circuits, such as bends, enlargements, contractions, valves, and most notably T-junctions. The author also treats cases of dividing and

combining flow. A simplified steady, frictionless, incompressible, one-dimensional flow approach was taken. In the case of a sudden contraction, which may be considered for the control volume immediately above the microchannel, a vena contracta is formed at the discharge inlet which accelerates the flow and converts the pressure energy into kinetic energy. For a 90^o dividing junction, the static pressure rises and equals the change in momentum across a control volume. Thus a loss coefficient is introduced to account for this effect. Defining this loss coefficient is a difficult matter and has given rise to several different formulations and must be formulated based on the experimental data and is related to the ratio of the branch and manifold cross sectional areas. The author states the empirical loss coefficient relations given by Gardel [1957].

For the present microchannel manifold system, interactions in the space between the array of T-junctions cannot be ignored by supposing that the tees are sufficiently (i.e. on the order of one pipe diameter) apart. For a dividing flow manifold, the static pressure rises along the length of the manifold due to the pressure rises which occur across the dividing T-junctions. The separation effects of the T-junctions create a situation in which there is a concentration of liquid towards the end of the manifold.

Giot [1981] used momentum and continuity balances to arrive at two-phase pressure drop equations for singularities. These singularities include sudden contractions, enlargements, orifices (Shannak et al. [1999]), and combinations of the former. Such a contraction occurs at the entrance to the microchannel, when the flow encounters a sudden change in area. As seen in Figure 2.4, the flow is reduced in area from (1) to (2), which creates a vena contracta at (2), and a subsequent enlargement at (3). The vena contracta pressure difference is reversible whereas the losses through the subsequent enlargement are irreversible friction losses.

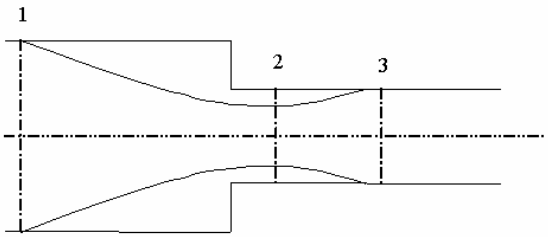

Figure 2.4: Area Contraction

Hewitt [1978] provides a very good explanation of fundamental momentum and energy balances for single and two-phase flow. An equation is derived for the separated two-phase flow pressure drop. This equation is used in the formulation of the model. The
Lockhart & Martinelli [1949] approach is also treated, though it has several deficiencies, such as in its description of the effects of changing mass flux. An empirically based formula of Casagrande [1962] is presented for pressure drop. Mochan [1969] studied pressure losses at resistances in two-phase flow and multi-tube distribution manifolds by taking a homogeneous approach.

Rouhani [1978] provides a realistic example of two-phase flow and its relation to working facilities. Two-phase flow exists in the coolant circuit of a Boiling Water Reactor (BWR). The boiling channels of a BWR are typically set in rod bundles, and flow rates vary across this bundle. The chief parameters are void fraction and

pressure drop. A two-fluid model approach is taken, based on Zuber & Findley [1965], in which the local relative velocity between the phases is considered, along with flow concentration over the flow area.

The following is a summary of the Martinelli & Nelson [1948] procedure used by Rouhani [1978]:

1) Based on work of Lockhart & Martinelli [1949]
2) Calculate single phase friction pressure drop for given geometry and mass flow
3) Multiply this by a two-phase factor
4) Thus
5) $$\left(\frac{dP_f}{dz}\right)_{two-phase} = \left(\frac{dP_f}{dz}\right)_{one-phase} \Phi^2 \qquad (2.1)$$
6) F can be plotted as a function of quality and is correlated by the (turbulent) Lockhart & Martinelli [1949] parameter X_{tt}

$$X_{tt} = \left(\frac{m_L}{m_V}\right)^{0.1}\left(\frac{r_V}{r_L}\right)^{0.5}\left(\frac{1-x}{x}\right)^{0.9} \qquad (2.2)$$

Baroczy [1966] modified the two-phase multiplier by relating it the property index $\left(m_L/m_V\right)^{0.2}\left(r_V/r_L\right)$ and a constant flux. A graphical technique is then used for fluxes other than this reference value. Rouhani [1978] maintains that there are two things which must be known, the variation of flow area and the local quality as a function of spatial coordinates, to obtain the two-phase pressure drop.

2.2.3.3 Flow Regimes

Meknassi et al [2000] present a mathematical model to characterize two-phase stratified flow, accounting for interfacial surface roughness. The authors cite the chief problem is modeling the momentum transfer among the two-phases. The momentum equation is solved by finite differencing, taking into account velocity fluctuations and averages.

Line & Lopez [1997] are concerned with finding a model to predict the localized behavior of two-phase stratified flow. The flow is not assumed as two single phases separated as layers by a flat interface. The predicted quantities are the pressure, velocity, and phase distribution. A rigorous derivation is performed to arrive at the momentum balance for separated two-phase flow in relation to a single phase form. A sinusoidal interface is assumed in order to determine the interfacial forces. The wave field is comprised of a dominant wave with superimposed ripples. To express interfacial transfer, a form drag coefficient is used, followed by a return to the two fluid separated two-phase flow model, and then determination of the phase distribution from momentum. In order to calculate the interfacial momentum, the interface shape and stress distribution must be known.

Lun et al. [1996] present a general background of two-phase flow and the complexities involved in modeling it. The authors examined the effect of grid density on the prediction of slug formation. When considering a numerical simulation, the size of the mesh is critical. The existence of a solution and the accuracy of this solution are dependent upon it.

Bankoff [1960] studied a two-phase flow regime which offers analytical complexities, bubbly flow. Previous research made variations on the separated flow model. Here, it is proposed that the phases flow as a

mixture with radial concentration gradients, and as a single fluid with a “mixture density” which varies radially. The two-phases have the same velocity at all points. The concentration of bubbles is greatest along the pipe axis and trails to zero at the pipe wall. A two-phase friction factor was defined in terms of the wall shear stress and mixture kinetic energy. Bankoff [1960] focused upon steam-water two-phase flows. Using this model, void fraction could be predicted and resulted in good agreement with available data.

Cook & Behnia [2000] studied intermittent flow, which has large bubbles traversing over a liquid film with liquid slugs separating it. An illustration of intermittent flow is seen in Figure 2.5.

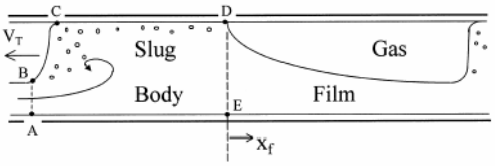

Figure 2.5: Intermittent Flow Illustration (Cook & Behnia [2000])

Through the application of a control volume mass balance, a relationship for the liquid hold up as a function of superficial velocity, slug holdup, and slug velocity was obtained. By using a momentum balance, a relation was derived for the film length as a function of superficial velocities and slug properties. This led to a relation for the pressure gradient along the slug length as the sum of hydrostatic head, wall shear stress, eddy motion viscosity, and gas expansion pressure loss, with an expansion upon each constituent term.

Cook & Behnia [2000] describe the shearing motion within the viscous eddies as arising from the expansion that occurs within the mixing vortex of the liquid film. The most significant factor for pressure drop in the slug is due to friction; the acceleration term comprised 5% and viscous losses comprised about 25%.

Costigan & Whalley [1997] studied void fraction in vertical air-water two-phase flow and differing flow patterns were observed. Impedance probes were used to measure the traces of void fraction and their probability distributions. Six regimes are defined: discrete bubble flow, “spherical cap bubble flow”, slug flow (stable), slug flow (unstable), churn flow, annular flow.

2.2.4 Two-Phase Experiments

This section provides the reader with a brief overview of attempts to measure and model parameters in two-phase flow. There are a vast number of quantities, forces, and interactions which are involved in two-phase flow.

2.2.4.1 Void Fraction

Iskandrani & Kojasoy [2001] studied air-water flow in a 50.3mm inner diameter horizontal pipe and measured void fraction, bubble frequency, liquid velocity (average), and turbulence fluctuations. Hot-film anemometry was used to measure void fraction and to identify the two-phase pattern of flow. Void fraction depends upon the phase separation and volume fraction; the velocity depends upon the mean and fluctuating velocity components. It was found that void fraction increases with increasing gas flow for a constant liquid flow.

Kim et al. [2002] examined the interfacial factors in two-phase bubbly flow in rectangular duct. A conductor probe was used to determine the average void fraction. The interfacial area concentration is a key parameter in two-phase flow analysis. The images were captured with a high-speed camera. The two-phase parameters are void fraction, interfacial area concentration, bubble velocity.

2.2.4.2 Friction Factor

Fore et al. [2000] used nitrogen and water in vertical upward annular flow. Interfacial shear stresses and friction factors were computed, and a new correction for interfacial friction factor.

2.2.4.3 Film

Shedd & Newell [2001] studied the film distribution of horizontal air-water flows in round, rectangular, and triangular channels. It was found that fully annular flow exists only in extreme conditions; mostly, film remained along the bottom and side walls, though some rivulets were present. Though a large body of data was presented, a phase separation model was not formulated.

2.2.4.4 Transient Effects

Sakaguchi et al. [1979] studied transient two-phase air-water flow in a horizontal tube. The authors examined the step responses of the phase velocities and static pressures for a step change in inlet phase flow rate while holding the other phase flow rate constant. Typical flow maps cannot contain transient information, such as the occurrence of a momentary slug flow in response to a step change in a stratified or wavy initial regime. Transient pressure effects were found to be due to transients in the gas flow rate.

2.2.4.5 Bubbly Flow

Young [1995] derived set of equations for the flow of dispersed spherical droplets in pure vapor with or without inert gas. The formulated model treats surface energy and entropy of droplets by modifying previous formulations. The interphase transfer process is modeled.

2.3 Presentation of Experiment

The experimental setup used for two-phase flow of air and water is the same as that presented in Section 1.4.1 for single phase flow.

2.3.1 Procedure

The only difference in procedure is that the two fluid phases of air and water meet at a T-junction, mix, and then travel to the manifold test section.

2.3.2 Sample Data Set

For two-phase experimentation, there are several control variables which may be changed. There are three spacer plate widths available for changing the manifold channel area: 12.7mm, 6.35mm, and 3.175mm. For each spacer, there is the possibility of the flow entering vertically downward (“top” entrance”) or vertically upward (“bottom” entrance) into the manifold. For each possibility of top or bottom entrance, the flow may travel from left to right over a distance of 5.4cm before encountering the first microchannel, or it may travel from right to left over a distance of 24cm. It has been shown earlier in Chapter 1 that the quantitative difference between the top and bottom entrance distribution data is negligible. In addition, differences between left and right entrances differ only qualitatively, not quantitatively. Therefore, since depicting the entire data set will be redundant, for purposes of model comparison, the data set modeled consists of the following experimental conditions:

1) Right entrance (entry length=24cm)
2) Top entrance (flow is vertically downward)
3) All three spacer plates: 12.7mm, 6.35mm, and 3.175mm

The reader is recommended to Yoo [2002] for a presentation of the complete two-phase flow data set.

2.4 Synopses of Models in Current Study

2.4.1 Momentum and Force Balance for Single Phase Fluid Element

To derive the two-phase models, one must first consider the basic mechanics involving moving fluid elements. The fundamental conservation laws of energy, continuity, and momentum must always be satisfied. The following assumptions are held:

1) Steady Flow
2) Incompressible Fluid
3) Negligible Body Forces
4) Due To Horizontal Orientation, Gravity Negligible
5) One Dimensional

Of these assumptions, 5) is the most restrictive. In actuality, two-phase flows are three-dimensional and unsteady. Such problems are best approached with three- dimensional commercially available computer codes. However, the goal of this physical model is to explore the physics which are not explicitly noticeable to the engineer running such codes. To approach this problem from a one-dimensional, physical perspective yields valuable information about the flow-field effects.

Consider the infinitesimal cube seen in Figure 2.6. It is a single phase fluid moving with a velocity *u* and density *?* in the *x* direction only. The *x*-direction faces have a constant cross-sectional area *A* comprised of the product of *dy* and *dz*, and with facial normal $d\vec{A}$.

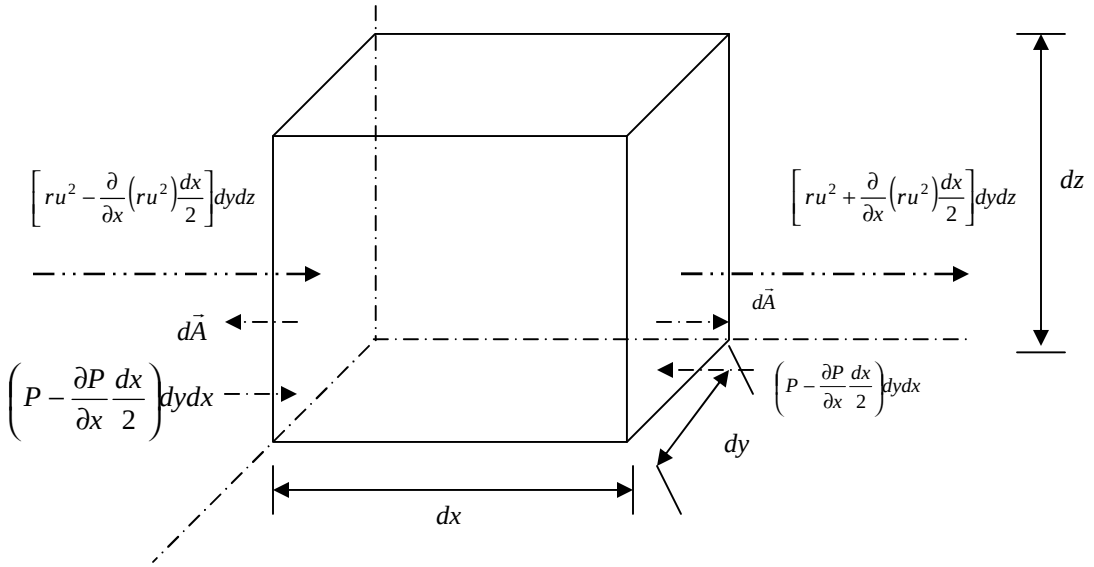

Figure2.6: Infinitesimal Fluid Element

The total pressure drop experienced within this control volume is the summation of three pressure head terms: acceleration, friction, gravitation.

$$\frac{dP}{dx} = \frac{dP}{dx}_{Acceleration} + \frac{dP}{dx}_{Friction} + \frac{dP}{dx}_{Gravitation} \qquad (2.3)$$

Applying a force-momentum balance on the control volume:

$$\sum \vec{F} = \vec{F}_S + \vec{F}_B = \frac{\partial}{\partial t}\int_{CV}\left(r\vec{V}\right)d\forall + \int_{CS}\vec{V}r\vec{V}\cdot d\vec{A} \tag{2.4}$$

$$\vec{F}_S = \int\left[\left(P - \frac{\partial P}{\partial x}\frac{dx}{2}\right)dydx - \left(P + \frac{\partial P}{\partial x}\frac{dx}{2}\right)dydx\right] - \int_S dx\,t_w dS \tag{2.5}$$

$$\vec{F}_B = \int r g dxdydz = 0 \tag{2.6}$$

$$\frac{\partial}{\partial t}\int_{CV}\left(r\vec{V}\right)d\forall = 0 \tag{2.7}$$

$$\int_{CS}\vec{V}r\vec{V}\cdot d\vec{A} = \int\left\{\left[ru^2 + \frac{\partial}{\partial x}\left(ru^2\right)\frac{dx}{2}\right]dydz - \left[ru^2 - \frac{\partial}{\partial x}\left(ru^2\right)\frac{dx}{2}\right]dydz\right\} \tag{2.8}$$

Thus

$$\int -\frac{\partial P}{\partial x}dxdydz - \int_S dx\,t_w dS = \int\frac{\partial}{\partial x}\left(ru^2\right)dxdydz \tag{2.9}$$

Letting $\int(\ )dydz = A$ and $\int(\ )dS = S$

$$\frac{\partial}{\partial x}\left(ru^2\right)dxA = -\frac{\partial P}{\partial x}dxA - dx\,t_w S \tag{2.10}$$

Canceling a common *dx* and assuming a total derivative in the x-dimension:

$$\frac{d}{dx}\left(ru^2\right) = -\frac{dP}{dx} - t_w\frac{S}{A} \tag{2.11}$$

We must now define the wall shear stress t_w. For the fluid element depicted above,

$$AdP = t_w S dx \tag{2.12}$$

and

$$t_w = \frac{dP}{dx}\left(\frac{A}{S}\right) \tag{2.13}$$

From basic fluid mechanics the frictional pressure drop across a fluid element is given by

$$\frac{dP}{dx} = \left(\frac{fG^2}{2r}\right)\left(\frac{S}{A}\right) \tag{2.14}$$

Thus:

$$\frac{dP}{dx} = \left(\frac{fG^2}{2r}\right)\left(\frac{S}{A}\right) = \left(\frac{S}{A}\right)t_w \therefore t_w = \left(\frac{fG^2}{2r}\right) \tag{2.15}$$

With this substitution we have, for a general fluid element:

$$\underbrace{\frac{d}{dx}\left(\rho u^2\right)}_{\text{Accelerational Pressure Gradient}} + \underbrace{\frac{1}{2}\frac{fG^2}{\rho}\frac{S}{A}}_{\text{Frictional Pressure Gradient}} = \underbrace{-\frac{dP}{dx}}_{\text{Total Pressure Gradient}} \tag{2.16}$$

This overall equation is central to the derivation of the subsequent two-phase flow models.

2.4.2 Homogeneous Flow Model

As a precursor to understanding two-phase flow distribution through the manifold, a homogeneous approach is taken. This is the simplest approach to a two-phase flow situation. The assumptions in this model are:

1) Homogeneous mixing of two-phase flow at the inlet
2) Phases flow as a single phase fluid with averaged or bulk properties based on inlet quality and mass flow
3) No relative velocity between mixture phases

Chisholm [1983], Hewitt [1978], and others define a homogeneous density:

$$\rho_H = \left[x\nu_V + (1-x)\nu_L\right]^{-1} \tag{2.17}$$

where *?* is the phasic specific volume.

2.4.3 Two-Phase Void-Fraction (TP-a) Model

In the Two-Phase Void Fraction (TP-a) Model, the two-phases are assumed to occupy their individual phasic areas A_L and A_V, as seen in Figure 2.7.

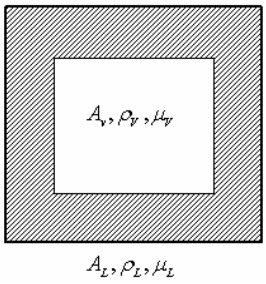

Figure 2.7: Phasic Areas for TP-a Model

Within each of these areas, the complimentary phasic velocity is defined as 0, e.g.

1) Within the area A_L, $u_V \equiv 0$
2) Within the area A_V, $u_L \equiv 0$

Each of the phases possesses its own distinct properties as well, such as density and viscosity. These assumptions do correspond to a general separated flow approach (Hewitt [1978]), however a true separated flow model is subtly different. In a truly separated flow problem, the interfacial interactions must be considered, since the phasic areas are constantly shifting due to the relative velocity between the phases.

In this TP-a model, the void fraction is a critical factor. It describes the fraction of overall flow area occupied by the gas. However, it admittedly has an inherent ambiguity. Consider Figure 2.8, which depicts snapshots of the total flow cross-sectional area as it shifts and morphs during two-phase flow. The shaded regions represent the area occupied by the liquid phase; the converse is occupied by the vapor phase.

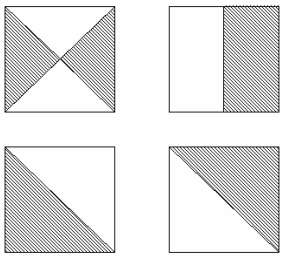

Figure 2.8: Relation Between Void Fraction and Phasic Areas

Each of the above diagrams represents a void fraction of a=0.5. However, this number does not communicate any geometrical information useful for the characterization of phase occupational boundaries. Such information is critical to a bona fide separated flow model, which calculates a phasic pressure drop within the specific phase boundary. The area within the boundary is necessary to quantify the pressure force. The TP-a Model differs from a true separated model in that *a* is assumed to communicate no specific information about what shape the phasic boundaries take and only provides information on the fraction of total manifold cross sectional area occupied by the gas phase. Anything more requires the description of a moving interface, which cannot be determined from this model.

2.5 Homogeneous Model Formulation, Results, and Discussion

2.5.1 Formulation

Recalling Section 2.4.2 the phasic velocities *u* are equal.

Thus $$u_V = u_L = \frac{G}{r_H} = u_H \tag{2.18}$$

Recalling Equation (2.16) and substituting these velocity relations, Equation (2.19) is obtained.

$$\frac{d}{dx}\left[x\frac{G^2}{r_H} + (1-x)^2 \frac{G^2}{r_H} \right] + \frac{1}{2}\frac{fG^2}{r_H}\frac{S}{A} = -\frac{dP}{dx} \tag{2.19}$$

In this analysis there is some ambiguity surrounding which friction factor *f* to use. The friction factor is a function of a two-phase Reynolds number Re_{TP}, or

$$f = g(\mathrm{Re}_{TP}) = g\left(\frac{GD_H}{m_{TP}}\right) \tag{2.20}$$

where m_{TP} is not defined uniquely, but typically includes $x, m_V, and\ m_L$ in a relation similar to Equation (2.17).

To predict the mass distribution, the single phase Physical Model presented in Chapter 1 was modified to allow for the inlet quality as parameter. Recall that this parameter is unnecessary for single phase flow; implicit in the solution of either an all-vapor or all-liquid single phase flow situation is the fact that *x*=1 or 0, respectively. Once the inlet quality has been specified, the specific volume (or density) and viscosity are averaged in the form of Equation (2.17). In contrast to the previous single phase model, the fraction factor for the TP-a Model is specified

with an average value of 0.04, as suggested by Niño [2001]. Recall for the single phase model the friction factor is solved implicitly according to the Colebrook equation as presented in Chapter 1.

One would expect generally poor agreement between the actual two-phase distribution and this overly-simplified approach, and its true value is only as a comparative reference. A gross departure from the data would signal the presence of effects that lie beyond the assumption of a single phase fluid, and emphasize the need for a more complete and descriptive model. This assertion would be further supported if the homogeneous mixture behavior is qualitatively different from that of the single phase model behavior from which the homogeneous mixture model is derived.

Recall that in the cases of pure liquid and pure vapor flow as outlined in Chapter 1, one of the most significant behaviors is that a pressure regain occurs near the end of the channel in the direction of flow. A slight pressure regain occurred at each dividing junction, resulting in an overall static manifold pressure increase and the propulsion of more flow in the flow direction and a resultant increase of mass distribution toward the furthest channels. Thus, pressure regain effects dominated over frictional or acceleration dissipation in the cases of single phase liquid or vapor.

2.5.2 Results and Discussion

Now consider the predictions using the homogeneous approach for the total discharge mass flow ($\dot{m}_{TOT,discharge} = \dot{m}_{L,discharge} + \dot{m}_{V,discharge}$). *Note*: For these and all other graphs presented in Chapter 2, the flow direction proceeds from Tube Number 1 to Tube Number 15.

2.5.2.1 3.175mm Spacer Plate

For the 3.175mm spacer plate two-phase tests, a sample pool of test conditions was formulated from the data set. The test names and conditions are summarized in Table 2.1. Yoo [2002] has described Test 2 as a stratified flow and the other tests as annular flow in the manifold.

Table 2.1: Sample Test Cases for the 3.175mm Spacer Plate

	$G_{in,TOT}$	X_{in}
Test	[kg/m^2-s]	[-]
Test 2	43	0.35
Test 5	130	0.37
Test 7	239	0.16
Test 10	379	0.08
Test 13	274	0.16

The full set of results is presented in Appendix B; predictions for Tests 2 and 13 will be discussed here. Predictions for Tests 2 and 13 can be seen in Figures 2.9 and 2.10.

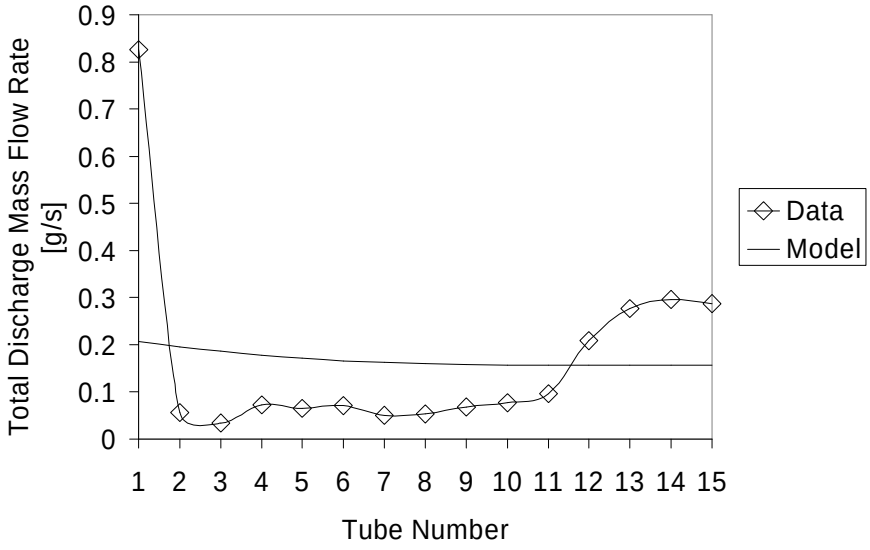

Figure 2.9: Homogeneous Prediction, 3.175mm Spacer Plate: Test 2

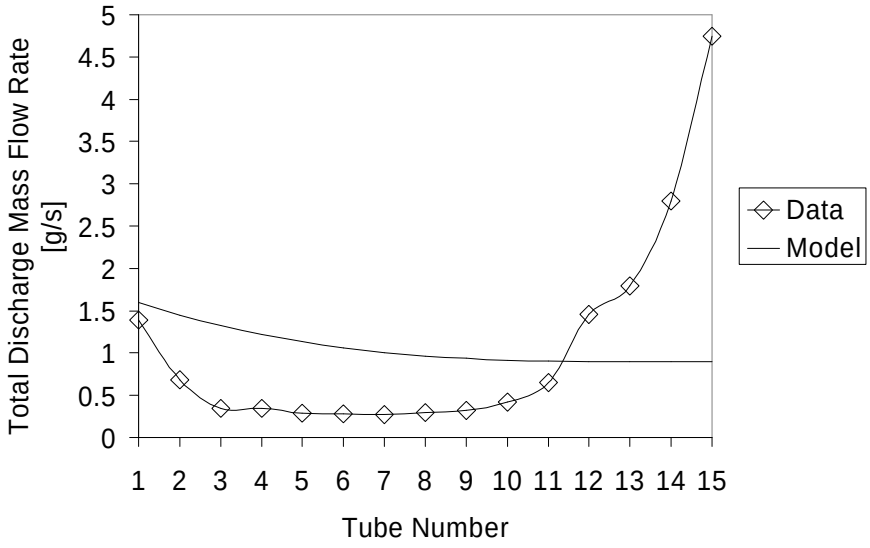

Figure 2.10: Homogeneous Prediction, 3.175mm Spacer Plate: Test 13

For Test 2, the homogeneous model yields a prediction which cannot account for the initial large drop-off in total discharge mass flow. Along the length of the manifold, this model predicts nearly the opposite trend as that found for single phase flow alone. Whereas the single phase model presented earlier accurately predicts the static pressure regain and resultant surge in discharge mass flow rate toward the end of the manifold, this modified single phase flow model predicts a pressure decrease and resultant decrease in magnitude of discharge along the manifold. Thus, frictional dissipation appears to dominate pressure regain effects when using this model.

For Test 13, prediction of the total mass flow rate in the initial channels is predicted, indicating a usefulness for high mass flux and lower quality. This is reasonable since at higher mass fluxes and lower qualities, the two-phase fluid becomes more like a single phase liquid. However, this model again cannot predict the surge in

discharge mass flow towards the end of the manifold, indicating the presence of effects which cannot be adequately described by a single phase approach. These effects include the production and dynamics of a momentum-carrying film which traverses the upper wall and is deposited toward the final discharge branches.

2.5.2.2 6.35mm Spacer Plate Comparisons

For the 6.35mm spacer plate two-phase tests, a sample pool of test conditions was formulated from the data set. The test names and conditions are summarized in Table 2.2.

Table 2.2: Sample Test Cases for the 6.35mm Spacer Plate

	$G_{in,TOT}$	X_{in}
Test	[kg/m^2-s]	[-]
Test 1	48	0.17
Test 4	145	0.09
Test 8	243	0.05
Test 11	374	0.04

The full set of results is presented in Appendix B. Predictions for Tests 1 and 11 will be discussed here. Figures 2.11 and 2.12 present model predictions for the data of Tests 1 and 11.

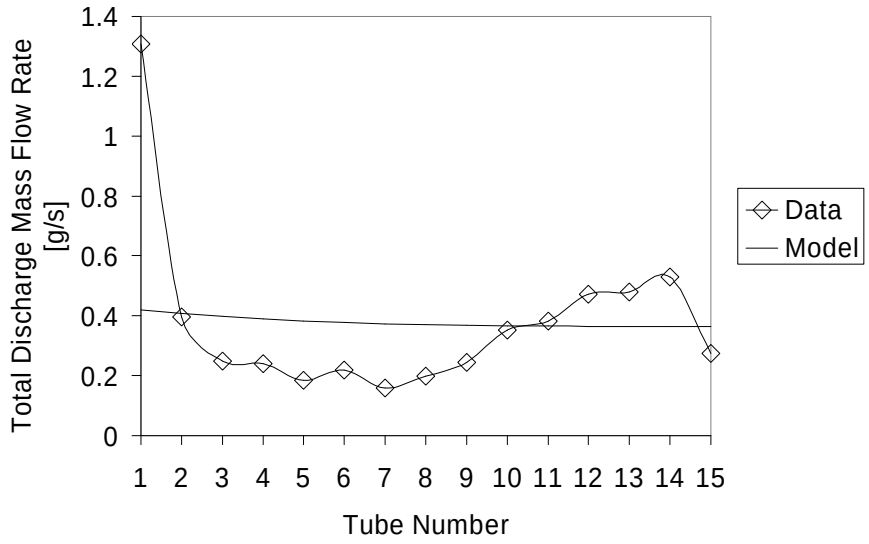

Figure 2.11: Homogeneous Prediction, 6.35mm Spacer Plate: Test 1

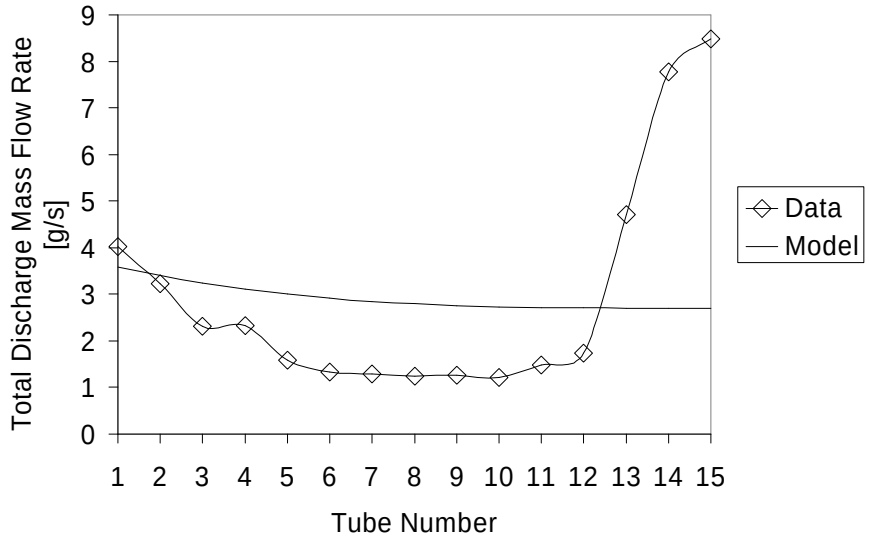

Figure 2.12: Homogeneous Prediction, 6.35mm Spacer Plate: Test 11

For Test 1, homogeneous model cannot account for the large exit mass flow drop when the inlet flow regime is of the lower-flux and resultantly more stratified type. The data seem to oscillate about the homogeneous model prediction, indicating that a homogeneous approach yields a mean-value prediction.

For Test 11, there is again an accurate prediction in the initial discharge channels of the total exit mass flow, and a decreasing behavior as the data decreases (qualitative agreement). However, again this model fails to encompass effects at the end of the manifold. The overall behavior of the homogeneous approach suggests a dominance of frictional dissipation, but an inability to account for effects which can only occur for a flow with a degree of separation, such as the creation of a film.

2.5.2.3 12.7mm Spacer Plate Comparisons

For the 12.7mm spacer plate two-phase tests, a sample pool of test conditions was formulated from the data set. The test names and conditions are summarized in Table 2.3.

Table 2.3: Sample Test Cases for the 12.7mm Spacer Plate

	$G_{in,TOT}$	X_{in}
Test	[kg/m^2-s]	[-]
Test 1	41	0.25
Test 2	41	0.27
Test 3	128	0.05
Test 4	140	0.11

The full set of results is presented in the Appendix B; predictions for Tests 1 and 3 will be discussed here. Predictions for Tests 1 and 3 can be seen in Figures 2.13 and 2.14.

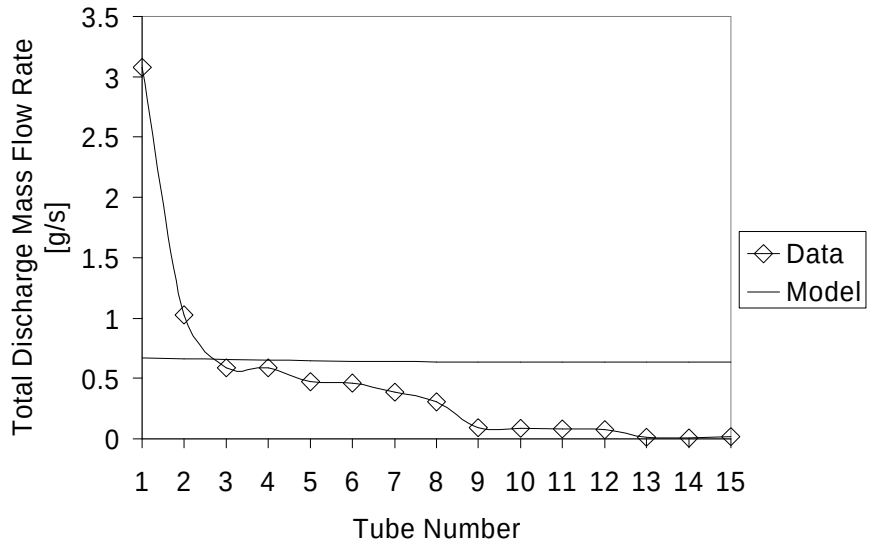

Figure 2.13: Homogeneous Prediction, 12.7mm Spacer Plate: Test 1

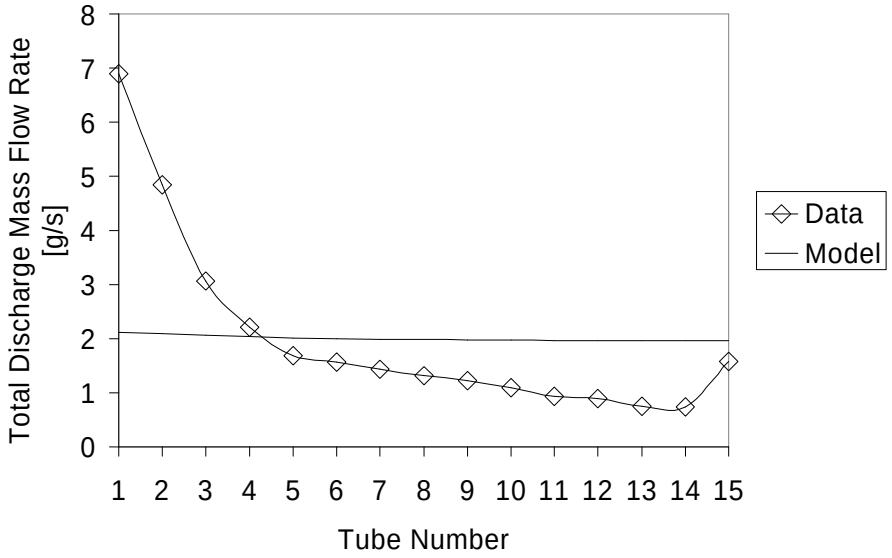

Figure 2.14: Homogeneous Prediction, 12.7mm Spacer Plate: Test 3

For both Tests 1 and 3, the drastic increases in exit mass flow at the manifold end are not as apparent, though there is an upward trend for Test 3. These effects are more likely due to area changes, since the increase in end discharge mass flow is evident for cases in which the manifold area is decreased but flow conditions are relatively the same. The total absence of this effect in Test 1 indicates that the inlet regime is most likely stratified, since little mass flow remains at the end of the manifold. Once the inlet mass flow is increased, as in Test 3, an upward trend at the end is noticed, which is due to the production of a momentum-carrying film depositing in the final branches. Again, the homogeneous model performs poorly in terms of quantitative predictions. Yet this is expected, and the homogeneous approach serves only as a baseline reference to highlight the need for a more descriptive two-phase model, which shall be presented now.

2.6 TP-a Model Formulation, Results, and Discussion

2.6.1 Formulation

Recalling the synopsis given in Section 2.4.3, define the following:

1) Void fraction a $$a \equiv \frac{A_V}{A_L + A_V} \tag{2.21}$$

2) Quality x $$x = \frac{\dot{m}_V}{\dot{m}_V + \dot{m}_L} = \frac{r_V \dot{V}_V}{r_V \dot{V}_V + r_L \dot{V}_L} \tag{2.22}$$

3) Vapor mass flux G_V $$G_V = \frac{GAx}{A_V} = \frac{Gx}{a} \tag{2.23}$$

4) Vapor velocity u_V $$u_V = \frac{Gx}{a r_V} \tag{2.24}$$

5) Liquid mass flux GL $$G_L = \frac{GA(1-x)}{A_L} = \frac{GA(1-x)}{A_V}\frac{a}{1-a} = \frac{G(1-x)}{1-a} \tag{2.25}$$

6) Liquid velocity uL $$u_L = \frac{G(1-x)}{(1-a)r_L} \tag{2.26}$$

Now take an infinitesimal element dA just at the interface of the two areas

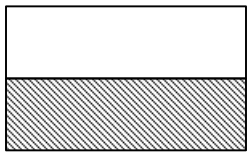

Figure 2.15: Infinitesimal Element dA

This area element is given by $$dA = dA_V + dA_L$$

A fluid point within dA is traveling with velocity $u = u_V + u_L$

Hewitt [1978] supports the concept of averaging properties over the entirety of the cross sectional A. Therefore return to Equation (2.16) and average over the entire area:

$$\frac{1}{A}\int -\frac{dP}{dx}dA = \frac{1}{A}\int \frac{d}{dx}\left(r u^2\right)dA + \frac{1}{A}\int_S t_w dS \tag{2.27}$$

$$-\frac{dP}{dx} = \frac{1}{A}\int \frac{d}{dx}\left[r\left(u_v + u_L\right)^2\right]\left(dA_V + dA_L\right) + \frac{1}{A}\int_S t_w dS \tag{2.28}$$

Recalling the definitions of zero phasic velocity in complementary phasic areas

$$-\frac{dP}{dx} = \frac{1}{A}\int \frac{d}{dx}\left[r_V u_V^{\,2}\right]dA_V + \frac{1}{A}\int \frac{d}{dx}\left[r_L u_L^{\,2}\right]dA_L + \frac{1}{A}\int_S t_w dS \tag{2.29}$$

$$-\frac{dP}{dx}=\frac{A_V}{A}\frac{d}{dx}\left[r_V u_V{}^2\right]+\frac{A_L}{A}\frac{d}{dx}\left[r_L u_L{}^2\right]+\frac{1}{A}\int_S t_w dS \tag{2.30}$$

$$-\frac{dP}{dx}=a\,\frac{d}{dx}\left[\frac{G^2x^2}{a^2 r_V}\right]+(1-a)\frac{d}{dx}\left[\frac{G^2(1-x)^2}{(1-a)^2 r_L}\right]+t_w\frac{S}{A} \tag{2.31}$$

Factoring out common terms and substituting for the wall shear stress

$$-\frac{dP}{dx}=\frac{d}{dx}\left[\frac{G^2x^2}{a r_V}\right]+\frac{d}{dx}\left[\frac{G^2(1-x)^2}{(1-a)r_L}\right]+\left(\frac{fG^2}{2r}\right)\frac{S}{A} \tag{2.32}$$

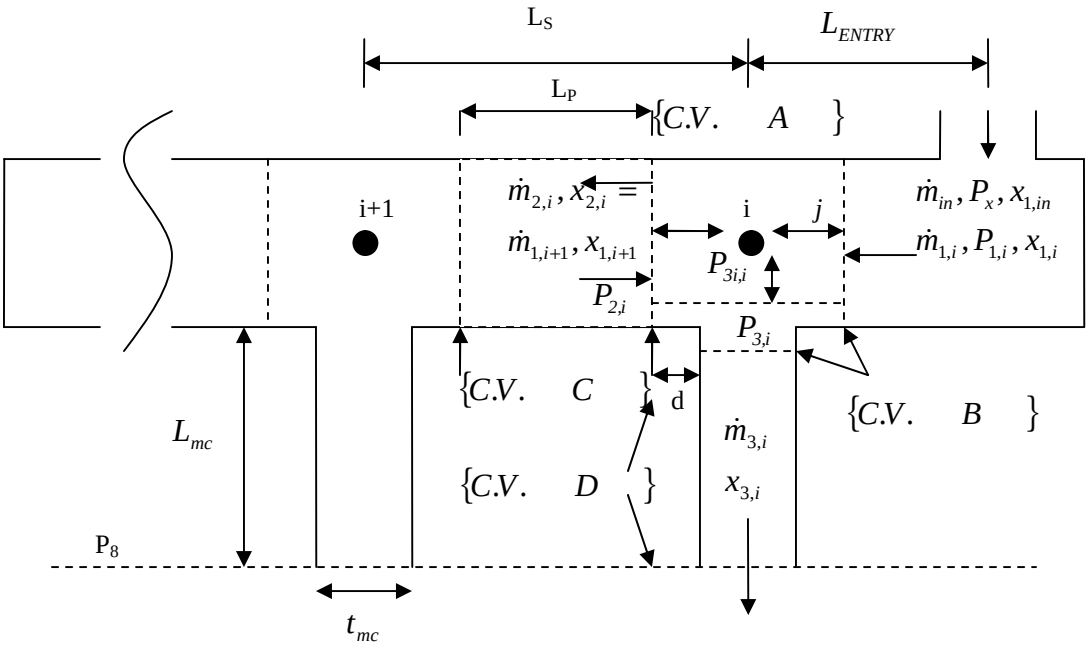

Figure 2.16: Control Volumes for the TP-a Model

Having presented the general equations for two-phase pressure drop, it is now necessary to present the formulation of the present model under study. Figure 2.16 represents the basic structure of non-uniform area control volumes used for analysis. A two-phase mixture possessing the quantities $\dot{m}_{in}, P_x, x_{1,in}$ enters the distribution system. It must be emphasized that these are the only parameters which are supplied from the experimental data. Previous researchers (Saba & Lahey [1984]) recommend the specification of up to three quantities entering a phase separation control volume.

Essentially, the problem consists of drawing relevant and judiciously chosen control volumes around and between nodes representing points of discharge. Phase separation occurs within the control volume labeled *A*. It covers the area above the discharge branch, and extends beyond the microchannel discharge thickness t_{mc} by an amount *d*, in order to account for the abrupt change in area between the channel and the microchannel by an area-contraction pressure drop equation. An imaginary junction point labeled by ● lay at the center of *A* equidistant from the faces of *A* by a distance of $t_{mc}/2$.

Immediately below the control volume in which phase separation occurs, an infinitesimally high yet physically dimensional width control volume is drawn to account for pressure drop resulting from an abrupt change in area (labeled *B*). An area contraction pressure equation applies within the control volume *B*. Note that the inlet pressure of *B* is given by $P_{3i,i}$, where (3*i*) refers to the inlet microchannel discharge static pressure before area contraction for a node *i*, and $P_{3,i}$ refers to the microchannel discharge static pressure following the change in area between the channel and microchannel inlet for the same node.

Having determined the flow quantities from phase separation equations in *A* and area-contraction equations in *B*, along with other governing equations which shall be explained later in detail, the flow enters a control volume drawn along the length of the microchannel itself, L_{mc}. This control volume is labeled *D*. The flow is driven by the static pressure difference between the $P_{3,i}$ and the common atmospheric pressure P_{∞}. It must be stated that the exit of each discharge microchannel is P_{∞}. Of course, this will be different for combinations of dividing and combining flow manifolds as discussed previously.

Relevant equations are written and solved simultaneously for a given node *i*. The resultant flow information is propagated to the (*i*+1) node via the exit control volume *C* by two-phase pressure equations. The fundamental "communication equations" responsible for this propagation of information are:

$$x_{2,(i-1)} = x_{1,i} \tag{2.33}$$

$$\dot{m}_{2,(i-1)} = \dot{m}_{1,i} \tag{2.34}$$

In words, the exit mass flow rate and two-phase quality of the previous node are specified inlet conditions of the current node. Note that no static pressure, nor static pressure drop, information at a node is supplied, only the pressure of the inlet flow, P_x. This basic process is repeated along the entire length of the distribution channel from *i* to *N*. In this particular case *N*=15. To fully describe the present system, a large array of simultaneous equations must be solved; a program was written for this purpose using EES®.

Control Volume Equations for TP-a Model

A presentation of the equations used in the program is now given. For convenience, they shall be segmented according to control volumes *A*, *B*, *C*, and *D*. It must be stated that each equation possesses an index *i* which cycles for all nodes to the final value of *i*=*N*. However, for clarity and convenience of presentation this subscript is omitted.

Control Volume *A*

Within the phase separation control volume *A*, the following hold true:

a) Continuity

$$\dot{m}_1 = \dot{m}_2 + \dot{m}_3 \tag{2.35}$$

b) Phasic Continuity

$$x_1\dot{m}_1 = x_2\dot{m}_2 + x_3\dot{m}_3 \tag{2.36}$$

This is specifically written for conservation of the vapor phase mass. Alternatively, each coefficient could be replaced by (1-*x*) for the conservation of liquid phase mass. However, the specification of both is redundant.

c) Pressure difference from inlet to discharge

$$\Delta P_{1\to 3i} = P_1 - P_{1j} + \Delta P_{1\to 3j} + P_{3j} - P_{3i} \tag{2.37}$$

Here the subscript *j* refers to the junction labeled by ● in Figure 2.16. To define the junction pressure losses of $P_1 - P_{1j}$ and $P_3 - P_{3j}$ Saba & Lahey [1984] recommend the following

$$\text{i)}\quad P_m - P_{mj} = K_m G_m{}^2 \frac{\Phi_{LOm}{}^2}{2 g r_L} \tag{2.38}$$

where *m* = the flow streams 1, 2, and 3

$$\text{ii)}\quad \Phi_{LOm}{}^2 = 1 + u_{LG}\frac{x_m}{u_L} \tag{2.39}$$

$$\text{iii)}\quad u_{LG} = \frac{r_L - r_V}{r_G r_L} \tag{2.40}$$

$$\text{iv)}\quad K_m = f_{TP}\frac{\tilde{L}}{2D_{h,m}} \tag{2.41}$$

where $\tilde{L}$ is either half of the control volume length of *A* or half of the height of control volume *A*, depending on whether one is determining *K1* or *K3*, respectively.

The pressure loss at the junction is comprised of reversible and irreversible pressure losses

$$\Delta P_{1\to 3j} = \Delta P_{1\to 3,IRR} + \Delta P_{1\to 3,REV} \tag{2.42}$$

These losses are formulated in terms of the Lockhart & Martinelli [1949] parameter X_{tt} and two-phase multiplier F in the following manner:

$$\text{v)}\quad \Phi = (1-x_m)^2\left[1 + \frac{C13}{X_{tt}} + \frac{1}{X_{tt}{}^2}\right] \tag{2.43}$$

$$\text{vi)}\quad X_{tt} = \left[\left(\frac{x_m}{1-x_m}\right)\left(\frac{r_L}{r_V}\right)^{0.5}\right]^{-1} \tag{2.44}$$

$$\text{vii)}\quad C13 = \left[1 + (C3-1)\left(\frac{r_L - r_V}{r_L}\right)^{0.5}\right]\left[\left(\frac{r_L}{r_V}\right)^{0.5} + \left(\frac{r_G}{r_L}\right)^{0.5}\right] \text{ Chisholm [1983]} \tag{2.45}$$

viii) *C3*=1.75 for separated flow, *C1*=1 for homogeneous flow

$$\text{ix)}\quad \Delta P_{1\to 3,IRR} = K13 * G_m{}^2 \frac{(1-x_m)^2}{2 g r_L}\Phi \tag{2.46}$$

Various correlations exist for *K13*, but Saba & Lahey [1984] recommend

x) $$K13 = \left[1.18 + \left(G_{discharge}\frac{A_{discharge}}{G_{inlet}A_{channel}}\right)^2 - 0.8G_{discharge}\frac{A_{discharge}}{G_{inlet}A_{channel}}\right]\frac{A_{channel}}{A_{discharge}} \quad (2.47)$$

Lahey & Moody [1977] define energy densities

xi) $$r'''_m = \sqrt{\left[\frac{(1-x_m)^3}{r_L{}^2(1-a_m)^2} + \frac{x_m{}^3}{r_V{}^2 a_m{}^2}\right]} \quad (2.48)$$

xii) $$a = \frac{G_3}{r'''_3}, \qquad b = \frac{G_1}{r'''_1} \quad (2.49)$$

xiii) $$r_{H,3} = (u_L + x3 * u_{LG})^{-1} \quad (2.50)$$

xiv) $$\Delta P_{1\text{–}3,REV} = \frac{r_{H,3}}{2g}(a^2 - b^2) \quad (2.51)$$

d) Pressure difference from inlet to run

i) $$\Delta P_{1\to 2} = P_1 - P_{1j} + \Delta P_{12j} + P_{2j} - P_2 \quad (2.52)$$

$P_1 - P_{1j}$ has been found already, and $P_{2j} - P_2$ can be determined using the aforementioned process in steps c. i)-iv).

ii) $$r' = \left[\frac{(1-x_m)^2}{r_L(1-a_m) + \frac{x_m{}^2}{r_V a_m}}\right]^{-1} \quad (2.53)$$

iii) $$\Delta P_{12j} = \frac{K12}{2g}\left[\frac{G_2{}^2}{r'_2} - \frac{G_1{}^2}{r'_1}\right] \quad (2.54)$$

Like *K13*, *K12* is an empirical loss coefficient. Based on the data of Saba & Lahey [1984],

iv) $$K12 = 0.11 + 5\left(G_1\frac{Dh_1}{m_L}\right)^{-0.17} \quad (2.55)$$

e) There remains yet one more equation to describe the pressure difference between inlet and run. By performing a force-momentum balance around the *entire* control volume *A*, it can be shown that

i) $$P_1 - P_2 = -r_{s,m}\left[V_2{}^2 - V_1{}^2 + \sin(q)\cos(q)V_3{}^2\frac{A_3}{A_{channel}}\right] \quad (2.56)$$

with

ii) $$r_{s,m} = r_V a_m + (1-a_m)r_L \quad (2.57)$$

? is the angle with respect to the horizontal that the initial stream bends into the discharge. Bajura [1971] introduces a factor *?* to account for whether the flow enters at right angles and arrived at a similar form of Equation (2.56). A choice must be made for which *a* to use, whether for *m*=1,2, or 3. In the program, *m*=1 was chosen based on the assumption that in within the phase separation control volume, the initial void fraction would have the greatest impact on a change in mixture density, and relatively little change in void fraction would occur for a_2 and a_3. One may modify Equation (2.56) by multiplying by the loss coefficient *K12*, as suggested by Collier [1976b]. The above set of equations, cycled for each node, represent the full set of phase separation equations.

Control Volume B

Once a two-fluid stream has traveled through *A*, it has been split into another two streams of two-phase flow with unique properties. One stream flows vertically downward through control volume *B*, driven by the static pressure difference between P_{3i} and P_8. However, it is not a simple matter to ascertain the actual inlet static pressure P_3 without taking into account the abrupt area change. To account for the sudden change in area, an area-contraction pressure equation is formulated. Giot [1981] proposes

$$\text{i)}\ P_{3i} - P_3 = \frac{G_3{}^2}{2r_L}\left[\left(\frac{1}{C_{mc}} - 1\right)^2 + 1 - \frac{1}{s^2}\right]\left[1 + x_3\left(\frac{r_L}{r_V} - 1\right)\right] \tag{2.58}$$

$$\text{ii)}\ s = \frac{A_{controlvolume,B}}{A_{discharge}} \tag{2.59}$$

$$\text{iii)}\ C_{mc} = \frac{1}{s} \tag{2.60}$$

Control Volume D

With the static pressure of the discharge, the flow is driven by a two-phase pressure difference

$$P_{3i} - P_\infty = \frac{s_{mc}}{2A_{discharge}} f_{TP} G_3^2 \frac{L_{mc}}{r_L} + G_3^2\left[\left(\frac{(1-x_3)^2}{1-a_3}\right)u_L + x_3^2\frac{u_V}{a_3}\right]L_{mc} \tag{2.61}$$

Control Volume C

At this stage, all of the flow properties for a given node *i* have been determined, and this flow information must be propagated to the *i*+1 node. This is performed by invoking three conditions. The first two are represented by the "communication relations" stated above in Equations (2.33) and (2.34). The third condition is that the inlet pressure of a control volume between nodes is the result of a two-phase pressure difference with the previous node. Thus, the two-phase cycling pressure equation is given by

$$P_{2,i-1} - P_{1,i} = L_P \frac{s_c}{A_c} f_{TP} \frac{G_{1,i}^2}{r_{1,i}} + G_{1,i}^2\left[\left(\frac{(1-x_{1,i})^2}{1-a_{1,i}}\right)u_L + x_{1,i}^2\frac{u_V}{a_{1,i}}\right]L_P \tag{2.62}$$

where s_c and A_c represent the channel perimeter and cross-sectional area, respectively. In this equation, the subscript *i* was included to emphasize the fact that the inlet pressure at the current node is directly related to the flow properties of the previous node.

Solution Procedure for the TP-a Model

Having formulated the equations for this model, the solution procedure is:

1) Specify $P_x, x_{1,(i=1)}, \dot{m}_{1,(i=1)}$
2) Use two-phase pressure equation across entry length to arrive at inlet pressure of node i=1
3) Use phase separation, area-contraction, and two-phase discharge pressure equation to determine flow properties at i=1
4) Link i=1 to i=2 via communication and two-phase pressure equations
5) Determine properties at i=2 using phase separation, area-contraction, and two-phase discharge pressure equation
6) Cycle all nodal equations from i=2 to i=*N*

A solution can only be determined via the simultaneous solution of a large number of arrayed equations.

2.6.2 TP-a Model Results

The TP-a model was applied to the sample data set in Tables 2.1-2.3. Approximately eighty flow variables are solved for each node, yielding a considerable array of flow information. Six flow variables have been chosen for presentation and discussion: inlet mass flux to each node, run quality after each node, total discharge mass flow rate, liquid discharge mass flow rate, and predictions of the void fractions for the inlet, run, and discharge at each node. It is important to preface this section by noting that the void fraction was not explicitly measured during experimentation. Nonetheless comments are presented from the void fraction predictions because these comments help to give a fuller picture of the trends in the data. The strength of these comments is limited by the accuracy of the predictions of the other data for a given test case.

2.6.2.1 12.7mm Spacer Plate

Test 1

The inlet flux for this case is 41 $\mathrm{kg/m^2 \cdot s}$, and the quality is 0.25. This particular test case is for a low mass flux flow of mid range quality, and the largest available manifold cross sectional area.

1) Inlet Mass Flux to Junction (Figure 2.17)

The model predicts the inlet mass flux to each node well. The sharp downward trend indicates that the effects of frictional dissipation decrease the pressure in the direction of flow.

2) Run Quality (Figure 2.18)

Agreement is good until about the tenth discharge junction. The overall trend is increasing, indicating that more vapor is present in the direction of flow. Thus, one would expect an increase in the void fraction.

3) Exit Quality (Figure 2.19)

The increasing trend in exit quality is irregular and almost cubic in nature. The model reflects a sharp increase in exit quality toward the final channels. Since there is no drop in quality toward the end of the channel, flow reversal is not a significant phenomenon in this case. Flow reversal would provide for a flux in the reverse direction of flow, lowering the exit quality toward the end.

4) Exit Total Mass Flow Rate (Figure 2.20)

The total mass flow rate through the discharge microchannels is always decreasing, substantiating the claim represented by the quality predictions that flow reversal does not occur. In addition, it is evident that a film is not produced, since a film shooting across the top of the manifold channel would deposit in the final channels when the vapor momentum which carries it begins to decrease. Since the data and model indicate sharp increases in the quality (run and exit) it is not possible for the vapor to lose momentum.

5) Exit Liquid Mass Flow Rate (Figure 2.21)

The mass flow of liquid toward the final channels approaches zero, indicating a dryout at about the tenth channel. Thus, above this channel the film has lost its momentum.

6) Void Fractions (Figure 2.22)

All the above trends are further substantiated by the predictions of void fraction. Notice that the void fractions reach a peak around the tenth channel and then decline until the end of the channel. Up to this point the vapor is occupying an increasing overall percentage of the manifold cross sectional area, and this share decreases after this maximum point. The fact that this point occurs at the tenth channel is not significant in itself, because inflection points may occur later in the flow direction, as will be seen. The important point is that the incoming liquid has lost its mass and momentum at this point, and whatever extraneous effects (entrainment or film production) have lost their momentum as well. The only flow remaining consists of vapor.

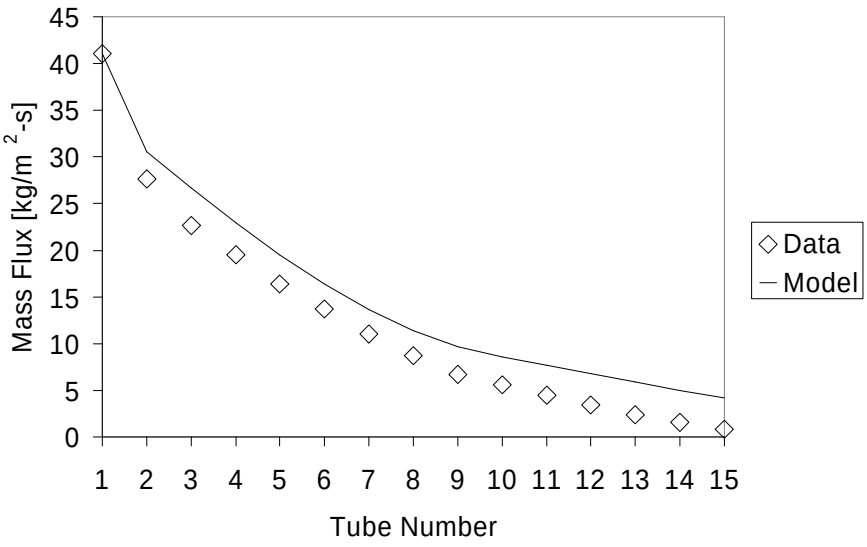

Figure 2.17: Junction Inlet Mass Flux (TP-a), 12.7mm Spacer Plate, Test 1

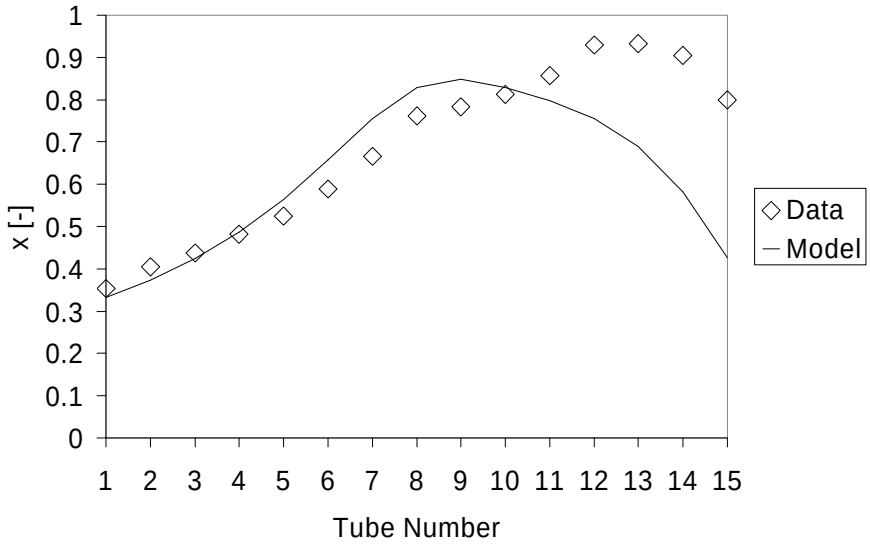

Figure 2.18: Run Quality (TP-a), 12.7mm Spacer Plate, Test 1

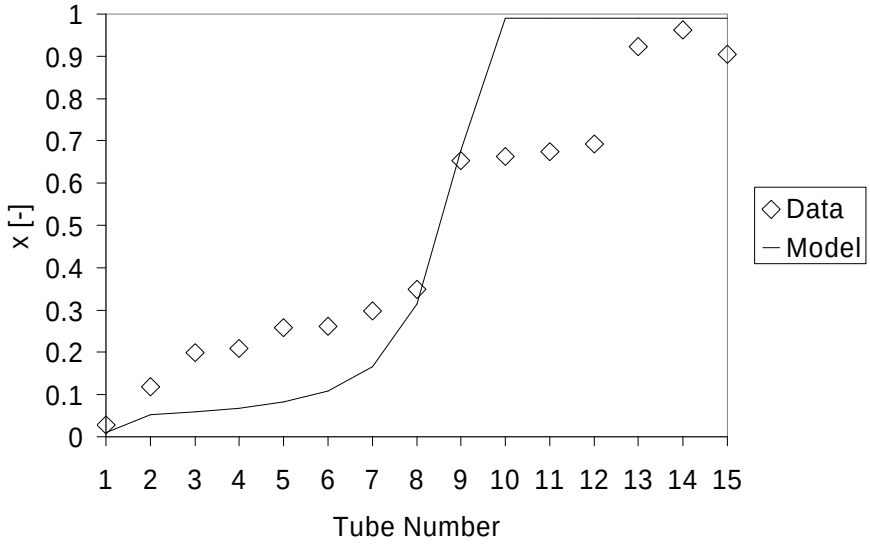

Figure 2.19: Discharge Quality (TP-a), 12.7mm Spacer Plate, Test 1

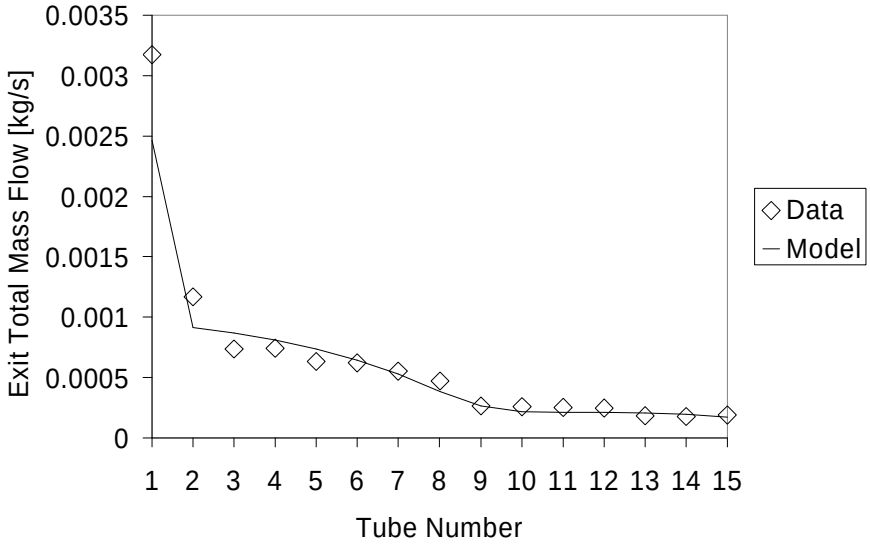

Figure 2.20: Total Discharge Mass Flow (TP-a), 12.7mm Spacer Plate, Test 1

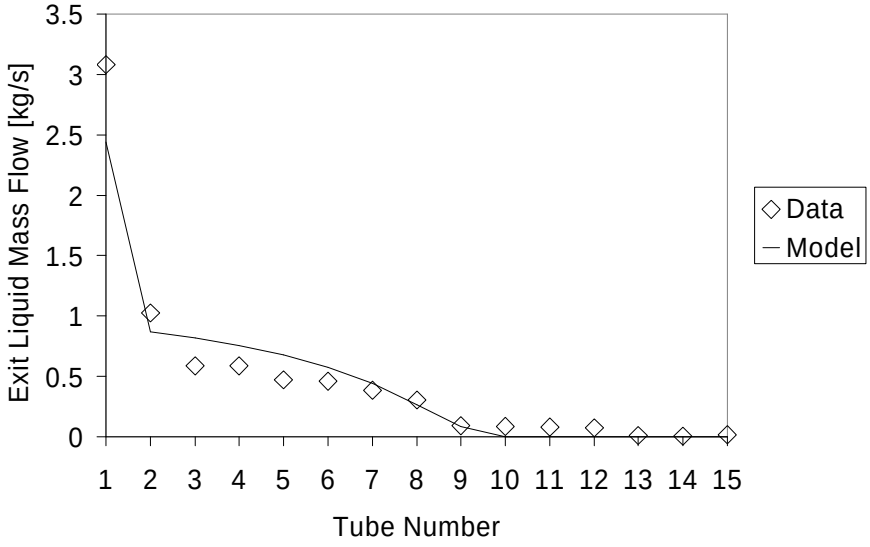

Figure 2.21: Discharge Liquid Mass Flow (TP-a), 12.7mm Spacer Plate, Test 1

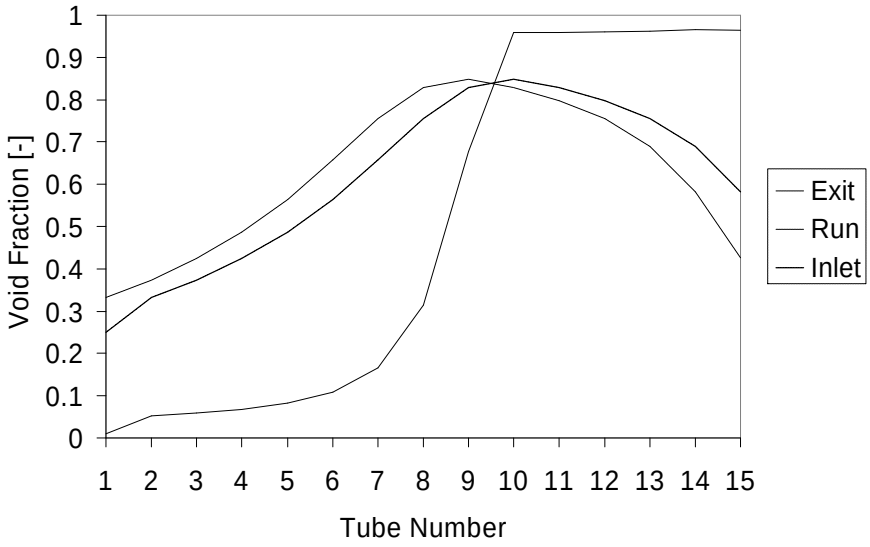

Figure 2.22: Void Fraction (TP-a), 12.7mm Spacer Plate, Test 1

Test 3

For this test case, the inlet mass flux is approximately three times that of Test 1, and the quality has been reduced by a factor of 5.

1) Inlet Mass Flux to Junction (Figure 2.23)

Here the predictive ability of the model breaks down. The inlet mass flux prediction is much higher than that of the data. Furthermore, the model prediction seems to flatten out as compared to Test 1.

2) Run Quality (Figure 2.24)

The model closely follows the data until about the ninth node. While the data continues to increase, indicating a decrease in film momentum, this point is prematurely predicted by the model.

3) Exit Quality (Figure 2.25)

The prediction is quite close until about Tube 13, at which point the exit quality decreases for the data and increases for the model.

4) Exit Total Mass Flow Rate (Figure 2.26)

When viewing the exit total mass flow it is evident that the model cannot predict the initial large drop off in discharge mass and in fact continues to underpredict the mass flow along the manifold and especially at the last node.

5) Exit Liquid Mass Flow Rate (Figure 2.27)

The data for the exit liquid mass flow indicates a large drop off in liquid mass flow which last from about Tube 1 to Tube 5. There is an increase at the last channel, which is the first evidence of a reverse flow at the manifold end.

6) Void fractions (Figure 2.28)

When viewing the void fraction predictions, those for the inlet and run are very small quantities (a˜ 0.05). The model appears to predict predominance of liquid flow, whereas the data indicates a drop off in liquid mass flow

along the manifold. The exception to this is the exit void fraction, which increases towards the end. These discrepancies may be attributed to the inputs which are specified to the model. When the model is supplied with a high mass flow and low quality, it predicts a mostly liquid flow.

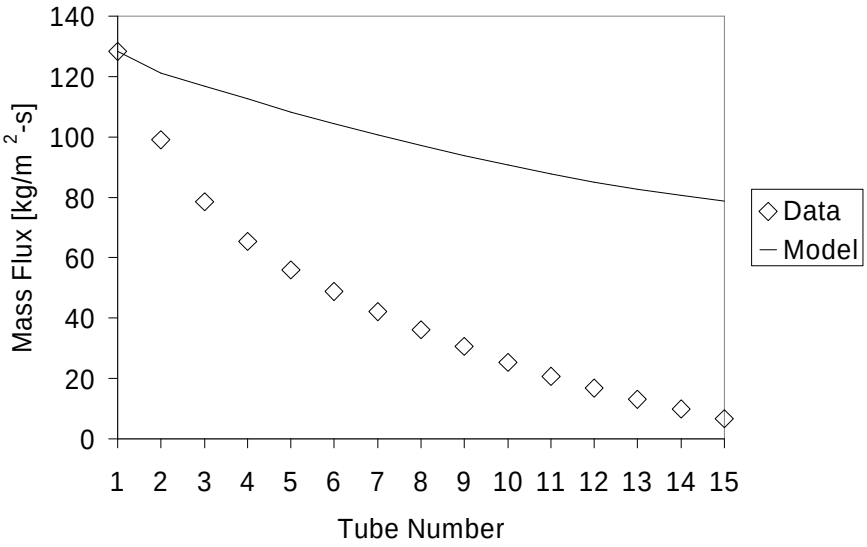

Figure 2.23: Junction Inlet Mass Flux (TP-a), 12.7mm Spacer Plate, Test 3

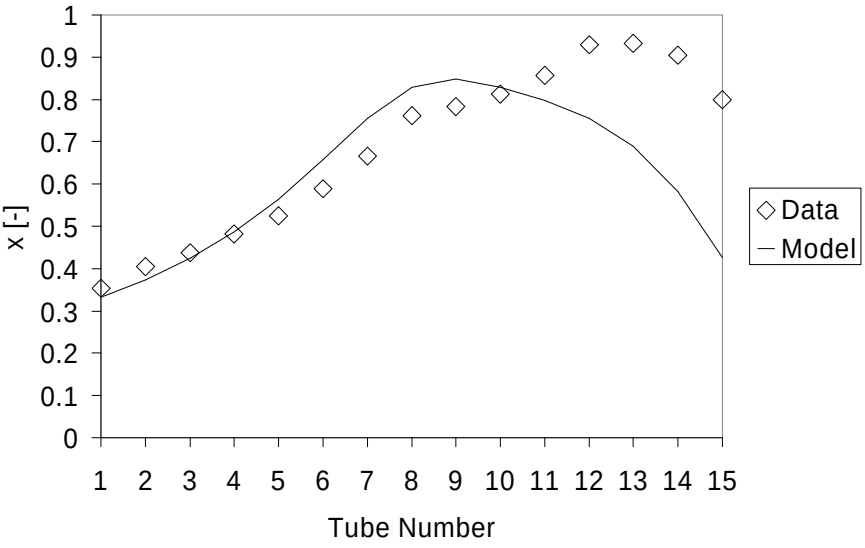

Figure 2.24: Run Quality (TP-a), 12.7mm Spacer Plate, Test 3

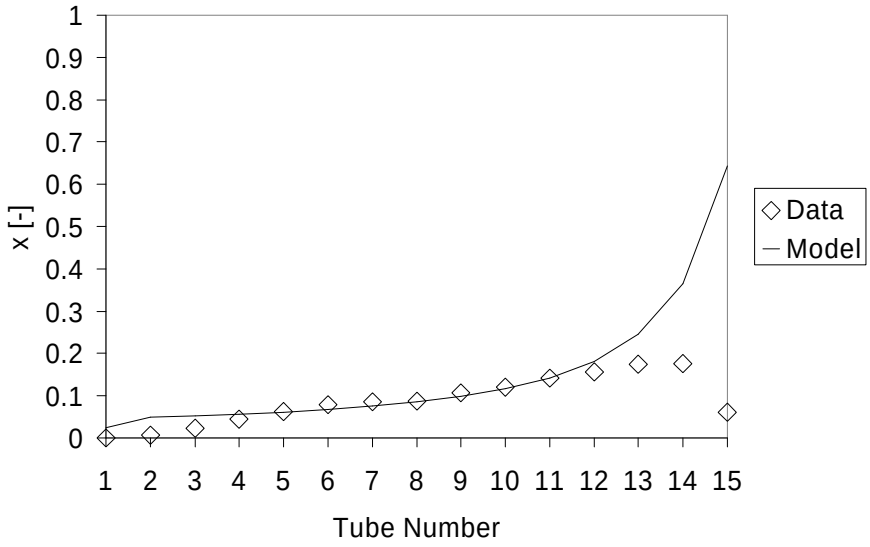

Figure 2.25: Discharge Quality (TP-a), 12.7mm Spacer Plate, Test 3

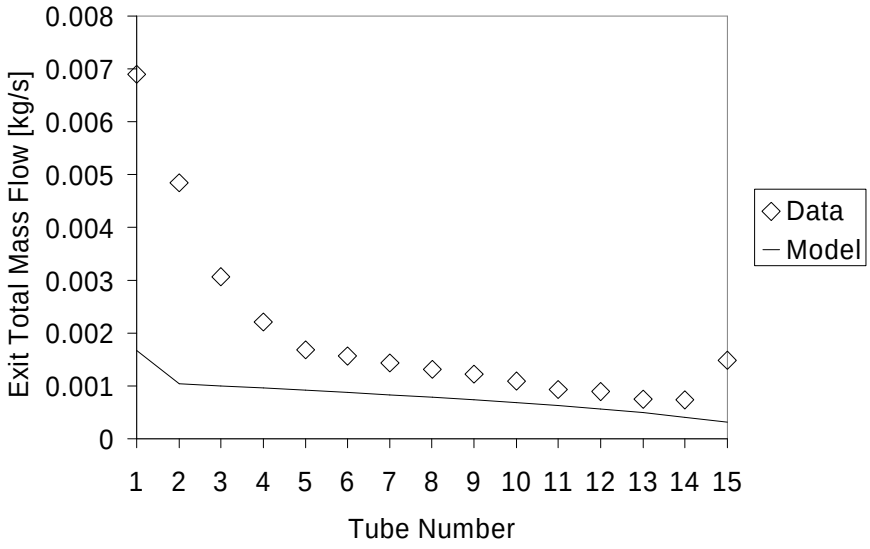

Figure 2.26: Total Discharge Mass Flow (TP-a), 12.7mm Spacer Plate, Test 3

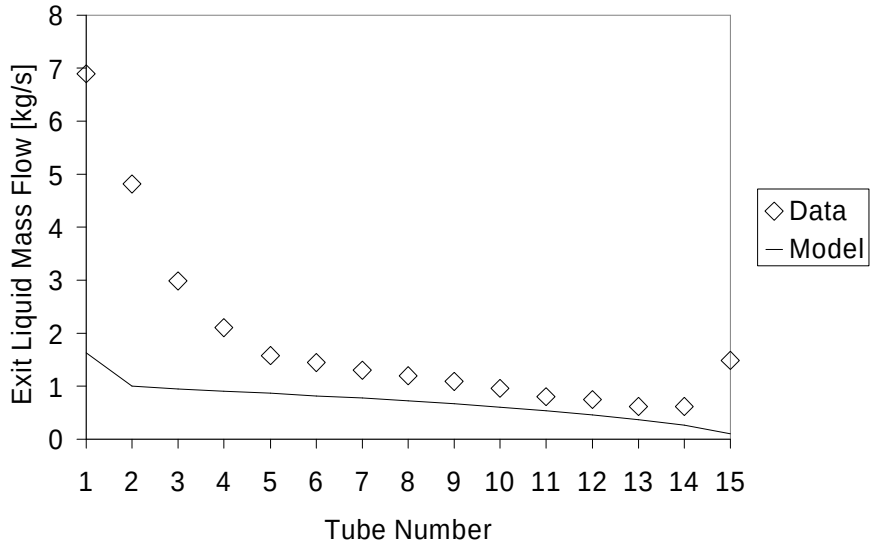

Figure 2.27: Discharge Liquid Mass Flow (TP-a), 12.7mm Spacer Plate, Test 3

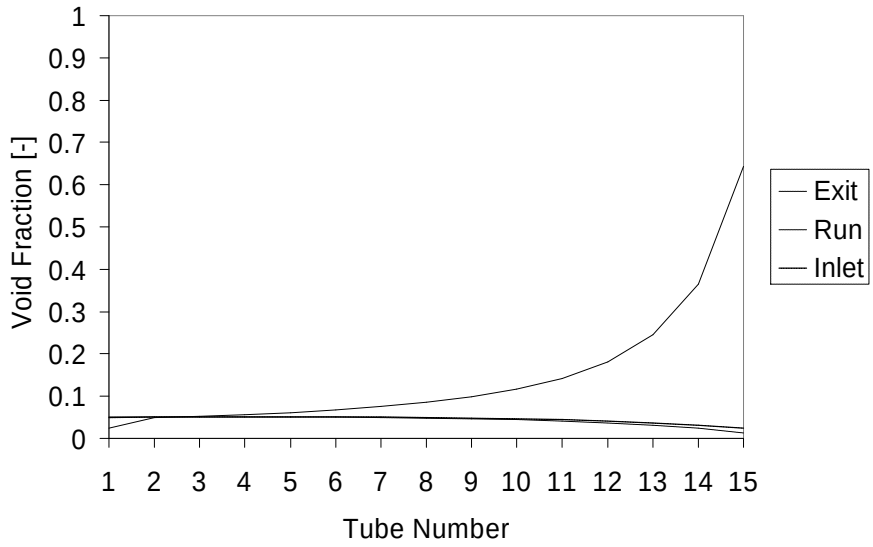

Figure 2.28: Void Fraction (TP-a), 12.7mm Spacer Plate, Test 3

2.6.2.2 6.35mm Spacer Plate

Test 4

In this particular test case the inlet mass flux is G=145 $\mathrm{kg/m^2 \cdot s}$ and the inlet quality is x=0.09.

1) Inlet Mass Flux to Junction (Figure 2.29)

The model predicts a qualitatively accurate trend for the inlet mass flux but exceeds the data by about 20%.

2) Run Quality (Figure 2.30)

The data demonstrate that the along all points in the flow direction the quality is below 0.1. While the model predicts run qualities always below 0.1, it does not predict the same decreasing trend along the manifold. However, when confined to such a small scale (e.g. below 0.1) the differences between data and model are not significant.

3) Exit Quality (Figure 2.31)

In the data, the exit quality never rises above x=0.26 and demonstrates a convex profile with a peak located near channel number 8. The model predicts a small increase and small decrease in the first and last channels, respectively, however the quality profile is flat between these two points. This seems to indicate that a key piece of information is missing from the model, which is the proper specification of flow regime at points along the manifold. The model is within 30% of the data within this region.

4) Exit Total Mass Flow Rate (Figure 2.32)

The model predicts a decrease commensurate with that of the data, however it is not quantitatively accurate. In the region from channel 3 to 13 the model passes through several of the data points. However, at the end of the channel the prediction is quite far from the final channel value. This may be due to the model's inability to account for backflow *a priori*.

5) Exit Liquid Mass Flow Rate (Figure 2.33)

The above discussion also applies to the liquid mass flow rate.

6) Void fractions (Figure 2.34)

The void fraction predictions all lay below 0.14, meaning that the vapor phase never occupies more than 14% of the total channel area. This indicates that the flow most likely does not contain a film of liquid, but the overshoot at the end indicates the presence of backflow effects.

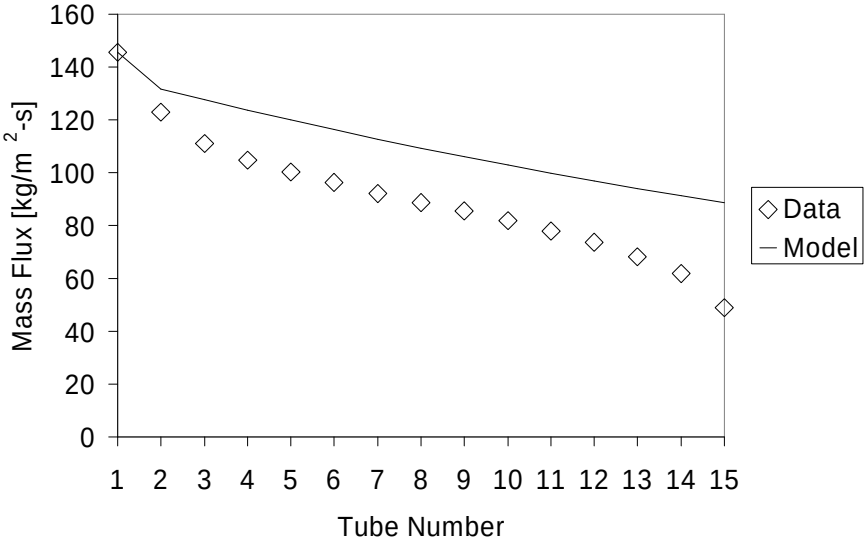

Figure 2.29: Junction Inlet Mass Flux (TP-a), 6.35mm Spacer Plate, Test 4

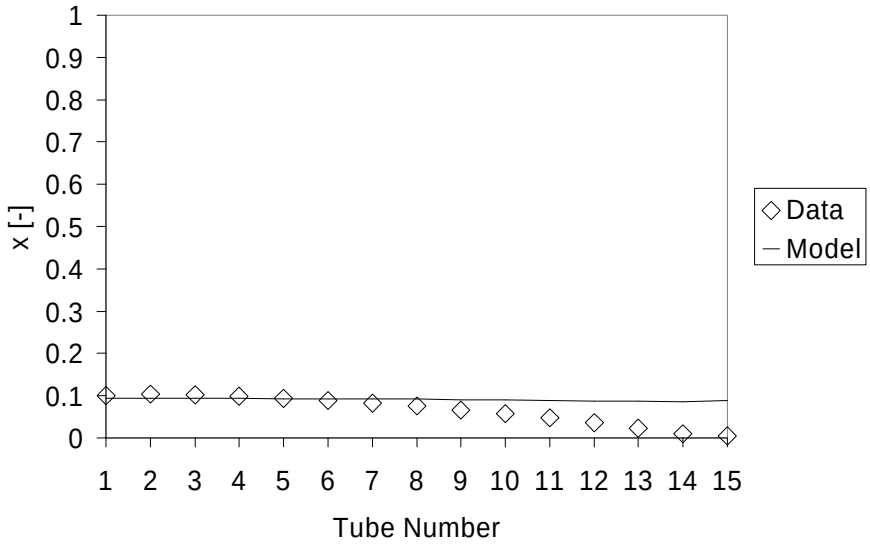

Figure 2.30: Run Quality (TP-a), 6.35mm Spacer Plate, Test 4

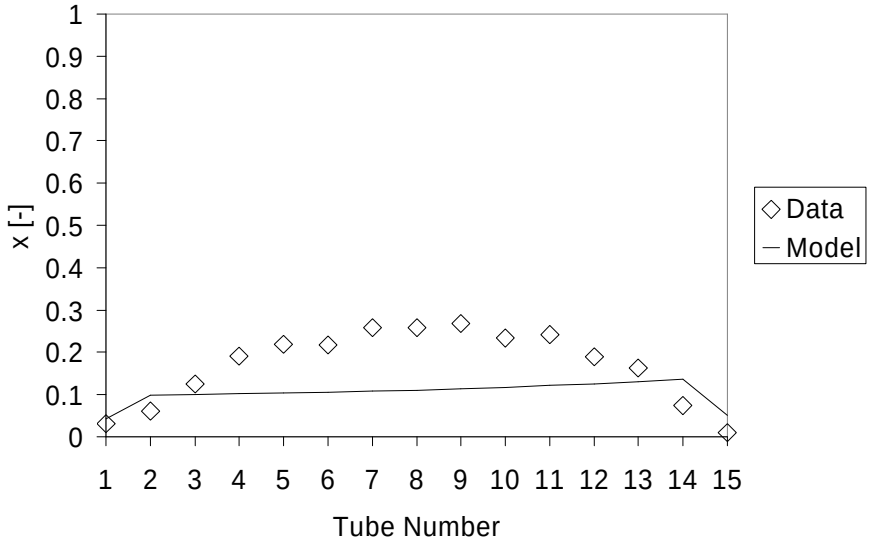

Figure 2.31: Discharge Quality (TP-a), 6.35mm Spacer Plate, Test 4

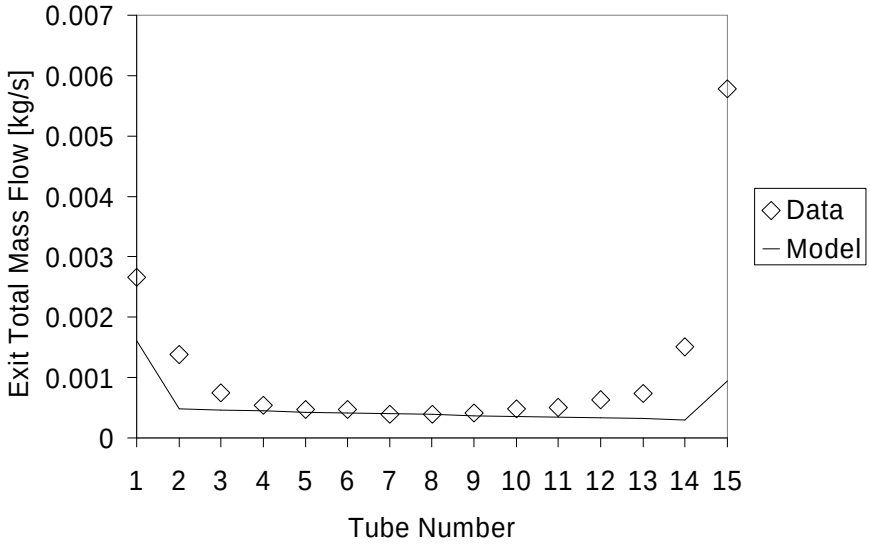

Figure 2.32: Total Discharge Mass Flow (TP-a), 6.35mm Spacer Plate, Test 4

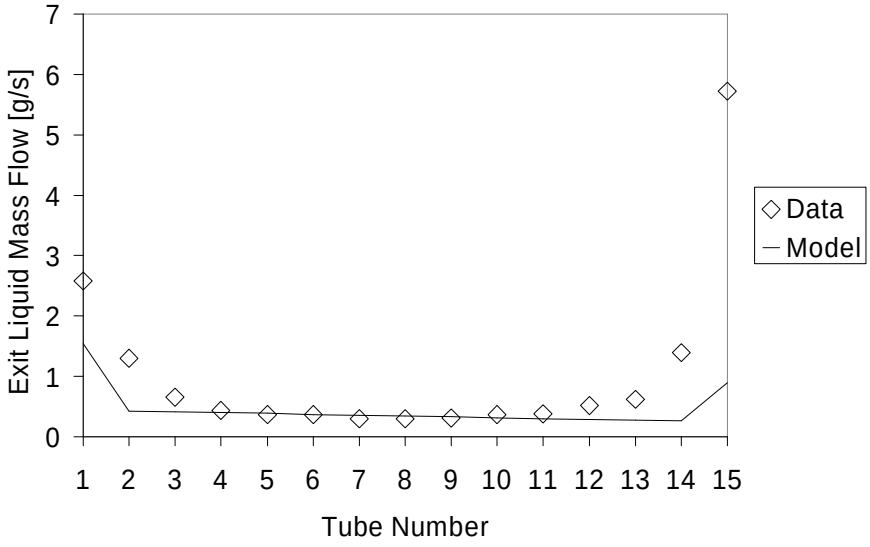

Figure 2.33: Discharge Liquid Mass Flow (TP-a), 6.35mm Spacer Plate, Test 4

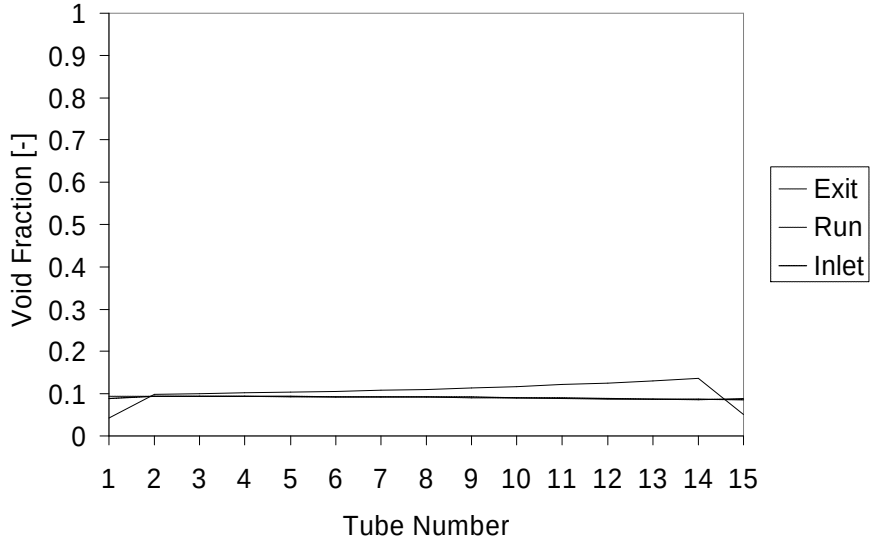

Figure 2.34: Void Fraction (TP-a), 6.35mm Spacer Plate, Test 4

Test 8

In this particular flow, the inlet mass flux is G=243 $\mathrm{kg/m^2 \cdot s}$ and the inlet quality is x=0.05. It is a low-quality flow much like that of the previous test, with a 68% increase in mass flux.

1) Inlet Mass Flux to Junction (Figure 2.35)

Here the model prediction is somewhat better than for Test 4, with the model over-predicting the junction inlet mass flux by about 17% as compared to 20% in the previous case. At higher mass fluxes for similarly low qualities, the flow acts more like a single phase liquid flow, which is much simpler to predict than a two-phase flow.

2) Run Quality (Figure 2.36)

The test run quality is never above 0.06, with a sharp decrease in quality along the flow direction. The model predicts a nearly constant quality near 0.05. Again these discrepancies must be viewed in the light of the extremely small scale, since quality should lie in the range of 0 to 1.

3) Exit Quality (Figure 2.37)

The exit quality lay below 0.15 with a convex profile with a maximum near channel 9. This peak is below that of Test 4, indicating that the flow is closer to the limiting case of purely liquid phase flow. The model predicts a slightly inclined trend from 0.1 to about 0.12.

4) Exit Total Mass Flow Rate (Figure 2.38)

The model predicts a total exit mass flow which is qualitatively in agreement with the data, but quantitatively accurate only from channel 3 to 13. The large surge in mass flow in the final channel indicates backflow behavior

5) Exit Liquid Mass Flow Rate (Figure 2.39)

The same discussion applies for the liquid mass flow rate.

6) Void fractions (Figure 2.40)

The void fraction profiles all lay below 0.06 and follow the same trends as described in above for Test 4. The inlet and run void fractions are nearly constant at 0.05.

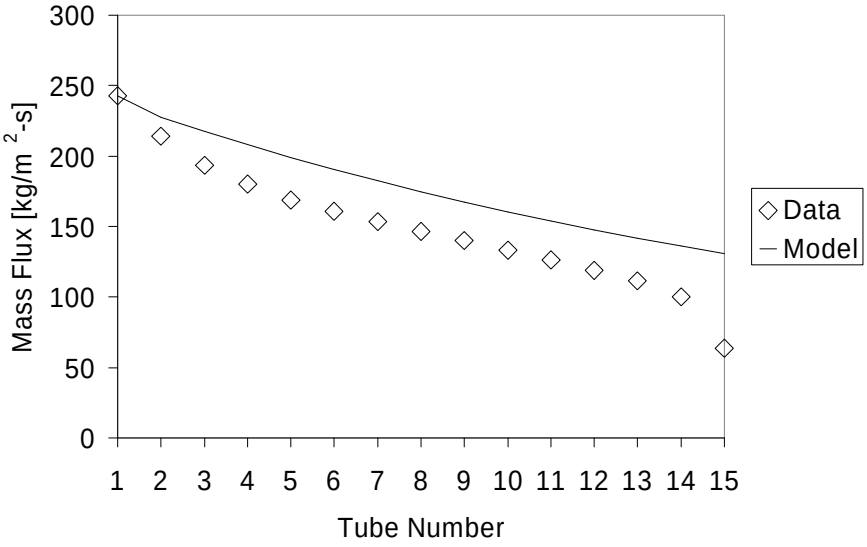

Figure 2.35: Junction Inlet Mass Flux (TP-a), 6.35mm Spacer Plate, Test 8

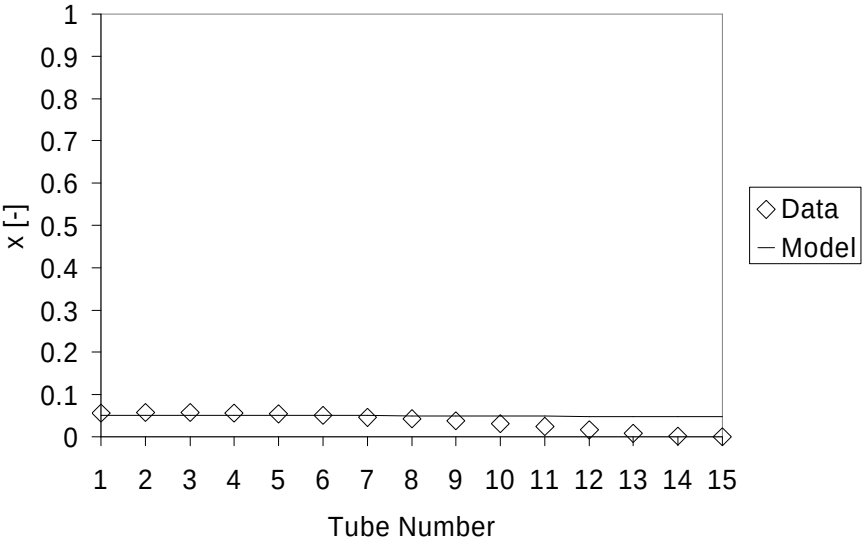

Figure 2.36: Run Quality (TP-a), 6.35mm Spacer Plate, Test 8

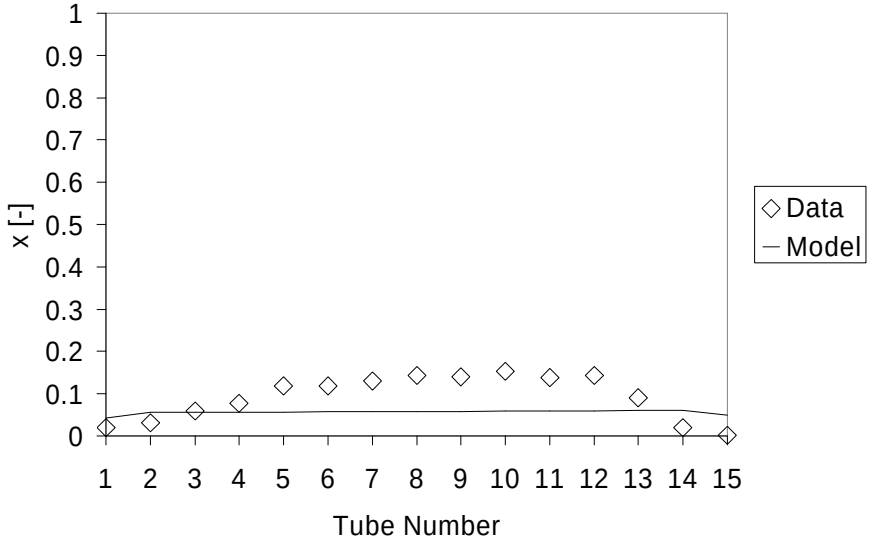

Figure 2.37: Discharge Quality (TP-a), 6.35mm Spacer Plate, Test 8

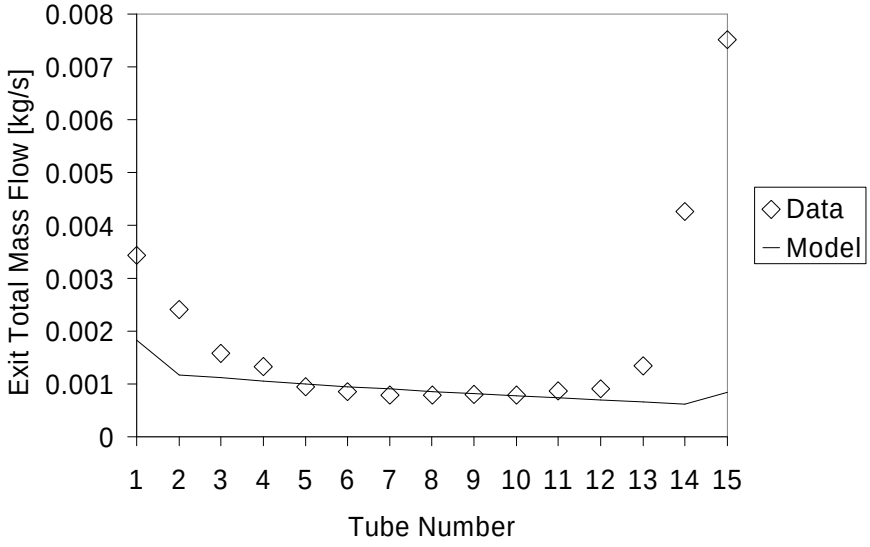

Figure 2.38: Total Discharge Mass Flow (TP-a), 6.35mm Spacer Plate, Test 8

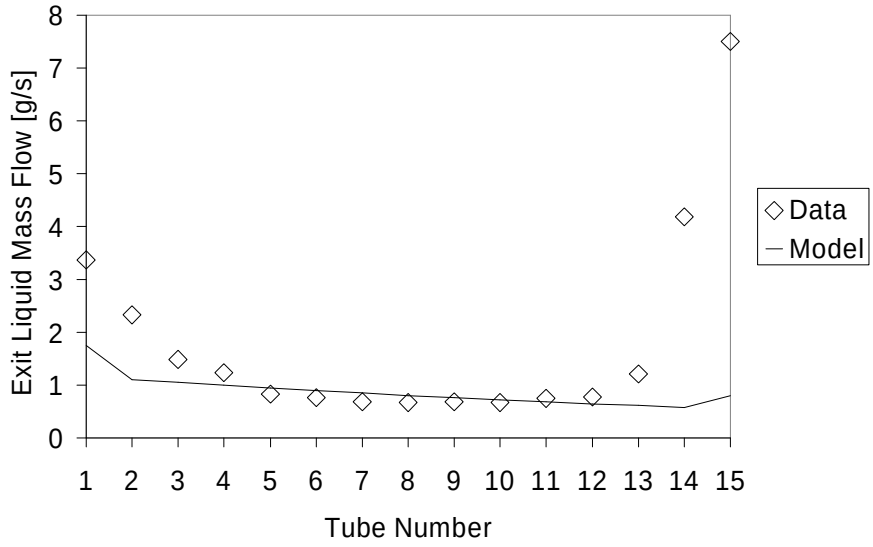

Figure 2.39: Discharge Liquid Mass Flow (TP-a), 6.35mm Spacer Plate, Test 8

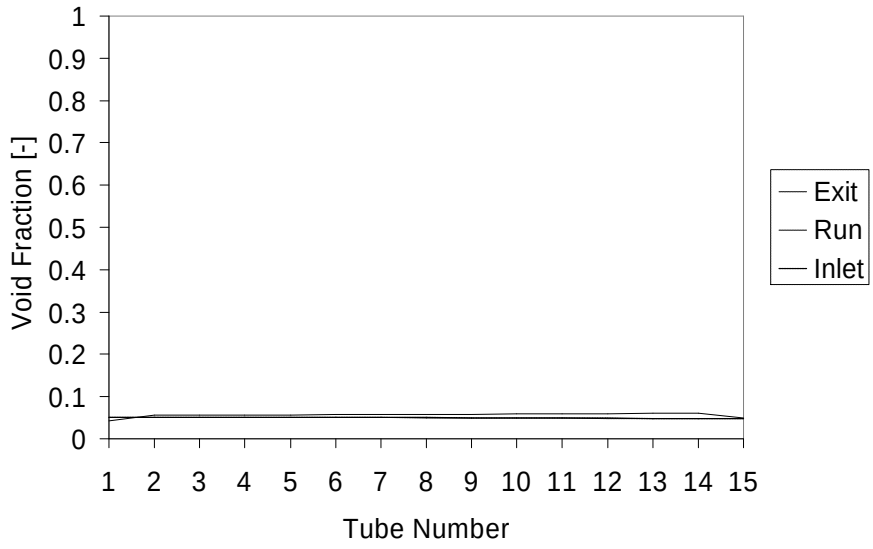

Figure 2.40: Void Fraction (TP-a), 6.35mm Spacer Plate, Test 8

Test 11

In this particular case the inlet mass flux is G=374 $\mathrm{kg/m^2 \cdot s}$ and the quality is 0.04, representing nearly identical conditions as for Test 8 but with a 54% increase in inlet mass flux. The comparisons are nearly identical as for the previous test case. Therefore these graphs are contained in Appendix B. However, there are some exceptions. For instance, the inlet mass flux trails off in sudden decreasing behavior for the last three channels. The run quality never lay above x=0.045. The exit quality is always below 0.13. The agreement for exit mass flow and exit liquid mass flow is even less for this test case. In fact there is a sharp increase in exit mass flow for channels 12 through 15 that the model cannot predict with any appreciable accuracy. This is most likely due to the fact that as the inlet mass

flux increases for low-quality flows, there is a strong potential for backflow at the manifold end. Liquid collects at the end and travels under the vapor layer to deposit in the final channels.

2.6.2.3 3.175mm Spacer Plate

Test 2

In this particular case the inlet mass flux and quality are $43\,\mathrm{kg/m^2 \cdot s}$ and 0.35, respectively.

1) Inlet Mass Flux to Junction (Figure 2.41)

Regarding the inlet mass flux comparisons, it is interesting to note the drop from initial value in the first channel. This is matched by the model accurately. The data demonstrates a nearly constantly declining trend from channel 2 to channel 12, whereas the model predicts an imperceptibly convex profile. From channels 12 to 15 a sharp drop-off occurs in the data which is not reflected by the model. In this case it appears that, since the inlet quality is relatively high at 0.35, a film has most likely been produced which carries along the top of the channel and deposits in these channels.

2) Run Quality (Figure 2.42)

The higher inlet quality is reflected in the higher run qualities in the flow direction for the data, which begin at 0.5 and decline to 0.3. Interestingly the model predicts the same initial run quality of 0.5 but drops to zero. Again, this is due to the model's inability to account for the film inside the channel.

3) Exit Quality (Figure 2.43)

The discharge quality trend reflected by the data is highly erratic; it begins from a low quality, rising sharply to values oscillating about 0.9, and decreasing sharply to a value of about 0.3. This is quite clear evidence that a film is being produced in the flow. If a film would exist, the quality in the channel would be quite high, then drop to a considerably lower value as this film loses its momentum and deposits in the final channels. The model does predict this large initial surge in exit quality; however, it never drops back down to a lower value but stays at its highest allowed variable limit in the simultaneous equation solver, which is 0.99.

4) Exit Total Mass Flow Rate (Figure 2.44)

Surprisingly, the model predicts the large drop-off which occurs for the exit mass flow in the initial channel. After the initial drop-off, the model accurately predicts the distribution until channel 11, at which point the data increases due to the film deposition.

5) Exit Liquid Mass Flow Rate (Figure 2.45)

See discussion for the total exit mass flow above.

6) Void fractions (Figure 2.46)

The void fraction predictions are very interesting. For the inlet and run the void fractions decrease from a relatively high value of 0.5 to below 0.1. The exit void fraction jumps to 0.9 by the second channel, decreases to about 0.67, then jumps at the last channel to 0.9. These trends lend further evidence to the presence of a liquid film, since less liquid is available for entry into the discharge channels and would increase the void fraction of the fluid entering the channels. However the decreasing trends in the channel void fraction indicate the liquid is occupying a larger fraction of the upper area of the channel, which decreases the area occupied by the vapor below the liquid film.

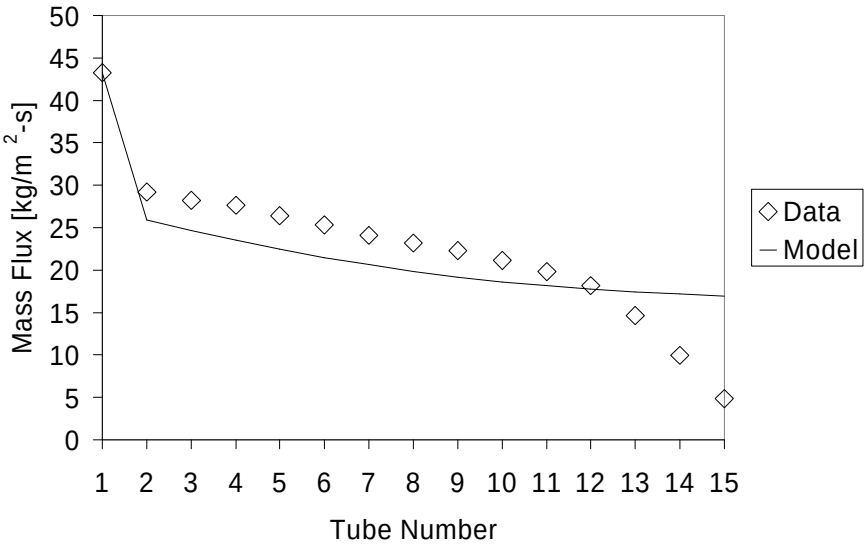

Figure 2.41: Junction Inlet Mass Flux (TP-a), 3.175mm Spacer Plate, Test 2

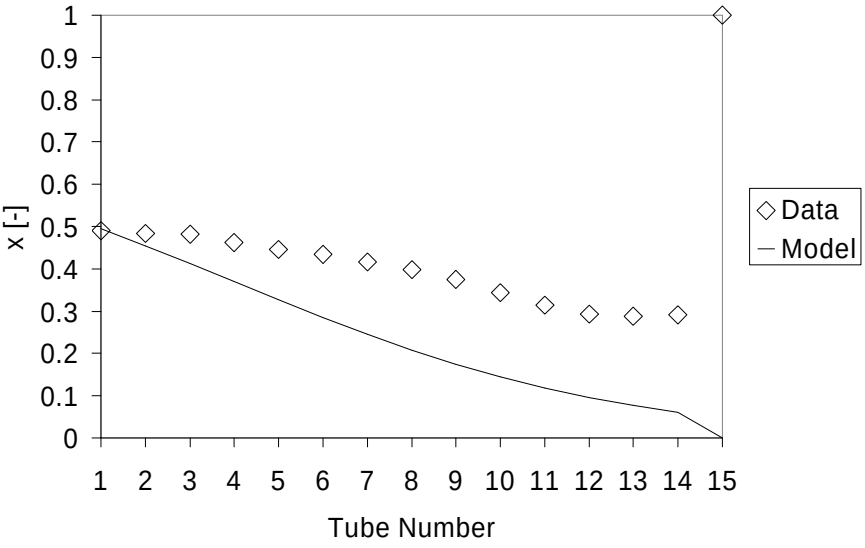

Figure 2.42: Run Quality (TP-a), 3.175mm Spacer Plate, Test 2

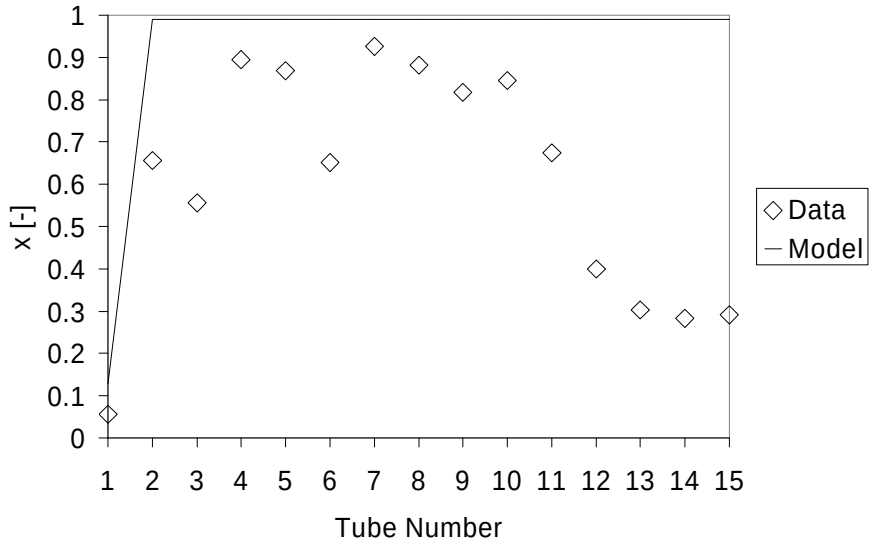

Figure 2.43: Discharge Quality (TP-a), 3.175mm Spacer Plate, Test 2

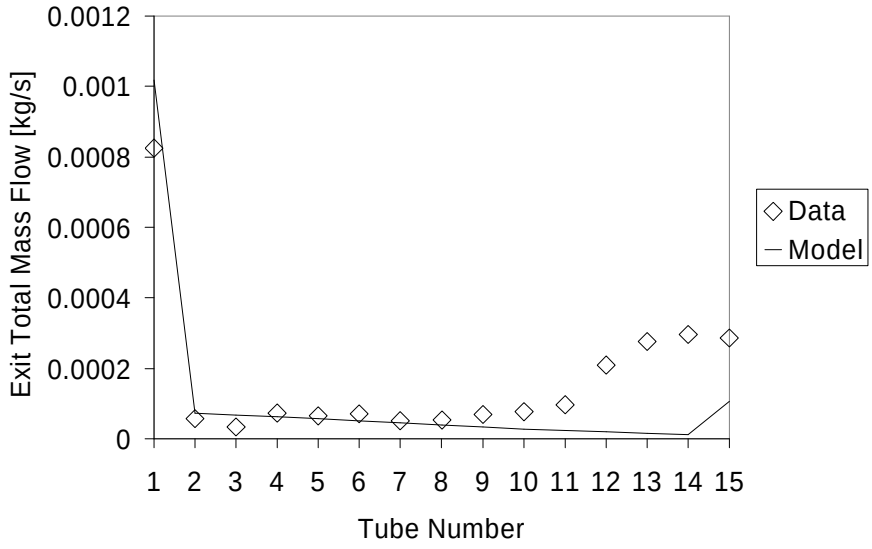

Figure 2.44: Total Discharge Mass Flow (TP-a), 3.175mm Spacer Plate, Test 2

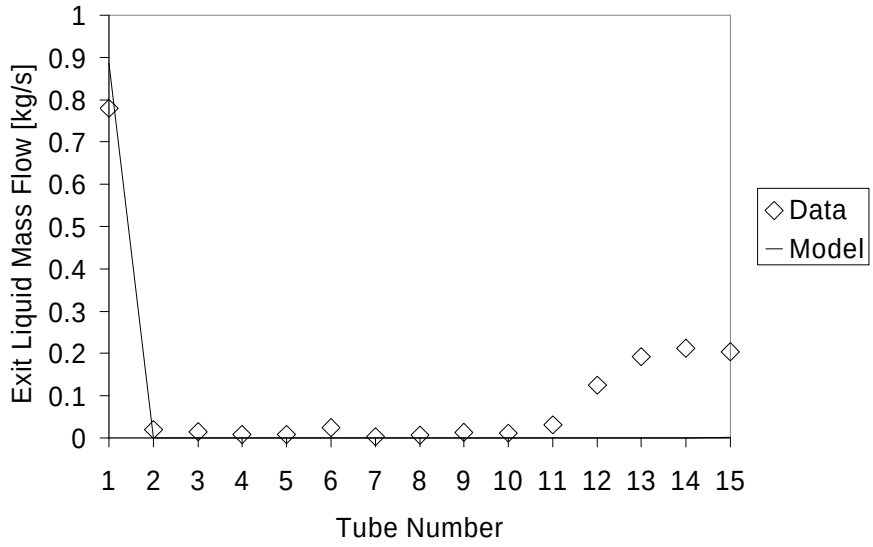

Figure 2.45: Discharge Liquid Mass Flow (TP-a), 3.175mm Spacer Plate, Test 2

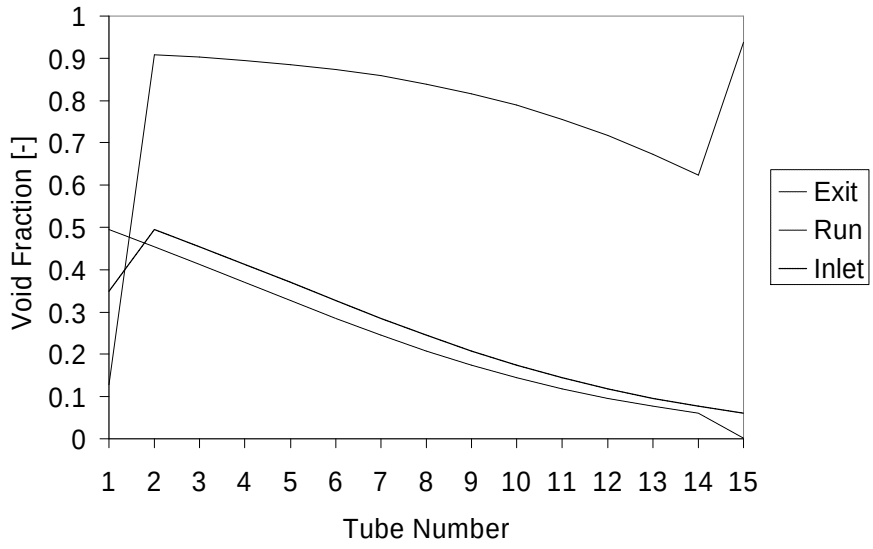

Figure 2.46: Void Fraction (TP-a), 3.175mm Spacer Plate, Test 2

Test 5

This particular case represents a threefold increase in inlet mass flux for the nearly the same quality as in Test 2.

1) Inlet Mass Flux to Junction (Figure 2.47)

The model accurately captures the initial drop-off in inlet mass flux through the first channel, but as in the case before an imperceptibly convex profile is predicted with a difficulty of prediction in the final channel. Values in the region from channel 2 to 12 are within roughly 18% of the data.

2) Run Quality (Figure 2.48)

As in the case previous to this, the initial quality is relatively high at 0.4. However, while in the previous case there is a large surge in quality at the last channel and a decrease to 0 for the model, in this case there is a surge in the model at the final channel and a decrease in the data to 0.

3) Exit Quality (Figure 2.49)

The exit quality assumes a convex profile with a maximum value near 0.9 at about channel 8. However, in the region between channel 2 and 14 the model prediction is slight concave and reaches a mean value near 0.65 in this region.

4) Exit Total Mass Flow Rate (Figure 2.50)

Interestingly for the exit mass flow predictions the exit mass flow for the first channel is overpredicted though it follows the qualitative trend in the data. At the channel end the surge is successfully predicted, though the trend is not as gradual as reflected in the data. In particular, the gentle upward increase is not described.

5) Exit Liquid Mass Flow Rate (Figure 2.51)

See discussion for the exit mass flow above.

6) Void fractions (Figure 2.52)

The exit void fraction is concave with a maximum value near 0.65. The inlet and run trends are nearly constantly decreasing from values near 0.5 to 0.4. The decrease in exit void fraction at the last channel describes a situation in which a film may be depositing. This is commensurate with the increase in run void fraction at this point.

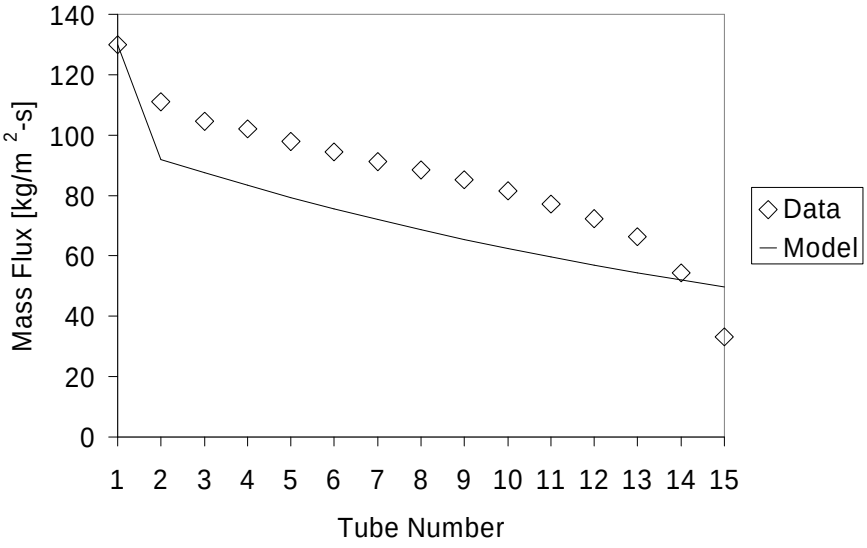

Figure 2.47: Junction Inlet Mass Flux (TP-a), 3.175mm Spacer Plate, Test 5

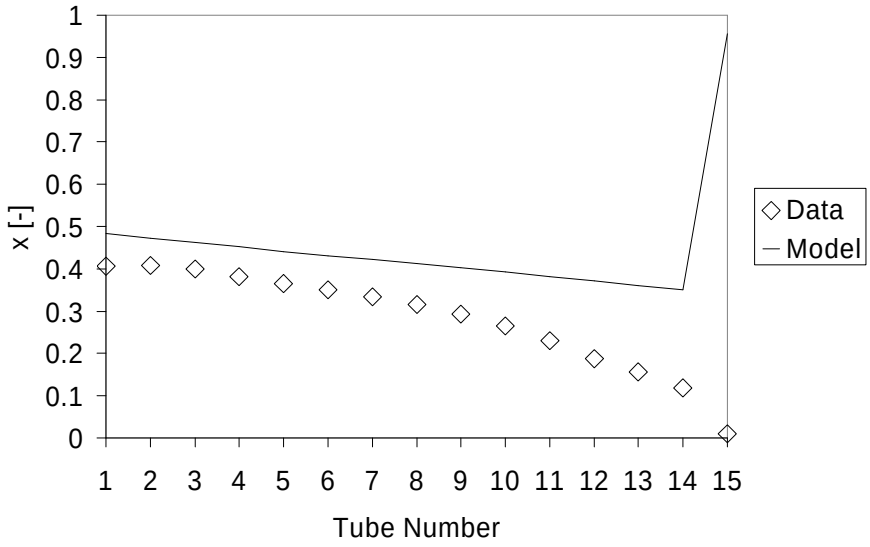

Figure 2.48: Run Quality (TP-a), 3.175mm Spacer Plate, Test 5

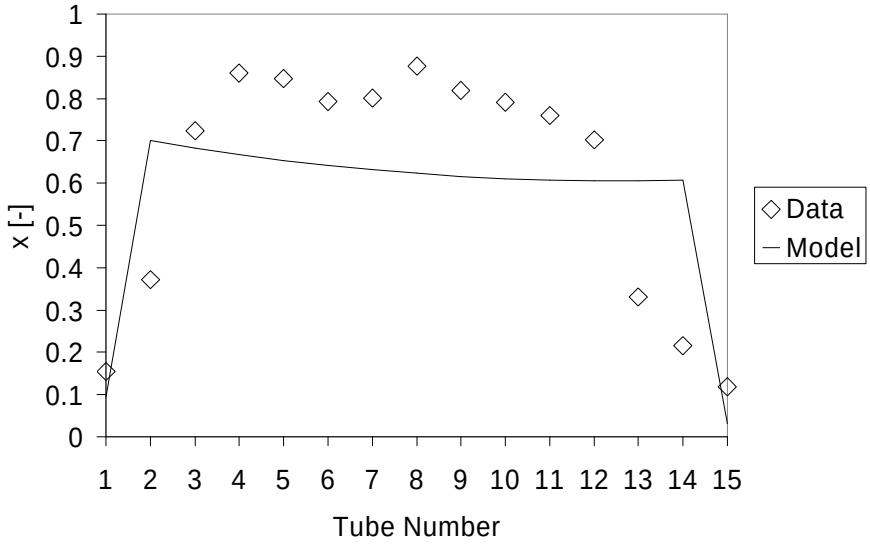

Figure 2.49: Discharge Quality (TP-a), 3.175mm Spacer Plate, Test 5

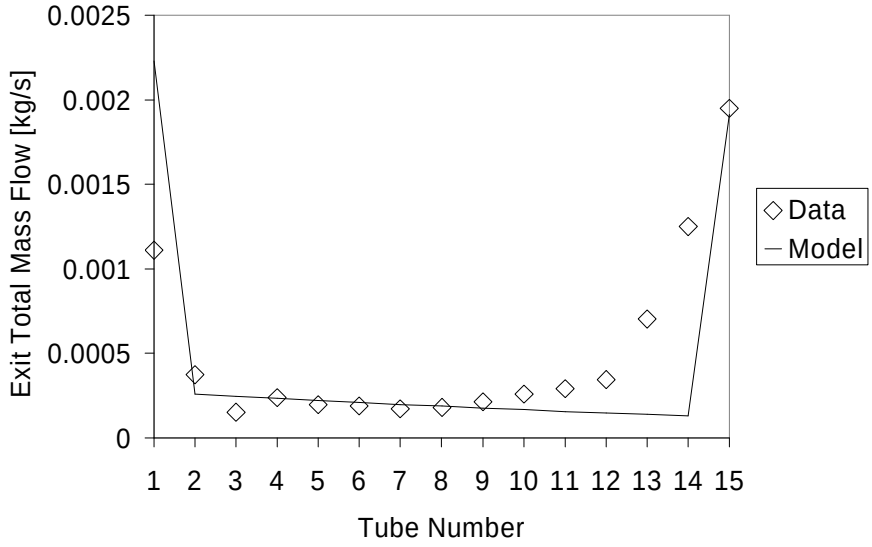

Figure 2.50: Total Discharge Mass Flow (TP-a), 3.175mm Spacer Plate, Test 5

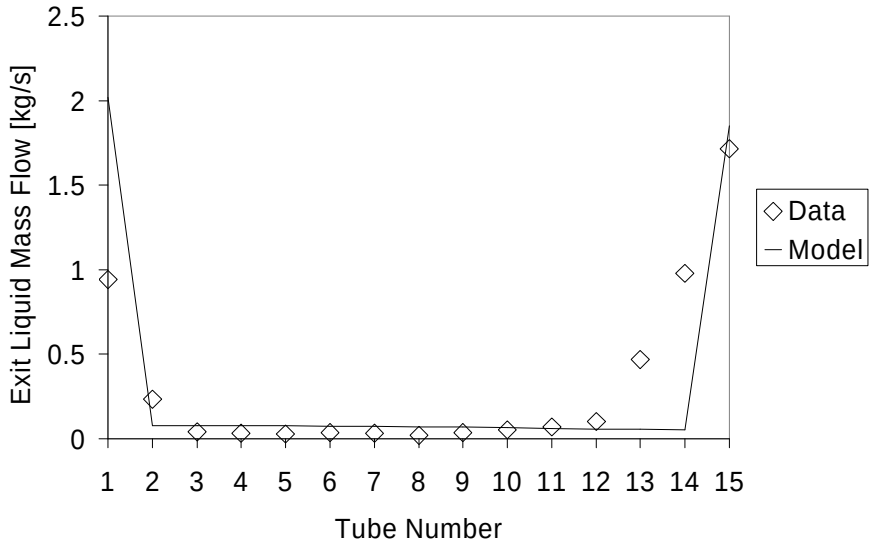

Figure 2.51: Discharge Liquid Mass Flow (TP-a), 3.175mm Spacer Plate, Test 5

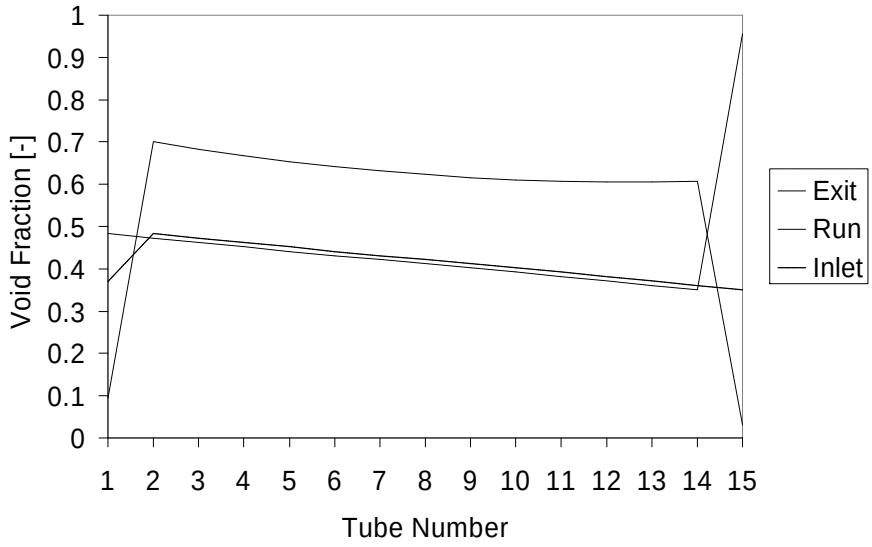

Figure 2.52: Void Fraction (TP-a), 3.175mm Spacer Plate, Test 5

Test 7

The inlet mass flux and quality to this test are G=239 $kg/m^2 \cdot s$ and x=0.16, respectively. This is an 84% increase in mass flux with a 46% reduction in quality as compared to Test 5.

1) Inlet Mass Flux to Junction (Figure 2.53)

The agreement of the model with the data for the prediction of the junction inlet mass flux is quite good; indeed the prediction lay along the majority of data points. However, at about 80% of the channel length, the data begins to trail off.

2) Run Quality (Figure 2.54)

Of predictions for the run quality up to this point, the agreement is greatest for this case, with the prediction passing directly through the majority of the data.

3) Exit Quality (Figure 2.55)

There is a vast discrepancy which occurs for the discharge quality, however, about 66% of the channel length. Here the model prediction immediately jumps to its maximum allowed value while the data presents a vast decrease in its behavior.

4) Exit Total Mass Flow Rate (Figure 2.56)

The drastic decrease in exit quality for the data is, of course, accompanied with an increase of discharge mass flow through the last few channels. The model cannot seem to convey the same information.

5) Exit Liquid Mass Flow Rate (Figure 2.57)

This difference is further accentuated when looking at the difference between the discharge liquid flow rate of the data and that of the model. The model cannot seem to predict the drastic increase in discharge mass flow arising from the film pooling phenomenon.

6) Void fractions (Figure 2.58)

The inlet and run void fractions seem to indicate a liquid flow, but very high (above 0.9) values of exit void fraction along the length of the tube and especially at about 80% of the channel length. This coincides with the assertion that a liquid film is traveling and depositing toward the end of the manifold.

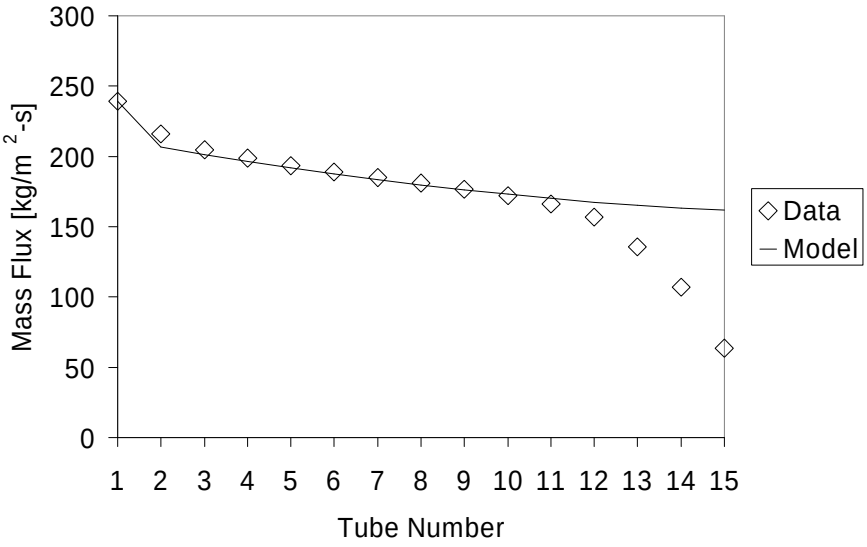

Figure 2.53: Junction Inlet Mass Flux (TP-a), 3.175mm Spacer Plate, Test 7

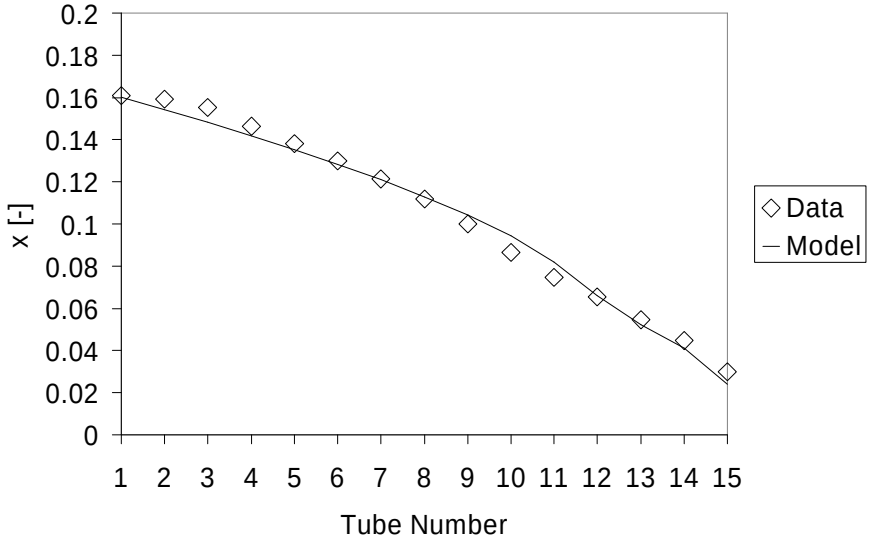

Figure 2.54: Run Quality (TP-a), 3.175mm Spacer Plate, Test 7

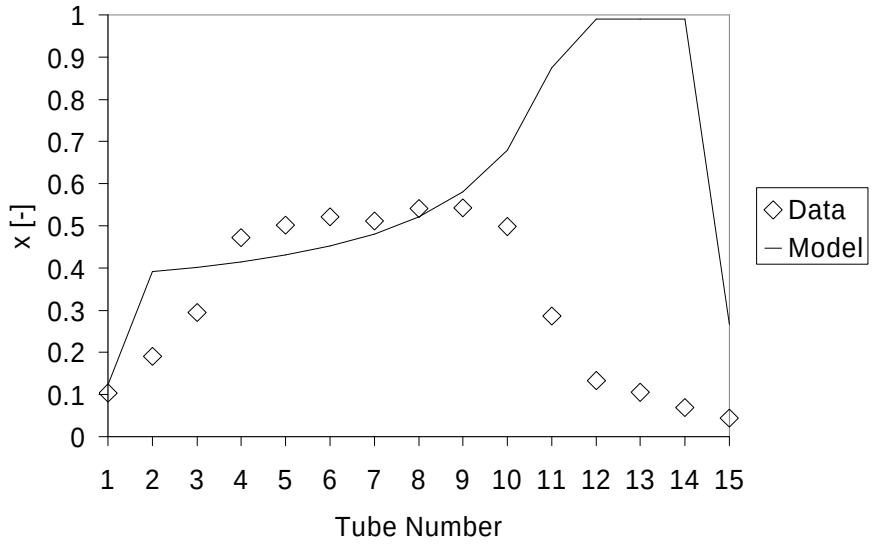

Figure 2.55: Discharge Quality (TP-a), 3.175mm Spacer Plate, Test 7

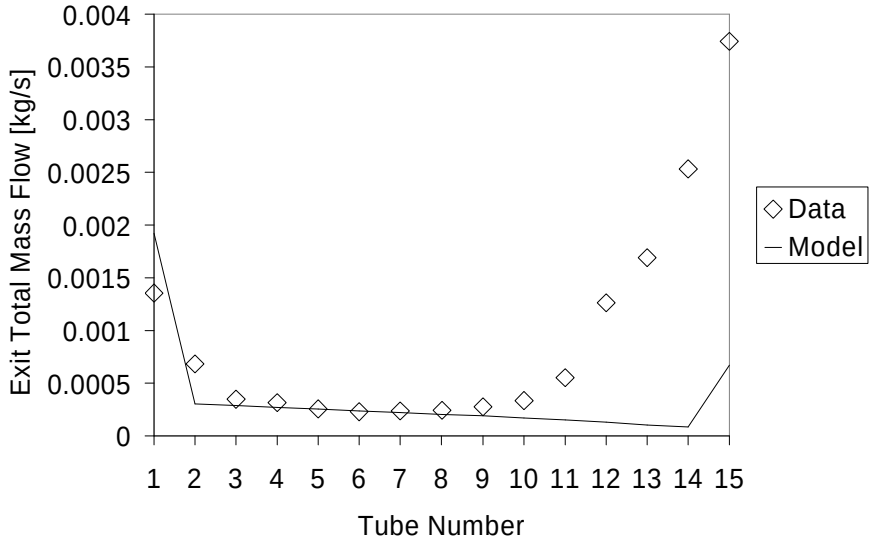

Figure 2.56: Total Discharge Mass Flow (TP-a), 3.175mm Spacer Plate, Test 7

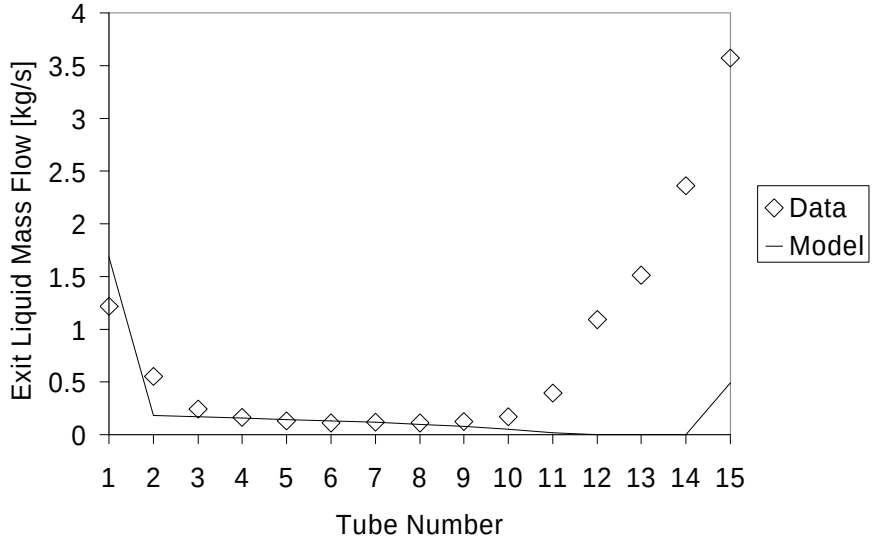

Figure 2.57: Discharge Liquid Mass Flow (TP-a), 3.175mm Spacer Plate, Test 7

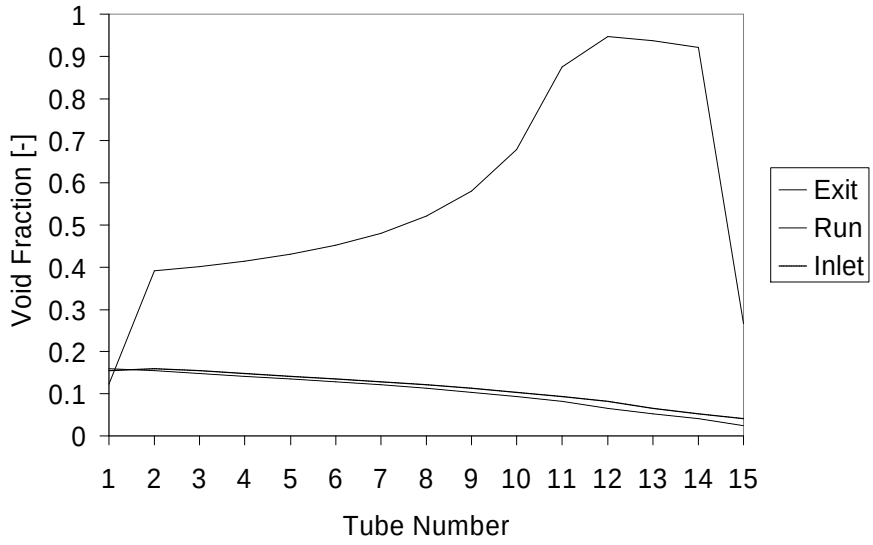

Figure 2.58: Void Fraction (TP-a), 3.175mm Spacer Plate, Test 7

Test 10

The inlet mass flux and quality for this case are 379 $\mathrm{kg/m^2 \cdot s}$ and 0.08, respectively. This represents an increase of 59% in mass flux and a reduction of 50% in the inlet quality.

1) Inlet Mass Flux to Junction (Figure 2.59)

Once again the agreement between the model and data for the junction mass flux deviates considerably at a point about 66% in the direction of flow. Given the high mass flux and low inlet quality, the fluid momentum is strong and propels it toward the end of the manifold, creating a pooling backflow in the last channels.

2) Run Quality (Figure 2.60)

The run quality is at all points below 0.085. Though the model begins at this point, the data deviates significantly, dropping to 0.02 at the channel end. However, the model declines to a value of 0.069. However, this difference is exaggerated, given the scale of the quality.

3) Exit Quality (Figure 2.61)

If the flow is exhibiting a pooling backflow phenomenon, one would expect the quality of the fluid exiting through the discharge tubes to be quite low in the channels beyond the 66% mark in the direction of flow. This is indeed the case for the data, which drops to a value of 0.022 after a sharp decline from a peak of 0.374. Though the model can demonstrate the quality increase and decrease in the first and last channels, respectively, there is no strongly convex quality profile in the quality trend, with a peak value of 0.168.

4) Exit Total Mass Flow Rate (Figure 2.62)

Regarding the prediction of exit mass flow through the microchannels, the model demonstrates good agreement until about channel 9, but then the data shoots sharply upward and this is not captured by the model.

5) Exit Liquid Mass Flow Rate (Figure 2.63)

The same discussion applies for the liquid discharge mass flow rate.

6) Void fractions (Figure 2.64)

The model predicts inlet and run void fractions which begin at 0.08 and decline gently to a value of 0.07. The exit void fraction rises from 0.089 to a value of 0.16 along the majority of the length of the channel, declining to 0.077. Again, this is evidence that the model cannot predict these backflow effects.

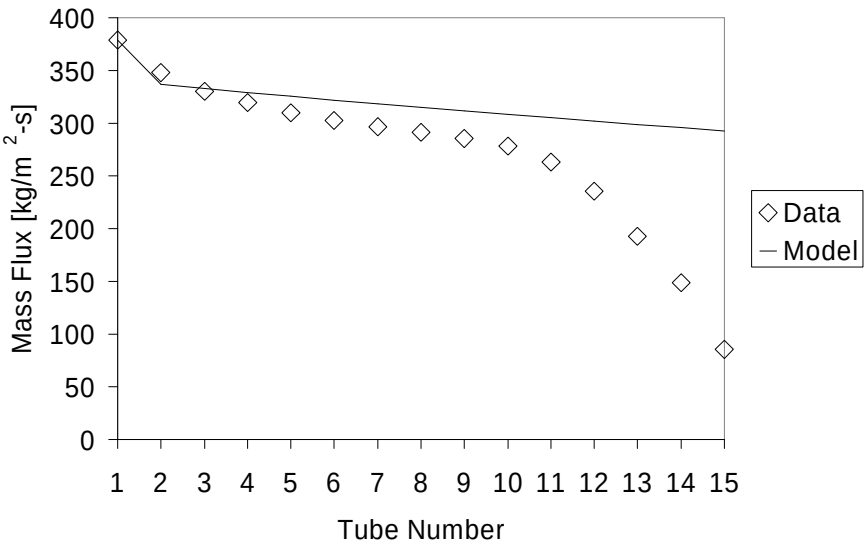

Figure 2.59: Junction Inlet Mass Flux (TP-a), 3.175mm Spacer Plate, Test 10

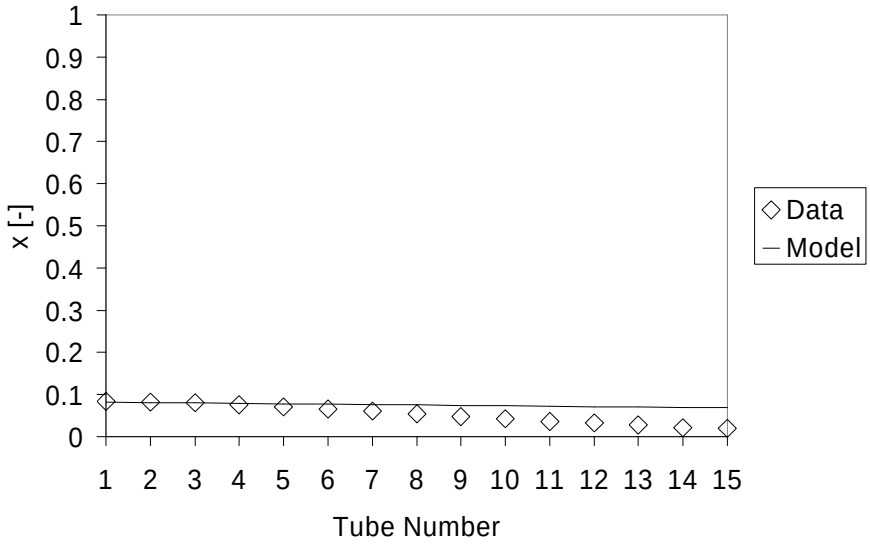

Figure 2.60: Run Quality (TP-a), 3.175mm Spacer Plate, Test 10

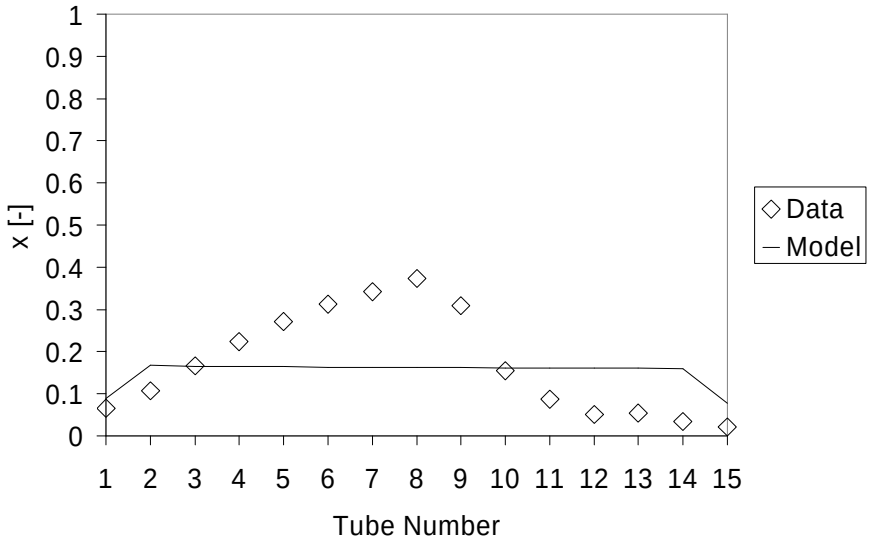

Figure 2.61: Discharge Quality (TP-a), 3.175mm Spacer Plate, Test 10

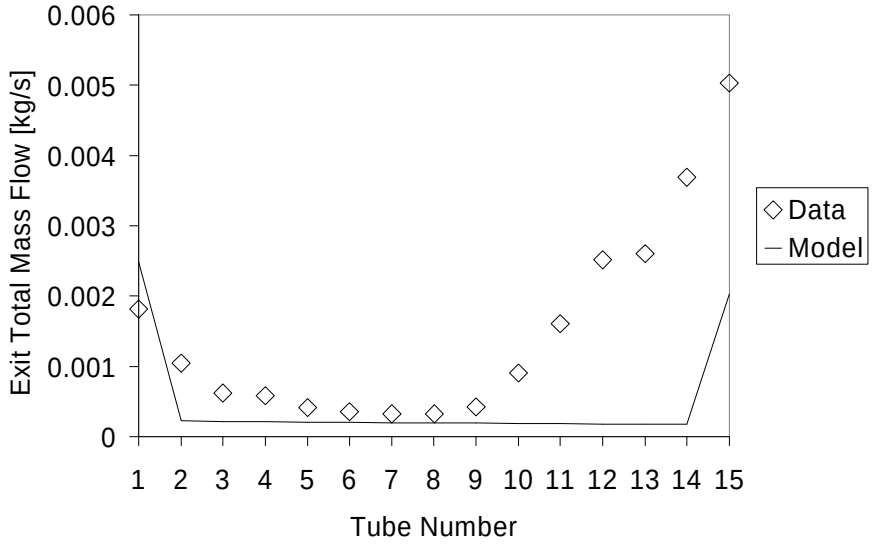

Figure 2.62: Total Discharge Mass Flow (TP-a), 3.175mm Spacer Plate, Test 10

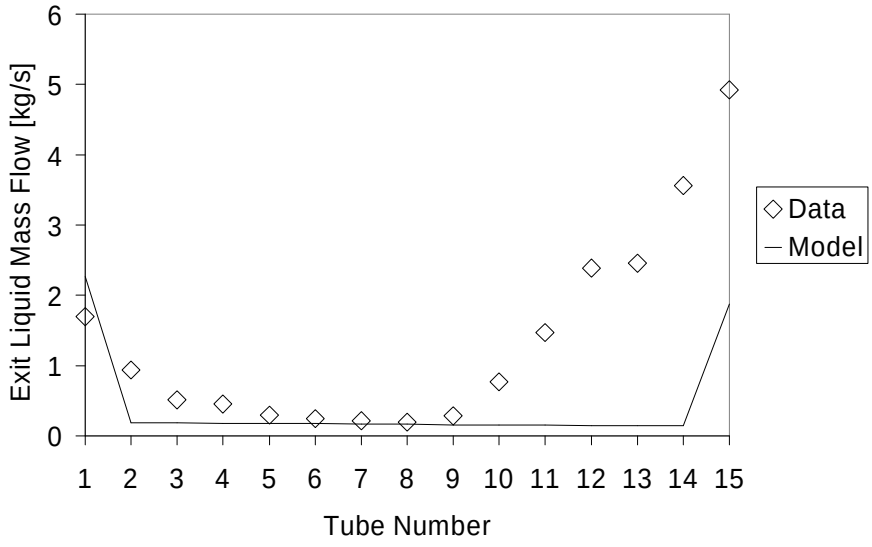

Figure 2.63: Discharge Liquid Mass Flow (TP-a), 3.175mm Spacer Plate, Test 10

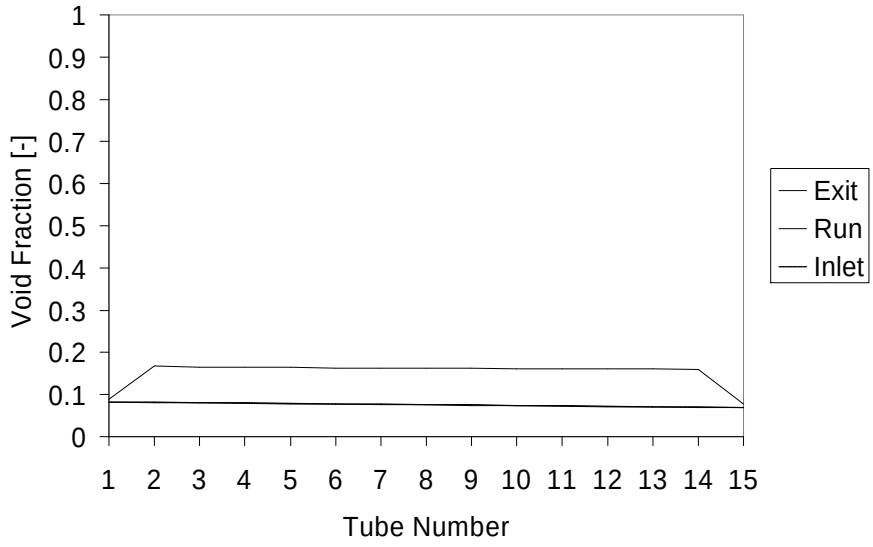

Figure 2.64: Void Fraction (TP-a), 3.175mm Spacer Plate, Test 10

Test 13

The inlet mass flux and quality for this case are 274 $kg/m^2 \cdot s$ and 0.16, respectively. These conditions represent a 72% reduction in inlet mass flux and a two-fold increase in quality as compared to Test 10.

1) Inlet Mass Flux to Junction (Figure 2.65)

The agreement is good for the junction mass flux until about the point of 75% of the flow direction; the data drops from a value of 184 to 81 over this range. The model cannot account for the phenomenon causing this effect.

2) Run Quality (Figure 2.66)

The agreement with the run quality for this case is one of the best agreements demonstrated. It follows the data trend quite well from an initial value of 0.167 to 0.032.

3) Exit Quality (Figure 2.67)

However, from about channel 10 to the end of the manifold the agreement deviates considerably for the exit quality. Though the data declines sharply, the model shows the opposite behavior. Agreement is maintained until only about channel 9.

4) Exit Total Mass Flow Rate (Figure 2.68)

The agreement is quite good over the range of the initial channels up until about channel 10, at which point the data surges upward while the model cannot describe this effect. Most likely the film is depositing at this point.

5) Exit Liquid Mass Flow Rate (Figure 2.69)

This difference is greatly heightened when examining the exit liquid mass flow, which deviates considerably in the last five channels.

6) Void fractions (Figure 2.70)

The exit void fraction increases along the length of the manifold and peaks at the tenth channel, when in fact it should decrease sharply at this point according to the data. The inlet and run void fractions are below 0.16 and

decrease along the manifold. One would expect higher run and inlet void fractions than those demonstrated, if a film is being produced.

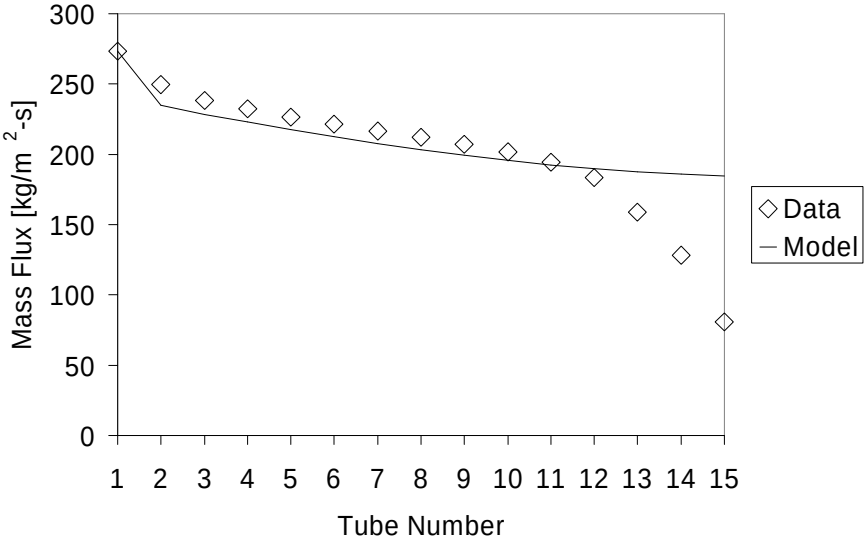

Figure 2.65: Junction Inlet Mass Flux (TP-a), 3.175mm Spacer Plate, Test 13

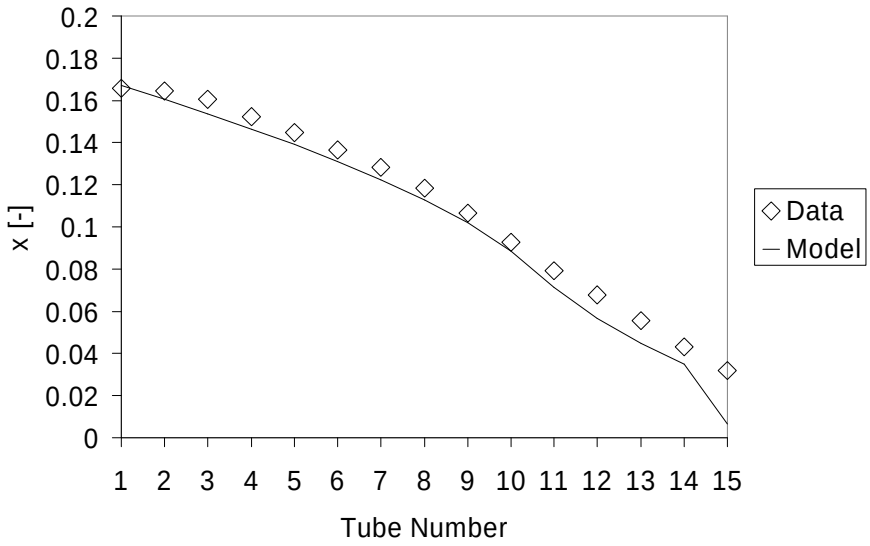

Figure 2.66: Run Quality (TP-a), 3.175mm Spacer Plate, Test 13

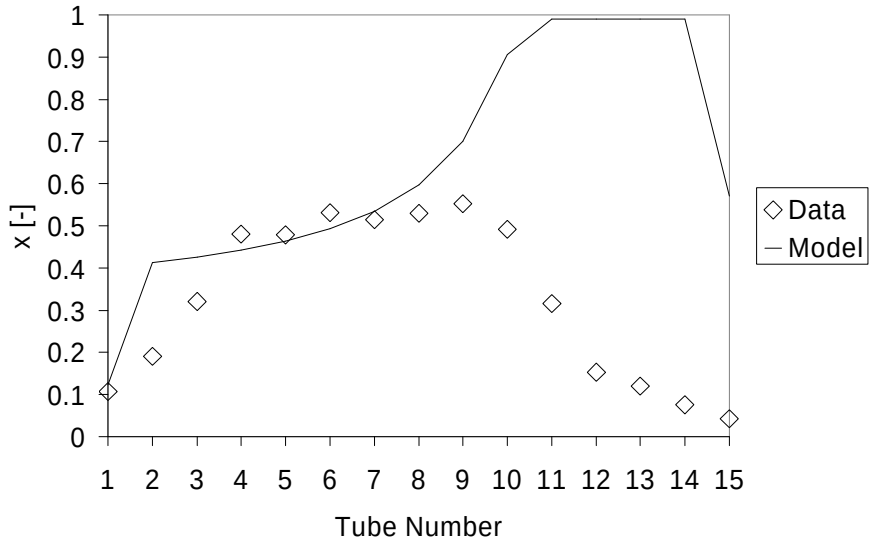

Figure 2.67: Discharge Quality (TP-a), 3.175mm Spacer Plate, Test 13

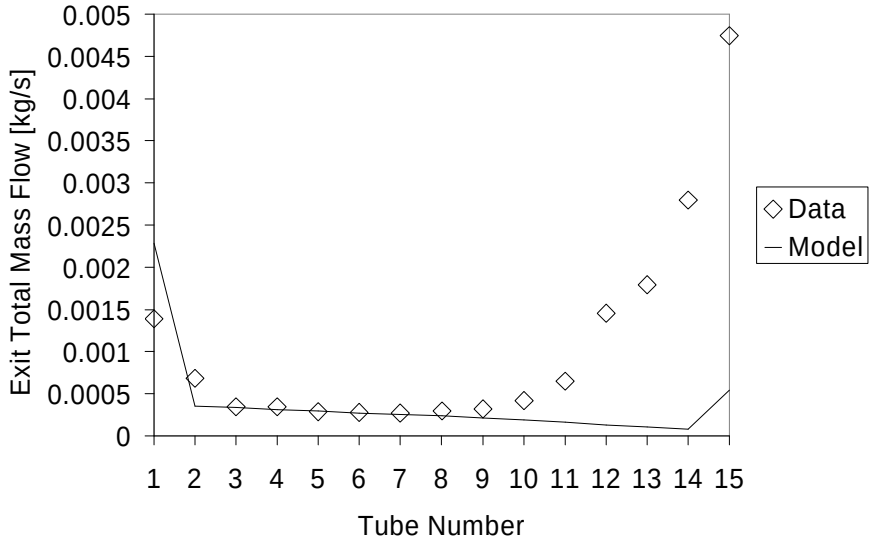

Figure 2.68: Total Discharge Mass Flow (TP-a), 3.175mm Spacer Plate, Test 13

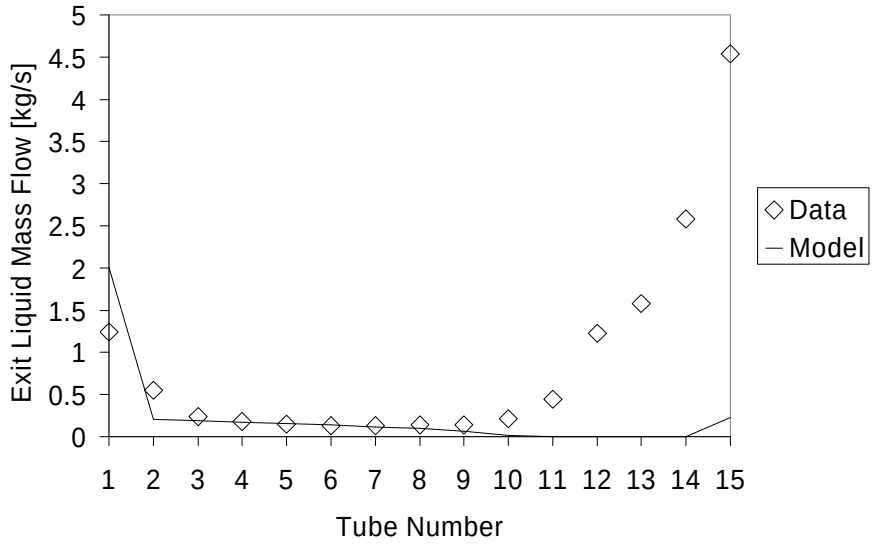

Figure 2.69: Discharge Liquid Mass Flow (TP-a), 3.175mm Spacer Plate, Test 13

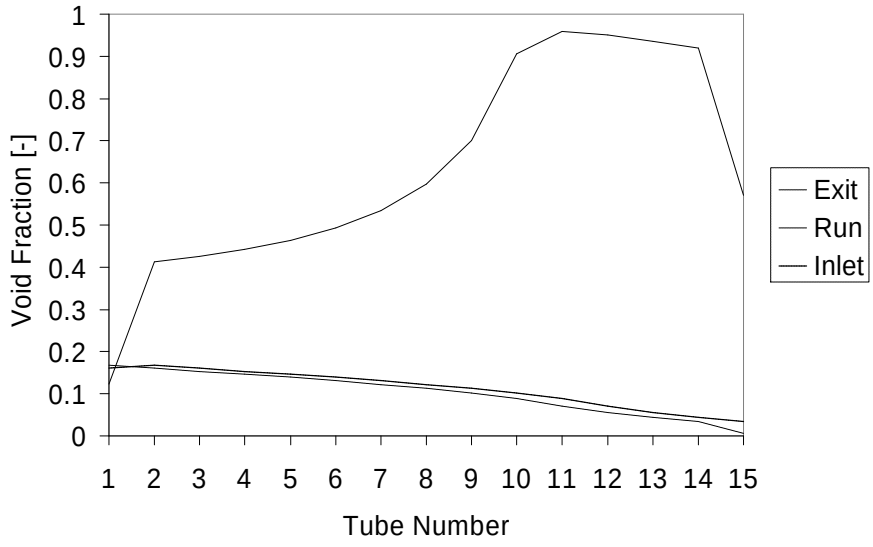

Figure 2.70: Void Fraction (TP-a), 3.175mm Spacer Plate, Test 13

2.6.3 TP-a Model Discussion

Sample results for the agreement between the model and a sample set of data have been presented. In some cases the results were quite good, in others there is a vast deviation. The purpose of this section is to discuss reasons why these agreements and disagreements have occurred. Again it must be stressed that no general manifold distribution model exists, that several have relied on the data to a far greater degree than the model presented here, and that in some cases the introduction of empirical coefficients was necessary, as long as these are accompanied with justification and explanation.

2.6.3.1 Pressure Loss Coefficients

Some parameters warranting discussion are the "pressure reduction factors" ß1, ß2, and ß3. These are presented in Tables 2.4-2.6 for the various test cases.

Table 2.4: Loss coefficients for the test cases of the 12.7mm Spacer Plate

12.7 mm (0.5" Spacer			
	b**1**	b**2**	b**3**
	[-]	[-]	[-]
Test 1	95	1.5	β2
Test 3	100	3.5	β2

Table 2.5: Loss coefficients for the test cases of the 6.35mm Spacer Plate

6.35 mm (0.25") Spacer			
	b**1**	b**2**	b**3**
	[-]	[-]	[-]
Test 4	4	0.5	β1+1
Test 8	6	2	β1
Test 11	8	2	β1

Table 2.6: Loss coefficients for the test cases of the 3.175mm Spacer Plate

3.175 mm (0.125") Spacer			
	b**1**	b**2**	b**3**
	[-]	[-]	[-]
Test 2	2	0.125	β1
Test 5	1	0.125	β1+4.9
Test 7	1	0.125	β1+9
Test 10	2	0.1	β1+2
Test 13	1	0.125	β1+5

The meaning of the parameters is as follows:

1) ß1=pressure loss reduction factor for first channel
2) ß2=pressure loss reduction factor for channels 2 to 14
3) ß3=pressure loss reduction factor for the last channel

ß1 represents a correction factor which divides two-phase pressure loss equation, Equation (2.32), written from the first to second face of the control volume for the very first channel. It must be stressed that when this factor is 1, no appreciable effect on the prediction occurs on the rest of the channel; in other words points downstream of where this correction factor is applied are not influenced by its presence. It is a factor whose value is dictated solely by the vast decrease in mass flow rate which occurs in the first channel. In addition when ß1=1 the only discrepancy is that the predicted value lay below that of the data but the discrepancy is not drastic, i.e. the mass flow prediction for the first channel is nearly the same value as that of the second channel. The fact that it is a number higher than one indicates that the pressure difference is indeed reduced across the first to second face. This means that without this factor, the kinetic energy of the incoming stream is much greater than that demonstrated by the data. As the

manifold area is reduced, as is demonstrated in Tables 2.4-2.6, this reduction becomes smaller. This highlights the need for a model which has the capability of incorporating flow regimes, since for a larger cross sectional area the phases have the potential to be more separated for a stratified flow case, or more dispersed for dispersed-bubbly regime, for example.

ß2 is a reduction factor on Equation (2.56) and is applied for the nodes from 2 to 14 because it was found in between these two channels the flow distribution behaved well (i.e. no significant surges at the first or last channels). The fact that it is sometimes less than one indicates that by dividing by this number, one is actually multiplying the equation by a number greater than 1. It must be stressed than when ß2=1, i.e. when its effect is not present, there is no significant deviation in its predictive ability. It was found that in some cases the mass flow distribution prediction was slightly convex, rather than slightly concave, as indicated by the data. This factor accounts for its lack of concavity.

ß3 is a reduction factor on Equation (2.32), but it is applied at the last channel. Obviously, as discussed in the results section for the TP-a model, there are definite mass flow surges in the final channels of the distribution manifold. When ß3=1, the difference between the data and model is that the model's mass flow prediction is flat at this point, rather than rising upwards. In addition, it is important to state that increasing ß3 to abnormally large values (e.g. up to 1000) does not make the model match the data more closely. Essentially, the extreme rises in mass flow occurring at the final channel could not be predicted, no matter how the reduction parameters were varied. ß3 was adjusted to only give rough agreement at the channel end; its presence and the fact that it does have an effect on the final channel's mass flow prediction are more important than its value. A final comment regarding the pressure correction factors is that when ß1=ß2=ß3=1 the resulting distribution is essentially a flat profile that lay through the majority of data from channel 2 to 14, but there are no mass decreases or increases at the inlet or exit, respectively.

2.6.3.2 Applicability

This model is derived from first principles of fluid mechanics and has been derived for the specific case of two-phase flow. Within the model, some empirical relations have been used, especially regarding the loss coefficients K12 and K13, for which the correlations of other researchers have been employed. Nonetheless, in contrast to several previous models which incorporate phenomenon such as phase separation, up to three quantities have been specified *at a node*. In this model, the inlet conditions are specified only *for all nodes*. This represents a significant improvement upon distribution models. For the designer interested in employing this specific model, it is important to keep the parameters of Tables 2.4-2.6 in mind, and that when the correction factors assume their initial values of 1, a predicted mass distribution profile will be applicable along 87% (or 13 out of 15) of the channel in the flow direction, and that entrance and exit mass flow predictions may not be accurate.

2.6.3.3 Criticisms

This model currently suffers from an inability to accurately predict the mass flow drop in the initial channel and the mass flow surge occurring in the very last channels of the manifold. This is due to the fact that it cannot account for the flow-regime, despite being accurate across the majority of the channels and for a majority of the test cases. Flow regime-specific information would be a valuable addition. For instance, if it is known that initially the flow is stratified, then initial mass flow drop in the first few channels is easily understood. However, at some point the flow regime has to change to an annular and/or bubbly regime which would create the film which has been seen

depositing in the final channels. Specifying this regime change solely based on the initial values of mass flux and quality is difficult, if not impossible, since one cannot predict when and where such a change would occur solely based on these parameters.

Another problem with this model is the solution procedure. The model is comprised essentially of a large matrix of simultaneous equations, and issues of stability and convergence are always present. It was found that slightly changing certain values near the true solution would make the solution procedure divergent. However, the model does not predict different values of the flow variables for the same inlet conditions. Computation time is also sometimes considerable, taking up to 30 seconds to arrive at a solution. One must also be conscientious of the variable limits and initial guesses for the flow variables. The solution range *cannot* be the default range of (-8 , +8). The computational solution range must lie in a reasonable physical range. If necessary, equations must be re-formulated to split up “troubled” powers, meaning powers of variables for which there may be multiple roots (powers of 2 and 4 especially), and setting reasonable variable limits such that these false roots are disallowed.

2.7 Conclusions

The complexities of modeling an inlet two-phase flow have been explored. A first-approach method to predict mass distribution was to assume the phases as a homogeneous mixture with average properties. This simplified approach was visited again, expanded, and a more accurate two-phase model was derived, the TP-a Model. This two-phase distribution model presented here is derived from first principles of fluid mechanics. Some restrictive assumptions have been employed, such as the assumption of one-dimensionality, invariability of quality between nodes, and steady flow. True manifolds would have situations of multi-dimensional and unsteady flow. However, taking a mechanical, integral-type approach is essential to understanding the physics behind complex flow phenomena which often lay beneath commercial fluid codes.

In some cases, particularly for larger manifold cross sectional areas, the agreement between the model and data is quite good. However, for higher quality flows and lower manifold cross sectional areas, flow effects occur which the model cannot account for without a priori knowledge of the flow regime, entrainment rate, or film production. During experimentation, it was noticed that a pooling backflow was created due to a film which traveled along the top of the channel, was carried along by the vapor momentum, and collected at the end of the channel. Agreement suffers for the first and last few distribution channels, though agreement is often reached for the discharge channels in between. A noteworthy advantage of this model, however, is its relatively weak reliance on experimental data. Previous models necessitated the input of several data at a single point in the flow, whereas this model only necessitates the specification of the inlet conditions only. Owing to the fact that no single comprehensive two-phase manifold distribution model exists, the proposed model represents an important step.

2.8 Bibliography

Asoh, M.; Hirao, Y.; Aoki, Y.; Watanabe, Y.; Fukano, T. *Phase Separation of Refrigerant Two-Phase Mixture Flowing Downward Into Three Thin Branches From a Horizontal Manifold Pipe.* ASME/JSME Thermal Engineering Proceedings. ASME. Vol. 2. pp. 159-164. 1991.

Azzopardi, B.J. *An Additional Mechanism in the Flow Split of High Quality Gas-Liquid Flows at a T-Junction*. UKAEA Report. AERE-R 13058. 1988.

Bajura, R.A. *A Model for Flow Distribution in Manifolds.* Journal of Engineering for Power. pp. 7-12. January 1971.

Ballyk, J.D.; Shoukri, M. *On the Development of a Model for predicting phase separation phenomena in dividing two-phase flow.* Nuclear Engineering and Design 123 pp. 67-75. 1990.

Ballyk, J.D.; Shoukri, M.; Chan, A.M. *Steam-Water Annular Flow in a Horizontal Dividing T-Junction*. Int. J. of Multiphase Flow. Vol. 14, No3. Pp. 265-285, 1988.

Bankoff, S.G. *A Variable Density Single-Fluid Model for Two-Phase Flow with Particular Reference to Steam-Water Flow*. J. Heat Transfer. pp. 265-272. Nov 1960.

Baroczy, S.G. *A Systematic Correlation for Two-Phase Pressure Drop*. Eighth Nat. Heat Trans. Conf. Chem. Eng. Progr. Symp. Ser. 64. Vol. 62, pg 232. 1966.

Bernoux, P.; Mercier, P.; Lebouche, M.. *Two-Phase Flow Distribution in a Compact Heat Exchanger*. Proc. of the 3rd Intl. Conf. on Compact Heat Exchangers. Davos, Switzerland. 2001.

Bouré, J.A. *Mathematical Modeling and the Two-Phase Constitutive Equations.* European Two-Phase Flow Group Meeting. Israel. 1975.

Bouré, J.A. *Constitutive Equations for Two-Phase Flows*. Two-Phase Flows and Heat Transfer with Application to Nuclear Reactor Design Problems. Ed. by J. Ginoux. pp. 157-178. 1978.

Buell, J.R.; Soliman, H.M.; Sims, G.E. *Two-Phase Pressure Drop and Phase Distribution at a Horizontal Tee Junction*. Int. J. Multiphase Flow, Vol. 20, No. 5, pp. 819-836. 1994.

Çabuk, H.; Modi, V. *On the Design of Optimum Flow Manifolds for Heat Exchangers*. National Heat Transfer Conference. HTD-Vol. 108, Heat Transfer Equipment Fundamentals, Design, Applications and Operating Problems. pp 161-167. 1989.

Casagrande, I. *Researches on Adiabatic Two-Phase Flow*. Energia Nucleare. Vol. 19 p. 148. 1962.

Chan, K.C.; Yadigaroglu, G. *Two-Phase Flow Stability of Steam Generators*. Two-Phase Flow Dynamics. Japan-US Seminar. Ed. by Arthur Bergles and Seikan Ishigai. pp. 365-377. 1979.

Charron, Y.; Whalley, P.B. *Gas-Liquid Annular Flow at a Vertical Tee Junction—Part I. Flow Separation*. Int. J. Mult. Flow, Vol.. 21, No. 4, pp. 569-589. 1995.

Collier, J.G. *Introduction to Two-Phase Flow and Heat Transfer Phenomena*. Proc. NATO Adv. Study Inst. Ed. By S. Kakaç & F. Mayinger. pp. 3-10. 1976a.

Collier, J.G. *Single-Phase and Two-Phase Flow Behavior in Primary Circuit Components.* Two-Phase Flows and Heat Transfer. Proc. NATO Adv. Study Inst. Ed. By S. Kakaç & F. Mayinger. pp. 313-355. 1976b.

Costa, J. *Two-Phase Flow Problems in Liquid-Metal Fast-Breeder Reactors*. Thermohydraulics of Two-Phase Systems for Industrial Design and Nuclear Engineering. Ed. by J.M. Delhaye, M. Giot, & M.L. Riethmuller. pp. 11-35. 1981.

Chen, L.; Li, Y.. *A Numerical Method for Two-Phase Flows With an Interface*. Environmental Modeling & Software 13. pp. 247-255. 1998.

Chisholm, D.; Wanniarachchi. *Maldistribution in Single-Pass Mixedh-Channel Plate Heat Exchangers.* HTD-Vol.. 201, Compact Heat Exchangers for Power and Process Industries. ASME. pp. 95-99. 1992.

Chisholm, D. *Two-Phase Flow in Pipelines and Heat Exchangers*. pp. 1-299. 1983.

Cook, M.; Behnia, M. *Pressure Drop Calculation and Modeling of Inclined Intermittent Gas-Liquid Flow*. Chemical Engineering Science. Vol. 55. pp. 4699-4708. 2000.

Costigan, G.; Whalley, P.B. *Slug Flow Regime Identification From Dynamic Void Fraction Measurements in Vertical Air-Water Flows.* Int. J. of Multiphase Flow. Vol. 23, No. 2. pp. 263-282. 1997.

Delhaye, J.M. *Two-Phase Flow Modeling*. Thermohydraulics of Two-Phase Systems for Industrial Design and Nuclear Engineering. Ed. by J.M. Delhaye, M. Giot, & M.L. Riethmuller. pp. 187-202. 1981.

Delhaye, J.M. *Some Issues Related to the Modeling of Interfacial Areas in Gas-Liquid Flows: The Conceptual Issues.* C. R. Acad. Sci. Paris, t. 329, Série II b. pp. 397–410. 2001.

Faille, I.; Heintze, E. *A Rough Finite Volume Scheme for Modeling Two-Phase Flow in a Pipeline*. Computers and Fluids. Vol. 28. pp. 213-241. 1999.

Fei, P; Cantrak, DJ.; Hrnjak, P. *Refrigerant Distribution in the Inlet Manifold of Plate Evaporators*. ACRC of the University of Illinois. SAE 2002 World Congress. pp.1-6. March 2002.

Fore, L.B.; S.G. Beus, R.C. Bauer. *Interfacial friction in Gas-Liquid annular Flow: Analogies to Full and Transition Roughness*. International Journal of Multiphase Flow. Vol. 26. 1755-1769. 2000.

Fouda, A.E. & Rhodes, E. *Two-Phase Annular Flow Stream Division in a Simple Tee.* Trans. Inst. Chem. Engrs. Vol. 52. pp. 354-360. 1974.

Friedel, L. *Momentum Exchange and Pressure Drop in Two-Phase Flow.* Proc. NATO Adv. Study Inst. Ed. By S. Kakaç & F. Mayinger. pp. 239-312. 1976.

Gardel, A. *Pressure Drops in Flows Through T-Shaped Fittings.* Bull. Techn. Suisse Rom. 83, 9 pp. 123-130 & 10, pp 143-148. 1957.

Giot, M. *Singular Pressure Drops*. Thermohydraulics of Two-Phase Systems for Industrial Design and Nuclear Engineering. Ed. by J.M. Delhaye, M. Giot, & M.L. Riethmuller. pp. 247-254. 1981.

Hsia, D.; Griffith, P. *Steam Generator Flow Instability Modeling*. Dept. of Mech. Eng., Massachusetts Institute of Technology. NUREG/CR-1712. U.S. Nuclear Regulatory Commission. pp. 1-134. 1980.

Hsu, Y.Y. *Two-Phase Flow Problems in Pressurized-Water Reactors*. Thermohydraulics of Two-Phase Systems for Industrial Design and Nuclear Engineering. Ed. by J.M. Delhaye, M. Giot, & M.L. Riethmuller. pp. 247-254. 1981a.

Hsu, Y.Y. *Codes and Two-Phase Flow Heat Transfer Calculations.* Thermohydraulics of Two-Phase Systems for Industrial Design and Nuclear Engineering. Ed. by J.M. Delhaye, M. Giot, & M.L. Riethmuller. pp. 453-477. 1981b.

Hassan, I.G.; Soliman, H.M.; Sims, G.E.; Kowalski, J.E. *Discharge from a Smooth Stratified Two-Phase Region Through Two Horizontal Side Branches Located in the Same Vertical Plane*. Int. J. of Multiphase Flow. Vol. 22, No. 6, pp. 1123-1142. 1996.

Hazi, G.; Imre, A.; Mayer, G.; Farkas, I. *Lattice Boltzmann Methods for Two-Phase Flow Modeling*. Annals of Nuclear Energy. Vol. 29. pp 1421-1453. 2002.

Heggs, Peter J., Scheidat, H.J. *Thermal Performance of Plate Heat Exchangers with Flow Maldistribution*. HTD-Vol. 201, Compact Heat Exchangers for Power and Process Industries, ASME. 1992.

Hewitt, G.F. *Simple Momentum and Energy Balances and Their Related Empirical Correlations.* Two-Phase Flows and Heat Transfer with Application to Nuclear Reactor Design Problems. Ed. by J. Ginoux. pp. 17-33. 1978.

Hwang, S.T.; Soliman, H.M.; Lahey, R.T. *Phase Separation in Dividing Two-Phase Flows*. Int. J. Mult. Flow, Vol. 14, No. 4. pp. 439-458. 1988.

Hwang, S.T. & Lahey, R.T. *A Study on Single- and Two-Phase Pressure Drop in Branching Conduits*. Exp. Thermal Fluid Sci. Vol. 1. pp 111-125. 1988.

Inayatullah, G.; Nicoll,W.B. *Application of the Drift-Flux Formulation to the Prediction of Steady, Periodic and Transient Two-Phase Flows.* Proc. NATO Adv. Study Inst. Ed. By S. Kakaç & F. Mayinger. pp. 209-237. 1976.

Ishii, M. *Drift Flux Model and Derivation of Kinematic Constitutive Laws.* Two-Phase Flows and Heat Transfer. Proc. NATO Adv. Study Inst. Ed. By S. Kakaç & F. Mayinger. pp. 187-208. 1976.

Iskandrani, A.; Kojasoy, G. *Local Void Fraction and Velocity Field Description in Horizontal Bubbly Flow*. Nuclear Engineering and Design. Vol. 204. pp. 117-128. 2001.

Kim, S; Ishii, M; Wu, Q; McCreary, D.; Beus, S.G. *Interfacial Structures of Confined Air-Water Two-Phase Bubbly Flow*. Experimental Thermal and Fluid Science. pp. 1-12. 2002.

Kubo, T.; Ueda, T.. *On the Characteristics of Confluent Flow of Gas-Liquid Mixtures in Manifolds.* Bulletin of the JSME. Vol.. 16, No. 99. pp. 1376-1384. Sept. 1973.

Kuo, T.C.; Pan, C.; Chieng, C.C; Yang, A.S. *Eulerian-Lagrangian Computations on Phase Distribution of Two-Phase Bubbly Flows*. Int'l Journal for Numerical Methods in Fluids. Vol. 24. pp. 579-593. 1997.

Lahey, R.T. *Current Understanding of Phase Separation Mechanisms in Branching Conduits. Nuclear Engineering and Design*. Vol. 95 pp. 145-161. 1986.

Lahey, R.T.; Drew, D. *The Analysis of Two-Phase Flow And Heat Transfer Using A Multidimensional, Four Field, Two-Fluid Model*. Nuc. Eng. And Design. Vol. 204. pp. 29-44. 2001.

Lahey, R.T. *Transient Analysis of Two-Phase Systems*. Two-Phase Flow Dynamics. Japan-US Seminar. Ed. by Arthur Bergles and Seikan Ishigai. pp. 165-184. 1979.

Lahey, R.T.; Moody, F.J. *The Thermal-Hydraulics of a Boiling Water Nuclear Reactor*. ANS Monograph. 1977.

Lalot, S.; Florent, P.; Lang, S.K.; Bergles, A.E. *Flow Maldistribution in Heat Exchangers*. Applied Thermal Engineering. Vol. 19. pp. 847-863. 1999.

Laurinat et al. *Pressure Drop And Film Height Measurements For Annular Gas-Liquid Flows*. Int. J. Multi. Flow. Vol.10. pp. 341-356. 1984.

Line, A.; Lopez, D. Two-Fluid Model of Wavy Separated Two-Phase Flow. Int. J. Multiphase Flow. Vol. 23, No. 6. pp. 1131-1146. 1997.

Lockhart, R.W.; Martinelli, R.C. *Proposed Correlation of Data for Isothermal Two-Phase Two-Component Flow in Pipes*. Chem. Eng. Prog. Vol 45, no. 1. pp. 39-48 January 1949.

Lun, I; Calay, R.K.; Holdo, A.E. *Modeling Two-Phase Flows Using CFD.* Applied Energy. Vol. 53. pp. 299-314. 1996.

Martinelli R. C.; Nelson D. B. *Prediction of Pressure Drop During Forced Circulation Boiling of Water*. Transactions of the ASME. Vol. 70. pp. 695-701. 1948.

Mayinger, F. *Emergency Core Cooling—Blowdown*. Two-Phase Flows and Heat Transfer with Application to Nuclear Reactor Design Problems. Ed. by J. Ginoux. pp. 411-432. 1978.

Meknassi, F.; Benkirane, R.; Line, A.; Masbernat, L. *Numerical Modeling of Wavy Stratified Two-Phase Flow in Pipes.* Chemical Engineering Science. Vol. 55. pp. 4681-4697. 2000.

Mochan, S.I. *Local Resistances in the Flow of Two-Phase Mixtures*. Problems of Heat Transfer and Hydraulics of Two-Phase Media, A Symposium. pp. 327-384. 1969.

Mudde, R.F.; Groen, J.S.; Van Den Akker, H.E.A. *Two-Phase Flow Redistribution Phenomena in a Large T-Junction*. Int. J. Mult. Flow. Vol. 19, No. 4. pp. 563-573. 1993.

Peng, F.; Shoukri, M.; Chan, A.M.C. *Effect of Branch Orientation On Annular Two-Phase Flow In T-Junctions*. Journal of Fluids Engineering. Vol. 118. pp. 166-171. March 1996.

Peng, F.; Shoukri, M. *Modeling of Phase Redistribution of Horizontal Annular Flow Divided In T-Junctions.* Can. J. of Chem. Eng. Vol. 75. pp 264-271. February 1997.

Penmatcha, V.R.; Ashton, P.J.; Shoham, O.; *Two-Phase Stratified Flow Splitting at a T-Junction with an Inclined Branch Arm*. Int. J. of Multiphase Flow. Vol. 22, No. 6. pp. 1105-1122. 1996.

Pokharna, H; Mori, M.; Ransom, V.H. *The Particle Fluid Model and Using Lagrangian Representation in Two-Phase Modeling.* Nuclear Engineering and Design. Vol. 175. pp. 59-69. 1997.

Ranade, V. *Computational Flow Modeling for Chemical Reactor Engineering*. Academic Press. pp. 1-452. 2002.

Reed, W.H.; Stewart, H.B. THERMIT: *A Computer Program for Three-Dimensional Thermal-Hydraulic Analysis of Light Water Reactor Cores.* MIT Report. Prepared for EPRI. 1978.

Reimann; Kahn. Flow *Through a Small Break at the Bottom of a Large Pipe with Stratified Flow*. Nucl. Sci. Eng. Vol. 88. pp. 297-310. 1984.

Reimann, J.; Seeger, W. *Two-Phase Flow In a T-Junction with Horizontal Inlet. Part II: Pressure Differences*. Int. J. Multiphase Flow. Vol. 12, No. 4. pp. 587-608. 1986.

Roberts, P.A.; Azzopardi, B.J.; Hibberd, S. *The Split of Horizontal Semi-Annular Flow at a Large Diameter T-junction*. Int. J. Multiphase Flow. Vol. 21, No. 3. pp. 455-466. 1995.

Rong, X.; Kawaji, M.; Burgers, J.G. *Two-Phase Flow Distribution in a Stacked Plate Heat Exchanger*. FED-Vol. 225, Gas Liquid Flows. pp. 115-122. 1995.

Saba, N.; Lahey, R.T. *The Analysis of Phase Separation Phenomena in Branching Conduits*. Int. J. Multiphase Flow. Vol. 10, No. 1. pp. 1-20. 1984.

Rouhani, Z. *Steady-State Void Fraction and Pressure Drop in Water-Cooled Reactors*. Two-Phase Flows and Heat Transfer with Application to Nuclear Reactor Design Problems. Ed. by J. Ginoux. pp. 241-273. 1978.

Sakaguchi, T.; Akagawa, K.; Hamaguchi, H.; Ashiwake, N.; Imoto, M. *Dynamic Behavior of Flow Characteristics in the Stratified Flow Regime*. Two-Phase Flow Dynamics. Japan-US Seminar. Ed. by Arthur Bergles and Seikan Ishigai. pp. 119-144. 1979.

Samson, E.B.; Stark, J. A.; Grote, M. G. *Two-phase Flow Manifold Tests*. Publication of McDonnell Douglas Astronautics Co. #871440. ASME. pp. 6.484-6.500. 1988.

Seeger W.; Reimann J ; Muller, U. *Two-Phase Flow In a T-Junction with a Horizontal Inlet*. *Part I: Phase Separation*. Int. J. Multiphase Flow. Vol.12, No. 4. pp. 575-585. 1986.

Shannak, B.B.; Friedel, L.; Alhusein, M. *Prediction of Single and Two-Phase Flow Contraction Through a Sharp-Edged Short Orifice*. Chem. Eng. Technol. Vol. 22. pp. 865-870. 1999.

Shedd, T.R.; Newell, T. *Characteristics of the Liquid Film in Horizontal Two-Phase Flow*. University of Illinois at Urbana-Champaign. ACRC TR-179. March 2001.

Shoham, O.; Brill, J.P.; Taitel, Y. *Two-Phase Flow Splitting in a Tee Junction—Experiment and Modeling*. Chem. Eng. Sci. Vol. 42, No. 11. pp 2667-2676. 1987.

Smoglie, C.; Reimann, J. *Two-Phase Flow Through Small Branches in a Horizontal Pipe with Stratified Flow*. Int. J. of Multiphase Flow. Vol. 12. No. 4. pp. 609-625. 1986.

Smoglie, C.; Reimann, J.; Muller, U. *Two-Phase Flow Through Small Breaks In A Horizontal Pipe With Stratified Flow*. Nucl. Eng. Des. Vol. 99. pp. 117-130. 1987.

Uygur-Onbasioglu, S. *Effect of Interfacial Drag Terms on Simulation of Two-phase Flow Distribution Through Narrow Channels*. Energy Convers. Mgmt. Vol. 39, No 8. pp 757-766. 1998.

Walters, L.C.; Soliman, H.M.; Sims, G.E. *Two-Phase Pressure Drop and Phase Distribution at Reduced Tee Junctions*. Int. J. Mult. Flow. Vol. 24. pp. 785-792. 1998.

Watanabe, M.; Katsuta, M.; Nagata, K. *Two-Phase Flow Distribution in Multi-Pass Tube Modeling Serpentine Type Evaporator*. ASME/JSME Thermal Engineering Conference: Vol. 2. ASME. pp 35-42. 1995.

Whalley, P.B.; Azzopardi, B.J. *Two-Phase Flow in a 'T' Junction*. AERE-R 9699. 1980.

Williams. *Entrainment Measurements in a 4-Inch Horizontal Pipe.* M.S. Thesis, University of Illinois. 1986.

Vist, S.; Pettersen, J. *Two-Phase Flow Distribution in Compact Heat Exchanger Manifolds.* Preliminary for Review. Glenoble Symposium. pp. 1-12. August 2002.

Yong, Q.; Zhilin, Y.; Jijun, X. *Experimental Study of Phase Separation in Dividing Two-phase Flow*. HTD-Vol. 334, Proceedings of the ASME Heat Transfer Division. Vol. 3. ASME. pp. 179-185. 1996.

Yoo, Tae. *An Experimental Investigation of Two-Phase Flow Distribution in Microchannel Manifolds*. M.S. Thesis. University of Illinois at Urbana-Champaign. 2002.

Young, J.B. *The Fundamental Equations of Gas-Droplet Multiphase Flow*. Intl. J. Multiphase Flow, Vol. 21, No. 2. pp 175-191. 1995.

Zuber, N.; Findlay, J.A. *Average Volumetric Concentration in Two-Phase Flow Systems*. J. Heat Transfer. Vol. 87. p. 453. 1965.

Chapter 3. X-Ray Visualization and Pressure Drop in Microchannel Tubes

3.1 Introduction

Industry has expressed an interest in the application of microchannel tubes for heat exchanger devices. Microchannels have a number of attractive design features, most significantly in terms of geometry. They offer small frontal area for air-side pressure drop, and relatively large convection surface area for heat transfer. For an effective design, it is important to arrive at an understanding of pressure drop and heat transfer. It is well understood in the field of two-phase flow studies that these quantities are affected by the flow patterns which are created as the coolant travels the length of the tube.

There have been several attempts at simulating a microchannel for flow visualization by creating a machined microchannel in translucent material, since it is impossible to see flow patterns in aluminum tubes with the unaided eye or with external photography. However, this approach has some drawbacks. The simulated microchannel does not have the same surface characteristics as a true aluminum tube, most surface notably surface roughness and energy. Furthermore, such simulations are performed at idealized experimental conditions. Designers need a tool that can explain unexpected data trends as the results of working phenomena, not experimental error.

The focus of this study is to determine whether the method of X-ray visualization is tenable for the description of flow regimes and the impact of these flow regimes on pressure drop for an actual working aluminum microchannel. It is desirable to know whether such a method can reveal trends in the behavior of the microchannels that cannot be seen when only looking at experimental data itself. For instance, should a potential problem be noticed in the pressure drop data, it is desirable to know if a phenomenon is occurring inside of the microchannel which cannot be seen with the unaided eye, or whether a technical oversight occurred. It is also interesting to make data comparisons with the information gained from studies of simulated microchannels. Such information shows potential for significant impact on design and diagnostics of heat exchangers.

Aluminum microchannels of hydraulic diameter 1.54mm, cross sectional area of 16.69mm^2, length 60.9cm, and with six arrayed ports were employed. The experimental setup accommodated the use of air-water and R134a two-phase flows. Mass fluxes ranged from G=50 $\mathrm{kg/m^2 \cdot s}$ to 300 $\mathrm{kg/m^2 \cdot s}$ and qualities ranged from x=0 to 1. Six different orientations of the microchannel test section were studied. X-ray visualization was performed by a diagnostic X-ray machine with versatility to orient itself about multiple axes. The images were digitized and processed for viewing with computer software.

3.2 Literature Review

3.2.1 Visualization-Based Studies

Niño [2002a] conducted a comprehensive study of R134a microchannel visualization, and serves as the precedent for the current study. R134a passed through a simulated 6 port microchannel etched in clear PVC. The hydraulic diameter of the simulated microchannel is 1.58±0.06mm and the cross sectional area is 17±1.2 mm^2. A test matrix was constructed for a quality range covering x=0 to 1 with mass fluxes of G=50 $\mathrm{kg/m^2 \cdot s}$ to 300 $\mathrm{kg/m^2 \cdot s}$. A digital camera and high frequency strobe light were used to capture detailed images. Due to differences in flow regimes among each of the channels, conventional two-phase flow maps could not be

formulated; rather, two-phase regime description was provided by the development of probability functions for the time that flow exists in a certain regime.

These probabilistic functions are defined as the number of observations of a particular flow regime divided by the total number of observations at for a particular flow condition. The studied flow regimes are liquid flow, stratified flow, intermittent flow, annular flow, dispersed flow, and vapor flow. These functions are dependent upon the quality, mass flux, tube diameter, and fluid properties.

Stratified, dispersed, or annular mist flow patterns were not found in the ranges of experimental conditions provided. Niño [2002a] found that refrigerant flow is evenly distributed for high mass flux and quality conditions when annular flow is dominant. A method is also presented for the formulation of a pressure drop model which incorporates these probabilistic functions and flow regime-specific pressure drop correlations.

Coleman & Garimella [2002] further assert that flow visualization is an aid in the characterization of heat transfer predictions and pressure drop in the design of heat exchangers. They studied R134a two-phase flow in round (D_h=4.91mm), square (D_h=4mm), and rectangular (D_h=4.8mm and 2.67mm) tubes. A test matrix was constructed for G=150 $kg/m^2 \cdot s$ to 750 $kg/m^2 \cdot s$, over the full range of quality. Typical flow maps were constructed using mass flux vs. quality coordinates. Four primary regimes were noticed: intermittent, wavy, annular, and dispersed. The authors provide excellent descriptions which are summarized here:

ANNULAR—Core of vapor with sparse drops, liquid along the pipe wall. Within Annular are Mist, Annular Ring, Wave Ring, Wave Packet, and Annular Film.

WAVY—In its own category apart from annular, waves caused by shears at the interface of the phases at differing velocities. Waves vary in intensity and properties, leading to discrete and disperse waves.

INTERMITTENT—Slug and plug flow

a. Slug Flow—vapor slugs followed by trail of bubbles in the liquid, large waves are present as well
b. Plug—vapor slugs along, without trailing bubbles, annular film of liquid around the pipe wall

DISPERSED—Liquid flow is turbulent, gas is either laminar or turbulent

a. Laminar—bubbles form in top of pipe, due to buoyancy. This is called bubble flow pattern.
b. As gas velocity increases, bubbles decrease and disperse across pipes. This is called dispersed flow pattern

See Figure 3.1 for sample images. Coleman & Garimella [2002] also used air-water as a precursor toward the understanding of refrigerant two-phase flows. Traditional round tube correlations were found to be deficient for these specialized rectangular tubes to predict pressure drop and heat transfer. The authors propose that previous two-phase maps may not be applicable for these specialized, small, non-circular geometries.

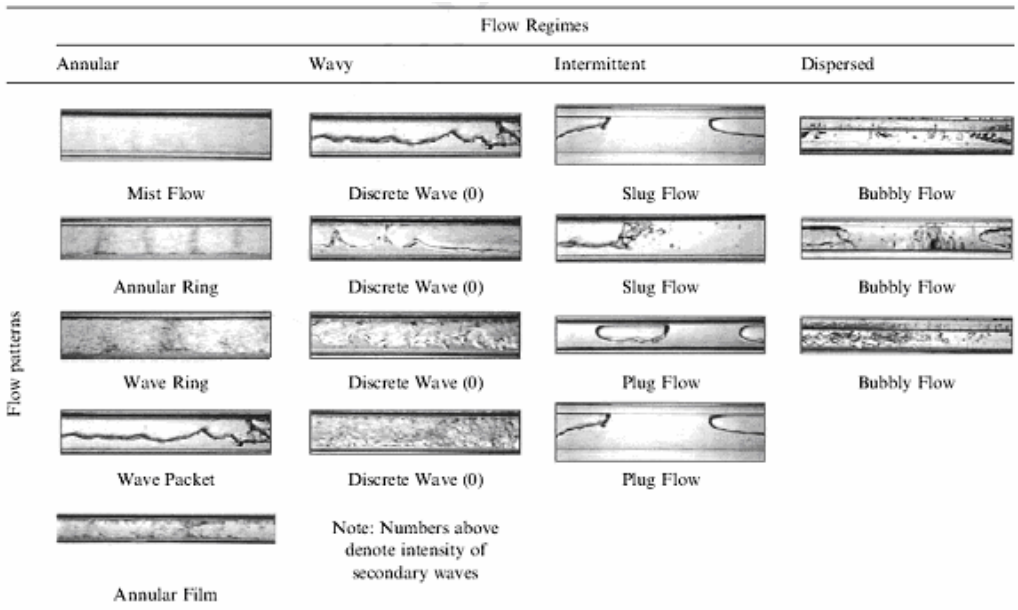

Figure 3.1: Flow Regimes (Coleman & Garimella [2002])

Coleman & Garimella [2002] also considered the effects of tube geometry, such as the aspect ratio (ratio of tube height to tube width) and diameter. When comparing different tube geometries, the authors found the following:

a. The intermittent region is larger for the round tube than square tube at low mass fluxes. The wavy flow region is also larger.
b. Rectangular tubes can sustain annular flow better.
c. Discrete waves are more prevalent for round tubes.
d. Due to surface tension, annular films are more prevalent for lower hydraulic diameters.

Coleman & Garimella [1999] also studied air-water mixtures flowing in small round and rectangular channels (D_h=1.3 to 5.5mm), citing that rectangular microchannel tubes are used in single phase radiators and two-phase condensers/evaporators. High-speed videography and flow maps were used to characterize flow regimes, which are established by the interaction of gravity, shear, and surface tension. The main patterns are bubble, dispersed, elongated bubble, slug, stratified, wavy, annular-wavy, and annular. The authors note that a tube with sharp rectangular corners allows liquid to be held more readily by the walls, allowing for plug, slug, and annular to be maintained at higher superficial velocities. The flow regime classification is similar to Coleman & Garimella [2002], but stratified is included:

STRATIFIED—complete phase separation; when waves occur, stratified wavy and smooth

Coleman & Garimella [2000] studied the condensation of R134a in a small round tube of 4.91mm diameter. The mass fluxes ranged from G=150 $\mathrm{kg/m^2 \cdot s}$ to 750 $\mathrm{kg/m^2 \cdot s}$ and quality from 0 to 100%. Slug and plug occurred for low qualities. The majority of the data lay in the wavy regime, with transitions between discrete and disperse waves with varying experimental conditions. Annular flow resulted for high flux and quality. The mechanism by which flow patterns are established is condensation inside the tubes as the fluid changes phase

along the tube length. The authors aim to address the issue of the effect of tube hydraulic diameter and shape on pressure drop and heat transfer during condensation.

The test section used by Coleman & Garimella [2000] was transparent. Flow regime maps were constructed using mass flux vs. quality. It is asserted that such flow maps and transition lines can be used to predict flow patterns for given conditions. When comparing with air-water data from Coleman & Garimella [1999], it was found that only a fraction of air water data and refrigerant data can be compared, due to the differences in fluid properties (i.e. density of liquid to gas). Differences in this ratio lead to higher air velocities as compared to refrigerant vapor velocities. Coleman & Garimella [2000] found that no air-water data are above the disperse-discrete wave line of transition, since high mass flux and quality are difficult to establish in air-water. Both working fluids occupy the same region of low quality in the intermittent flow regime. The wavy-annular transition for air-water is relative to the refrigerant discrete wave/slug-plug flow regime. The air-water annular flow data lay in the range of refrigerant discrete wave flow. Overall, transitions for refrigerant occur at lower gas and liquid velocities than air-water data. The authors provide a treatment of the Bond and Froude numbers as discussed previously [2002].

Damianides & Westwater [1988] performed extensive studies of two-phase flow patterns in a compact heat exchanger (channel D_h=1.74mm) and in a series of small diameter tubes from D_h=1 to 5mm. The working fluid was air-water. Through the creation of flow maps for the heat exchanger and for straight, round tubes of comparable diameter, it was desired to see if two-phase flow in a working exchanger can be predicted from conventional tube maps.

The test section used by Damianides & Westwater [1988] was transparent, horizontal, adiabatic, and close to atmospheric conditions. Flow regimes were determined by visual inspection and high-speed photography. A novel method was the use of fast-response pressure transducers which gauge the pressure difference when a fluid disturbance (e.g. fluid slug or dispersed, random flow) is created. The resulting pressure traces indicated the flow regimes.

When examining straight round tubes, Damianides & Westwater [1988] note the following general trends. With an increase in liquid flow, tubes of greater diameter require more fluid flow to transition from intermittent to dispersed. With increasing gas flow, tubes of lesser diameter need more gas flow to change from intermittent to annular. As the tube diameter decreases, the stratified regime begins to disappear and vanishes altogether for the 1mm tube.

Using impedance probes to measure the traces of void fraction and their probability distributions, Costigan & Whalley [1997] defined six regimes: discrete bubble flow, “spherical cap bubble flow”, slug flow (stable), slug flow (unstable), churn flow, annular flow. The chief concern of this work is to define the slug to churn flow transition point. The following flow regime descriptions were formulated:

1. Discrete bubble flow—small bubbles are relatively uniformly distributed without congealing. Void fraction always below 0.45
2. Spherical cap bubble flow—essentially a transition between bubbly and slug flow with void fraction characteristics which are distinct from either region. Irregular void fraction peaks between 0.4 and 0.8

3. Slug flow (stable)—slugs of liquid with air, separated by bubbles, low void fraction at the slug front, which increases along the length of the slug, maximum void fractions of 0.35-0.45 for liquid slugs, separated by Taylor bubbles with fractions of 0.8 and higher
4. Slug flow (unstable)—higher liquid velocities, slug flow (fractions of 0.4 and higher) with higher bubble void fractions of around 0.8, some but not all of the slug formation has degenerated, for higher gas flows the slugs break down and this leads to churn flow
5. Churn flow—no low void fraction slugs, bubble/annular void fractions below 0.8, essentially annular, waves carried up the side of the tube by the gas flow, void fraction above 0.8 which means about annular, erratic film thicknesses
6. Annular flow—a wavy fluid on the channel surface flowing regularly, all void fractions usually above 0.9.
7. For constant liquid flow and increasing gas flow, bubble lengths increase and void fractions decrease, the slug lengths decrease and void fractions increase.
8. For constant gas flow and increasing liquid flow, bubble lengths decrease and void fractions remain constant, slug lengths and fractions remain constant and the number of slugs and bubbles increases

Barnea & Luninski [1983] studied two-phase flows of air and water in round glass tubes with diameters of D_h=4, 6, 8, 15, 9.85, and 12.3mm. Both horizontal and vertical configurations were studied. Patterns and transition lines were determined by visual inspection and conductance probes. The authors found large discrepancies for the stratified/non-stratified transition line when comparing with flow maps of larger diameter tubes (Taitel & Dukler [1976]); most of the other data agreed well. The authors note that when the walls of small tubes are wetted, capillary forces causes intermittent flow by forming a “liquid bridge”.

Yang & Shieh [2001] studied flow patterns for R134a and air-water. The diameters are 1 to 3mm and mass flux varied between G=300 $\mathrm{kg/m^2 \cdot s}$ to 1600 $\mathrm{kg/m^2 \cdot s}$. A prime factor in the determination of flow pattern is the surface tension force. With increasing surface tension force, bubbles maintain their spherical shape and the tube walls create liquid holdup. The surface tension of air-water is higher than that of R134a, thus causing the transition from intermittent to bubble. For a lower value of gas velocity for R134a, there is a shift in the slug to annular transition. The authors identify six regimes: bubble, slug, plug, wavy stratified, dispersed, annular. When the working fluid changes to R134a, there is a shift in the slug to annular transition to a lower value of gas velocity.

Fourar & Bories [1995] created narrow channels with an inlet two-phase flow of air and water (width on the order of 1 mm). Experiments were performed with gaps of 0.54, 0.4, and 0.18mm. The flow rates of fluid phases were varied to observe the different flow patterns. Pressure drop and liquid volume fraction were measured to arrive at a two-phase pressure gradient. The authors opt for a separated flow model by treating the phases as distinct to determine the phase friction factor and Reynolds number. The results are analyzed using the Lockhart & Martinelli [1949] model, homogeneous model, and general Darcy model.

Fourar & Bories [1995] investigated five regimes: bubble flow, fingering bubble flow (bubbles with split tips), complex flow (chaotic, no defined characteristics), annular flow (gas occupies most of fracture, for increasing flow rate), and droplet flow (films replaced by dispersed droplets). The authors characterized the flow regimes

according to liquid velocity vs. gas velocity, and pressure gradient versus gas superficial velocity. It was noted that increasing gas superficial velocity increases pressure drop.

Triplett et al. [1999a, 1999b] conducted air-water visualization in microchannels. The circular channels had diameters of 1.1 and 1.45mm; semi-triangular cross-section microchannels had hydraulic diameters of 1.09 and 1.49mm. The authors observed the bubbly, churn, slug, slug-annular, and annular patterns. The experiment used by Triplett et al. [1999a, 1999b] is a continuation of the simulation method of making test sections from materials such as Pyrex, acrylic, or polycarbonate. However, the authors do not mention how such simulated experiments would contrast with microchannels made of real working material such as metals. The authors cite relatively fair agreement when comparing with previous data; however, poor agreement was obtained when locating the data within the frame of previous flow map transition lines.

3.2.2 Work Focusing on Specific Flow Regimes

Wong & Yau [1997] attempted to codify the vast range of subjective and sometimes contradictory flow pattern classifications into a standard system. Drawing upon the work of previous researchers, the authors arrived at a set of sixteen flow patterns. Yet, such a process has led to such names as “roll-wave-droplet-annular” and “pseudo-slug-thin-annular” which render such terms quite awkward for visualization studies.

Cook & Behnia [2000] studied intermittent flow, which has large bubbles traversing over a liquid film with liquid slugs separating it. The authors aimed to identify and predict pressure drop in intermittent flows. Pressure gradients in air-water two-phase horizontal and inclined pipes were measured. Horizontal air-water test sections of length 16m and 32, 50mm ID were used. See Figure 2.5 for an illustration of intermittent flow.

Joseph & Bannwart [1996] studied the stability of annular flow and its transition to other regimes using air-water. The mechanism of slug formation is the creation of nonlinear waves by a high stagnation pressure at the front of a wave on the liquid which the gas passes over. This is illustrated in Figure 3.2.

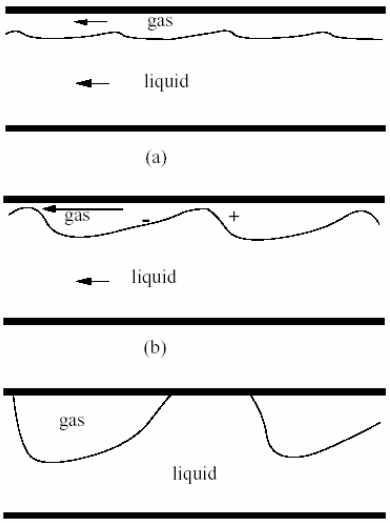

Figure 3.2: Wave Formation from Stratified Flow (Joseph & Bannwart [1996])

Thus, high stagnation pressure precedes a wave which is initially small. In annular gas-liquid flows, undercutting and droplet “shatter” may exist as in Figure 3.3; the proposition of a preceding high stagnation pressure region would explain this as well.

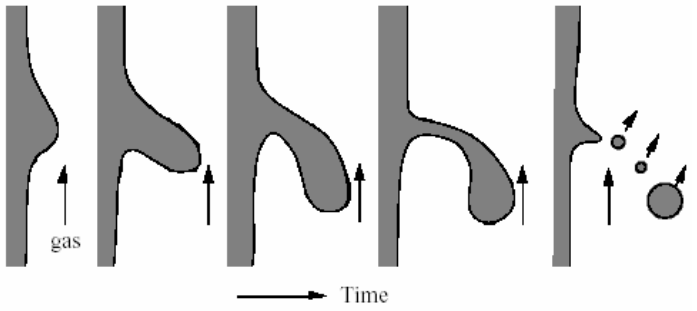

Figure 3.3: Droplet Shatter in Annular Flow (Joseph & Bannwart [1996])

Lun et al. [1996] studied two-phase flow and defined the following:

a) Bubble Flow—High liquid velocity bubbles

b) Plug Flow—Bullet-nosed bubbles

c) Stratified—Liquid on bottom, gas on top

d) Wavy—Increasing gas velocity, stratified turns into waves

e) Slug—Waves touch pipe top due to increased gas velocities

f) Annular—Very high gas flow, slugs penetrated by core of gas

See Figure 3.4 for graphical illustrations of these.

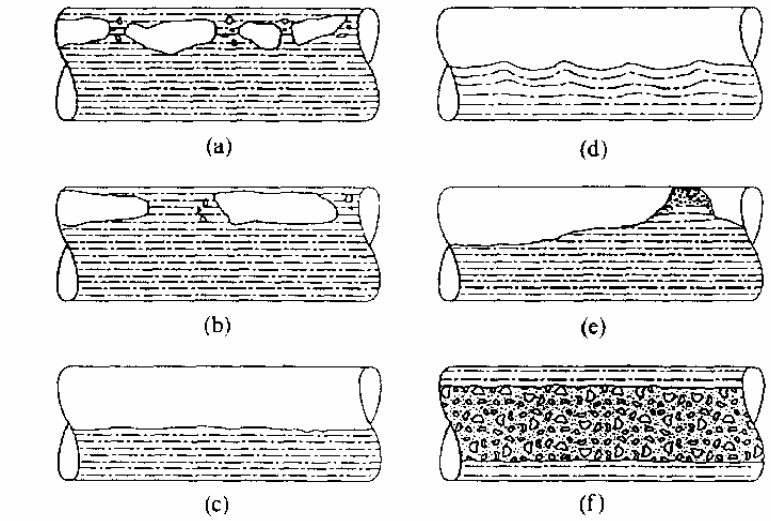

Figure 3.4: Flow Regime Examples (Lun et al. [1996])

Ghiaasiaan & Abdel-Khalik [2001] provide a comprehensive review of experimentation in microchannel tubes for which the hydraulic diameter lay between 0.1 to 1mm and with high ratios of fluid inertia to surface tension. Applications cited include fusion reactor coolers and miniature heat exchangers. Flow regime study is crucial to the understanding of pressure drop, heat transfer, and stability of flow.

3.2.3 Two-Phase Factors: Pressure Drop, Void Fraction

Niño [2001] conducted an in-depth study of microchannel two-phase pressure drop. The microchannels consisted of 6 and 14 ports with D_h=1.54mm and 1.02mm, respectively. The working fluids were R134a, R410a, nitrogen, and air-water. The microchannel tube length was varied. The author also studied the entrance and exit pressure losses to determine their influence on the flow behavior. Refrigerant single and two-phase pressure drop data were also obtained.

Pressure drop data is obtained for a horizontal adiabatic microchannel. The pressure drop data is comprised of the frictional pressure drop in addition to exit/entrance pressure drops caused by area changes created by the transition pieces. When the transition pressure drops were made dominant by decreasing the length of the microchannel (7.62cm), the transition pressure drops were under-predicted by literature correlations. The same behavior was found among all working fluids. When comparing single phase pressure drops with the Churchill friction correlation, good agreement was found throughout the laminar and turbulent region, but the laminar-to-turbulent transition occurred sooner than in the literature.

Niño [2002b] performed an extensive investigation of void fraction (defined as the ratio of the area of the vapor to the total area of the channel) in 6-port and 14-port microchannel tubes with D_h=1.54mm and 1.02mm, respectively. The working fluids are R134a and R410a, and the experimental conditions span a full range of qualities for G=100 $\mathrm{kg/m^2 \cdot s}$ to 300 $\mathrm{kg/m^2 \cdot s}$. Void fraction was found to depend upon mass flux and diameter.

The approach of the determination of void fraction is novel: once the two-phase conditions are set, pneumatic crimpers are used to crimp the microchannel at both ends and it is then weighed in order to determine the charge of trapped refrigerant. Low void fractions occur for intermittent flow; high void fractions occur for annular flow. As the diameter decreases, the void fraction decreases. In general, void fractions are lower for R410a than for R134a for the same conditions. Qualitative information was gained through the use of visualization employing a simulated microchannel.

Triplett et al. [1999b], referring to Triplett et al. [1999a], measured void fraction and pressure drop for horizontal round tube diameters of D_h=1.1 and 1.45mm, along with semi-triangle channels with hydraulic diameters of D_h=1.09 and 1.49mm. Void fraction was estimated and assumed from analysis of photographs. The authors note a systematic overprediction of void fraction in annular flow from literature correlations, which indicates that microchannels have lower interphase slip when compared with large channels; thus, interfacial friction phenomenon are significantly different between large and microchannels. Void fraction and pressure drop were best predicted using the homogeneous mixture assumption. Tandon et al. [1985] developed an analytical void fraction model for annular two-phase flows.

Yang & Webb [1995a, 1995b] used plain and 0.2mm micro-finned 4 port aluminum tubes with D_h= 2.64 and 1.56mm. They are measuring single phase and two-phase pressure drop for R12. For increases in flux and quality in two-phase flow, the pressure gradient increases; for each condition the pressure drop of the finned microchannels, in one case about 2.2 times higher. The authors used a microchannel tube 560mm long, horizontal, and adiabatic. They account for sudden contraction and expansion pressure drops at the entrances/exits.

Yang & Webb [1995a, 1995b] found that the friction factors are 14% and 36% higher for the plain and micro-finned tubes as that predicted by the Blasius equation. To get an idea of the importance of correct diameter determination, the authors cite that a 15.7% uncertainty in friction factor for a given condition if the maximum tolerance of 0.05mm was examined.

Yao & Ghiaasiaan [1996] studied wall-liquid film friction in annular flow. The authors found that gross errors resulted when calculating the wall friction from traditional two-phase frictional pressure gradient correlations from empirical flow regime maps. Often, physically impossible hydrodynamic behavior was predicted. The authors used an adapted two fluid model of Wallis [1969] and better agreement was obtained.

3.3 Presentation of Experiments

3.3.1 Air Water System

3.3.1.1 Setup

The entire air-water system was built on-site at the Arçelik A.S. Research and Development Center in Istanbul, Turkey. An overall schematic is seen in Figure 3.5.

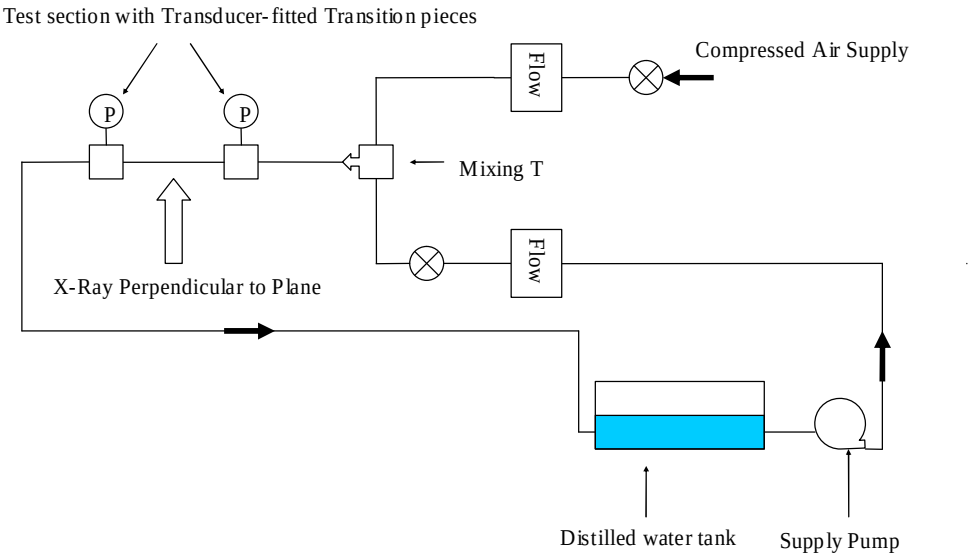

Figure 3.5: Air-Water System Schematic

Air is supplied from the central building supply, through an outlet in the X-ray room, and into a bank of three gas rotameters in a parallel array, each fitted with one-way selection valves. Each rotameter was calibrated individually using compressed nitrogen and a MicroMotion® mass flow rate meter with an accuracy of ±0.5%. The flow then travels to a needle valve to the mixing T-junction. The water is supplied from a circulation tank containing distilled water via a 50Hz pump, which supplies water at about 25°C into a liquid variable-area flow meter (±10% full scale accuracy, ±0.5% repeatability). The flow meter was calibrated with 65 data points and yielded a calibration curve with a coefficient of linearity of 0.9977. Water travels to a regulation needle valve. Both streams mix at a T-junction, then flow through a calming length of 42.0cm (44 tube diameters). All tubing is 9.525mm hard copper, fitted with 9.525mm nuts and copper welding.

After traversing the calming length and a one-way ball valve, the flow enters the first aluminum transition piece. The aluminum transition pieces are explained in detail by Payne & Niño [2000]. Each is fitted with an absolute pressure transducer. The flow then enters the microchannel test section. The microchannel has a hydraulic diameter of 1.54mm, a length of 60.9cm, and an overall cross-sectional area of 16.69±0.8% mm^2. The two-phase flow then enters the second aluminum transition piece, which is also fitted with an absolute pressure transducer. The two-phase flow exits into reinforced flexible tubing and then enters the circulation tank. Thus, a continuous air-water flow loop is established.

Pressure measurements are made using two pressure transducers (0-1000KPa absolute). A DMM was used to measure the output voltage signal from a 4 channel serial bus card. The pressure transducers were powered by a DC power supply (nominal 28V, max 40V) and were calibrated using compressed nitrogen and a standard precision laboratory pressure gage (0.1 F.S. accuracy). Each transducer was calibrated with data points taken along the full range, from 0 to 621kPa at 1.4kPa increments, and repeated four times. Calibration curves were obtained with coefficient of linearity of at least 0.9999. Power for all equipment was supplied by standard European 220V outlets.

The X-ray machine is the Microfocus FSX, Model FXT 160.51, manufactured by FeinFocus ®. The maximum operating conditions are 160kV and 1mA. It has the capacity to translate a moving platform longitudinally as well as rotate the platform about its vertical rotational axis. The X-ray emitter and collector lie along the same axis on a U-shaped arm. The X-ray collector and emitter may also elevate vertically upward and downward. This arm has the ability to rotate to a maximum of 45° in order to view samples along a 45° plane. See Figures 3.6-3.8 for views of the X-ray system with enclosed experimental setup.

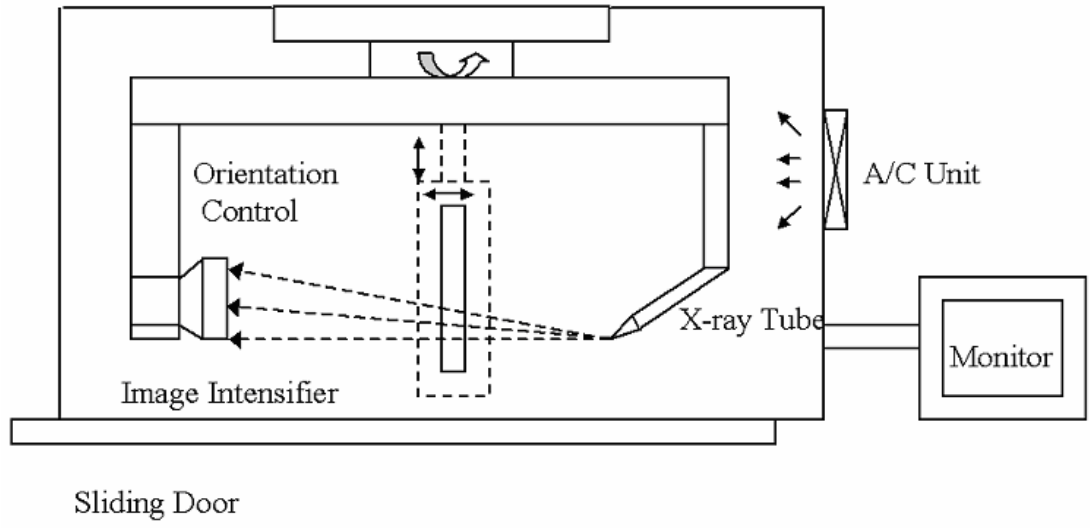

Figure 3.6: View from Above X-Ray Room

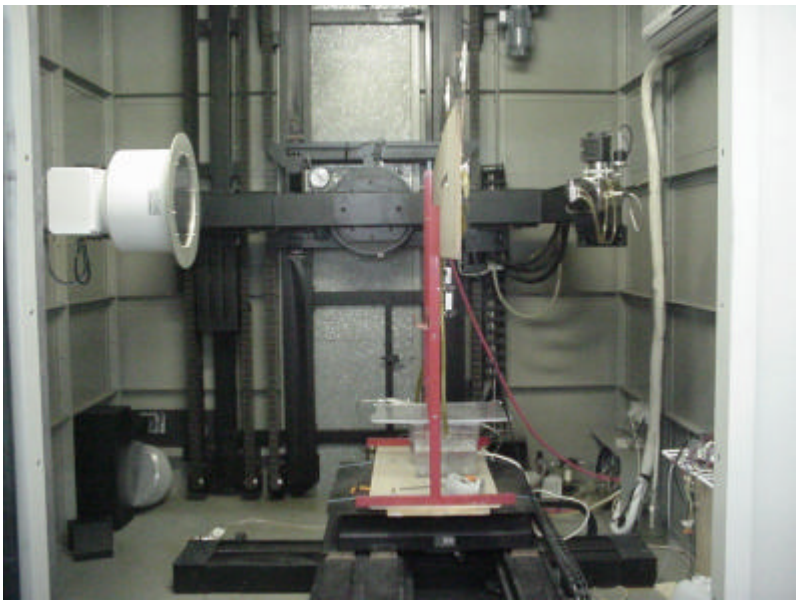

Figure 3.7: X-Ray Setup, Air-Water, Side View

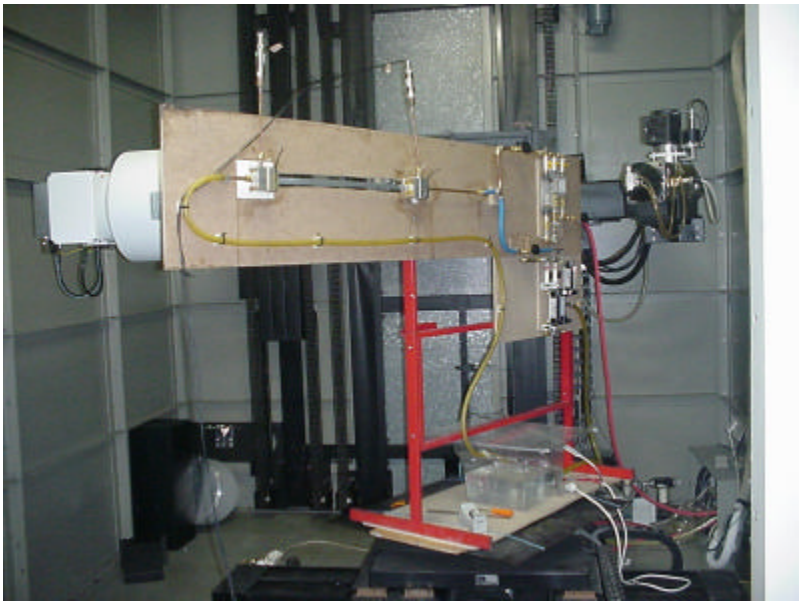

Figure 3.8: X-Ray Setup, Air-Water, Open View

Images are first captured by a resolution monitor in order for the operator to adjust resolution, focus, and manually change the position of the sample. This image is then output to a second television monitor, which is connected in series to another television monitor equipped with a video cassette recorder, as seen in Figure 3.9. This allows images to be recorded onto standard VHS cassettes, which are then digitally recorded to compact discs for processing by computer imaging software. The test system is encased in a vacuum-sealed room which is locked during operation to ensure radiological safety. Adjustments in voltage and current are made by the X-ray operator in order to achieve a clear image and ensure that the X-rays penetrate the sample under study. The system is fully computerized to monitor and tune the X-ray machine's performance.

Figure 3.9: X-Ray Acquisition Equipment

3.3.1.2 Methodology

The experimental parameters of interest are pressure drop and flow pattern identification. A variety of mass flux and quality conditions were formulated based upon the calibration curves, equipment capacity, and microchannel geometry. The conditions were established until steady state was achieved. At this stage, pressure drop data was obtained. The X-ray machine was then configured for optimum resolution, and real-time video was obtained using its acquisition system. The videos were then digitized to compact discs, and still images are capture using computer software. Figure 3.10 depicts the different microchannel configuration axes that are discussed in subsequent paragraphs.

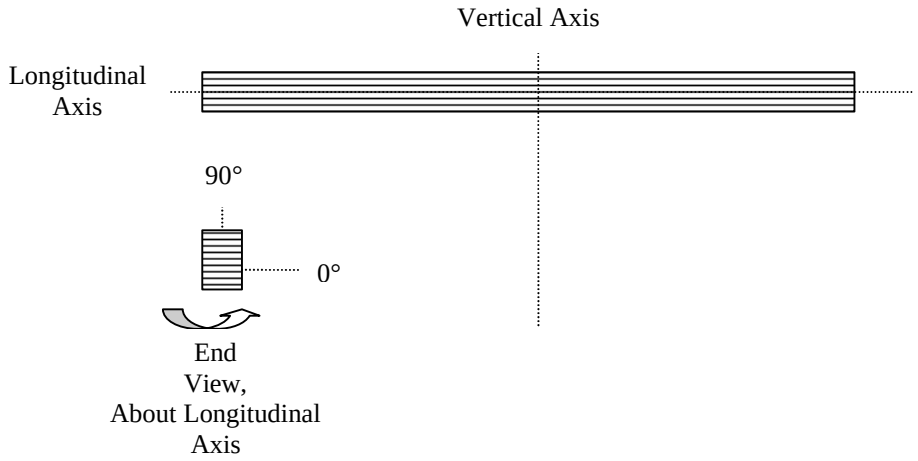

Figure 3.10: Axes of Microchannel Orientation

In the first experiment, the microchannel was aligned 90° from horizontal about its longitudinal axis and fitted with the aluminum transition pieces with pressure transducers. It was observed during experimentation that the aluminum transition pieces created inlet maldistribution of the established two-phase flow; however,

experimentation proceeded and a solution for this apparent dilemma was later obtained. After the completion of the first experiment, it was additionally observed that static plugs of fluid existed even when the air was at full release. The reason for this was that the first pump used in the building of the experiment contained a trace of ethylene glycol. All data was kept, however, as an interesting comparison to the behavior of a microchannel with no introduced coatings.

The microchannel was then replaced with a new, identical microchannel free of internal coatings. Additionally, an identical microchannel was fitted with smooth connection pieces that did not contain the same rectangular cavity as the first transition pieces. The two-phase flow was by-passed to either microchannel depending on whether flow visualization or pressure drop was desired. It was not possible to obtain pressure drop data with the smooth connection pieces.

It was hypothesized that the angular position (about the longitudinal axis) of the microchannel might create gravity effects at the inlet and cause the inlet flow to prefer the lower microchannel ports over the upper microchannel ports. To study these effects, the microchannel was configured in three different angular orientations about the microchannel's longitudinal axis: 0°, 45°, and 90°. Using the microchannel fitted with the pressure transducers, the pressure drops were obtained. Using the microchannel fitted with the smooth connection pieces, flow visualization was performed for the 90 and 45° cases, since the maximum rotation of the X-ray machine's arms is 45°. The solution for both the inlet maldistribution and the preferential gravity effects was to introduce a bend of gentle radius which brought the microchannel from 0 to 90°. Using this configuration, both pressure drop data and flow visualization were obtained using the same microchannel fitted with the aluminum transition pieces which possessed pressure transducers.

The following experimental conditions were for the microchannel aligned 90° from horizontal about its longitudinal axis, with a trace of ethylene glycol, as seen in Figure 3.11.

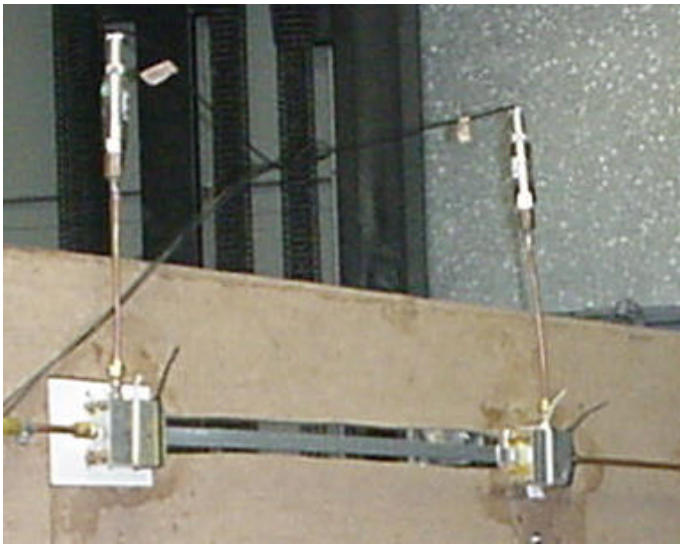

Figure 3.11: 90° Orientation.

The transducer-fitted aluminum transition pieces were employed during the collection of pressure drop data and X-ray visualization. Test conditions are seen in Table 3.1. *Note*: "COND X" refers to an arbitrary trial experimental condition.

Table 3.1: Air-Water Conditions for First 90° Orientation

Ethylene Glycol Trace, 90°, AL Transition Pieces				
	Quality			
Mass Flux	0.1	0.3	0.5	0.7
G=50	v	v	v	
G=100	v	v	v	v
G=150	v	v	v	COND X
G=200	v	v		
G=250	v			
G=300	v			

The microchannel was replaced with a clean microchannel free of inner coatings. Studies of visualization and pressure drop were made for three angular orientations about the microchannel's longitudinal axis: 0°, 45°, and 90°. For pressure drop collection, the aluminum transition pieces were fitted with transducers. For visualization, an identical microchannel was fitted with connection pieces with tapered geometry in order to attempt to eliminate maldistribution effects at the inlet. Note: for the 90° it was possible to achieve a quality of 0.5 for a flux of $200\,\mathrm{kg/m^2 \cdot s}$. The settings in Table 3.2 were used.

Table 3.2 Air-Water Conditions for 0, 45, and Second 90° Orientation

0, 45, 90° Roll, Smooth Connections				
	Quality			
Mass Flux	0.1	0.3	0.5	0.7
G=50	v	v	v	v
G=100	v	v	v	v
G=150	v	v	v	v
G=200	v	v		
G=250	v			

The microchannel was aligned 90° vertically down and fitted with pressure transducers to obtain pressure drop only. No visualization was performed. The experimental settings in Table 3.3 were employed.

Table 3.3: Air-Water Conditions for 90° Vertically Down Orientation

90° Vertically Down, AL Transition Pieces				
	Quality			
Mass Flux	0.1	0.3	0.5	0.7
G=50	v	v	v	v
G=100	v	v	v	
G=150	v	v		
G=200	v			
G=250	v			
G=300	v			

The experimental conditions for a 0 to 90° Twist (Figure 3.12) are in Table 3.4.

Figure 3.12: 0 to 90° Twist Orientation

The separate microchannel mentioned previously was not used for visualization, since the twist provided for more uniform inlet distribution. The aluminum transition pieces were employed during the collection of pressure drop data and X-ray visualization.

Table 3.4: Air-Water Conditions for 0 to 90° Twist Orientation

0 to 90° Twist, AL Fittings									
	Quality								
Mass Flux	0.02	0.04	0.06	0.1	0.15	0.2	0.3	0.5	0.7
G=50				v	v	v	v	v	
G=100	v	v	v	v			v	v	v
G=150	v	v	v	v			v	v	
G=200	v	v	v	v			v	v	
G=250	v	v	v	v			v		
G=300	v	v	v	v					

3.3.2 Refrigerant System

3.3.2.1 Setup

The air-water system was significantly modified to accommodate for the employment of R134a. A schematic of the system is seen in Figure 3.13.

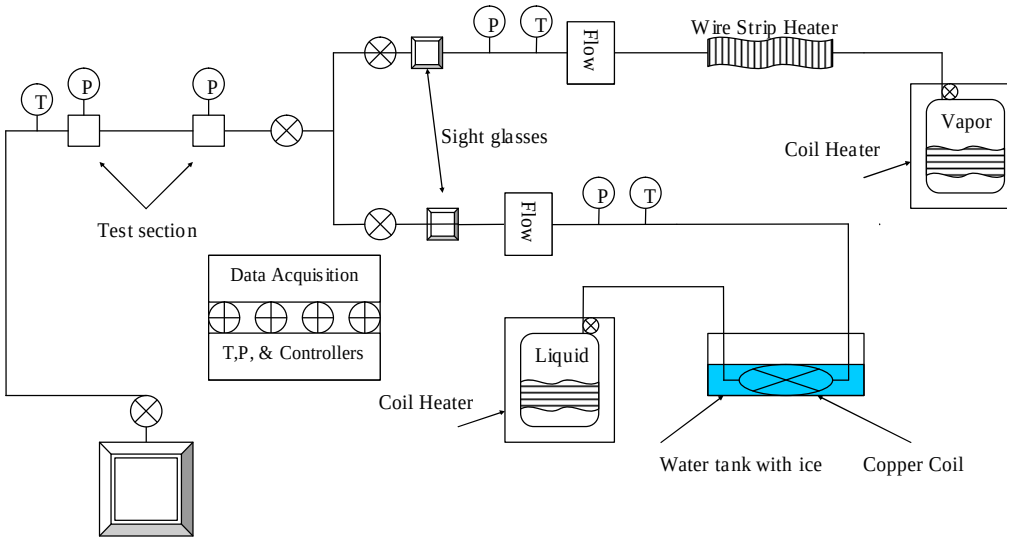

Figure 3.13: R134a Experimental Setup Schematic

It is an “open loop” or “once through” system in that the exit flow is not immediately returned into the system to provide for continuous use. In contrast to the several orientations described in the air-water system, only one test section orientation was employed, a twist from a 0° to 90°.

Charge is supplied by two separate 13.6kg refrigerant tanks. For the liquid supply, a 150W heater is wound around the top section, wrapped with insulation, and is placed upside down to create a pressure-driven liquid flow. A temperature controller is affixed to the outer surface to regulate the tank temperature. The tank temperature was held near 35-40°C. The liquid then travels through 9.525mm copper tubing to a condensing coil to ensure against vapor flashing. The coil has a coil length of 4.1m and a total length of 5.8m. The condensing coil was submerged in an ice-water bath held near 2-4°C. Flow is regulated by a parallel series of flow meters, calibrated with a Micromotion ® digital mass flow meter as described previously, specifically for refrigerant liquid. Refrigerant vapor is supplied by a tank wound with a 150W, insulation, and temperature controller which kept the tank near 40°C. To ensure against liquid flashing, a 150W is wound around a 1m section of copper tubing and held at a nominal temperature of 45°C to act as an evaporator. The vapor travels through a bank of three parallel flow meters calibrated specifically for R134a vapor. All of the exposed sections of copper tubing were insulated. The liquid and vapor lines mix at a T-junction before flowing through a calming length of about 40 tube diameters and into the test section. The flow exited to a large reservoir at nearly atmospheric pressure.

A data acquisition system was employed to collect data and monitor the system. To regulate the temperature of the supply tanks and evaporator, set-point temperature controllers were employed that turn the 220V current supply on or off, depending on whether the surface temperature exceeds or falls below the setpoint value. To measure the vapor and liquid temperatures, platinum RTD’s were employed for each line. They were calibrated against a constant temperature bath of ethylene glycol-water with a precision digital laboratory thermometer and datalogger over the range of 0 to 40°C. Correlation equations were obtained with linear correlation coefficients of

1.000. To measure temperature at the exit of the test section, a type-T thermocouple was employed. All temperature readings were performed using a datalogger. Pressure measurements were obtained for the vapor, liquid, test section inlet, and test section exit using four pressure transducers (0-1000KPa absolute), a DC voltage supply and DMM. Correlation details are provided in the Air-Water system description. Using these values of pressure, temperature, and flow, the thermodynamic and flow conditions could be described comprehensively. An Engineering Equation Solver® (EES) program was written for data reduction. X-ray images were obtained using the method and FeinFocus ® system described in the air-water system description.

3.3.2.2 Methodology

The experimental parameters of interest are pressure drop and flow pattern identification. In contrast to the several orientations described in the air-water system, only one test section orientation was employed: a twist from a 0° to 90°. A variety of *expected* mass flux and quality conditions were formulated based upon the calibration curves, equipment capacity, and microchannel geometry. The conditions were established until steady state was achieved. At this stage, readings were obtained for liquid and vapor pressure and temperature, test section inlet and exit pressure, and test section exit temperature. The temperature controllers of the refrigerant vapor and liquid supply, as well as the evaporator were continuously monitored to ensure qualities of near 0 for liquid and 1 for vapor. The X-ray machine was then configured for optimum resolution, and real-time video was obtained using its acquisition system. The videos were then digitized to compact discs, and computer software was obtained to capture still images. Following experimentation, data reduction was employed using an EES ® thermodynamic program. See Appendix C. Only then were the *actual* experimental conditions, specifically mass flux and quality, formulated.

After data reduction, it was determined that experimentation was performed for the combinations of mass flux and quality seen in Figure 3.14. The following general ranges of combinations of mass flux and quality were studied: G=50 $\mathrm{kg/m^2 \cdot s}$ to 150 $\mathrm{kg/m^2 \cdot s}$, quality from 0.1 to 0.85; G=200 $\mathrm{kg/m^2 \cdot s}$ to 300 $\mathrm{kg/m^2 \cdot s}$, quality from 0.1 to 0.5; G=300 $\mathrm{kg/m^2 \cdot s}$ to 400 $\mathrm{kg/m^2 \cdot s}$, quality from 0 to 0.1. Data for mass fluxes above 250 $\mathrm{kg/m^2 \cdot s}$ with qualities above 0.5 were difficult to sustain during experimentation, most likely due to the large pressure losses in the flow meter banks.

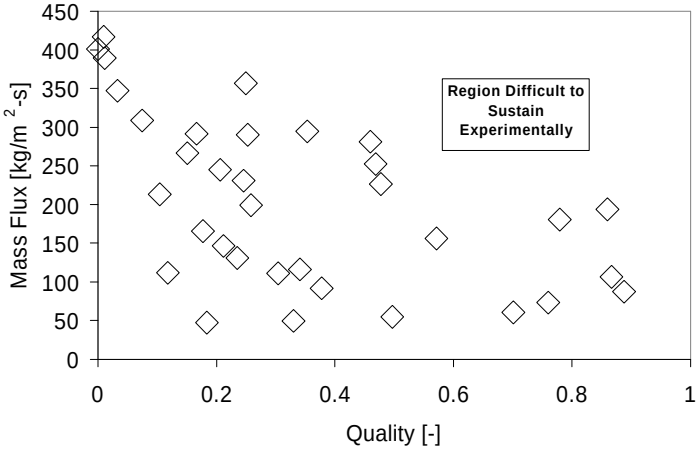

Figure 3.14: R134a Visualization Experimental Conditions

3.4 Results

3.4.1 Air Water Results

3.4.1.1 Flow Maps

Conventional flow maps often use experimental parameters, such as superficial fluid velocities, mass flux, and quality, for the coordinate axes. However, as Niño [2002a] notes, conventional flow maps are ultimately not applicable to a microchannel with multiple ports. During experimentation, there exists a definite probability that each port may have a flow regime which is different from the other ports for a certain experimentation condition. Furthermore, a given port may exhibit more than one flow pattern for a certain interval of time and spatial location.

To compensate for this, Niño [2002a] suggests the development of time probability functions. In this method, a given set of flow regimes is chosen for flow description. A certain number of visualization frames is chosen; for this interval, the flow regime exhibited in each individual channel is recorded. Thus, when the number of observations of a particular flow regime is divided by the total number of observations, a probability function is obtained. A value of 1 indicates that all of the ports will exhibit the same flow regime for a given condition. This value can be viewed as a frequency, probability, or fraction. The frequency is usually plotted against quality for a given mass flux. For this experiment, twenty frames still frames were selected and one observation was made per each of the six ports, resulting in 120 observations for a given flow condition and consequently several thousand manual observations for each microchannel orientation. The flow regimes selected for observation were dispersed-bubbly, intermittent, stratified, all liquid, and vapor/annular.

Some special comments must be stated at this point. First, the all-vapor and annular flow regimes were combined into a vapor/annular classification, though it is possible to separate them. The reason for this modification is that the X-ray images are not as distinct as traditional transparent visualization methods. Though an exit flow of air and water is observed, it is not possible to distinguish a film thickening around the microchannel walls from distortions in the X-ray images themselves; one may only safely assume that because there is an exit two-phase flow, and that the liquid forms on the walls when it appears that all vapor is present. Second, there is a possibility of dispersed flow at all times due to visual distortions in the black-and-white images. Dispersed/bubbly flow was only recorded when there was an obvious and clearly distinct formation of bubbles encapsulated in the moving fluid and not connected to the channel walls. Third, one can only distinguish the difference between vapor/annular and intermittent with confidence. Stratified flow and all-liquid flow were found to be quite rare for the flow conditions. Fourth, by definition the probability functions are defined as 1 for all-liquid at a quality of 0, and 1 for all-vapor at a quality of 1. Given these statements, it is proposed that this method yields a confident separation between vapor/annular and intermittent, with the possibility of dispersed/bubbly throughout all conditions, and with the all-liquid and stratified regimes occurring for very limited cases.

Figures 3.15 and 3.16 show probability maps for the G=50 $\mathrm{kg/m^2 \cdot s}$ and G=100 $\mathrm{kg/m^2 \cdot s}$ cases over a common range of qualities. These are for the first orientation of 90° about the microchannel longitudinal axis (termed 90°-1) and represent a typical sample from the pool of data ranging in mass flux from G=50 $\mathrm{kg/m^2 \cdot s}$ to 300 $\mathrm{kg/m^2 \cdot s}$.

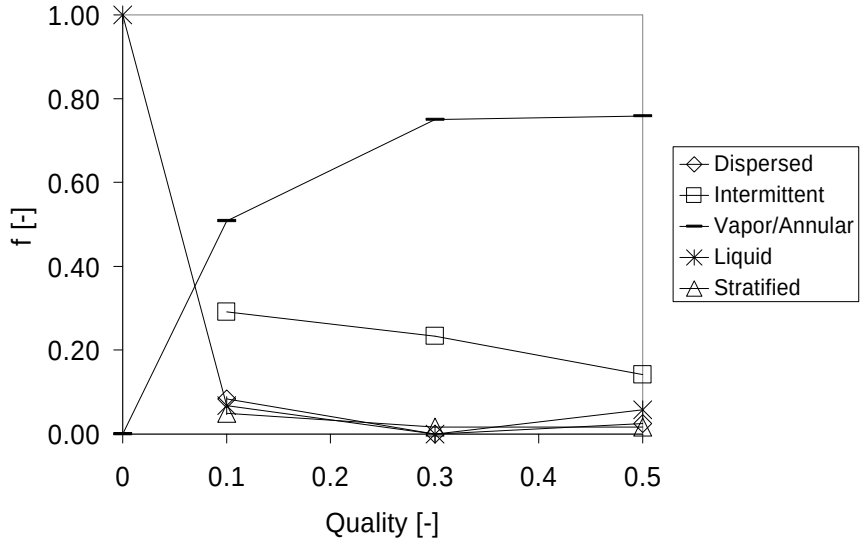

Figure 3.15: G=50 Flow Patterns, 90°-1

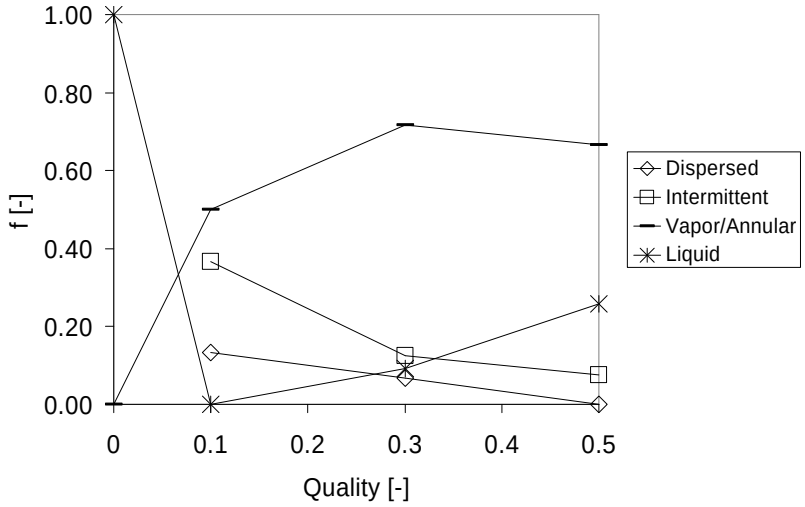

Figure 3.16: G=100 Flow Patterns, 90°-1

When comparing these probability maps, it is noted that stratified flow occurs only for the lower flux condition; moreover, from examining the remaining data, stratified flow does not occur for mass fluxes higher than this except when G=300 $\mathrm{kg/m^2 \cdot s}$ and x=0.1. As quality increases, the probability of all microchannel ports having the vapor/annular flow regime increases. The probability of intermittent flow is approximately the same for both conditions of mass flux. Meanwhile, the probability of occurrence of the remaining flow regimes decreases. The only apparent anomaly occurs for the all liquid regime. In both mass flux conditions the probability of all-liquid trails from its defined value of 1 at a quality of 0, then increases slightly with quality. This phenomenon will be addressed after the presentation of pressure drop data.

Now consider the probability maps for the same cases of G=50 $\mathrm{kg/m^2 \cdot s}$ and 100 $\mathrm{kg/m^2 \cdot s}$ for a second orientation of the microchannel about the longitudinal axis (termed 90°-2), given in Figures 3.17 and 3.18.

As mentioned in the methodology section, the microchannel was replaced and the experiments were repeated using an identical microchannel oriented in the precisely same fashion.

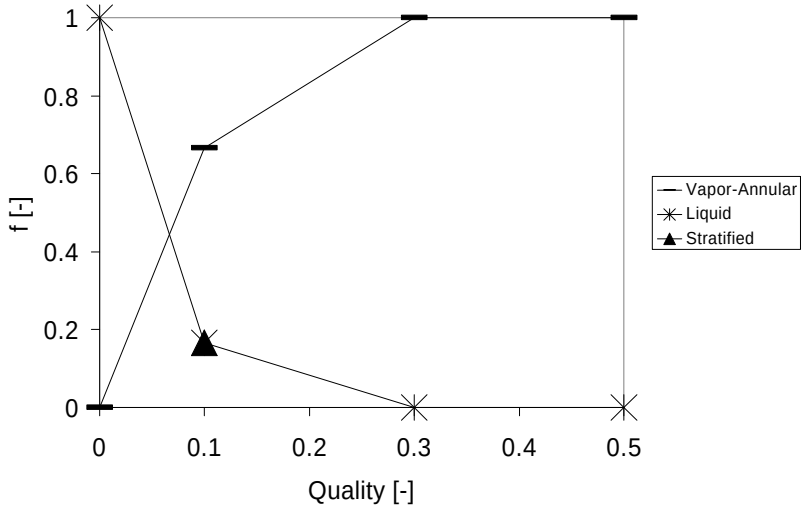

Figure 3.17: G=50 Flow Patterns, 90°-2

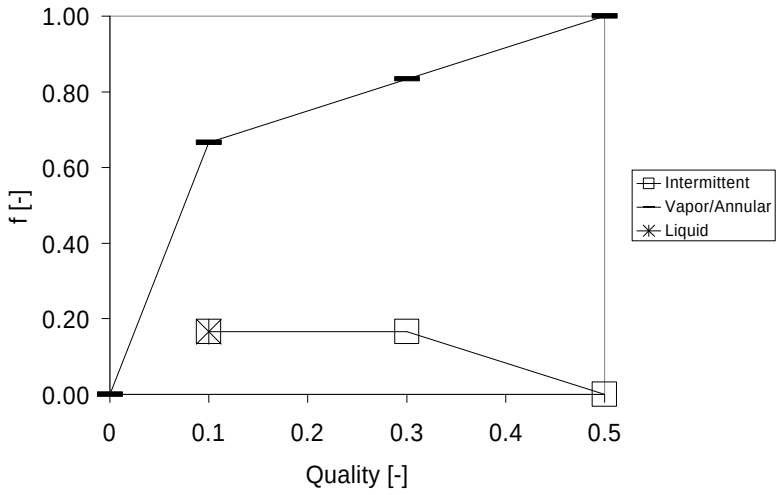

Figure 3.18: G=100 Flow Patterns, 90°-2

These maps differ quite considerably from the first 90° orientation. The dispersed flow regime is not found at all. Intermittent flow was not observed for G=50 $\mathrm{kg/m^2 \cdot s}$. All-liquid flow does not occur for G=100 $\mathrm{kg/m^2 \cdot s}$ as it does in the first 90° orientation. The stratified and all-liquid regimes do not extend over the range of qualities.

For further comparison, consider the probability maps for the same cases of G=50 $\mathrm{kg/m^2 \cdot s}$ and 100 $\mathrm{kg/m^2 \cdot s}$ when a 0 to 90° twist is created in the microchannel, presented in Figures 3.19 and 3.20. Differences do exist between the 0 to 90° twist maps and the second 90° orientation maps. The all-liquid regime seems to be more prominent for the second 90° orientation. This is due to gravity effects. The introduction of a twist from horizontal to vertical inlet reduces a preference for liquid to collect in the bottom channels; thus, the all-liquid

regime is not depicted, as one would expect. However, these two sets of probability maps demonstrate more similarity than for the first 90° orientation, especially in the behavior of the vapor/annular flow probability function. Something must account for the considerable difference between the flow map for the first 90° orientation and the flow maps for the other configurations. To develop a logical answer, a treatment of the pressure drop data is now presented.

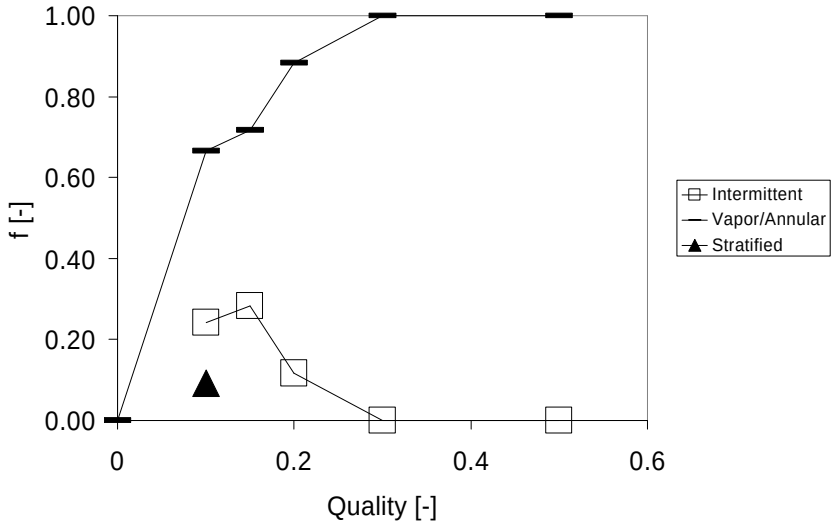

Figure 3.19: G=50 Flow Patterns, 0 to 90°

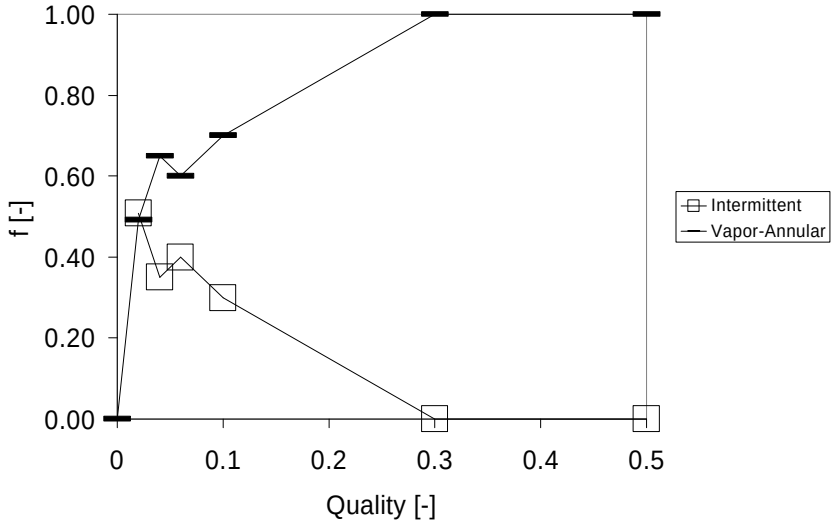

Figure 3.20: G=100 Flow Patterns, 0 to 90°

3.4.1.2 Pressure Drop

Figure 3.21 shows the pressure drop data across the length of the microchannel as a function of mass flux for a given quality, that of x=0.1.

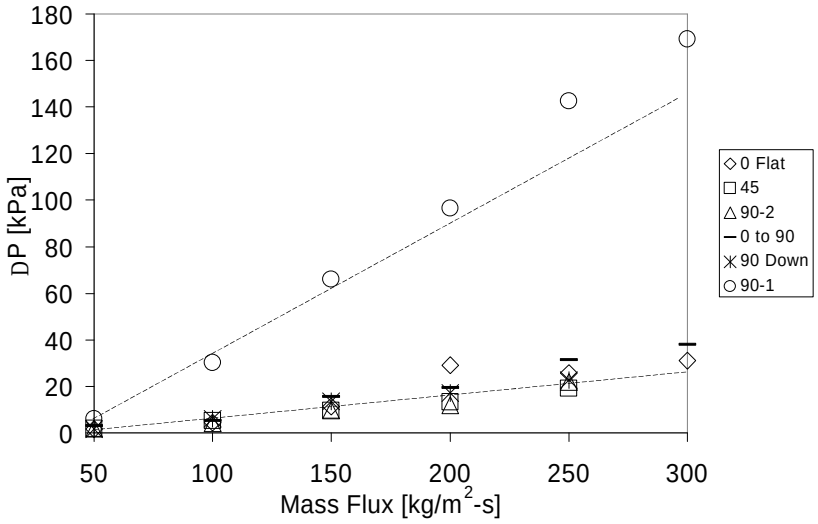

Figure 3.21: Pressure Drop for Quality of 0.1

The six different microchannel orientations are included on this graph. Clearly, pressure drop varies linearly with mass flux. Yet, this graph exhibits some peculiar characteristics. One immediately notices that the pressure drop for five of the six orientations is nearly identical and lay along the same trendline. However, the data for the first run of the 90° orientation experimentation lay along a much higher trend line and at the highest mass flux there is a difference of almost 800%. Either the trend exhibited for this particular quality is an anomaly, or there may be a broader implication. To decide if the trend is a function of quality, a second graph for a quality of 0.5 is displayed in Figure 3.22.

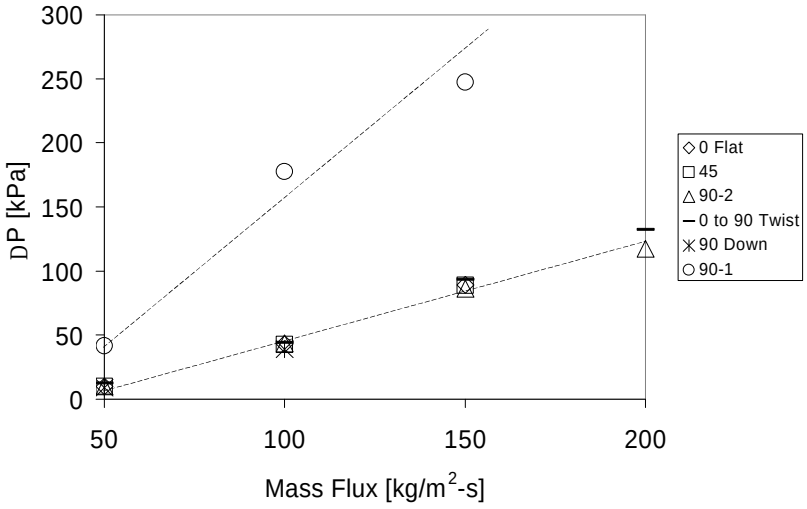

Figure 3.22: Pressure Drop for Quality of 0.5

When examining Figures 3.21 and 3.22 it is quite clear that the discrepancy in the data for the first 90° orientation experiment is not a function of quality. Once again, all five of the six orientations lay along a very similar trend line except for the first 90° orientation. Another important conclusion pertinent to heat exchanger design is that pressure drop appears to be insensitive to the orientation of the microchannel, even with a 0 to 90° twist. It is clear that a broader effect must account for the data discrepancy.

To examine pressure drop characteristics further, consider the graph of pressure drop per unit length in Figure 3.23 for a 0 to 90° twist. The reason for the selection of the 0 to 90° twist orientation is due to the wider range of quality conditions that were conducted for this orientation for qualities below 0.1.

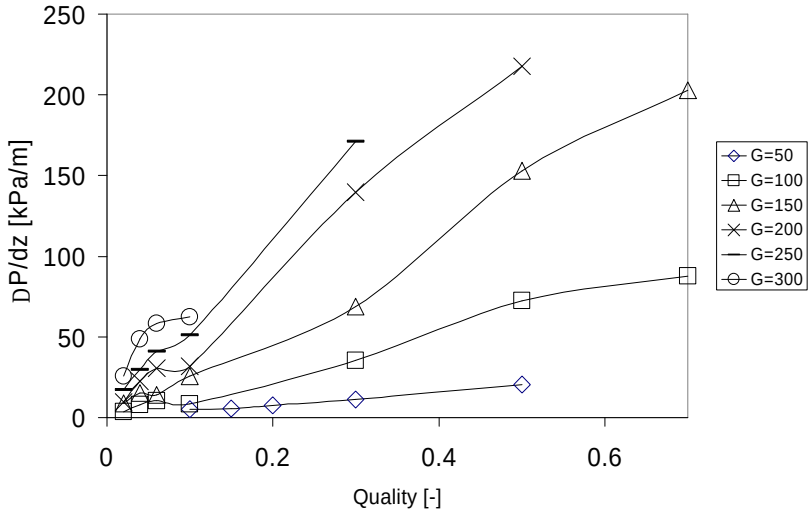

Figure 3.23: Pressure Drop/Unit Length for 0 to 90°

Some interesting conclusions may be gained from Figure 3.23. As the quality increases for a given mass flux, the pressure drop increases, which is logical for higher vapor velocity flows. It is also evident that as the mass flux is increased, the derivative of the ? P/dz becomes steeper. Thus, there is more change in pressure drop as the mass flux increases. Niño [2001] attributes this as characteristic of a shift from intermittent-type flows to more annular-type flows. This is reflected specifically in Figures 3.18 and 3.20, the probability flow maps for G=100 $kg/m^2 \cdot s$ for the second 90° orientation and the 0 to 90° twist; with increases in mass flux, there is a definite departure of vapor/annular flow from intermittent flow.

Now consider the same graph of ? P/dz for the first 90° orientation, presented in Figure 3.24.

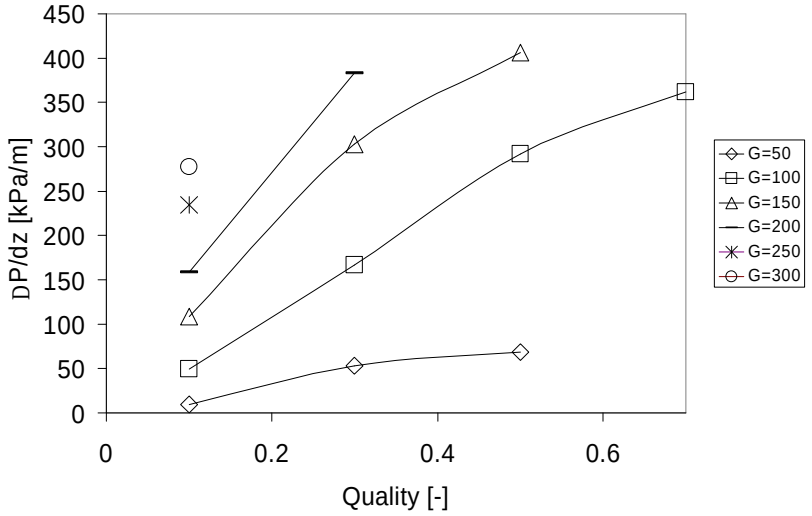

Figure 3.24: Pressure Drop/Unit Length for 90°-1

The same general trends may be observed for Figure 3.24 as in Figure 3.23. Pressure drop increases with quality, and the derivative of the curve becomes much steeper for higher mass fluxes, indicating flow pattern transitions, which are reflected in the probability flow maps. What is even more significant is that the pressure drop/unit length values for the first 90° orientation are much higher than for the 0 to 90° twist (and may be safely assumed as greater than the other orientations, including the second 90° orientation). For instance, at a mass flux of 150 $\mathrm{kg/m^2 \cdot s}$ and quality of 0.5, a value of about 150 kPa/m is obtained from the 0 to 90° twist whereas about 400 kPa/m is obtained from the first 90° orientation.

3.4.1.3 Flow Visualization

At this stage discrepancies have been noticed in the flow maps, pressure drop as a function of two qualities, and pressure drop per unit length for the same range of mass fluxes between the first 90° orientation and the rest of the configurations. Either the experimental process was flawed, or there is a problem with the microchannel itself. However, it is quite clear that the pressure drop data is nearly identical for five of the six orientations, indicating substantial repeatability over a wide range of experimental conditions. Consider sample images obtained from analysis of the X-ray videos. Due to the large number of pictures obtained from analysis, only one case will be presented for discussion. This case is for G=200 $\mathrm{kg/m^2 \cdot s}$, x=0.3 case. See Figure 3.25.

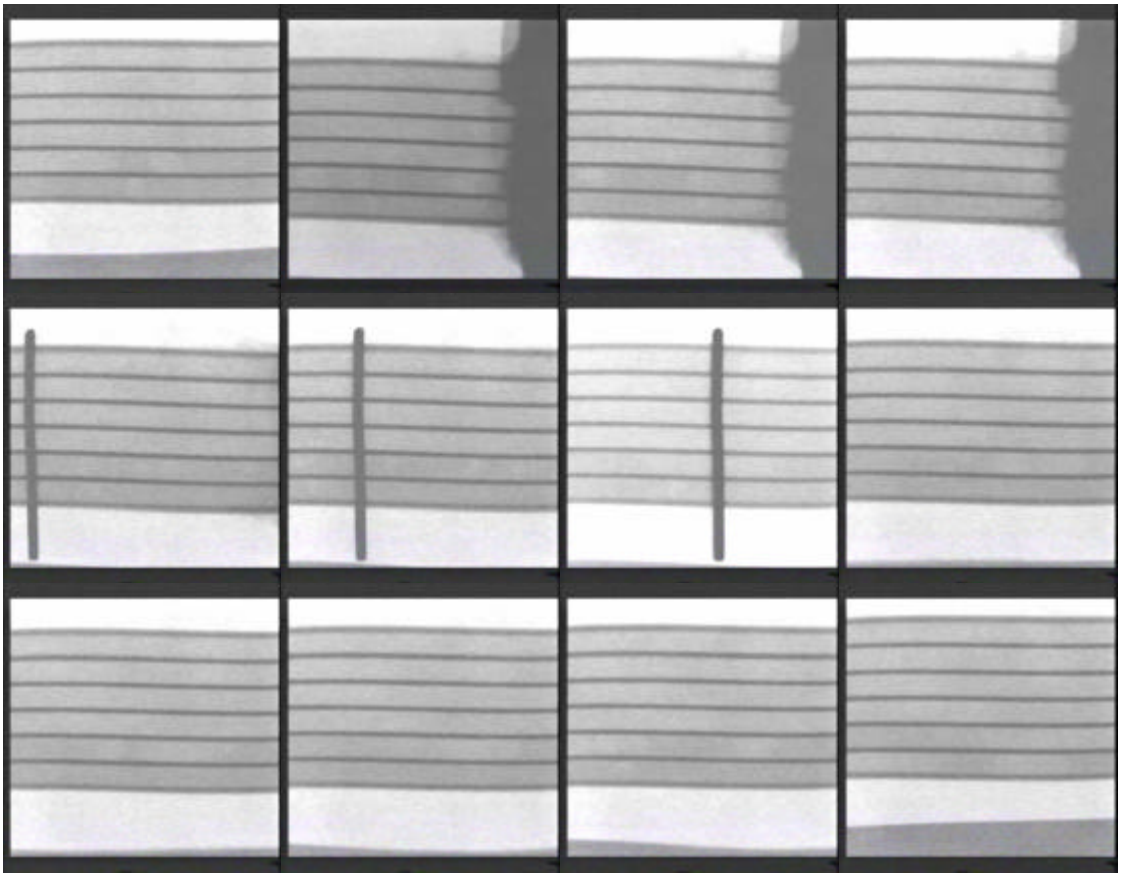

Figure 3.25: Sample Images: Air-Water, First 90° Orientation

From these images, it is clear that the regimes of bubbly flow and intermittent flow dominate. Incidentally, these two regimes are dominant over nearly the entire spectrum of combinations of mass flux and quality.

Now consider sample images from the second 90° orientation in Figure 3.26. The flux and quality conditions are G=200 kg/m^2·s, x=0.3.

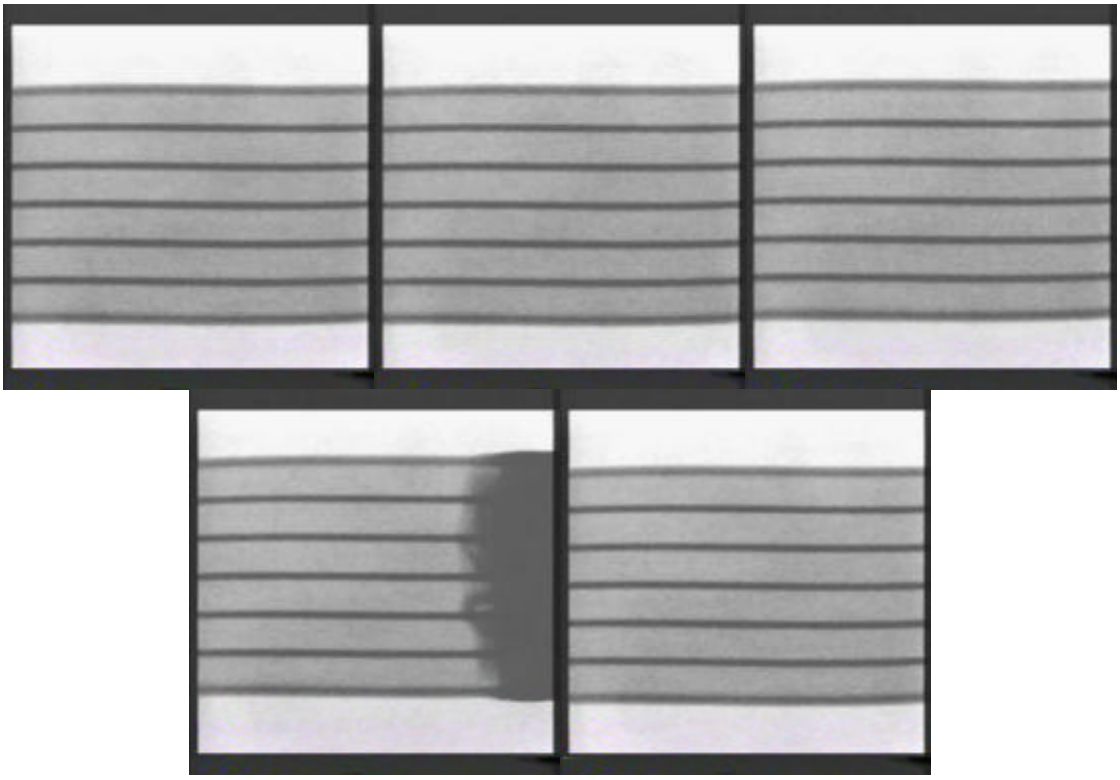

Figure 3.26: Sample Images: Air-Water, Second 90° Orientation

When viewing the actual experimental video at slow frame rates, and doing so provides more certainty than still pictures alone, it is quite conclusive that the dominant pattern is vapor/annular in this case. As opposed to the former collection of images, there are no suspended bubbly-type flows nor is there evidence of intermittent slug flow disturbances.

In actuality, small traces of ethylene-glycol were introduced into the distilled water prior to the first 90° orientation experiment. This ethylene-glycol/water mixture was inadvertently introduced by the first pump that was considered for the experimental setup. This pump was replaced, since its capacity was not sufficient for adequate flow, with another which supplied distilled water. The introduction of ethylene glycol was not known prior to the conduction of the experiments. During X-ray visualization it was noticed that viscous plugs remained in the microchannel even though no water was supplied and the air was supplied at maximum flow. This “oversight” actually led to the first realization that the X-ray system was indeed functioning as a useful diagnostic tool. When the inadvertency was discovered, the test section microchannel was replaced with another microchannel which was manufactured identical to the first microchannel. In addition, distilled water and air was flowed through the system

at high flow rates and for extended periods of time to ensure that any trace of ethylene glycol did not remain in other sections of the system. The experimental setup was configured exactly as before, and experimentation proceeded.

Thus, the odd discrepancies in the flow maps and pressure data can now be explained. The introduction of ethylene glycol created a much more viscous two-phase flow. Indeed, the live digitized video shows that the slugs and suspended bubbles of the overlapped intermittent and bubbly regimes seem to actually move against the direction of flow. However, this is hydro-dynamically impossible since an exit two-phase flow of air and water was observed at all times with no flow reversals. The slugs of higher-viscosity fluid appear to collapse in on themselves and then immediately reform; during this process air and water flow forward, creating the illusion of flow reversing its direction. For viscous fluids, surface tension increases and bubbles are capable of maintaining shape; in addition, liquid holdup occurs (Yang & Shieh [2001]). Yang & Shieh [2001] also note that viscosity is crucial to the interaction of the intermittent and bubbly regimes. These factors explain why the bubbly and intermittent flow patterns are seen throughout nearly the entire range of experimental conditions. Recall as well from Figures 3.15 and 3.16 that the probability function of the all-liquid flow regime seems to increase with quality, which is counter-intuitive and contradictory. What was actually occurring is that as the vapor velocity increased, a greater pressure force was exerted upon the face of the nearly-static plugs of viscous fluid and caused them to move forward. The static plugs combined and gave the appearance of moving liquid. In conclusion, the X-ray images give direct evidence of flow phenomenon that cannot be concluded simply from examining the raw data alone, which is the essential value of a non-invasive diagnostic tool.

3.4.2 R134a Results

3.4.2.1 Flow Maps

Probability flow maps were generated by employing the method described previously. However, some general statements must first be made. Due to the variation of two-phases of R134a resulting from pressure and temperature differences, only a matrix of expected mass fluxes and qualities could be formulated. These settings for vapor and liquid flow were approximated from flow meter calibrations as mentioned previously. Only after experimentation was completed could the actual experimental conditions be determined. The result was a wide range of qualities and fluxes, but not fixed arrays of qualities for mass fluxes, as seen in Figure 3.14. Thus, description is best attained by viewing the data points in groups.

Following visualization, it was determined that only two of six possible flow regimes were noticed with confidence: vapor-annular and intermittent. Figure 3.27 depicts a qualitative upper bound curve for the intermittent probability function for the range of mass flux.

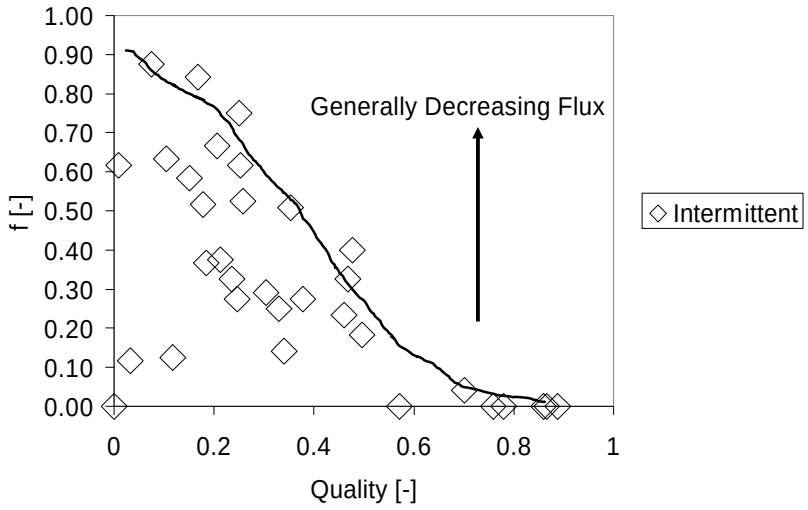

Figure 3.27: Intermittent Probability over Range of Fluxes

When examining the probability function values, it is noticed that as a group of similar fluxes decreases for a range of qualities, the probability heads toward 1. This indicates that for high mass fluxes and high qualities, the probability of the majority of the ports possessing intermittent flow is small; the converse is true. In comparison to previous work (Niño [2002a]), similar trends were noticed.

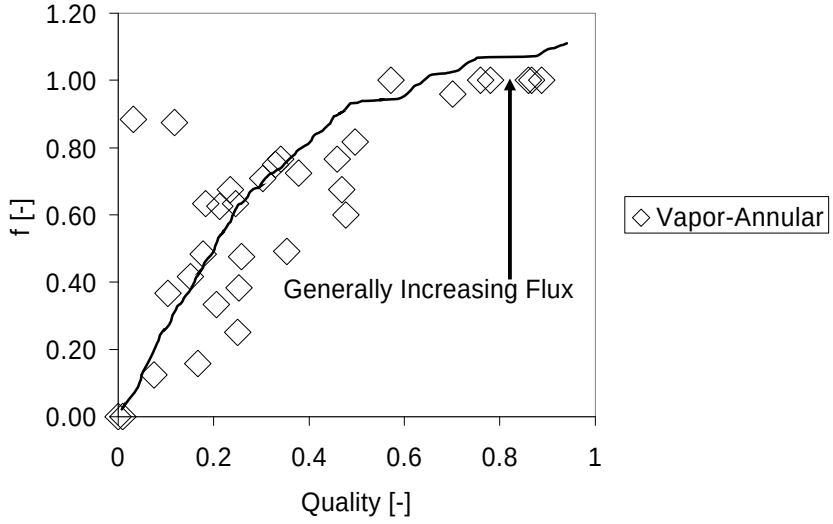

Figure 3.28: Vapor-Annular Probability over Range of Fluxes

Since there are two dominant flow regimes, the expected probability flow map for vapor/annular flow is seen in Figure 3.28 (above). When comparing the trends between Figures 3.27 and 3.28, the opposite behavior is present. For high mass fluxes and qualities, the probability of vapor-annular dominating is high; for low mass fluxes and qualities, the probability of seeing vapor-annular in the majority of the channels is low.

3.4.2.2 Pressure Drop

Figure 3.29 displays the pressure drop/unit length data over the experimental conditions when grouped into mass flux ranges.

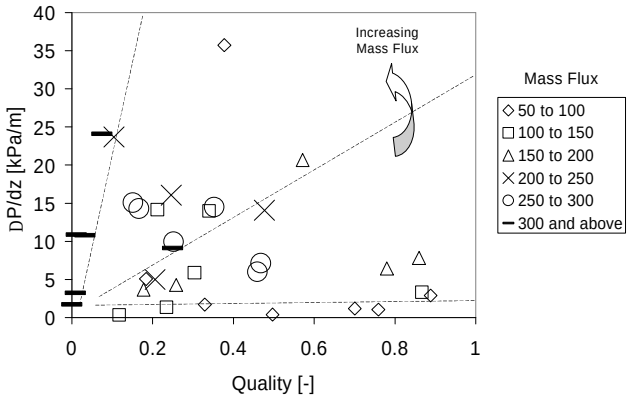

Figure 3.29: Pressure Drop/Unit Length for R134a

One notes the same general trends as those observed in the air-water case. Generally, with increasing mass flux there is more change in pressure drop. The values obtained are in general agreement with those of Niño [2001].

3.5 Conclusions

3.5.1 Representative Visualization Sample

A table of representative pictures displaying flow regimes can be seen in Figure 3.30. These are the primary flow regimes noticed during experimentation for both air-water and R134a.

Flow Regimes				
Vapor-Annular	Stratified	Intermittent	Bubbly-Dispersed	All-Liquid
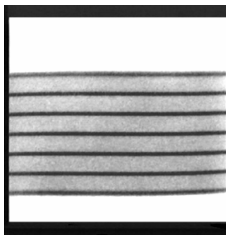	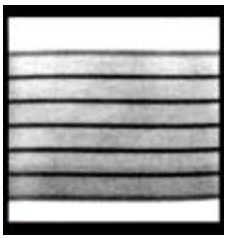	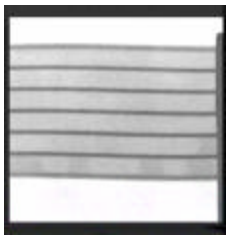		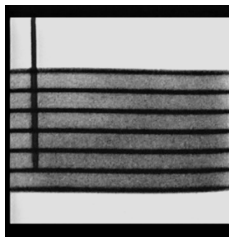

Figure 3.30: Representative Samples of Flow Regimes

3.5.2 Air-Water

The most important conclusion from the air-water study is that X-ray diagnostics yield visible, tangible proof of flow effects that cannot be observed simply from the raw data alone. Moreover, such a tool helps to explain the data even further. This is valuable for designers interested in examining heat exchanger phenomena in a non-invasive fashion. Bubbly dispersed, stratified, intermittent, all-liquid, and vapor-annular flow regimes were observed. Pressure drop does not appear to be related to microchannel orientation, which is important in design. As mass flux increases, the derivative of pressure drop increases with increasing quality, indicating flow pattern transitions. Probabilistic function flow maps derived from visualization can qualify such things as orientation, fluid properties, and pressure drop. Direct observation of these effects was obtained, as opposed to idealized transparent visualization methods.

3.5.3 Air-Water/R134a Differences

R134a and Air-Water behave differently due to vapor/liquid ratios (0.0016 for air-water, 0.0625 for R134a). Due to the much higher density of R134a vapor, more annular flow is expected because of higher inertia for given flux and quality. The surface tension of air-water is higher than for R134a, which affects regime transition. Pressure drop/unit length is lower for R134a because of its lower dynamic viscosity (~3 times lower for liquid, ~8 times lower for vapor.

When comparing refrigerant results to air-water results, Coleman & Garimella [2002] note the transitions between flow patterns occur at lower gas and liquid velocities than the same air-water flow map would predict. The primary differences between air-water and R134a studies are that the gas-phase densities are quite different, which lead to higher gas velocities for air-water when compared to R134a. The authors note that the ratio of liquid to vapor density is about 600, whereas that for R134a is about 16. Some regions were found to be in common, such as the intermittent region located at relatively the same quality conditions for air-water and R134a. Coleman & Garimella [2002] found that the air-water wavy-annular flow regime corresponds roughly to the transition between wave and slug/plug flow exist. The air-water annular flow regime corresponds to the R134a discrete wave flow regime. Some similarity may be gained, however, since wavy flow is often characterized as annular flow. The authors found that discrete wave R134a patterns correspond to air-water intermittent flow.

Furthermore, the authors also studied the Froude number, which describes the ratio of inertia to gravity forces. They note that the Froude number is 900% larger for the air-water tests for a mass flux of $450\,\mathrm{kg/m^2 \cdot s}$ and a quality of 50%, leading to the conclusion that for R134a the gravitational forces are stronger. They note that the transition from wavy to annular occurs at a much lower quality for the air-water system, if the transition is performed at relatively constant Froude number. Another dimensionless number, the Bond number (ratio of gravity to surface tension) is 16 times higher for R134a than air-water.

3.5.4 R134a

The main contribution of this work is that this represents the first time a real microchannel has been used for flow visualization. Furthermore, with improvement in the X-ray diagnostic procedure, more insights may be gained. Only the intermittent and vapor-annular flow regimes were observed with confidence. This study cannot yield any conclusions about heat transfer, since tests were run at adiabatic conditions.

3.5.5 Recommendations

At present, this technique has only been applied for air-water and R134a. IN the future, it may be interesting to explore other refrigerants such as CO_2 or butanes. To improve the clarity of the image, the injection of radioactive ionic solutions (e.g. Barium) may help. This technique may also prove useful for microchannels of smaller diameter.

3.6 Bibliography

Barnea, D.; Luninski, Y.; Taitel, Y. *Flow Pattern in Horizontal and Vertical Two-phase Flow in Small Diameter Pipes*. Canadian J. of Chem. Eng. Vol. 61. pp. 617-620. October 1983.

Coleman, J.W.; Garimella, S. *Characterization of Two-Phase Flow Patterns in Small Diameter Round and Rectangular Tubes*. Intl J. of Heat and Mass Transfer. Vol. 42 pp. 2869-2881. 1999.

Coleman, J.W.; Garimella, S. *Two-Phase Flow Regimes in Round, Square, and Rectangular Tubes During Condensation of Refrigerant R134a*. Intl. J. of Refrigeration. pp. 1-12. 2002.

Coleman, J.W.; Garimella, S. *Visualization of Refrigerant Two-Phase Flow During Condensation*. Proc. 34th NHTC '00. pp 1-14. Aug 2000.

Cook, M.; Behnia, M. *Pressure Drop Calculation and Modeling of Inclined Intermittent Gas-Liquid Flow*. Chemical Engineering Science. Vol. 55. pp. 4699-4708. 2000.

Costigan, G.; Whalley, P.B. *Slug Flow Regime Identification From Dynamic Void Fraction Measurements in Vertical Air-Water Flows*. Int. J. of Multiphase Flow. Vol. 23, No. 2. pp. 263-282. 1997.

Damianides, C.A.; Westwater, J.W. *Two-Phase Flow Patterns in a Compact Heat Exchanger and in Small Tubes*. C128/88, Amoco Research Center. 1988.

Fourar, M; Bories, S. Experimental *Study of Air-Water Two-Phase Flow Through a Fracture (Narrow Channel).* Intl J. Multiphase Flow. Vol. 21, No.4. pp. 621-637. 1995.

Ghiaasiaan, S.M.; Abdel-Khalik, S.I. *Two-Phase Flow in Microchannels*. Advances in Heat Transfer. Vol. 34. pp. 145-254. 2001.

Joseph, D.D.; Bannwart, A.C.; Liu, Y.J. *Stability of Annular Flow and Slugging*. Dept. of Aerospace Engineering and Mechanics, University of Minnesota. pp. 1-10. 1996.

Lockhart, R, W.; Martinelli, R.C. *Proposed Correlation of Data for Isothermal Two-Phase Two-Component Flow in Pipes*. Chem. Eng. Prog. Vol 45, no. 1. pp. 39-48 January 1949.

Lun, I; Calay, R.K.; Holdo, A.E. *Modeling Two-Phase Flows Using CFD.* Applied Energy. Vol. 53. pp. 299-314. 1996.

Niño, Victor et al. *Two-phase Pressure Drop in Microchannels*. University of Illinois. IIF - IIR – Commission B1 – Paderborn, Germany. 2001.

Niño, Victor. *Analysis of Void Fraction in Microchannels*. University of Illinois. 2002.

Niño, Victor. *Two-Phase Flow Visualization of R134a in Multi-Port Microchannel Tube*. University of Illinois. 2002.

Payne, W.T.; Niño, V.G. *Void Fraction and Pressure Drop in Microchannels.* ACRC TR-178, University of Illinois Air Conditioning & Refrigeration Center. Dec. 2000.

Tandon, T.N.; Varma, H.K.; Gupta, C.P. *A Void Fraction Model for Annular Two-Phase Flow*. Intl. J. Heat Mass Transfer. Vol. 28, No. 1. pp. 191-198. 1985.

Triplett, K.A.; Ghiaasiaan, S.M.; Abdel-Khalik, S.I.; LeMouel, A.; McCord, B.N. *Gas-Liquid Two-Phase Flow in Microchannels. Part II: Void Fraction and Pressure Drop*. Intl J. Mult. Flow. Vol. 25. pp. 395-410. 1999b.

Triplett, K.A.; Ghiaasiaan, S.M.; Abdel-Khalik, S.I.; Sadowski, D.L. *Gas-Liquid Two-Phase Flow in Microchannels. Part I: Two-Phase Flow Patterns.* Intl J. Mult. Flow. Vol. 25. pp. 377-394. 1999a.

Wallis, G.B. *One-Dimensional Two-Phase Flow*. McGraw-Hill, New York. 1969.

Wong, T.N.; Yau, Y.K. *Flow Patterns in Two-Phase Air-Water Flow*. Int. Comm. Heat Mass Transfer Vol. 24, No. 1. pp. 111-118. 1997.

Yang, Chien-Yuh; Shieh, Cheng-Chou. *Flow Pattern of Air-Water and Two-Phase R134a In Small Circular Tubes.* Intl. J. of Multiphase Flow. Vol. 27. pp. 1163-1177. 2001.

Yang, C.Y., Webb, R.L. *Condensation of R-12 in Small Hydraulic Diameter Extruded Aluminum Tubes with and Without Micro-Fins*. Intl. J. of Heat and Mass Transfer. Vol. 39 No 4. pp 791-800. 1995a.

Yang, C.Y. Webb, R.L. *Friction Pressure Drop of R-12 in Small Hydraulic Diameter Extruded Aluminum Tubes with and Without Micro-Fins.* Intl. J. of Heat and Mass Transfer. Vol. 39 No 4. pp 801-809. 1995b.

Yao, G.F.; Ghiaasiaan, S.M. *Wall Friction in Annular-Dispersed Two-Phase Flow*. Nuclear Engineering and Design. Vol. 163. pp. 149-161. 1996.

Appendix A: Single Phase Modeling

A.1 Piezometric Head Loss Equations from McKnown & Asce [1952]

Manifold equation:
$$\frac{\Delta h}{\frac{V^2}{2g}} = \frac{p_c - p}{\frac{rV^2}{2}} = 1 - \left(\frac{V_c}{V}\right)^2 - \frac{h_f}{\frac{V^2}{2g}} = \frac{Q_l}{Q}\left(2 - \frac{Q_l}{Q}\right) - \frac{h_f}{\frac{V^2}{2g}} \quad \text{(A.1)}$$

Where h is the pressure head, V is velocity, p is the manifold pressure, ? is density, c refers to the manifold channel, Q is the flow rate, l refers to the laterals, g is the gravitational constant, and h_f is the loss of head due to frictional losses. The equation for the laterals is given below

Lateral Equation:
$$\frac{\Delta h'}{\frac{V^2{}_l}{2g}} = \frac{p_l - p}{\frac{rV^2{}_l}{2}} = \left(\frac{V}{V_l}\right)^2 - 1 - \frac{h'_f}{\frac{V^2{}_l}{2g}} \quad \text{(A.2)}$$

An overall manifold channel momentum equation is also provided which casts the channel piezometric head loss in terms of a bulk force F opposing the channel momentum:

Momentum Equation:
$$\frac{\Delta h}{\frac{V^2}{2g}} = 2\left[1 - \left(\frac{V_c}{V}\right)^2 - \frac{F}{rQV}\right] \quad \text{(A.3)}$$

A theoretical coefficient of contraction C_c , which depends on the area ratio and channel velocity ratio Vc/V, was derived. This coefficient is useful to describe the head loss for the lateral:

$$\frac{\Delta h'_f}{\frac{V^2{}_l}{2g}} = \left(\frac{1}{C_c} - 1\right) \quad \text{(A.4)}$$

A.2 Bajura-Chou-Cheng (BCC) Remaining Cases for a and ß

Chou & Cheng [2001] then apply a perturbation method to arrive at a solution when a is small but not negligible. The solution is presented here without the formidable derivation:

$$V_r = \frac{V'_c(1)}{V'_c(0)} = \frac{1 + a^2\left\{\frac{1}{8b^3}\left[\left[2b - \sin(2b)\right] + \frac{8(2\ln\cos b + \sin^2 b)\cos b}{\sin b} - \frac{4\sin^3 b}{b}\right]\right\}}{\cos b + a^2\left[\frac{(2\ln\cos b + \sin^2 b)(\sin^2 b + 4\cos^2 b}{4b^3 \sin b}\right]} \quad \text{(A.5)}$$

where V_r is the parameter of uniformity and relates the microchannel discharges of the initial and dead ends.

Using Chou & Cheng's perturbation method, the following graph was obtained relating a, ß, and V_r :

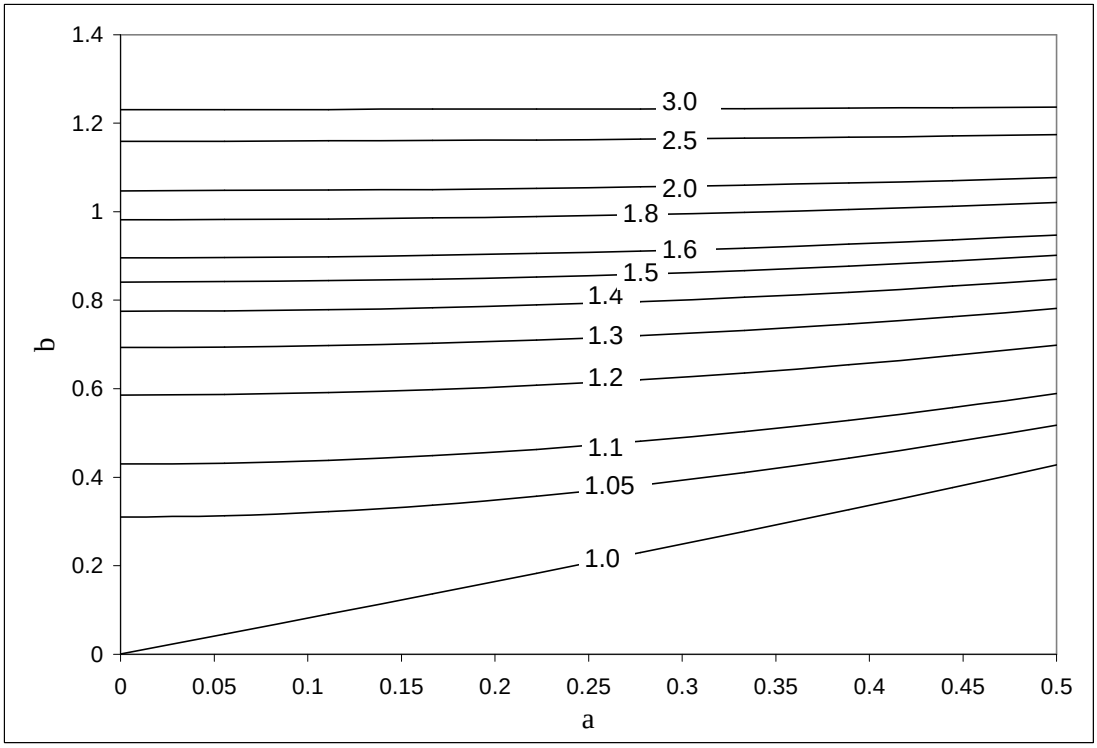

Figure A.1: Range of a and ß for Vr Contours

The authors note that the *Vr*=1 contour is obtained for $b = 0.594a$. In addition, the lateral discharge diameter which maintains discharge uniformity is given by

$$D_h = \frac{0.353}{2 - g_d} f_c L_c \tag{A.6}$$

For hydraulic diameters below this critical diameter, the discharge decreases downstream; conversely, the discharge increases downstream for diameters larger than this critical diameter.

The second classification of manifolds describes manifolds for which α dominates and β dominates. Such would be the case for a very long, frictional manifold diffuser. The overall governing equation then reduces to:

$$\frac{d}{d\hat{x}}\left[\left(\frac{d\hat{V}_c}{d\hat{x}}\right)^2\right] + \left(a\hat{V}_c\right)^2 = 0 \tag{A.7}$$

The following solution is presented with boundary conditions $\hat{V}_c = 1$ at $\hat{x} = 0$ and $\hat{V}_c = 0$ at $\hat{x} = 1$:

$$\int_1^0 \frac{dV_c}{\sqrt[3]{-\frac{a^2}{2}V_c^3 + 3c}} = 1 \tag{A.8}$$

with

$$c = 0.0195a^2 + 0.0237a - 0.3387 \tag{A.9}$$

and

$$V_r = \frac{1}{\sqrt{1 - \frac{a^2}{6c}}} \tag{A.10}$$

Equation (A.10) is plotted in the following graph:

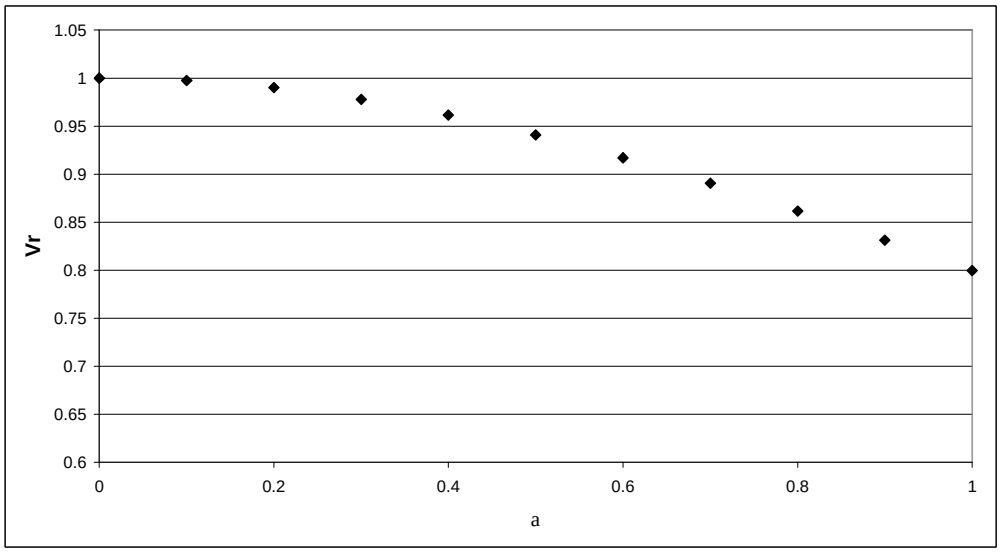

Figure A.2: Uniformity Parameter versus Friction Parameter

Thus, as the friction parameter increases, the downstream discharge decreases along the length of the manifold.

A.3 Single Phase Distribution Data

Table A.1: Air Mass Flow for 12.7mm Spacer Plate, Top Right Entrance

	Inlet mass flow Rate [g/s]		
	0.273086	3.1573	4.367557
Tube #	Tube Discharge Mass Flow Rate [g/s]		
1	0.018824	0.19503	0.278496
2	0.018824	0.204304	0.283133
3	0.018824	0.19503	0.278496
4	0.00955	0.204304	0.28777
5	0.018824	0.213578	0.28777
6	0.018824	0.204304	0.28777
7	0.018824	0.213578	0.297044
8	0.018824	0.204304	0.28777
9	0.018824	0.213578	0.297044
10	0.018824	0.250674	0.297044
11	0.018824	0.213578	0.297044
12	0.018824	0.213578	0.297044
13	0.018824	0.213578	0.297044
14	0.018824	0.204304	0.297044
15	0.018824	0.213578	0.297044

Table A.2: Air Pressure Profile for 12.7mm Spacer Plate, Top Right Entrance

	Inlet mass flow Rate [g/s]		
	0.273086	3.1573	4.367557
	Manifold Static Pressure [kPa]		
P1	1.185275	10.802935	17.59625
P2	1.225913	10.681021	17.33888
P3	1.232686	10.823254	17.63689
P4	1.273324	11.24318	18.32097
P5	1.280097	11.344775	18.55125

Table A.3: Air Mass Flow for 12.7mm Spacer Plate, Top Left Entrance

	Inlet mass flow Rate [g/s]		
	0.273086	3.231492	4.288728
Tube #	Tube Discharge Mass Flow Rate [g/s]		
1	0.018824	0.222852	0.297044
2	0.018824	0.222852	0.297044
3	0.018824	0.222852	0.297044
4	0.018824	0.222852	0.297044
5	0.018824	0.222852	0.297044
6	0.018824	0.222852	0.28777
7	0.018824	0.213578	0.28777
8	0.018824	0.213578	0.278496
9	0.018824	0.222852	0.28777
10	0.018824	0.213578	0.278496
11	0.018824	0.213578	0.278496
12	0.018824	0.204304	0.278496
13	0.00955	0.204304	0.278496
14	0.018824	0.204304	0.278496
15	0.018824	0.204304	0.269222

Table A.4: Air Pressure Profile for 12.7mm Spacer Plate, Top Left Entrance

	Inlet mass flow Rate [g/s]		
	0.273086	3.231492	4.288728
	Manifold Static Pressure [kPa]		
P1	1.192048	11.541192	17.50821
P2	1.327508	11.656333	17.63689
P3	1.246232	11.636014	17.6098
P4	1.21914	11.297364	17.09505
P5	1.178502	10.694567	16.16715

Table A.5: Air Mass Flow for 12.7mm Spacer Plate, Bottom Right Entrance

	Inlet mass flow Rate [g/s]		
	0.263812	3.073834	4.353646
Tube #	Tube Discharge Mass Flow Rate [g/s]		
1	0.00955	0.185756	0.278496
2	0.00955	0.19503	0.278496
3	0.018824	0.185756	0.278496
4	0.018824	0.19503	0.278496
5	0.018824	0.204304	0.28777
6	0.018824	0.204304	0.297044
7	0.018824	0.204304	0.28777
8	0.018824	0.204304	0.28777
9	0.018824	0.213578	0.297044
10	0.018824	0.213578	0.297044
11	0.018824	0.213578	0.297044
12	0.018824	0.213578	0.297044
13	0.018824	0.213578	0.297044
14	0.018824	0.213578	0.297044
15	0.018824	0.213578	0.297044

Table A.6: Air Pressure Profile for 12.7mm Spacer Plate, Bottom Right Entrance

	Inlet mass flow Rate [g/s]		
	0.263812	3.073834	4.353646
	Manifold Static Pressure [kPa]		
P1	1.253005	10.90453	17.20342
P2	1.063361	10.667475	16.89864
P3	1.300416	10.931622	17.21697
P4	1.347827	11.358321	17.88749
P5	1.347827	11.459916	18.02295

Table A.7: Air Mass Flow for 12.7mm Spacer Plate, Bottom Left Entrance

	Inlet mass flow Rate [g/s]		
	0.28236	3.20367	4.298002
Tube #	Tube Discharge Mass Flow Rate [g/s]		
1	0.018824	0.222852	0.297044
2	0.018824	0.222852	0.297044
3	0.018824	0.222852	0.297044
4	0.018824	0.222852	0.297044
5	0.018824	0.222852	0.297044
6	0.018824	0.204304	0.297044
7	0.018824	0.222852	0.297044
8	0.018824	0.222852	0.28777
9	0.018824	0.222852	0.297044
10	0.018824	0.213578	0.28777
11	0.018824	0.213578	0.278496
12	0.018824	0.204304	0.269222
13	0.018824	0.19503	0.269222
14	0.018824	0.19503	0.259948
15	0.018824	0.19503	0.269222

Table A.8: Air Pressure Profile for 12.7mm Spacer Plate, Bottom Left Entrance

	Inlet mass flow Rate [g/s]		
	0.28236	3.20367	4.298002
	Manifold Static Pressure [kPa]		
P1	1.198821	11.629241	17.94845
P2	1.21914	11.71729	18.08391
P3	1.253005	11.71729	18.05005
P4	1.21914	11.351548	17.50821
P5	1.192048	10.979033	16.9325

Table A.9: Water Mass Flow for 12.7mm Spacer Plate

	Entrance		
	Right		Left
Tube #	Tube Discharge Mass Flow Rate [g/s]		
1	17.18333333		20.13666667
2	18.80333333		20.75
3	16.56666667		20.44666667
4	20.35333333		21.19
5	17.16		19.58333333
6	18.97		18.6
7	20.42666667		19.68
8	16.74		19.91666667
9	22.13333333		20.8
10	19.13333333		20.15
11	20.24333333		18.79
12	21.83333333		17.24666667
13	20.81666667		19.08
14	13.59		18.22333333
15	15.79333333		18.4
Sum	279.75		292.99

Table A.10: Air Mass Flow for 6.35mm Spacer Plate, Top Right Entrance

	Inlet mass flow Rate [g/s]		
	0.98	4.475	5.33
Tube #	Tube Discharge Mass Flow Rate [g/s]		
1	0.05	0.23	0.28
2	0.06	0.27	0.33
3	0.05	0.26	0.29
4	0.055	0.265	0.33
5	0.06	0.28	0.35
6	0.07	0.3	0.36
7	0.07	0.3	0.35
8	0.06	0.3	0.355
9	0.07	0.32	0.39
10	0.07	0.32	0.38
11	0.07	0.31	0.385
12	0.07	0.32	0.39
13	0.075	0.34	0.38
14	0.075	0.33	0.38
15	0.075	0.33	0.38

Table A.11: Air Pressure Profile for 6.35mm Spacer Plate, Top Right Entrance

	Inlet mass flow Rate [g/s]		
	0.98	4.475	5.33
	Manifold Static Pressure [kPa]		
P1	1.246232	16.66158	22.14771
P2	1.08368	14.76514	19.634927
P3	1.164956	15.10379	20.054853
P4	1.178502	16.763175	22.879194
P5	1.551017	17.799444	23.7055

Table A.12: Air Mass Flow for 6.35mm Spacer Plate, Top Left Entrance

	Inlet mass flow Rate [g/s]		
	0.905	4.39	5.08
Tube #	Tube Discharge Mass Flow Rate [g/s]		
1	0.065	0.33	0.38
2	0.06	0.32	0.37
3	0.06	0.32	0.37
4	0.065	0.32	0.37
5	0.065	0.31	0.36
6	0.06	0.3	0.35
7	0.06	0.29	0.34
8	0.06	0.29	0.34
9	0.07	0.32	0.37
10	0.055	0.27	0.31
11	0.06	0.31	0.35
12	0.055	0.25	0.28
13	0.06	0.25	0.29
14	0.05	0.23	0.27
15	0.06	0.28	0.33

Table A.13: Air Pressure Profile for 6.35mm Spacer Plate, Top Left Entrance

	Inlet mass flow Rate [g/s]		
	0.905	4.39	5.08
	Manifold Static Pressure [kPa]		
P1	1.293643	17.386291	22.28317
P2	1.361373	17.521751	22.44572
P3	1.347827	17.393064	22.24931
P4	1.232686	15.862366	20.27159
P5	1.110772	13.796601	27.49838

Table A.14: Air Mass Flow for 6.35mm Spacer Plate, Bottom Right Entrance

	Inlet mass flow Rate [g/s]		
	0.95	4.59	5.43
Tube #	Tube Discharge Mass Flow Rate [g/s]		
1	0.05	0.24	0.29
2	0.06	0.28	0.34
3	0.05	0.24	0.29
4	0.06	0.27	0.33
5	0.06	0.29	0.35
6	0.06	0.31	0.36
7	0.06	0.31	0.36
8	0.06	0.31	0.36
9	0.07	0.34	0.4
10	0.07	0.33	0.39
11	0.07	0.33	0.38
12	0.07	0.33	0.39
13	0.07	0.33	0.39
14	0.07	0.34	0.4
15	0.07	0.34	0.4

Table A.15: Air Pressure Profile for 6.35mm Spacer Plate, Bottom Right Entrance

	Inlet mass flow Rate [g/s]		
	0.95	4.59	5.43
	Manifold Static Pressure [kPa]		
P1	1.266551	23.09593	22.89274
P2	1.341054	20.982754	19.953258
P3	1.341054	21.74133	21.043711
P4	1.517152	23.725819	23.780003
P5	1.591655	24.335389	24.58599

Table A.16: Air Mass Flow for 6.35mm Spacer Plate, Bottom Left Entrance

	Inlet mass flow Rate [g/s]		
	1.01	4.51	5.34
Tube #	Tube Discharge Mass Flow Rate [g/s]		
1	0.07	0.34	0.39
2	0.07	0.34	0.39
3	0.07	0.33	0.39
4	0.07	0.33	0.39
5	0.07	0.32	0.38
6	0.07	0.31	0.37
7	0.07	0.3	0.36
8	0.07	0.3	0.36
9	0.07	0.33	0.39
10	0.06	0.28	0.34
11	0.07	0.31	0.34
12	0.06	0.27	0.32
13	0.06	0.24	0.29
14	0.06	0.23	0.29
15	0.07	0.28	0.34

Table A.17: Air Pressure Profile for 6.35mm Spacer Plate, Bottom Left Entrance

	Inlet mass flow Rate [g/s]		
	1.01	4.51	5.34
	Manifold Static Pressure [kPa]		
P1	1.395238	16.356795	22.78437
P2	1.266551	16.444844	23.01465
P3	1.205594	16.112967	22.71664
P4	1.185275	14.649999	20.58992
P5	1.117545	12.225265	17.29824

Table A.18: Water Mass Flow for 6.35mm Spacer Plate

	Entrance		
	Right		Left
Tube #	Tube Discharge Mass Flow Rate [g/s]		
1	14.6703171		10.9034908
2	9.85237614		9.80182002
3	11.1156707		11.508079
4	13.69759		14.0244305
5	15.8294753		19.2592593
6	17.8976378		20.7165354
7	18.2692308		14.7559172
8	19.811155		21.7830479
9	20.3670473		14.3311582
10	20.0909947		18.6413555
11	19.4929078		20.9539007
12	22.1419676		38.5678705
13	22.1730245		46.9959128
14	22.5701944		29.4924406
15	22.2590546		24.3585021
Sum	270.24		316.09

Table A.19: Air Mass Flow for 3.175mm Spacer Plate, Top Right Entrance

	Inlet mass flow Rate [g/s]		
	0.439466	3.092382	4.427838
Tube #	Tube Discharge Mass Flow Rate [g/s]		
1	0	0.093016	0.14866
2	0.018824	0.185756	0.28777
3	0	0.028098	0.074468
4	0.00955	0.130112	0.213578
5	0.00955	0.14866	0.232126
6	0.018824	0.19503	0.2414
7	0.018824	0.185756	0.259948
8	0.028098	0.204304	0.306318
9	0.046646	0.278496	0.389784
10	0.0392268	0.259948	0.352688
11	0.0429364	0.250674	0.343414
12	0.046646	0.269222	0.352688
13	0.05592	0.278496	0.408332
14	0.0485008	0.28777	0.408332
15	0.05592	0.297044	0.408332

Table A.20: Air Pressure Profile for 3.175mm Spacer Plate, Top Right Entrance

	Inlet mass flow Rate [g/s]		
	0.439466	3.092382	4.427838
	Manifold Static Pressure [kPa]		
P1	2.587286	22.82501	46.53051
P2	1.733888	16.79704	34.731944
P3	1.618747	14.83287	62.413195
P4	1.862575	16.20102	33.1877
P5	2.025127	18.05005	36.946715

Table A.21: Air Mass Flow for 3.175mm Spacer Plate, Top Left Entrance

	Inlet mass flow Rate [g/s]		
	0.513934	3.055286	N/A
Tube #	Tube Discharge Mass Flow Rate [g/s]		
1	0.05592	0.28777	
2	0.05592	0.28777	
3	0.046646	0.278496	
4	0.05592	0.278496	
5	0.046646	0.250674	
6	0.037372	0.222852	
7	0.028098	0.19503	
8	0.037372	0.222852	
9	0.05592	0.278496	
10	0.00955	0.120838	
11	0.028098	0.157934	
12	0	0.083742	
13	0.000276	0.111564	
14	0	0.00955	
15	0.065194	0.269222	

Table A.22: Air Pressure Profile for 3.175mm Spacer Plate, Top Left Entrance

	Inlet mass flow Rate [g/s]		
	0.513934	3.055286	N/A
	Manifold Static Pressure [kPa]		
P1	1.937078	20.000669	
P2	2.004808	20.156448	
P3	1.970943	19.811025	
P4	1.517152	14.304576	
P5	1.605201	16.011372	

Table A.23: Air Mass Flow for 3.175mm Spacer Plate, Bottom Right Entrance

	Inlet mass flow Rate [g/s]		
	0.384098	3.055286	N/A
Tube #	Tube Discharge Mass Flow Rate [g/s]		
1	0	0.083742	
2	0.018824	0.19503	
3	0	0.028098	
4	0.00955	0.139386	
5	0.018824	0.14866	
6	0.018824	0.185756	
7	0.018824	0.176482	
8	0.028098	0.19503	
9	0.046646	0.278496	
10	0.046646	0.250674	
11	0.046646	0.259948	
12	0.046646	0.259948	
13	0.046646	0.278496	
14	0.028098	0.278496	
15	0.018824	0.297044	

Table A.24: Air Pressure Profile for 3.175mm Spacer Plate, Bottom Right Entrance

	Inlet mass flow Rate [g/s]		
	0.384098	3.055286	N/A
	Manifold Static Pressure [kPa]		
P1	2.864979	22.62859	
P2	2.004808	15.97751	
P3	1.794845	14.37908	
P4	2.018354	16.0046	
P5	2.255409	17.91459	

Table A.25: Air Mass Flow for 3.175mm Spacer Plate, Bottom Left Entrance

	Inlet mass flow Rate [g/s]		
	0.398009	3.092382	N/A
Tube #	Tube Discharge Mass Flow Rate [g/s]		
1	0.046646	0.297044	
2	0.046646	0.297044	
3	0.042009	0.278496	
4	0.046646	0.278496	
5	0.037372	0.278496	
6	0.028098	0.213578	
7	0.018824	0.185756	
8	0.028098	0.222852	
9	0.046646	0.28777	
10	0.000276	0.111564	
11	0.018824	0.157934	
12	0	0.074468	
13	0.000276	0.111564	
14	0	0.018824	
15	0.046646	0.278496	

Table A.26: Air Pressure Profile for 3.175mm Spacer Plate, Bottom Left Entrance

	Inlet mass flow Rate [g/s]		
	0.398009	3.092382	N/A
	Manifold Static Pressure [kPa]		
P1	2.038673	19.113406	
P2	2.106403	19.208228	
P3	2.079311	19.052449	
P4	1.571336	13.498589	
P5	1.666158	15.17152	

Table A.27: Water Mass Flow for 3.175mm Spacer Plate

	Entrance		
	Right		Left
Tube #	Tube Discharge Mass Flow Rate [g/s]		
1	2.1529844		9.938736216
2	17.399042		20.14373717
3	0		10.65062876
4	6.3335569		13.76481109
5	5.2460114		7.36137454
6	14.693252		21.14860259
7	13.657382		16.15877437
8	15.809802		19.10094125
9	24.316832		26.36138614
10	21.644042		2.202111614
11	21.031308		15.5985267
12	22.619926		2.387981023
13	24.021207		7.108482871
14	24.594937		13.47257384
15	23.930718		18.77341817
Sum	237.45		204.17

A.4 FORTRAN Code for BCC Non-Dimensional Model

```
!SOURCE CODE FOR BAJURA Q EQUATION
!AUTHOR: DANIEL M. TOMPKINS
!2002
!THIS PROGRAM SOLVES THE 2ND ORDER NONLINEAR ODE GIVEN BY BAJURA
!THIS PROGRAM IS FOR USE IN THE BAJURA-CHOU-CHENG NON-DIM MODEL

   PROGRAM BAJURA

!  VARIABLE DECLARATIONS
   INTEGER N      !NUMBER OF DE'S:2

         REAL*8  Y(2)

         REAL*8  F(2)

         REAL*8  Y1(0:1000)

         REAL*8  Y2(0:1000)

         REAL*8          DELP(0:1000)

         REAL*8          Z
         REAL*8          PINIT

REAL*8  X     !IND VAR, IN THIS CASE ETA
REAL*8  XMAX
REAL*8  H
INTEGER M
INTEGER K

!INITIAL MASS FLOW RATE
REAL*8          MINIT

!MICROCHANNEL AND MANIFOLD PROPERTIES
REAL*8 SPACER
REAL*8 DMC
REAL*8 LMC
REAL*8 FMC
REAL*8 AMC
REAL*8 CTD
INTEGER         MCNUMBER
!PARAMETERS WHICH COMPRISE PHI
REAL*8          AC
REAL*8          DC
REAL*8          LC
REAL*8          FC
REAL*8          RES
REAL*8          AR
REAL*8          PHI
!PARAMETERS WHICH COMPRISE M1
REAL*8          THETA
REAL*8          MONE

REAL*8          GAMMA
```

```
REAL*8          BETA
REAL*8          ALPHA



SPACER=0.0127/4 !SPACER=INPUT. NOTE THERE ARE THREE DIFFERENT SPACERS
DMC=                    !HYDRAULIC DIAMETER OF THE MICROCHANNELS
LMC=                    !LENGTH OF THE MICROCHANNELS
FMC=                      !MICROCHANNEL FRICTION FACTORS
AMC=                      !AREA OF THE MICROCHANNELS
CTD=                    !TURNING COEFFICIENT
MCNUMBER=15                     !NUMBER OF MICROCHANNELS

AC=.0185*SPACER                         !AREA OF THE MANIFOLD CHANNEL
DC=(4*AC)/(2*SPACER+2*0.0185)       !HYDRAULIC DIAMETER OF THE CHANNEL
LC=                                     !LENGTH OF THE CHANNEL
FC=                                     !CHANNEL FRICTION FACTORS
RES=1+CTD+FMC*LMC/DMC               !LATERAL RESISTANCE
AR=MCNUMBER*AMC/AC                  !AREA RATIO
PHI=AR*AR*FC*LC/(RES*2*DC)                  !PARAMETER PHI

THETA=                                  !PARAMETER THETA

MONE=AR*AR*THETA/RES                !PARAMETER M1

GAMMA=                                  !GAMMA COEFFICIENT

!DEFINING ALPHA AND BETA TO USE INSTEAD
ALPHA=SQRT(FC*LC/(DC*RES))*AR
BETA=SQRT((2-GAMMA)/RES)*AR


Z=AR*SQRT(2/RES)

H=0.07142857142857142857142857142857

!       OPEN OUTPUT FILE

    OPEN(UNIT=1,FILE='OUTPUT.DAT',STATUS='UNKNOWN')

!       PROMPT USER FOR NEEDED INFORMATION
    WRITE(*,*) 'ENTER THE INITIAL VALUE OF Q`(0)'
    READ(*,*)   Y(1)

          WRITE(*,*) 'ENTER THE INITIAL M-DOT'
          READ(*,*)         MINIT

          WRITE(*,*) 'ENTER THE MAXIMUM ETA'
    READ(*,*) XMAX


!       PUT MANIFOLD ON OUTPUT FILE
    WRITE(1,5) Y(1)


    WRITE(1,*)  'ETA     Q       Q`(X)/Q`(0)      !DELP'
```

```
!                    ORIGINAL FILE
!     Y(1)=Q'

!     Y(2)=Q

!     SET INTIAL VALUES OF Y(N)

      M=0         !0

      N=2   !5

      X=0

      Y(2)=1.D0       !INITIAL CONDITION OF Q(0)=1

      Y1(0)=Y(1)

      Y2(0)=Y(2)  !I'M SEEING IF THIS WILL SOLVE A BOUNDARY PROBLEM
            !Y2(XMAX)=0.D0


!     CALCULATION OF Q, Q'

      XMAX=XMAX/H

      DO 200 I=1,INT(XMAX)

9     CALL RUNGE(N,Y,F,X,H,M,K)

            GOTO (30,40),K


!     DERIVATIVES OF Y(1)-Y(2)



30    F(1)=(-1*MONE*Y(2)*Y(1)-1*PHI*Y(2)*Y(2))/(2*Y(1))

      F(2)=Y(1)       !Y(1)


      GOTO 9


!     STORE VALUES OF Y(1)-Y(2)


40    CONTINUE

      Y1(I)=Y(1)

      Y2(I)=Y(2)
      DELP(I)=Y1(I)*Y1(I)/Z

200   CONTINUE
```

```
300     CONTINUE
!       OUTPUTE FINAL DATA

      X=0
      DO 400 I=0, XMAX
          WRITE(1,15) X,Y2(I),Y1(I)/Y1(0)*MINIT!, (DELP(I)+PINIT)/PINIT
          X=X+H
400     CONTINUE

!       CLOSE OUTPUT FILE
      CLOSE(UNIT=1)

!       FORMAT STATEMENTS

5       FORMAT(' INITIAL VALUE OF Q`(0) ',F7.5)
15      FORMAT(F5.3,2X,F8.6,2X,F8.6,2X,F8.6,2X,F8.6,2X,F8.6)
END
SUBROUTINE RUNGE(N,Y,F,X,H,M,K)
!       RUNGE ROUTINE
   REAL*8 Y(N),F(N),Q(N),X,H,A
   INTEGER N,M,K
   M=M+1
     GOTO(1,4,5,3,7),M
1       DO      2       I=1,N
           Q(I)=0.D0
2       CONTINUE
      A=0.5
      GOTO 9
```

```
3     A=1.7071067811865475244
4     X=X+0.5*H
5     DO 6 I=1,N
        Y(I)=Y(I)+A*(F(I)*H-Q(I))
        Q(I)=2.D0*A*H*F(I)+(1.D0-3.D0*A)*Q(I)
6     CONTINUE
      A=0.2928932188134524756
      GOTO 9
7     DO 8 I=1,N
        Y(I)=Y(I)+H*F(I)/6.D0-Q(I)/3.D0
8     CONTINUE
      M=0
      K=2
      GOTO 10
9     K=1
10    RETURN

      END
```

A.5 Pictures of Manifold

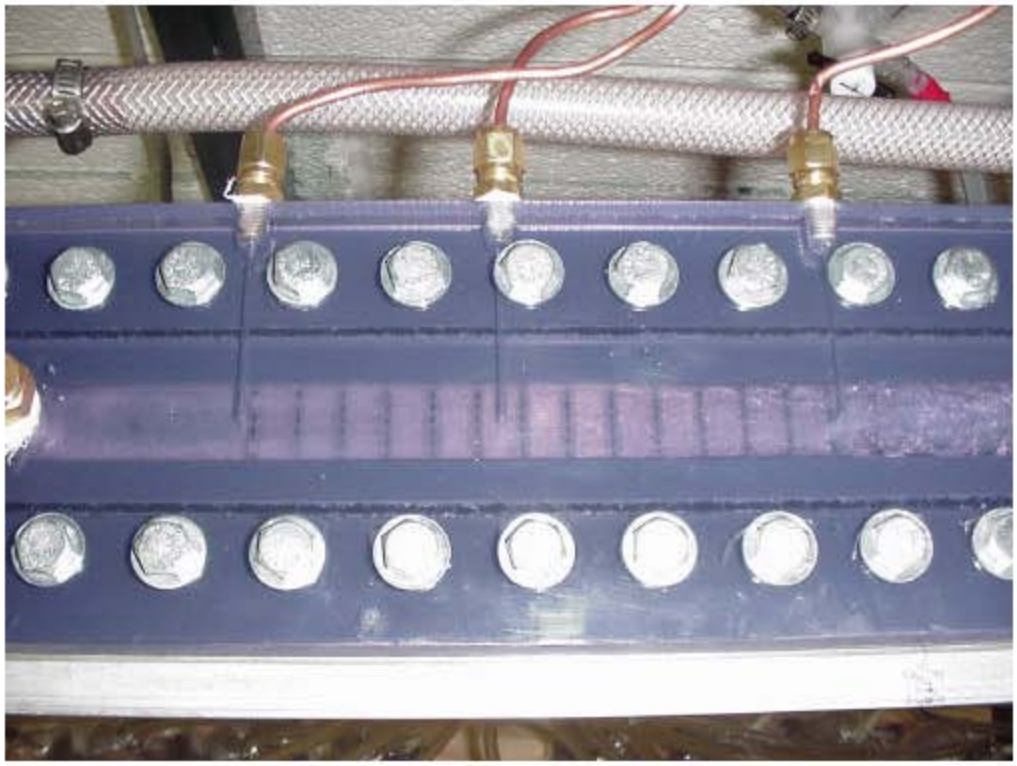

Figure A.3: Top View of Manifold Showing Flow

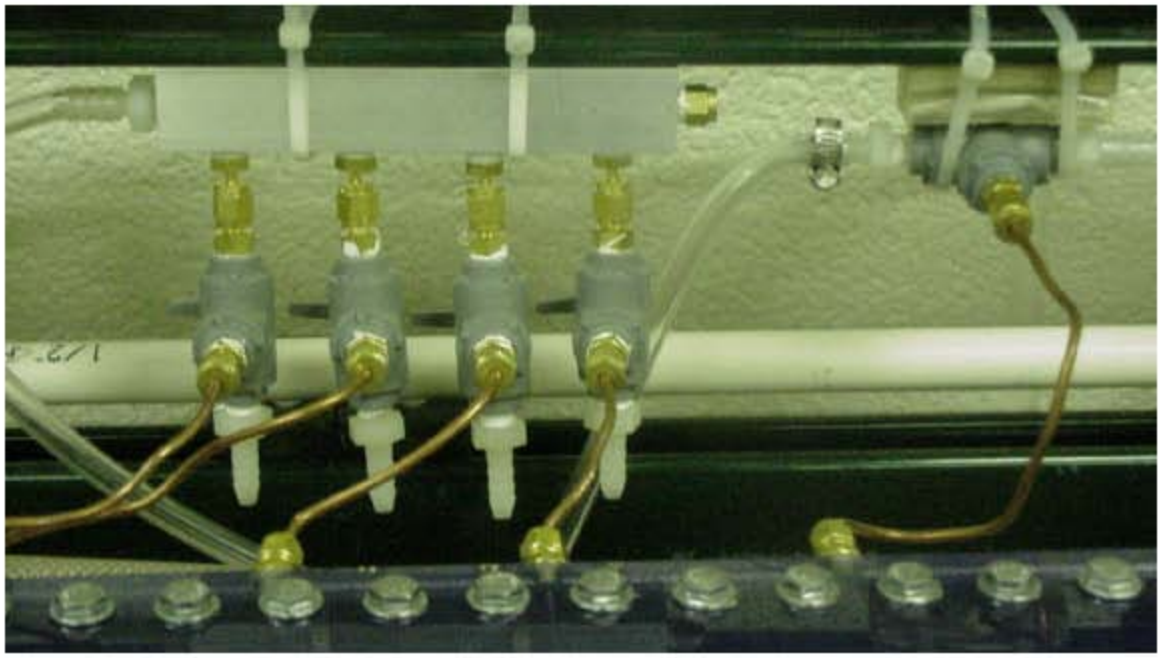

Figure A.4: Pressure System for Manifold

Appendix B: Two-Phase Modeling

B.1 Homogeneous Model Predictions—Remaining

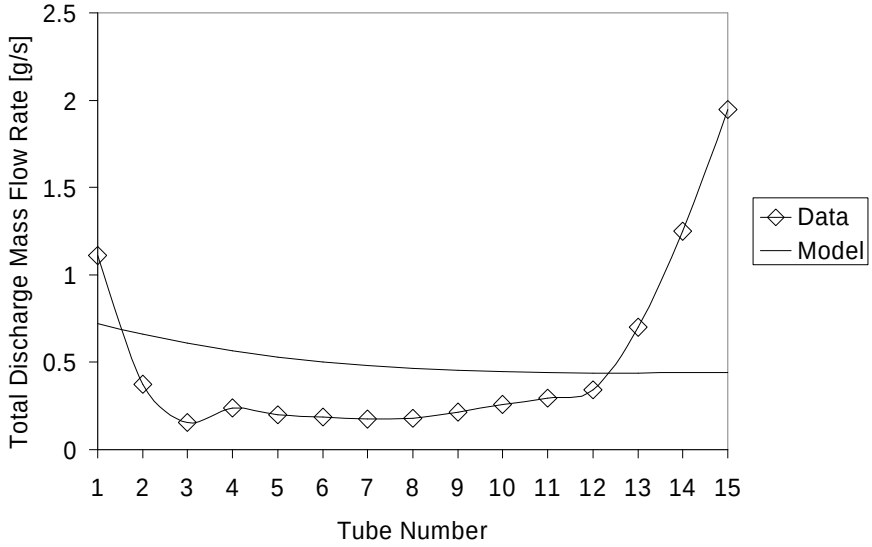

Figure B.1: Homogeneous Prediction, 3.175mm Spacer Plate: Test 5

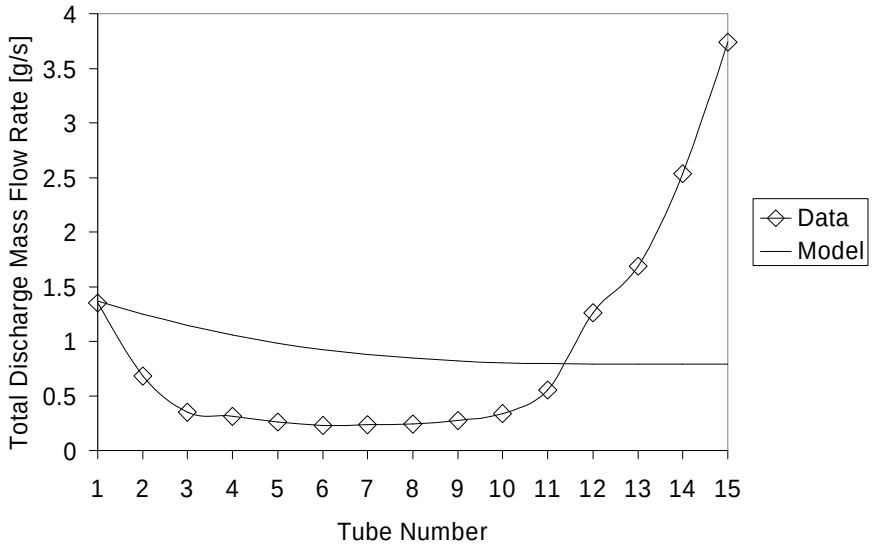

Figure B.2: Homogeneous Prediction, 3.175mm Spacer Plate: Test 7

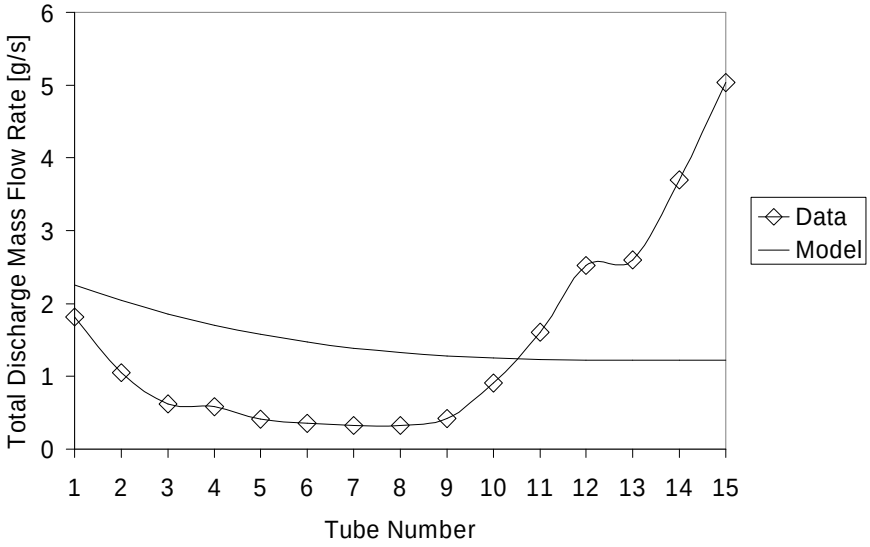

Figure B.3: Homogeneous Prediction, 3.175mm Spacer Plate: Test 10

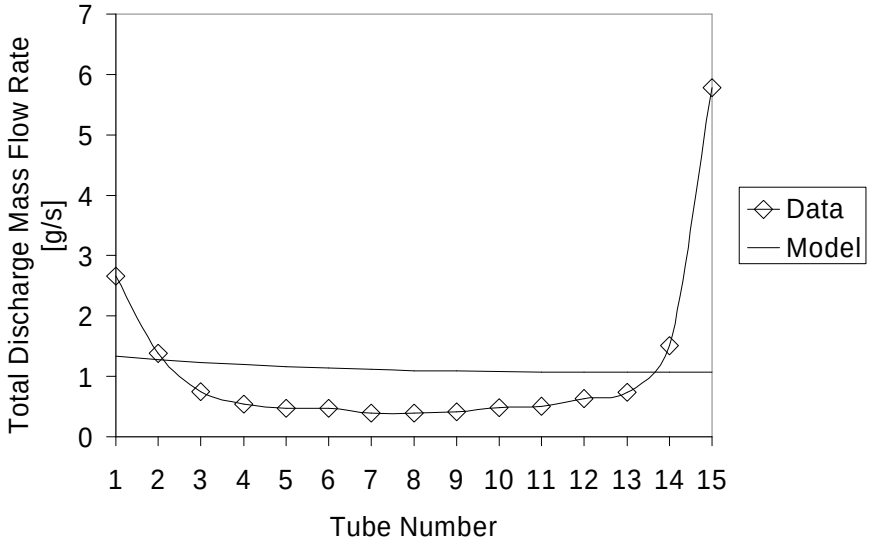

Figure B.4: Homogeneous Prediction, 6.35mm Spacer Plate: Test 4

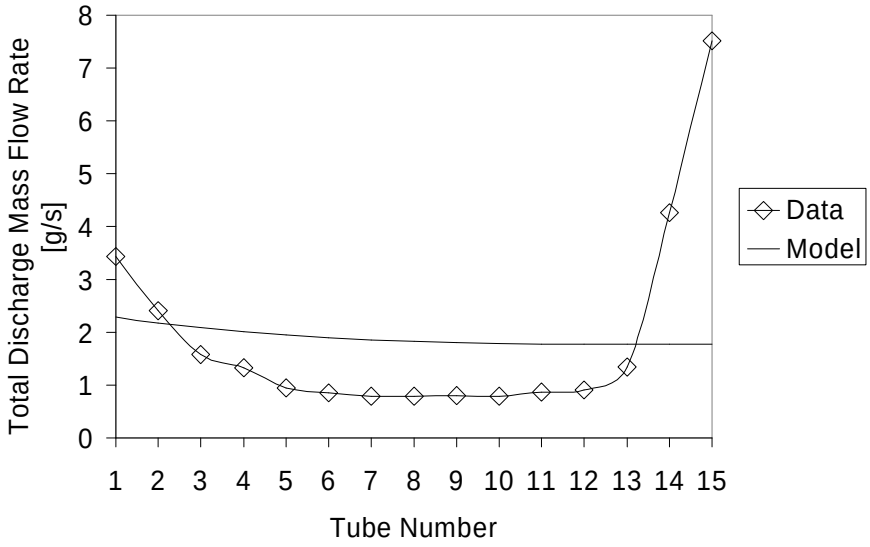

Figure B.5: Homogeneous Prediction, 6.35mm Spacer Plate: Test 8

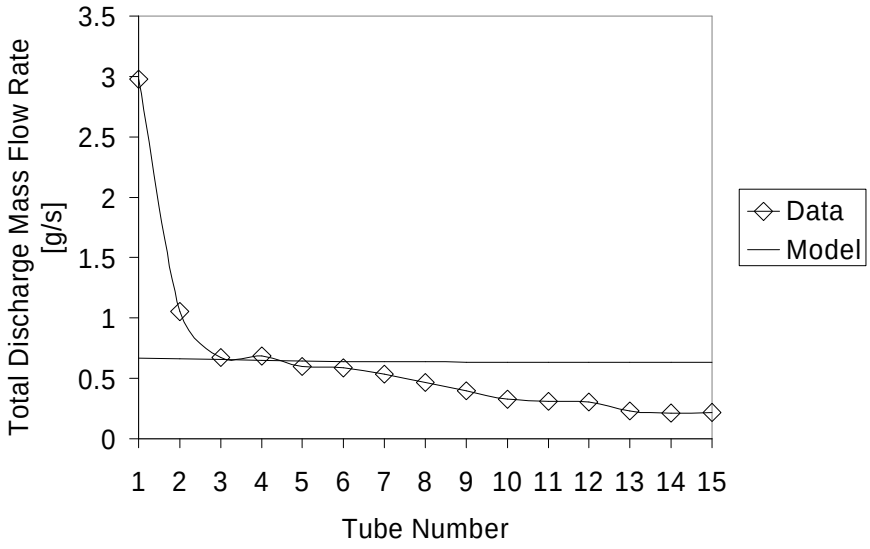

Figure B.6: Homogeneous Prediction, 12.7mm Spacer Plate: Test 2

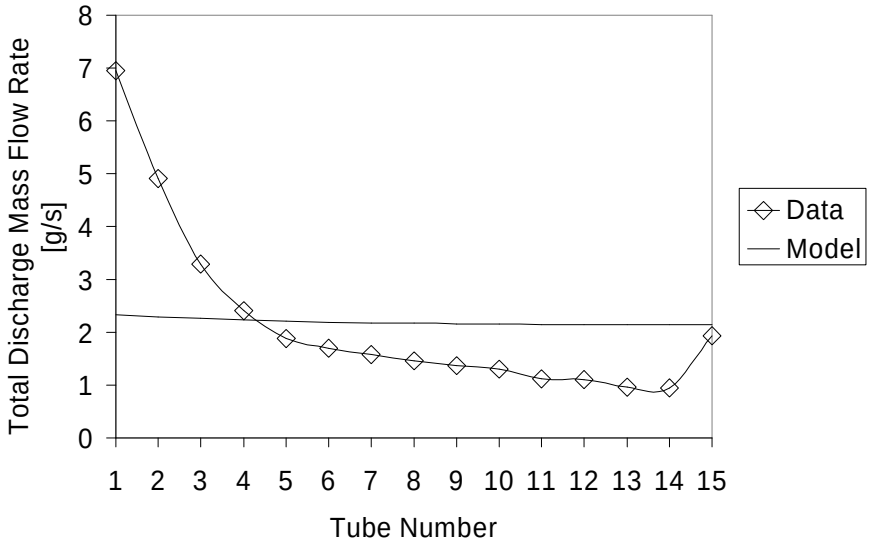

Figure B.7: Homogeneous Prediction, 12.7mm Spacer Plate: Test 4

B.2 TP-a Model Predictions—Remaining

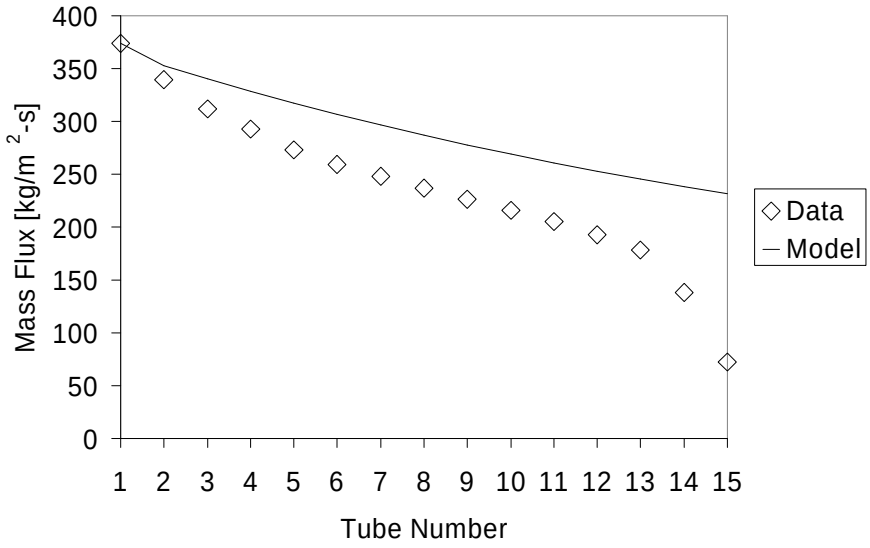

Figure B.8: Junction Inlet Mass Flux (TP-a), 6.35mm Spacer Plate, Test 11

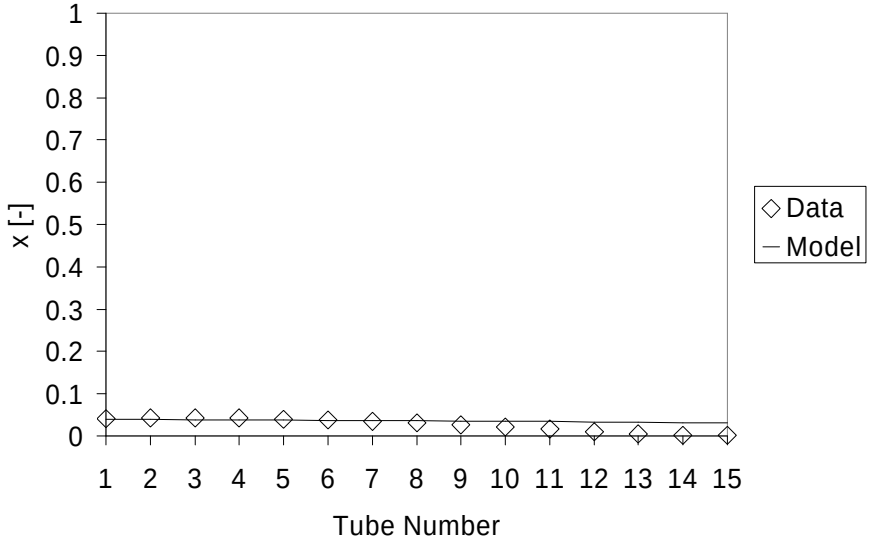

Figure B.9: Run Quality (TP-a), 6.35mm Spacer Plate, Test 11

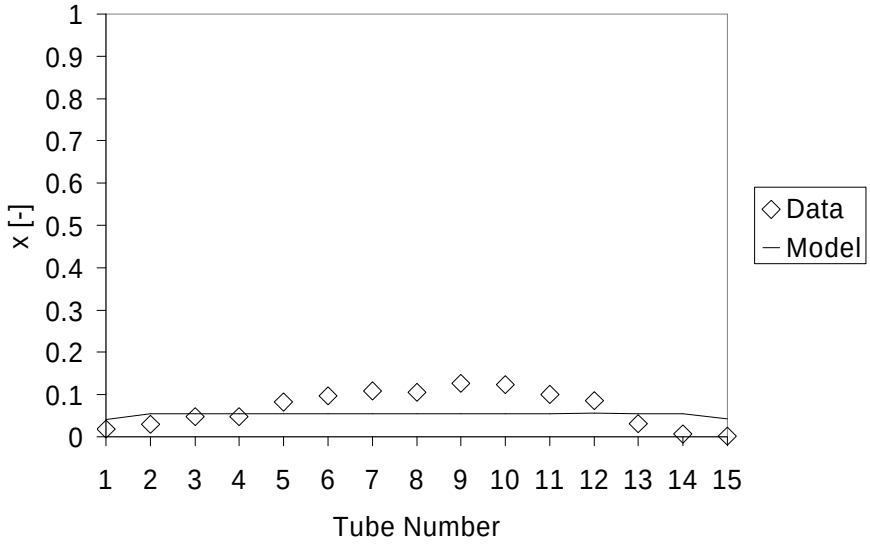

Figure B.10: Discharge Quality (TP-a), 6.35mm Spacer Plate, Test 11

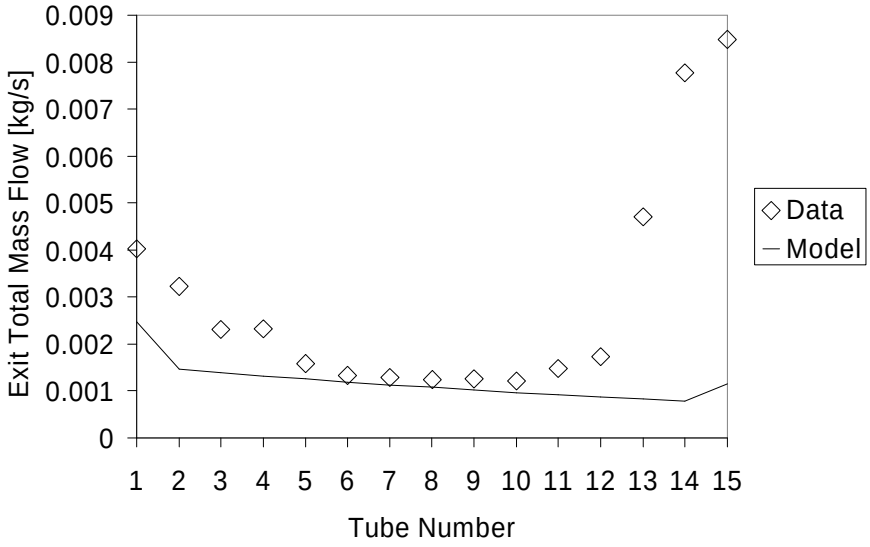

Figure B.11: Total Discharge Mass Flow (TP-a), 6.35mm Spacer Plate, Test 11

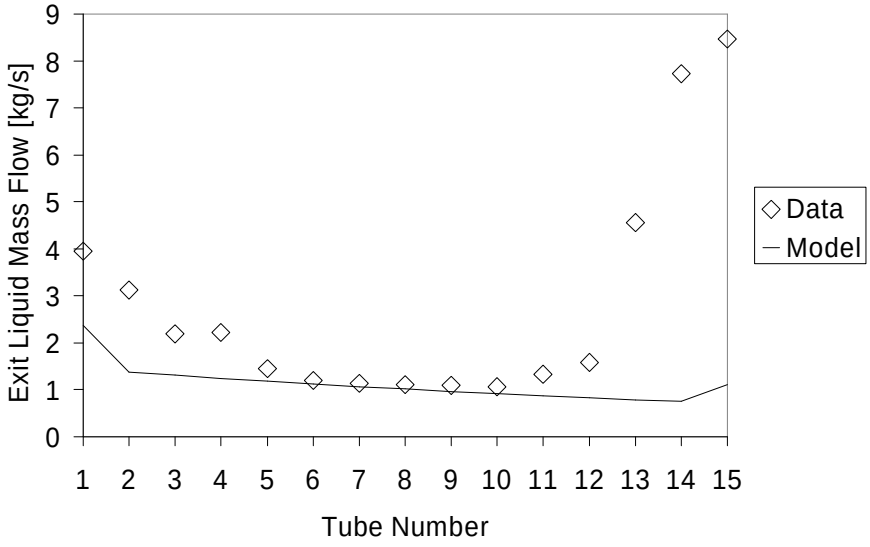

Figure B.12: Discharge Liquid Mass Flow (TP-a), 6.35mm Spacer Plate, Test 11

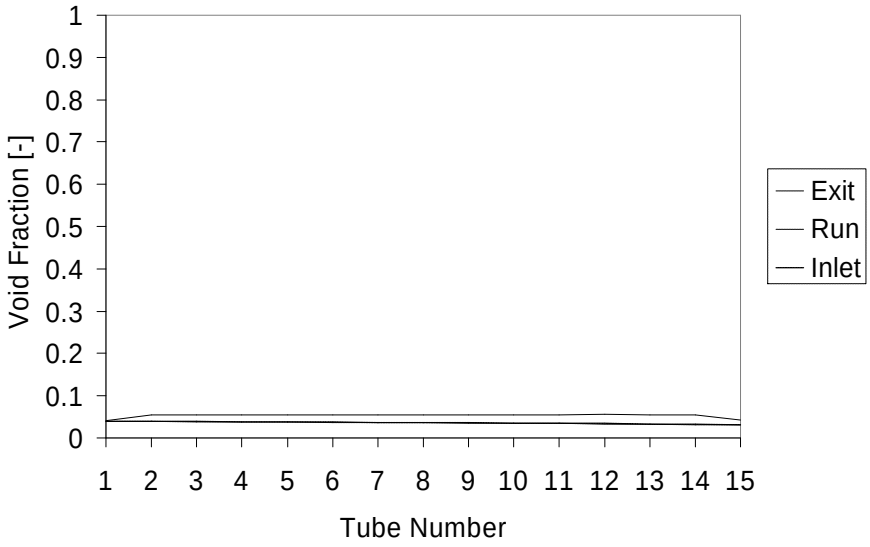

Figure B.13: Void Fraction (TP-a), 6.35mm Spacer Plate, Test 11

Appendix C: X-Ray Visualization

C.1 EES Code to Determine Experimental Conditions

This code uses a table of experimental values, such as temperature, pressure, and volumetric flow rate, to set the qualities at the exit of the test section during testing of R134a x-ray visualization experiments.

```
"Lookup Table"
"column 1---Q_dot_liq
        2---Q_dot_vap
        3---P_vap
        4---T_vap
        5---P_liq
        6---T_liq
        7---P_TSi {pressure at test section inlet}
        8---P_TSe {pressure at test section exit}
        9---T_TS {test section outlet Temp}
        10--atmos pressure"
"mass flow in kg/min"
"T in C"
"pressures in bar"

{variables}
        ports=6;
        refrig$='R134a'
        Nrow=34
        A_port=1.669e-5

Duplicate i=1,Nrow
{Inlet conditions}
        {Liquid Line}
        P_liq[i]=lookup(i,5)*6.894757 "+lookup(i,10) The pressure measured by the transducers is absolute"
        T_liq[i]=lookup(i,6)
        Q_dot_liq[i]=lookup(i,1)
        h_liq[i]=enthalpy(refrig$,x=0,T=T_liq[i])
{Vapor Line}
        P_vap[i]=lookup(i,3)*6.894757  "+lookup(i,10)*0.1 The pressure measured by the transducers is absolute"
        T_vap[i]=lookup(i,4)
        Q_dot_vap[i]=lookup(i,2)
        h_vap[i]=enthalpy(refrig$,P=P_vap[i],T=T_vap[i])
{Test Section Conditions}
{Temperature}
        T_TS[i]=lookup(i,9)
{Pressure Drop}
        P_TSe[i]=lookup(i,8)*6.894757 "+lookup(i,10) The pressure measured by the transducers is absolute"
        P_TSi[i]=lookup(i,7)*6.894757 "+lookup(i,10) The pressure measured by the transducers is absolute"
        dP[i]=P_TSi[i]-P_TSe[i]
       dPdz[i]=dP[i]/.609

{Properties}
        rho_liq[i]=density(refrig$,T=T_TS[i],x=0);
        rho_vap[i]=density(refrig$,T=T_TS[i],x=1);
        mu_liq[i]=viscosity(refrig$,T=T_TS[i],x=0);
        mu_vap[i]=viscosity(refrig$,T=T_TS[i],x=1);

m_dot_liq[i]=lookup(i,1)*rho_liq[i]
m_dot_vap[i]=lookup(i,2)*rho_vap[i]
```

```
{Enthalpy}
        h_mix[i]=(h_liq[i]*m_dot_liq[i]+h_vap[i]*m_dot_vap[i])/(m_dot_liq[i]+m_dot_vap[i])
{Quality}
        x[i]=quality(refrig$,P=P_TSi[i],h=h_mix[i])
{Mass Flux Calculation}
        MFlux[i]=(m_dot_liq[i]+m_dot_vap[i])/(A_port)

{Analysis of Conditions at equilibrium}
        P_2[i]=P_TSi[i]-dP[i]
        Tsat[i]=Temperature(refrig$,P=P_2[i],x=0.5);
        Error[i]=Abs(T_TS[i]-Tsat[i])
End
```

C.2 X-Ray Setup Pictures

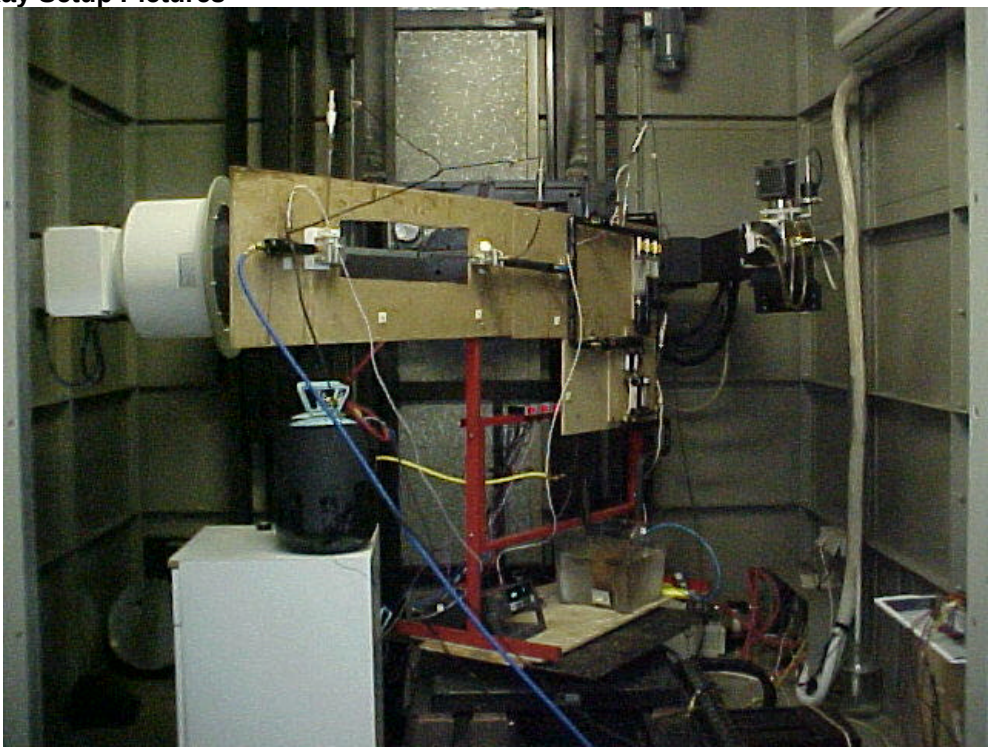

Figure C.1: X-Ray Experimental Setup, R134a, Open View

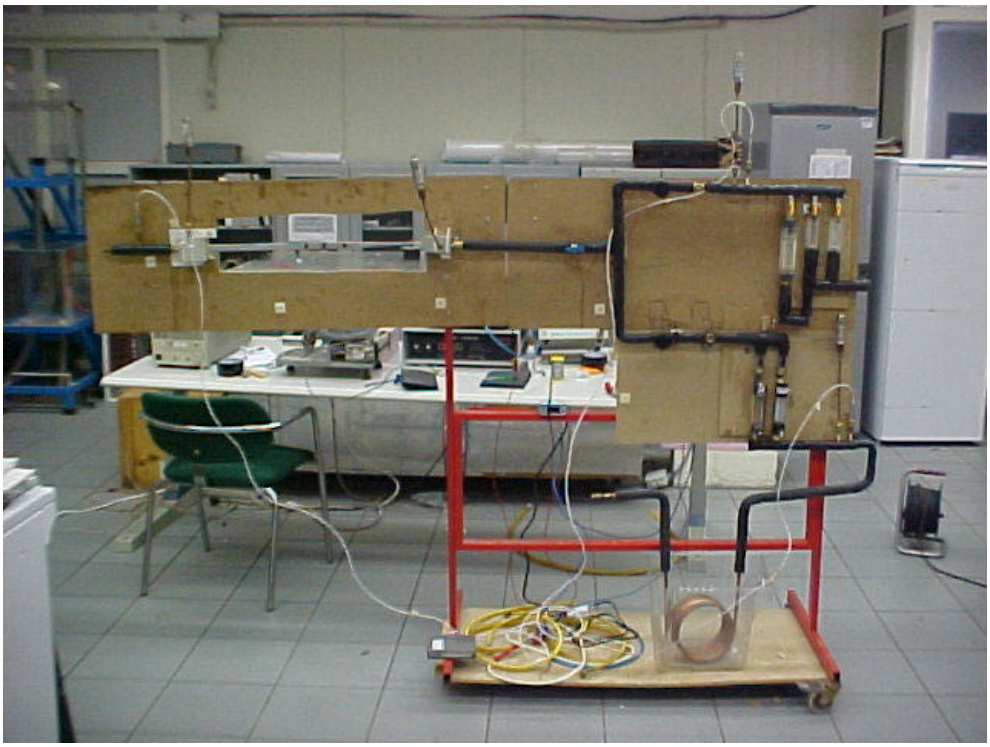

Figure C.2: X-Ray Experimental Setup, R134a, Frontal View

C.3 X-Ray Visualization Samples

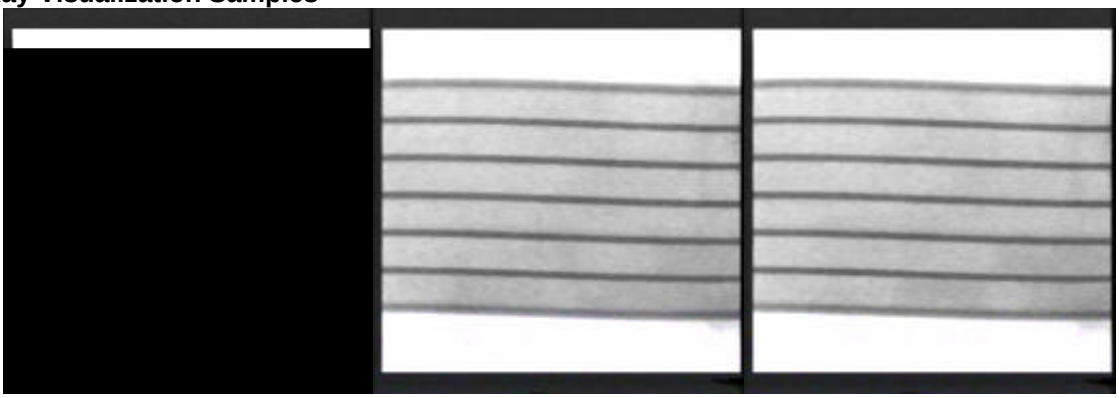

Figure C.3: Sample Pictures for Air-Water, G=50 kg/m^2·s, x=0.1

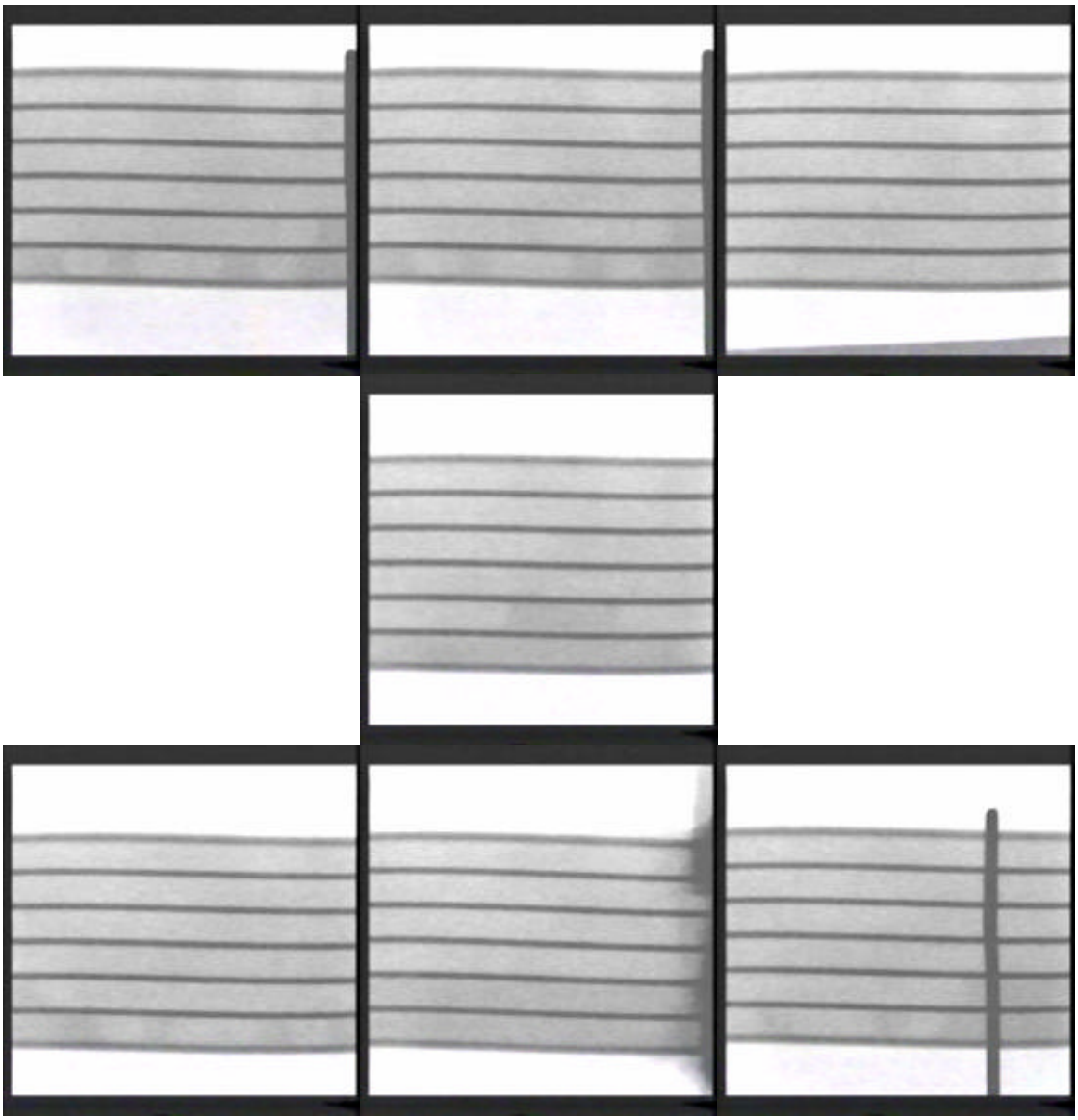

Figure C.4: Sample Pictures for Air-Water, G=50 kg/m^2·s, x=0.3

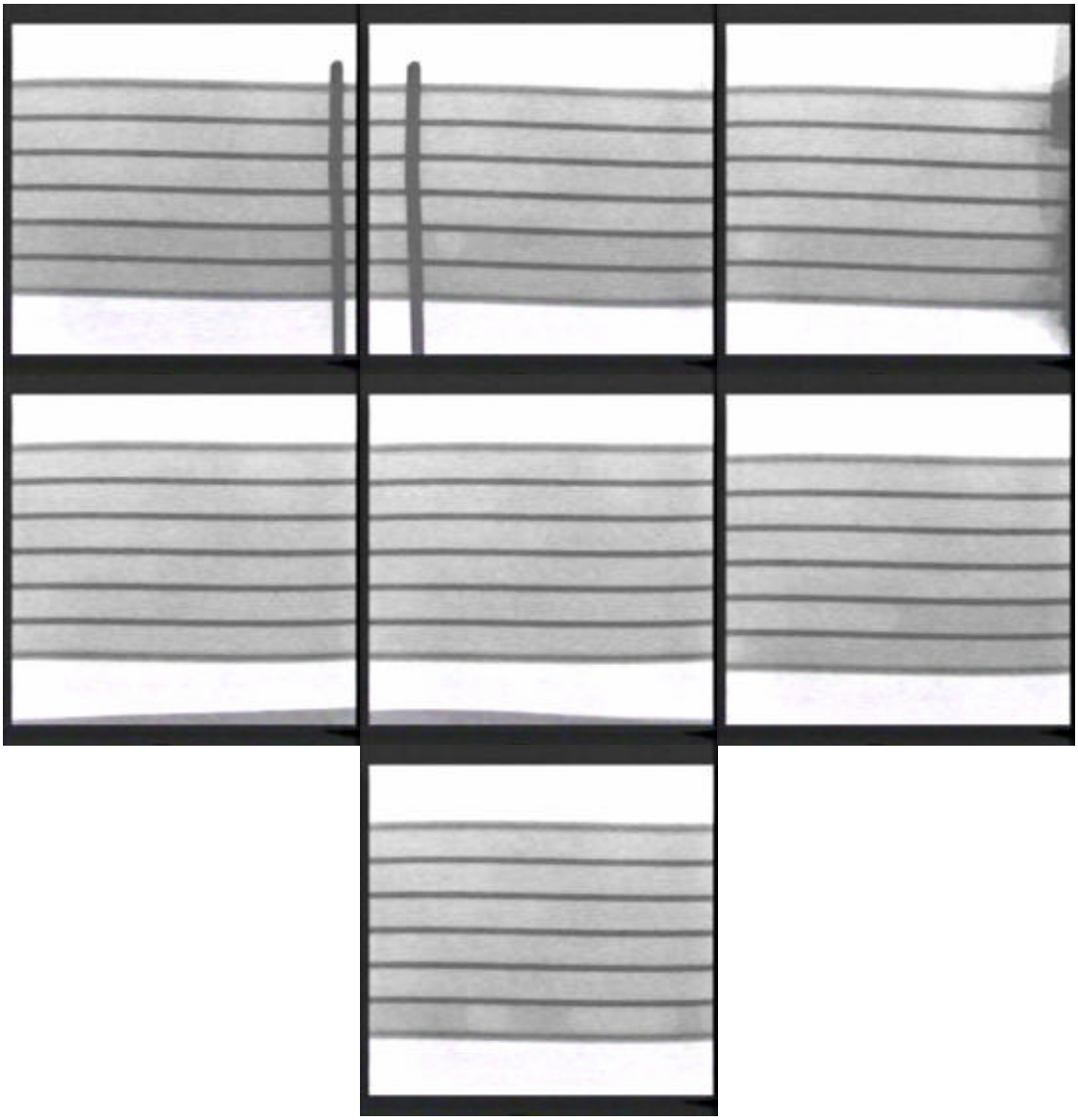

Figure C.5: Sample Pictures for Air-Water, G=50 kg/m^2·s, x=0.5

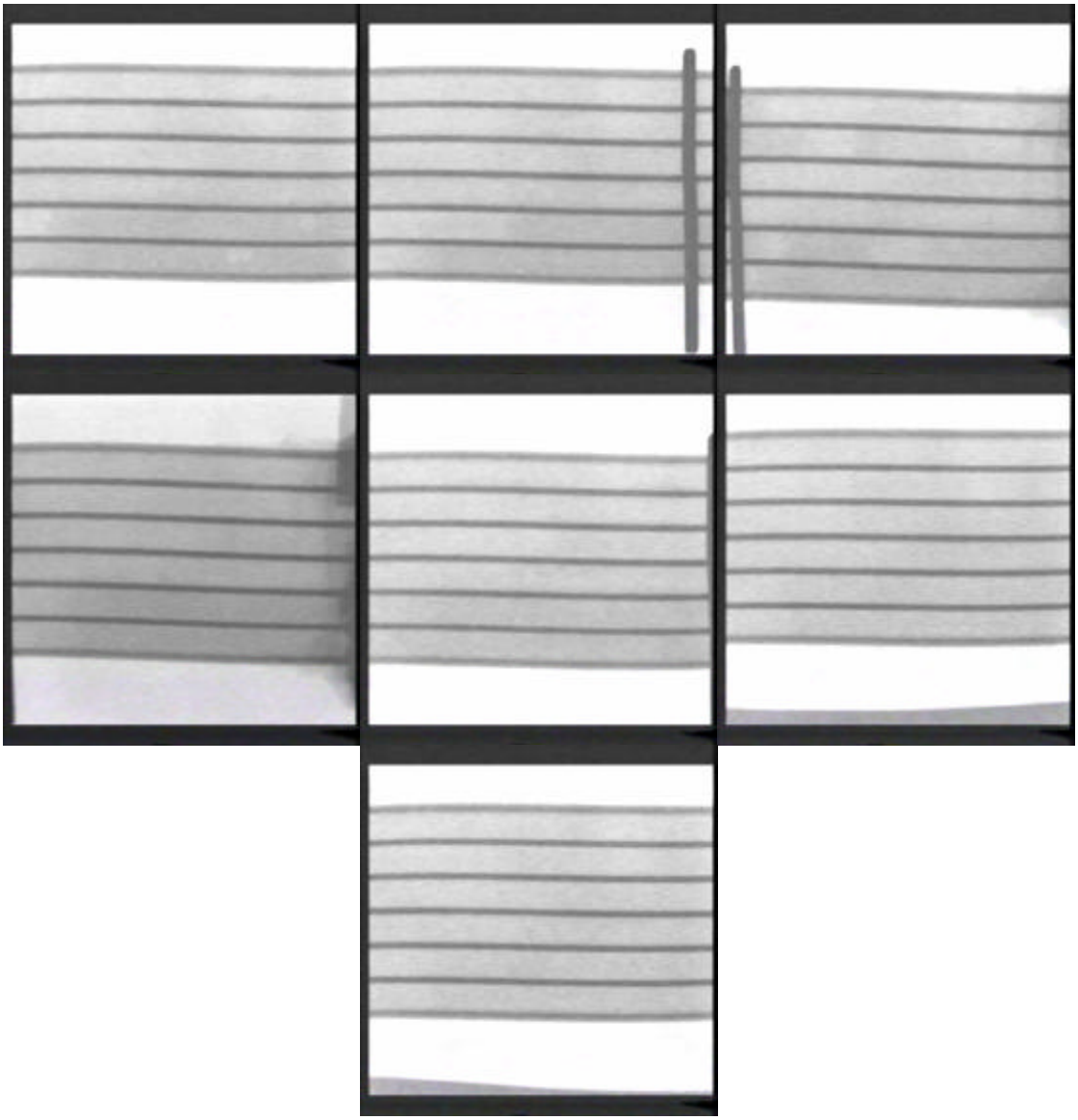

Figure C.6: Sample Pictures for Air-Water, G=100 kg/m^2·s, x=0.1

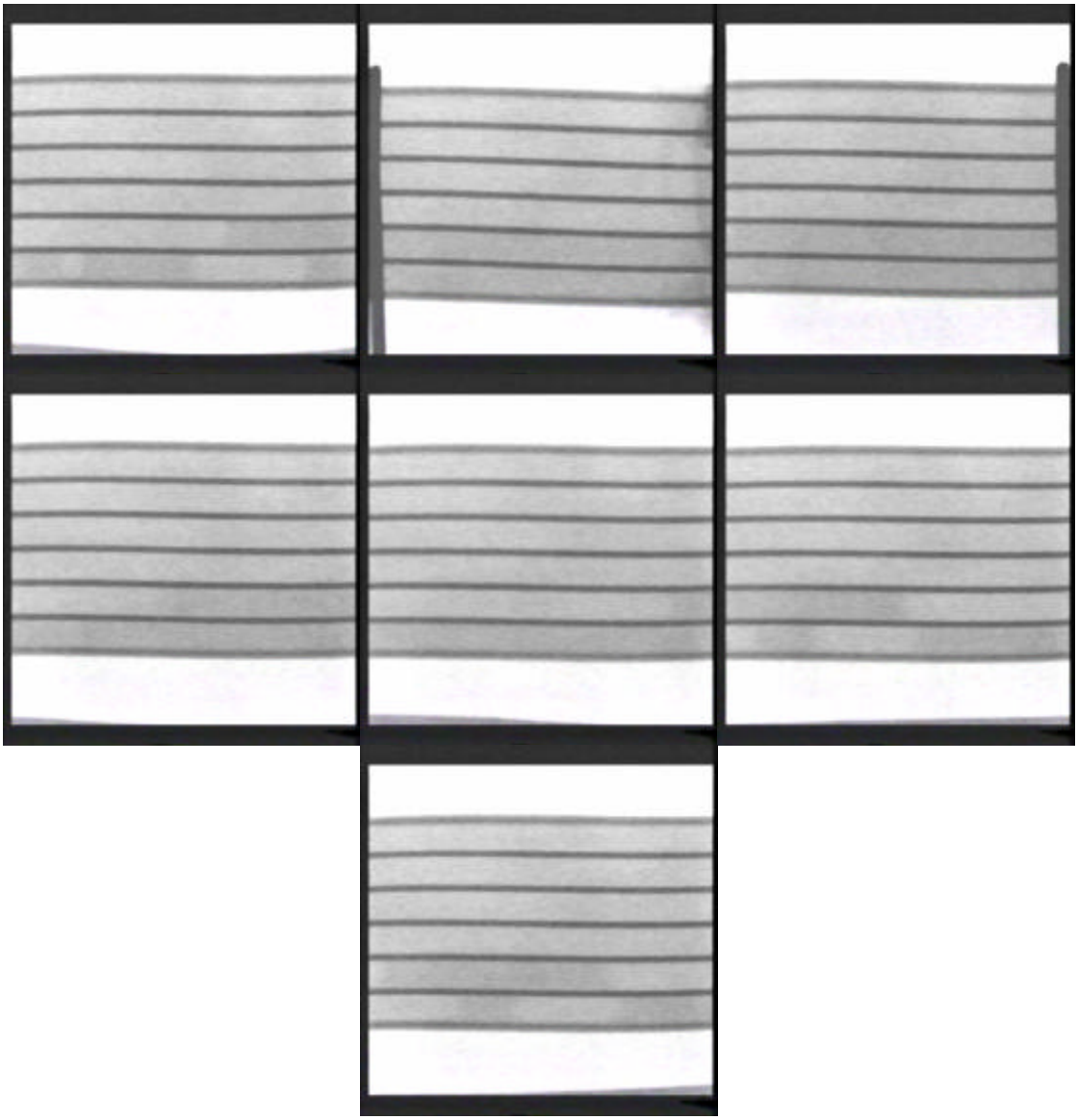

Figure C.7: Sample Pictures for Air-Water, G=100 kg/m^2·s, x=0.3

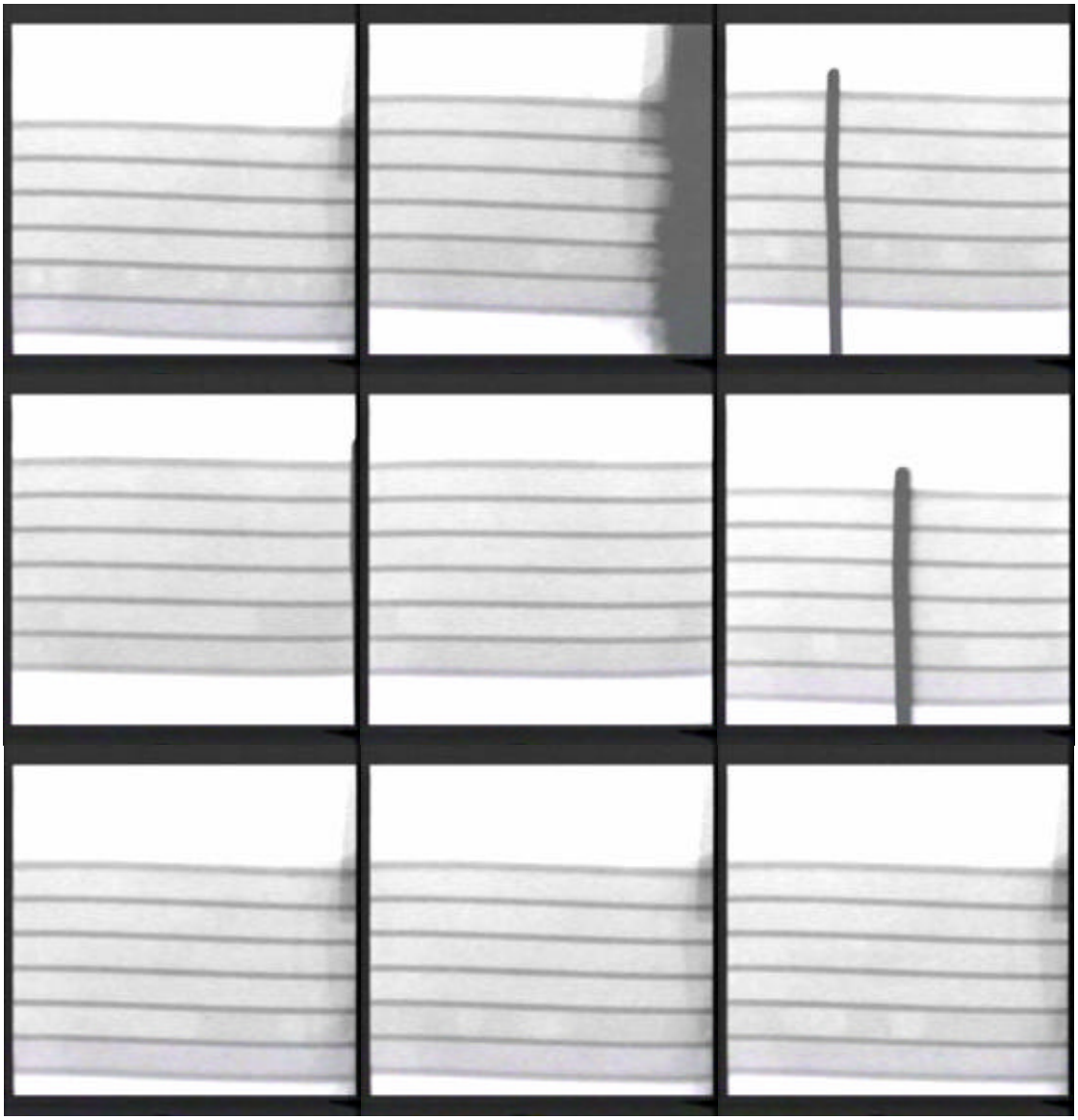

Figure C.8: Sample Pictures for Air-Water, G=100 kg/m^2·s, x=0.7

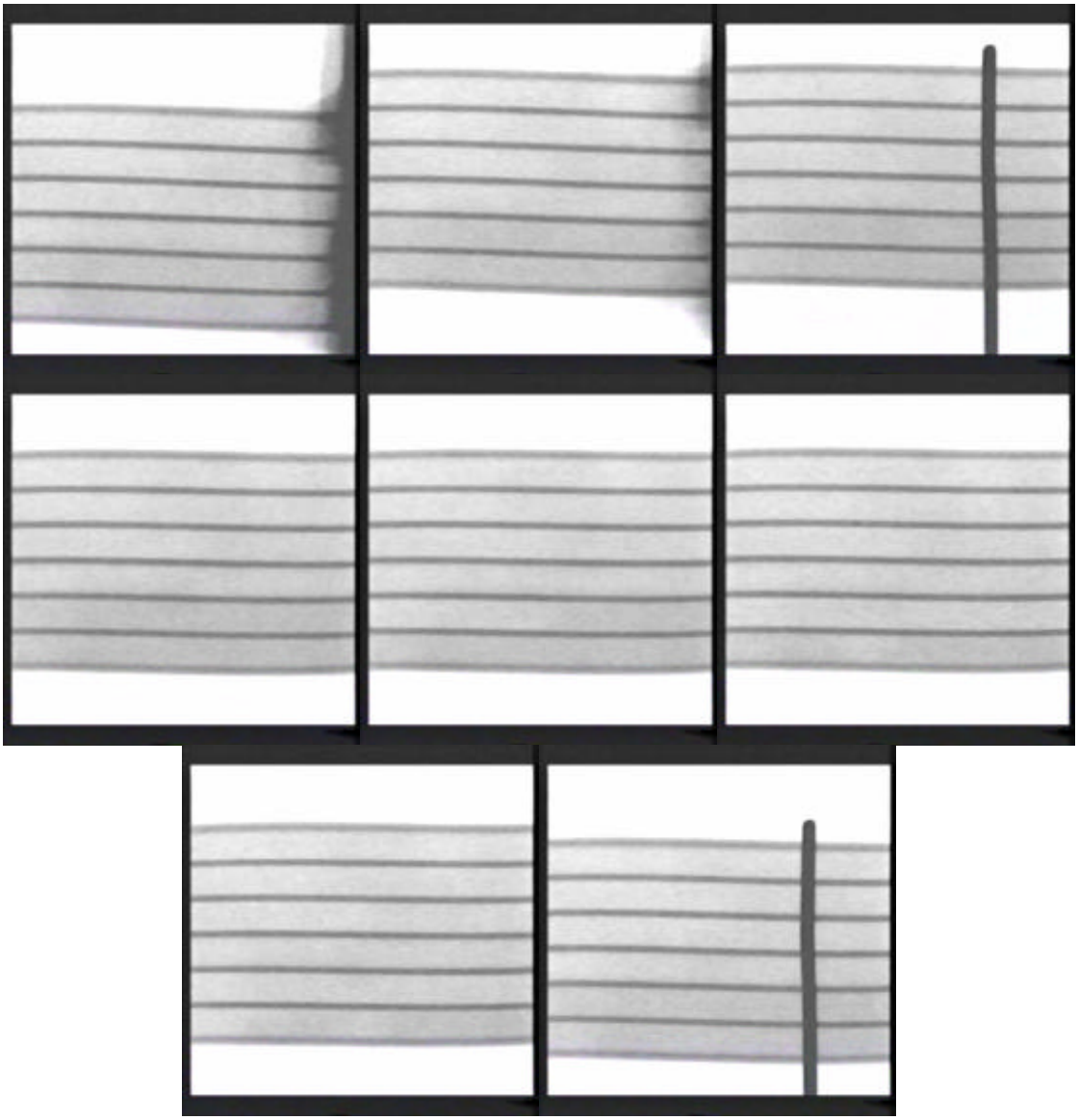

Figure C.9: Sample Pictures for Air-Water, G=150 kg/m^2·s, x=0.1

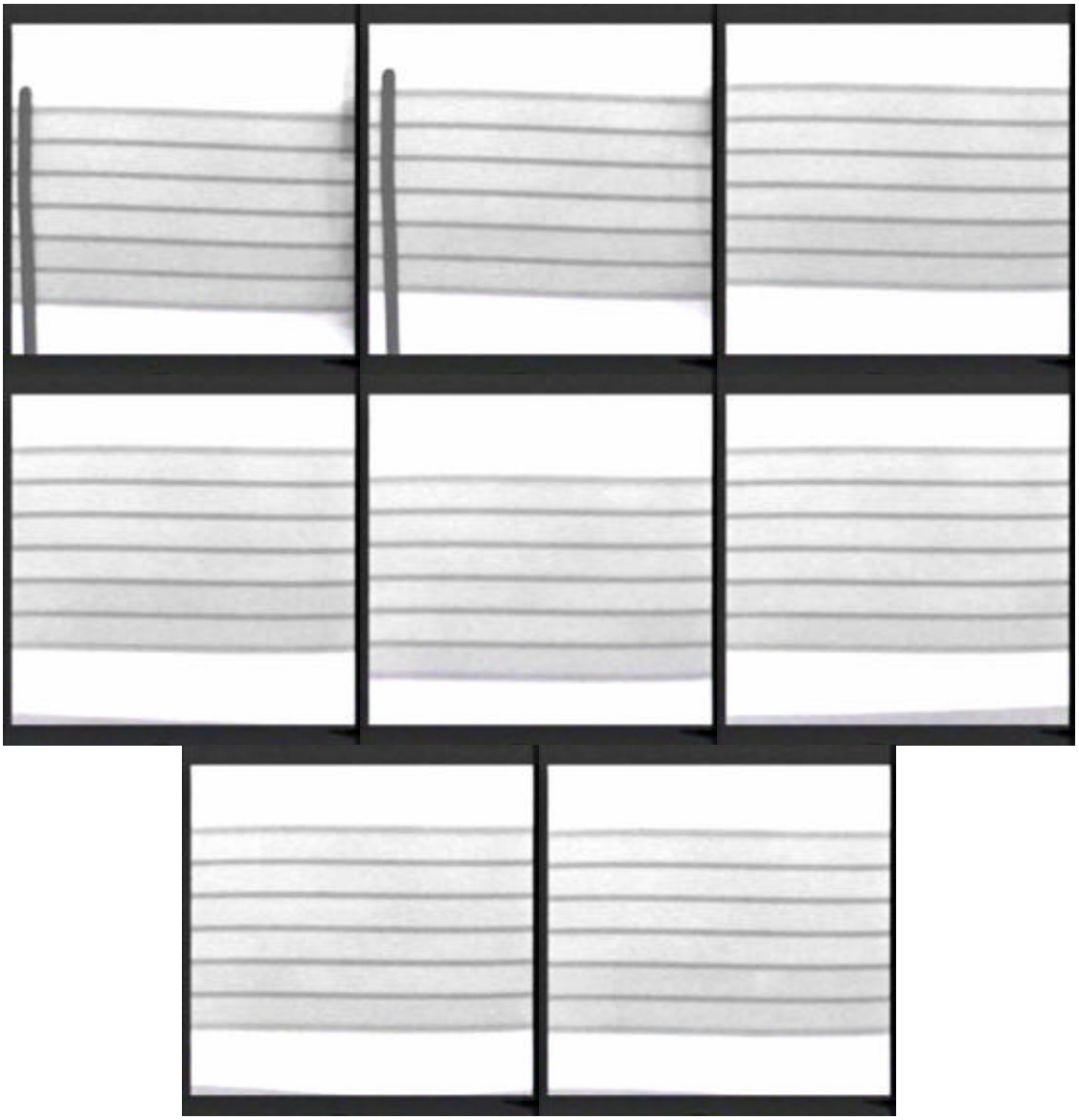

Figure C.10: Sample Pictures for Air-Water, G=150 kg/m^2·s, x=0.3

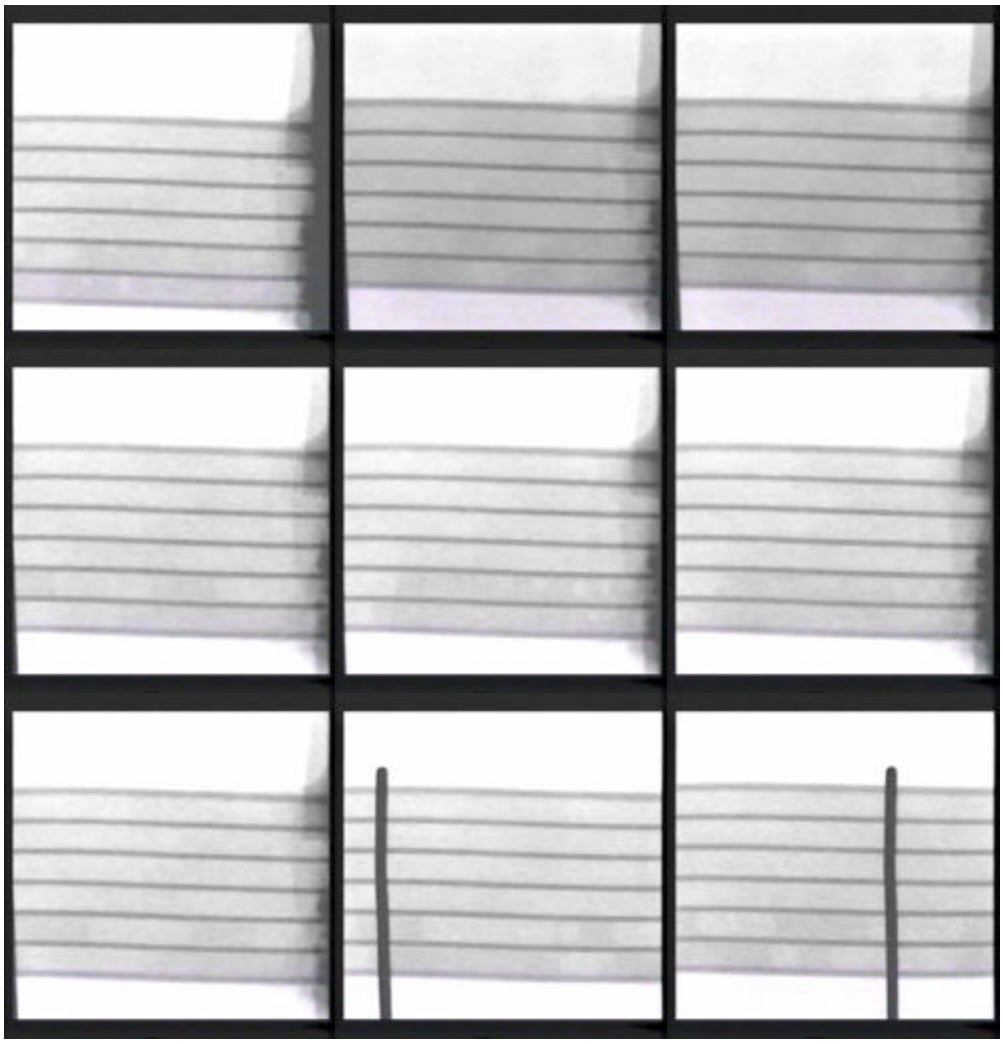

Figure C.11: Sample Pictures for Air-Water, G=150 kg/m^2·s, x=0.5

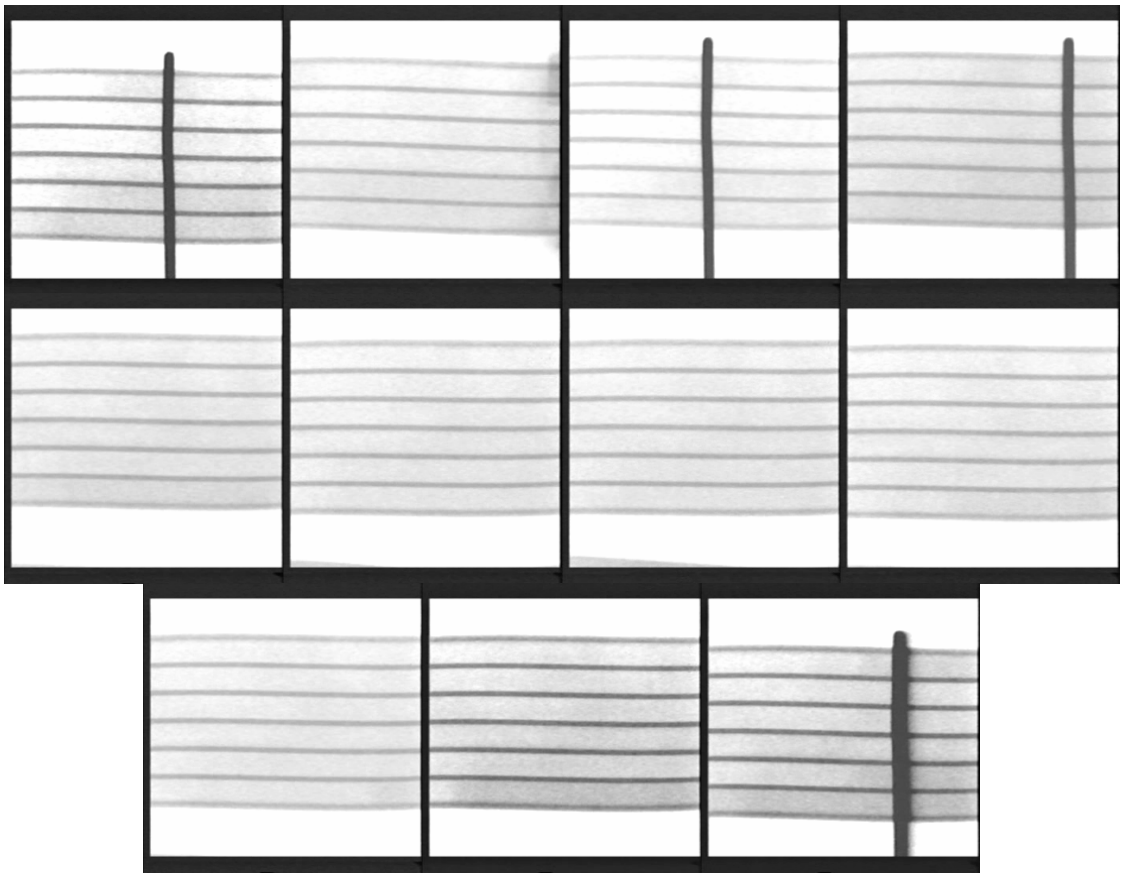

Figure C.12: Sample Pictures for Air-Water, G=200 kg/m^2·s, x=0.1

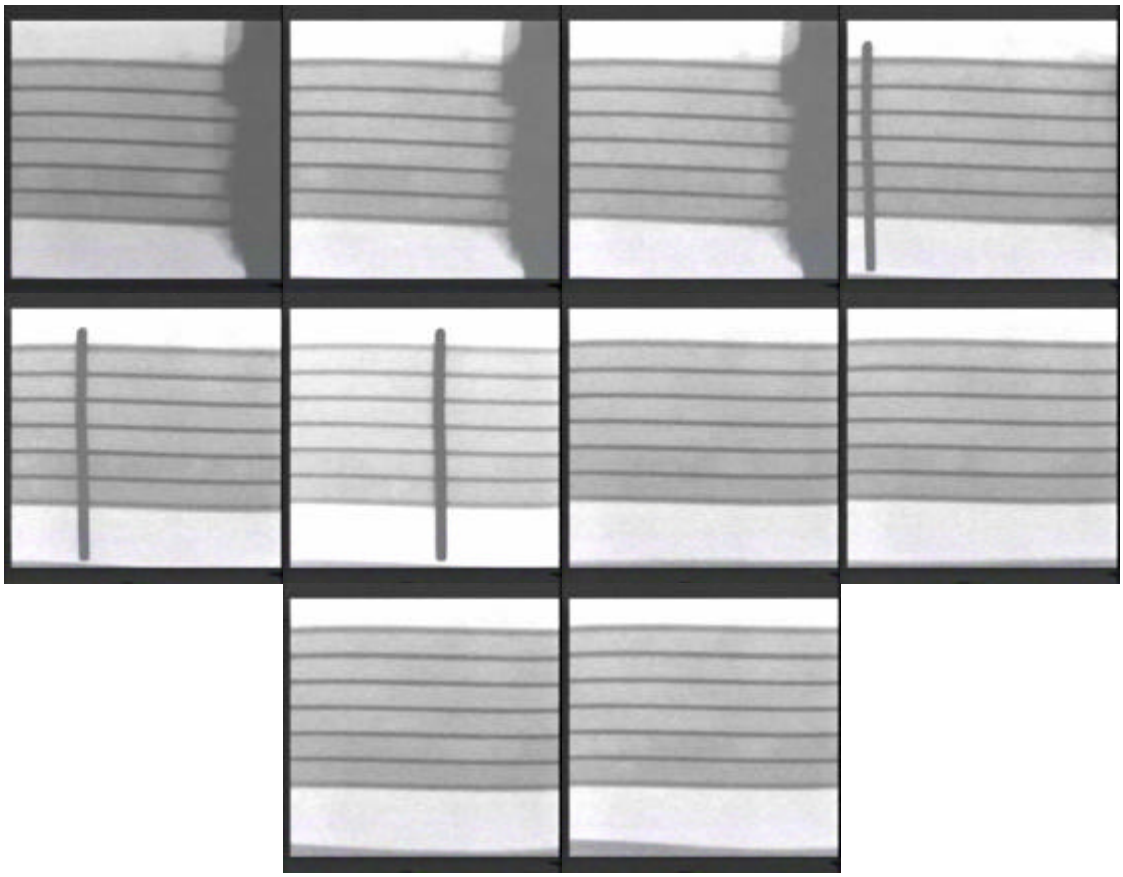

Figure C.13: Sample Pictures for Air-Water, G=200 kg/m^2·s, x=0.3

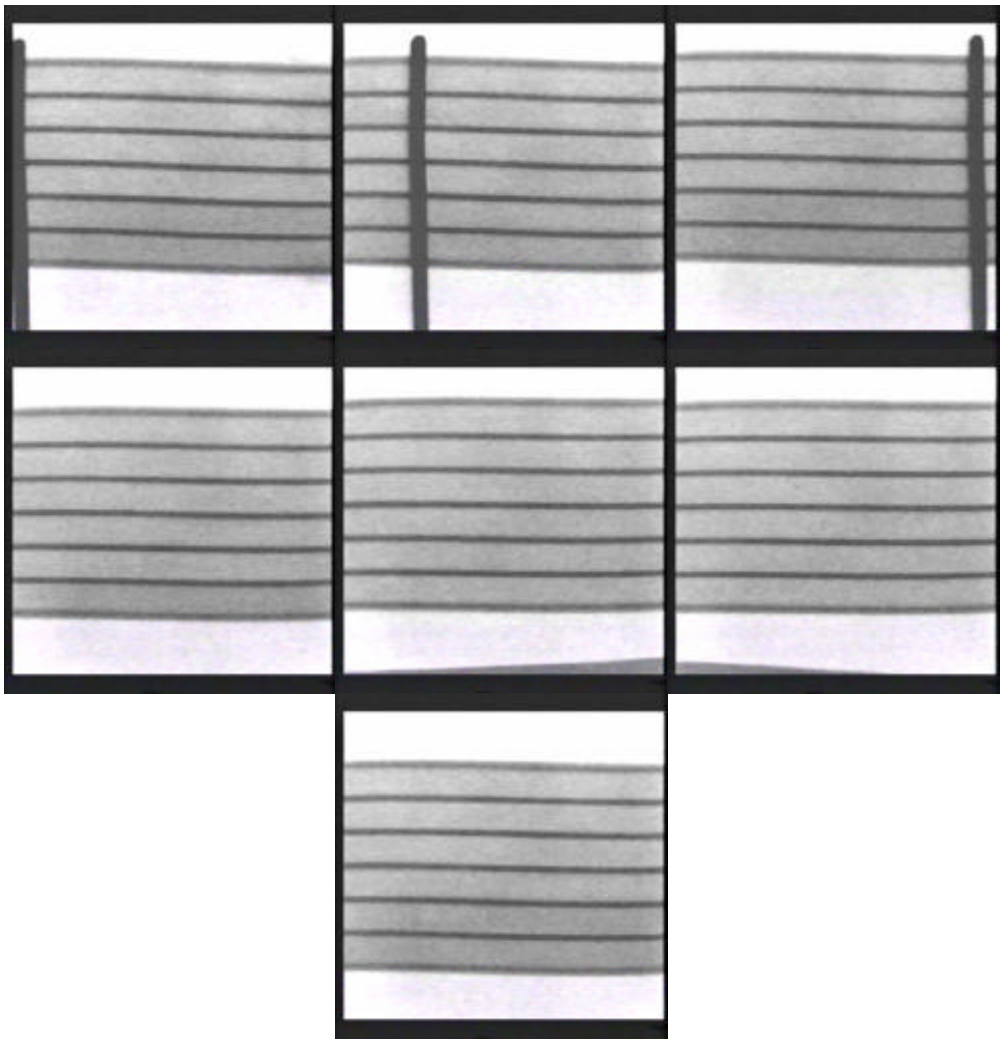

Figure C.14: Sample Pictures for Air-Water, G=250 kg/m^2·s, x=0.1

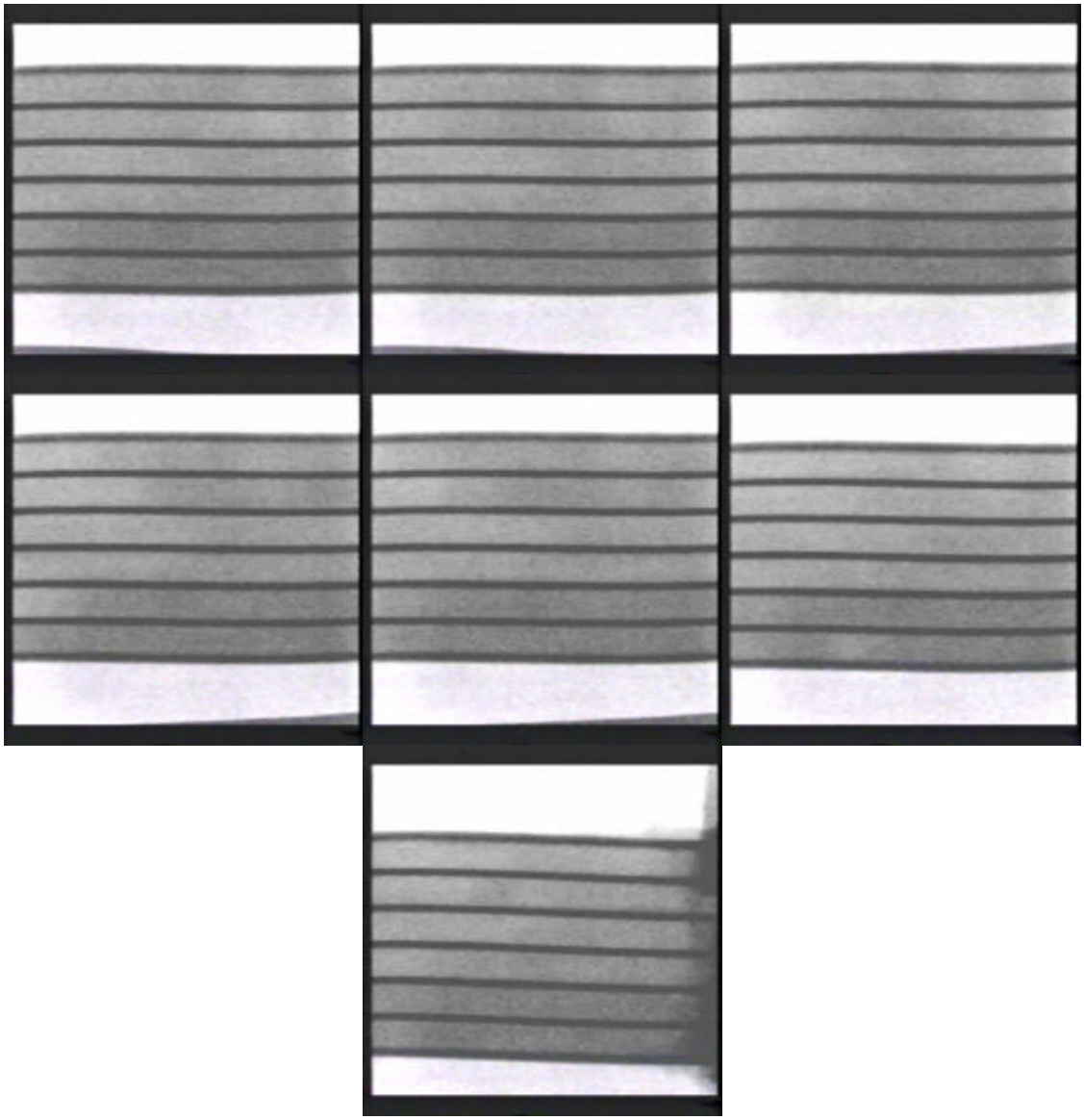

Figure C.15: Sample Pictures for Air-Water, G=300 kg/m^2·s, x=0.1